

Electronic Thesis and Dissertation Repository

7-9-2018 2:00 PM

Crop monitoring and yield estimation using polarimetric SAR and optical satellite data in southwestern Ontario

Chunhua Liao, *The University of Western Ontario*

Supervisor: Wang, Jinfei, *The University of Western Ontario*

A thesis submitted in partial fulfillment of the requirements for the Doctor of Philosophy degree in Geography

© Chunhua Liao 2018

Follow this and additional works at: <https://ir.lib.uwo.ca/etd>



Part of the [Remote Sensing Commons](#)

Recommended Citation

Liao, Chunhua, "Crop monitoring and yield estimation using polarimetric SAR and optical satellite data in southwestern Ontario" (2018). *Electronic Thesis and Dissertation Repository*. 5465.
<https://ir.lib.uwo.ca/etd/5465>

This Dissertation/Thesis is brought to you for free and open access by Scholarship@Western. It has been accepted for inclusion in Electronic Thesis and Dissertation Repository by an authorized administrator of Scholarship@Western. For more information, please contact wlsadmin@uwo.ca.

Abstract

Optical satellite data have been proven as an efficient source to extract crop information and monitor crop growth conditions over large areas. In local- to subfield-scale crop monitoring studies, both high spatial resolution and high temporal resolution of the image data are important. However, the acquisition of optical data is limited by the constant contamination of clouds in cloudy areas. This thesis explores the potential of polarimetric Synthetic Aperture Radar (SAR) satellite data and the spatio-temporal data fusion approach in crop monitoring and yield estimation applications in southwestern Ontario.

Firstly, the sensitivity of 16 parameters derived from C-band Radarsat-2 polarimetric SAR data to crop height and fractional vegetation cover (FVC) was investigated. The results show that the SAR backscatters are affected by many factors unrelated to the crop canopy such as the incidence angle and the soil background and the degree of sensitivity varies with the crop types, growing stages, and the polarimetric SAR parameters. Secondly, the Minimum Noise Fraction (MNF) transformation, for the first time, was applied to multi-temporal Radarsat-2 polarimetric SAR data in cropland area mapping based on the random forest classifier. An overall classification accuracy of 95.89% was achieved using the MNF transformation of the multi-temporal coherency matrix acquired from July to November. Then, a spatio-temporal data fusion method was developed to generate Normalized Difference Vegetation Index (NDVI) time series with both high spatial and high temporal resolution in heterogeneous regions using Landsat and MODIS imagery. The proposed method outperforms two other widely used methods. Finally, an improved crop phenology detection method was proposed, and the phenology information was then forced into the Simple Algorithm for Yield Estimation (SAFY) model to estimate crop biomass and yield. Compared with the SAFY model without forcing the remotely sensed phenology and a simple light use efficiency (LUE) model, the SAFY incorporating the remotely sensed phenology can improve the accuracy of biomass estimation by about 4% in relative Root Mean Square Error (RRMSE). The studies in this thesis improve the ability to monitor crop growth status and production at subfield scale.

Keywords

Crop monitoring, polarimetric SAR, crop height, fractional vegetation cover, crop type classification, random forest, minimum noise fraction, spatio-temporal data fusion, phenology detection, biomass and yield estimation

Co-Authorship Statement

This thesis was prepared according to the integrated-article layout designed by the Faculty of Graduate Studies at Western University, London, Ontario, Canada. All the work stated in this thesis including methodology and algorithm development, modelling, experimental testing, results interpretation, and writing draft manuscripts for publication was carried out by the author under the supervision of Dr. Jinfei Wang. Dr. Wang contributed in the development of methodology ideas and provided valuable comments, editing and revision on the manuscripts. She also provided financial support, software, hardware, and data etc. Dr. Xiaodong Huang contributed to the Radarsat-2 data preparation for Chapter 3. Dr. Taifeng Dong contributed to the methodology design for Chapter 5. All co-authors provided help on editing and proofreading of the manuscripts.

Chunhua Liao, Jinfei Wang, Xiaodong Huang, Jiali Shang. (2018). Contribution of minimum noise fraction transformation of multi-temporal RADARSAT-2 polarimetric SAR data to cropland classification. *Canadian Journal of Remote Sensing*, 44(4). (*In press*)

Chunhua Liao, Jinfei Wang, Jiali Shang, Xiaodong Huang, Jianguai Liu, Ted Huffman. (2018). Sensitivity study of RADARSAT-2 polarimetric SAR parameters to crop height and fractional vegetation cover of corn and winter wheat in Southwest Ontario, Canada. *International Journal of Remote Sensing*, 39(5): 1475-1490.

Chunhua Liao, Jinfei Wang, Ian Pritchard, Jianguai Liu, Jiali Shang. 2017. A spatio-temporal vegetation index image fusion model for generating high spatial and temporal resolution NDVI images in cropland areas. *Remote Sensing*, 9(11):1125.

Acknowledgments

First and foremost, I would like to express my deepest gratitude to my supervisor, Dr. Jinfei Wang, for her years of guidance, caring, patience, encouragement, and providing me with excellent atmosphere for doing research. Without her academic support, my research could not be conducted smoothly. I would like to thank my advisory committee members, Dr. James A. Voogt, Dr. Philip J. Stooke for their support and assistance on my Ph.D. program, no matter the comprehensive examination or the annual diagnostics meetings. I would like to thank Dr. Danielle Way from Department of Biology for supporting my comprehensive examination as a comprehensive examination committee. My sincere gratitude goes to Dr. Jiali Shang from Agriculture and Agri-Food Canada (AAFC) for providing the Radarsat-2 data and help on editing every draft of the paper. I would like to acknowledge Jianguo Liu, Taifeng Dong from AAFC for providing valuable suggestions on my research.

I would like to express my special thanks to Boyu Feng, Hongyu Zhang, Ian Pritchard, Matthew Roffey, Peter Crawford, Xiaoxuan Sun, Yang Song, and Dr. Xiaodong Huang, the visiting scholar Yurong Shi, Dr. Zengpei Li, Dr. Jianbing Shi, Dr. Mingfeng Xing, and Dr. Yuecheng Li. They are not only my lab mates but also friends who accompanied me in the lab during the past four years. Thanks goes to Tianyu Qi and Jun Zhang for their kind help when I first came to Canada. Appreciation goes to the staffs of the Department of Geography, Lori Johnson, Angelica Lucaci for their assistance. I would like to thank Daryl Patterson and Bo Shan from A&L Canada Laboratories Inc. for offering me a part-time job as a GIS specialist. I learned a lot from this valuable work experience.

I would like to acknowledge the Ontario Trillium Scholarship for providing me financial support during my Ph.D. program.

Finally, I am deeply grateful to my parents for their understanding and sacrifice. Special thanks go to my husband, Yongjun He, for his love and being my everlasting supporter. He is always there cheering me up in the hard times. Without their love and support, I could never complete my Ph.D. program.

Table of Contents

Abstract.....	i
Co-Authorship Statement.....	iii
Acknowledgments.....	iv
Table of Contents.....	v
List of Tables.....	x
List of Figures.....	xii
List of Appendices.....	xix
List of Acronyms, Symbols, Nomenclature.....	xx
Chapter 1.....	1
1 Introduction.....	1
1.1 Background.....	1
1.2 Research questions.....	3
1.3 Research objectives.....	3
1.4 Study areas.....	4
1.5 Structure of the dissertation.....	5
References.....	7
Chapter 2.....	10
2 Sensitivity Study of Radarsat-2 Polarimetric SAR to Crop Height and Fractional Vegetation Cover of Corn and Wheat.....	10
2.1 Introduction.....	10
2.2 Methodology.....	12
2.2.1 Study site.....	12
2.2.2 Field data collection and analysis.....	13
2.2.3 Radarsat-2 data acquisition and processing.....	17

2.2.4	Correlation analysis	20
2.3	Results and Discussion	21
2.3.1	Correlation analysis between Radarsat-2 polarimetric SAR parameters and crop height.....	21
2.3.2	Correlation analysis between Radarsat-2 polarimetric SAR parameters and FVC	25
2.4	Conclusions.....	28
	References	30
Chapter 3	35
3	Contribution of Minimum Noise Fraction Transformation of Multi-temporal Radarsat-2 Polarimetric SAR Data to Cropland Classification	35
3.1	Introduction.....	35
3.2	Methodology.....	38
3.2.1	Study site.....	38
3.2.2	Ground reference data collection	39
3.2.3	Satellite data acquisition	41
3.2.4	Satellite image preprocessing	42
3.2.5	Image classification	45
3.3	Results and discussion	47
3.3.1	Effects of MNF transformation on cropland classification in terms of different polarimetric SAR parameter sets	51
3.3.2	Effects of MNF transform on cropland classification in terms of the timing of Radarsat-2 datasets.....	55
3.3.3	Assessment of the best classification result and the random forest classifier	62
3.3.4	Comparison of the classification accuracies using the MNF transformation of multi-temporal Radarsat-2 polarimetric SAR data with the accuracies using other strategies	65
3.4	Conclusions.....	67

References	69
Chapter 4.....	74
4 A Spatio-Temporal Data Fusion Model for Generating NDVI Time Series in Heterogeneous Regions.....	74
4.1 Introduction.....	74
4.2 Methodology.....	79
4.2.1 Theoretical Basis.....	79
4.2.2 Weighting System.....	82
4.2.3 Implementation of the STVIFM	87
4.3 Results of Data Fusion	91
4.3.1 Test Sites and Data.....	91
4.3.2 Selection of Window Size for Deriving the Coefficients	96
4.3.3 Algorithm Tests in Regions with Different Landscapes.....	98
4.3.4 Tests with Time Series Data	108
4.4 Discussion.....	112
4.4.1 Advantages of the STVIFM.....	112
4.4.2 Limitations and Uncertainties of the STVIFM	114
4.4.3 Applications of the STVIFM	115
4.5 Conclusions.....	116
References	117
Chapter 5.....	123
5 Phenology, Biomass and Yield Estimation for Corn and Soybean Using Spatio-Temporal Fusion of Landsat-8 and MODIS Data.....	123
5.1 Introduction.....	123
5.2 Materials	126
5.2.1 Study site.....	126

5.2.2	Field data collection	127
5.2.3	Regional weather data.....	128
5.2.4	Crop classification data.....	129
5.2.5	Remote sensing data	130
5.3	Methodology.....	130
5.3.1	Spatio-temporal data fusion	131
5.3.2	Crop phenology detection based on an improved TSF approach	132
5.3.3	Dry aboveground biomass and yield estimation based on the SAFY model.....	137
5.4	Results.....	145
5.4.1	Evaluation of fitted fAPAR based on the CSDM	145
5.4.2	Verification of detected phenology with ground-based observations.....	146
5.4.3	Performance of the SAFY model.....	149
5.5	Discussions	156
5.5.1	Factors that affect the crop biomass and yield.....	156
5.5.2	Uncertainties of the estimated crop biomass and yield.....	157
5.5.3	Application of this study in crop production forecasting.....	158
5.5.4	Contributions and limitations of this study.....	159
5.6	Conclusions.....	160
	References	161
Chapter 6	167
6	Discussion and Conclusions.....	167
6.1	Summary	167
6.2	Conclusions and research contributions.....	170
6.3	Future research.....	173
6.3.1	Crop height estimation using PolInSAR.....	173

6.3.2	Crop classification using polarimetric SAR data and optical remotely sensed data based on deep learning method	173
6.3.3	Crop yield forecasting using Unmanned Aerial Vehicle (UAV)-based remotely sensed data	174
	References	176
	Appendices.....	179
	Curriculum Vitae	209

List of Tables

Table 2-1: Characteristics of the acquired Radarsat-2 data and the phenology of crops associated with each image	18
Table 2-2: Correlation coefficients (r) between in situ measured crop height and Radarsat-2 polarimetric SAR parameters. The minus means negative correlation.....	23
Table 2-3: Correlation coefficients (r) between in situ measured FVC and Radarsat-2 polarimetric SAR parameters. The minus means negative correlation.....	26
Table 3-1: Field data collected in the field work and the number of pixels used for training and testing	39
Table 3-2: The acquired Radarsat-2 data	41
Table 3-3: The acquired Landsat-8 data	42
Table 3-4: Different combination of multi-temporal Radarsat-2 data	44
Table 3-5: Overall classification accuracies (%) for different polarimetric SAR parameter sets using single-date Radarsat-2 data	48
Table 3-6: Overall classification accuracies (%) using the original and the MNF transformation of multi-temporal Radarsat-2 parameters for different scenarios	49
Table 3-7: Overall classification accuracies using different combinations of coherency matrix datasets acquired on different dates and the MNF transformation of the datasets. The coloured cells mean the dates when the RADARSA-2 data were used for the classification (Red: two-date; Orange: three-date; Yellow: four-date; Green: five-date; Blue: six-date; Purple: seven-date; Cyan: eight-date; Pink: nine-date; Gray: Ten-date)..	58
Table 3-8: Confusion matrix for the land cover mapping obtained using the MNF transformation of the coherency matrix at Scenario 5 (B=Built-up, C=Corn, F=Forest, FG=Forage, S=Soil, SB=Soybean, T=Tobacco, WM=Watermelon, W=Wheat).....	64

Table 3-9: Comparison of the classification accuracies using the MNF transformation of multi-temporal Radarsat-2 polarimetric SAR data with the accuracies using other strategies at Scenario 5 based on RF and SVM classifier (B=Built-up, C=Corn, F=Forest, FG=Forage, S=Soil, SB=Soybean, T=Tobacco, WM=Watermelon, W=Wheat)	66
Table 4-1: Dates of MODIS and Landsat-8 OLI images.....	92
Table 4-2: Correlation analysis between Landsat-8 NDVI image and correspondent synthetic NDVI image based on different algorithm using different window size at the Ontario site.....	98
Table 4-3: Statistical parameters of the correlation analysis between synthetic and original Landsat NDVI image.	106
Table 4-4: Images used for the four methods in the four experiments.	108
Table 5-1: The dates for field work and crop types	128
Table 5-2: The acquired dates for remote sensing data.	130
Table 5-3: The data used for regression analysis between NDVI and fAPAR.....	133
Table 5-4: The optimized parameters in CSDM obtained for soybean and corn	135
Table 5-5: LUE or LUEmax for corn and soybean reported in literature	142
Table 5-6: The twelve SAFY parameters	144
Table 5-7: The accuracy of the biomass estimation using different strategies	155
Table D-1: Biomass Field Datasheet (Corn/Soybean).....	189
Table D-2: Biomass Lab Datasheet (Corn).....	190
Table D-3: Biomass Lab Datasheet (Soybean).....	191

List of Figures

Figure 1-1: Overview of the study areas.....	5
Figure 1-2: The relationships among Chapter 2, 3, 4 and 5.....	6
Figure 2-1: Map of study site and the sample sites.....	13
Figure 2-2: Photos of different growth stages of (a-h) wheat and (i-p) corn: (a) leaf development, (b) tillering (c) beginning of stem elongation, (d) middle of stem elongation, (e) end of heading, (f) development of fruit, (g) ripening (hard dough), (h) fully ripe; (i) leaf development (3 leaves), (j) leaf development (4 leaves), (k) Leaf development (6 leaves), (l) beginning of stem elongation, (m) end of stem elongation, (n) tassel emergence; (o) tassel in flower and stigmata fully emerged, (p) end of flowering and stigmata completely dry.	15
Figure 2-3: Relationship between crop height and BBCH scale for (a) corn and (b) winter wheat.....	16
Figure 2-4: Correlation between FVC and (a) corn height and (b) wheat height.....	17
Figure 2-5: Scatterplots between (a) corn height and $ HV ^2$ (C_{22}), (b) corn height and $ HH-VV ^2$ (T_{22}).....	24
Figure 2-6: Scatterplots between (a) wheat height and $ HV ^2$ (C_{22}), (b) wheat height and Yamaguchi Helix Scattering.....	25
Figure 2-7: Scatterplots between (a) corn FVC and $ HV ^2$ (C_{22}), (b) corn FVC and $ HV/VV ^2$	27
Figure 2-8: Scatterplots between (a) wheat FVC and $ VV ^2$ (C_{33}), (b) wheat FVC and $ HH+VV ^2$ (T_{11}).....	28
Figure 3-1: Location of the study site.....	39
Figure 3-2: Map of the (a) surveyed fields, (b) training data and (c) testing data.....	40

Figure 3-3: The first two bands and the last band of the MNF transformation of multi-temporal coherency matrix of Radarsat-2 data	50
Figure 3-4: Eigenvalues of the MNF transformation of the multi-temporal Radarsat-2 coherency matrix for Scenario 5. Eigenvalues of the MNF transformation of the multi-temporal Radarsat-2 coherency matrix for Scenario 5.	50
Figure 3-5: The average overall accuracy before and after the MNF transformation for different polarimetric SAR parameter sets	52
Figure 3-6: The average producer's accuracies of all scenarios for 5 dominant land cover types using different SAR parameter sets	53
Figure 3-7: The average overall accuracy before and after the MNF transformation for different scenarios	56
Figure 3-8: Maximum OA using original and MNF transformation of two-date to seven-date coherency matrix datasets	59
Figure 3-9: The average producer's accuracies of all SAR parameter sets for 5 dominant land cover types at different scenarios	60
Figure 3-10: The land cover mapping using the MNF transformation of the coherency matrix at Scenario 5	63
Figure 3-11: The variable importance of different input features (a) before and (b) after the MNF transformation	65
Figure 3-12: Learning curve (OOB accuracy) of the random forest classifier with different numbers of trees (a) original image, (b) MNF transformed image	65
Figure 4-1: Diagram of simulated Normalized Difference Vegetation Index (NDVI) profiles for different crop pixels.	83
Figure 4-2: Flowchart of the spatio-temporal vegetation index image fusion model (STVIFM) algorithm. The steps are shaded by different colors (blue: satellite data	

preprocessing; green: NDVI change detection; orange: weight calculation; purple: coefficients determination; yellow: NDVI prediction).	88
Figure 4-3: Landsat (upper row); and MODIS (lower row) NDVI images from three dates in 2014 over a cropland area in Ontario, Canada.....	93
Figure 4-4: Landsat (upper row) and MODIS (lower row) NDVI images from three dates in 2014 over a mixed crop and grassland area in Kansas, U.S.	94
Figure 4-5: Landsat (upper row) and MODIS (lower row) NDVI images from three dates in 2014 over a cropland area in Xinjiang, China.	95
Figure 4-6: The dates for the available cloud free Landsat imagery and the MODIS time series data for the Ontario site.	96
Figure 4-7: The Landsat and MODIS NDVI image pairs acquired throughout the growing season in Ontario, Canada.....	96
Figure 4-8: The variations of: R^2 (a); a (b); and b (c) with the increasing window size for fine- and coarse-resolution NDVI pairs over different study sites.	97
Figure 4-9: Comparison of the (a) observed Landsat image; and the synthetic images based on: (b) spatial and temporal adaptive reflectance fusion model (STARFM); (c) enhanced spatial and temporal adaptive reflectance fusion model (ESTARFM); (d, e)flexible spatiotemporal data fusion (FSDAF); and (f) spatio-temporal vegetation index image fusion model (STVIFM), in Ontario, Canada. Red boxes show small-area land cover changes occurred on Landsat-8 images acquired at t_p (6 May 2014) and t_n (7 June 2014).	100
Figure 4-10: Scatter plots of the observed and synthetic Landsat NDVI produced by: (a) STARFM; (b) ESTARFM; (c) FSDAF_m; (d) FSDAF_n; and (e) STVIFM in Ontario, Canada.....	101
Figure 4-11: Comparison of the (a) observed Landsat image; and the synthetic images based on: (b) STARFM; (c) ESTARFM; (d, e) FSDAF; and (f) STVIFM, in Kansas, U.S.	

Red boxes show that the harvesting of crops appeared in Landsat-8 images acquired at t_n (20 June 2014) are accurately predicted in the synthetic NDVI image based on the STVIFM and ESTARFM. 102

Figure 4-12: Scatter plots of observed and synthetic Landsat NDVI by: (a) STARFM; (b) ESTARFM; (c) FSDAF_m; (d) FSDAF_n; and (e) STVIFM in Kansas, U.S. 103

Figure 4-13: Comparison of the (a) observed Landsat image; and the synthetic images based on: (b) STARFM; (c) ESTARFM; (d) FSDAF_m; (e) FSDAF_n; and (f) STVIFM in Xinjiang, China. (A–F) Zoom-in images shown in the black boxes on the original NDVI and the all the results generated by the four methods. Red boxes show the senescent fields. 104

Figure 4-14: Scatter plot of observed and synthetic Landsat NDVI by: (a) STARFM; (b) ESTARFM; (c) FSDAF_m; (d) FSDAF_n; and (e) STVIFM in Xinjiang, China. 105

Figure 4-15: The accuracy of predicted NDVI obtained by different methods on four different dates in Ontario site during the growing season: (a) R^2 ; (b) RMSE; (c) MAD; and (d) MD. 109

Figure 4-16: Time series of the average NDVI of: (a) the cornfield; and (b) the wheat field, generated by the STARFM, ESTARFM, FSDAF, and STVIFM algorithms. The predictions shown in the black box (DOY 185) present large difference between the FSDAF and STVIFM. The pictures were collected two days before that date (DOY 183). 111

Figure 5-1: The study site observed on Landsat-8 image in July 2015 (Nir-Red-Green band). The green and yellow polygons are corn fields and soybean fields where the field data were collected; Green and yellow points are the sample sites for corn and soybean. 127

Figure 5-2: Annual time series of (a) daily shortwave solar radiation and (b) daily mean temperature 129

Figure 5-3: Flowchart for crop phenology, biomass, and yield estimation 131

Figure 5-4: Relationship between average NDVI and average $fAPAR$ of the samples collected within each field	134
Figure 5-5: The shape model for (a) corn (BBCH=13, 16, 19, 31, 33, 37, 66, 67, 69, 75, 85, 87, 97) and (b) soybean (BBCH=9, 10, 12, 14, 25, 29, 65, 67, 70, 75, 85, 95, 97). The red lines represent the SOS. The green lines represent the DOS and the blue lines represent EOS.	136
Figure 5-6: Relationship between $fAPAR$ and effective GLAI.....	140
Figure 5-7: Relationship between Pl_a and Pl_b for (a) corn and (b) soybean.....	143
Figure 5-8: Comparison of the $fAPAR$ derived from the remotely sensed images, fitted by the CSDM, and measured in the field for different sample sites: (a) C05-02; (b) C24-02; (c) S09-03; (d) S114-02.	146
Figure 5-9: Comparison of phenological dates between the ground-based observations and estimations, (a) corn, (b) soybean.....	147
Figure 5-10: The spatial patterns of the dates of key phenological events (SOS, DOS, EOS) in the study area in 2015	148
Figure 5-11: Pixel-based ELUE for (a) corn and (b) soybean generated from the SAFY	150
Figure 5-12: Scatter plots showing the relationship between the ELUE derived from SAFY and $fAPAR_{max}$ derived from the CSDM: (a) corn, (b) soybean.....	151
Figure 5-13: Comparison of GLAI simulated by the SAFY (GLAI_SAFY), the remotely sensed GLAI based on the original Landsat data (GLAI_Landsat), and the synthetic GLAI (GLAI_Synthetic) and the in situ measured GLAI (GLAI_CAN-EYE) for sample site (a) C05-02, (b) C24-02, (c) S09-03, (d) S114-02.....	152
Figure 5-14: Spatial map of estimated total biomass using the SAFY model for (a) corn and (b) soybean.....	153

Figure 5-15: Comparison between measured biomass and the estimated biomass by the SAFY with and without forcing the phenology information for (a) corn, (b) soybean..	154
Figure 5-16: Comparison between measured biomass and estimated biomass by the CSDM-LUE model for (a) corn, (b) soybean	155
Figure 5-17: Comparison between measured and estimated yield for (a) corn and (b) soybean	156
Figure A-1: Example of EM wave. E: Electric vector, M: Magnetic vector, C: Propagation direction (https://earth.esa.int/handbooks/asar/CNTR5-5.html).....	179
Figure A-2: Examples of the four polarizations: (a) HH, (b) VV, (c) HV, (d) VH (Retalis, 2010)	180
Figure A-3 Illustration of radar geometry.....	181
Figure A-4: Radarsat-2 SAR beam modes (MacDonald, Dettwiler and Associates Ltd, 2016)	182
Figure A-5: Single beam mode (MacDonald, Dettwiler and Associates Ltd, 2016).....	183
Figure B-1: The spatial relationship between the first two principal components: (a) Scatter-plot of data points collected from two remotely bands labeled X_1 and X_2 with the means of the distribution labeled μ_1 and μ_2 . (b) A new coordinate system is created by shifting the axes to an X' system. (c) The X' axis system is then rotated about its origin (μ_1 , μ_2) so that PC_1 is projected through the semi-major axis of the distribution of points and the variance of PC_1 (Component 1) is a maximum. PC_2 (Component 2) must be perpendicular to PC_1 (Jensen, 2016).....	186
Figure D-1: Work photos	192
Figure D-2: Examples of hemispherical photos (a) corn, (b) soybean	193
Figure D-3: Example of hemispherical photos recoding sheets	194

Figure D-4: Example of biomass recoding sheets	195
Figure D-5: Example of general survey recoding sheets	196
Figure D-6: Detailed locations of the winter wheat sample points and Radarsat-2 image for Stratford study site	198
Figure D-7: Detailed locations of the corn sample points and Radarsat-2 image for Stratford study site	200
Figure D-8: Detailed locations of the corn sample points and Landsat-8 image for Komoka study site	202
Figure D-9: Detailed locations of the soybean sample points and Landsat-8 image for Komoka study site.....	204

List of Appendices

Appendix A: Polarimetric SAR basics	179
Appendix B: Principal component analysis (PCA)	185
Appendix C: Minimum/Maximum Autocorrelation Factors (MAF)	187
Appendix D: Field data collection forms and photos	189
Appendix E: Copyright Releases from Publications	205

List of Acronyms, Symbols, Nomenclature

AAFC: Agriculture and Agri-Food Canada

AAFS: Agriculture and Agri-food System

ALOS: Advanced Land Observing Satellite

ANN: Artificial Neural Networks.

APAR: Absorbed Photosynthetically Active Radiation

AVHRR: Multi-temporal Advanced Very High Resolution Radiometer

BBCH: Biologische Bundesanstalt, Bundessortenamt and Chemical. A scale that describes the crop phenology.

BI: Blend-then-Index

DAM: Dry Aboveground Mass. Dry aboveground biomass.

DHP: Digital Hemispherical Photograph

DOS: Day of Senescence

DOY: Day of Year

DT: Decision Tree. A method for image classification.

EBSCDL: Error-Bound-Regularized Semi-Coupled Dictionary Learning. An algorithm for spatio-temporal data fusion.

ELUE: Effective Light Use Efficiency. The light use efficiency that accounts for all agro-environmental stresses excluding temperature stress.

ENL: Equivalent Numbers of Looks. An indicator to evaluate the speckle filter performance for polarimetric SAR data.

EO: Earth Observation

EOS: End of Season

ESTARFM: Enhanced Spatial and Temporal Adaptive Reflectance Fusion Model.

*f*APAR: Fraction of Absorbed Photosynthetically Active Radiation

FSDAF: Flexible Spatiotemporal Data Fusion

FVC: Fractional Vegetation Cover. The fraction of green vegetation area including leaves and stems projected on the flat surface in unit area.

GDP: Gross Domestic Product

GLAI: Green Leaf Area Index

HH: Horizontal transmitting and Horizontal receiving polarization

HV: Vertical transmitting and Horizontal receiving polarization

IB: Index-then-Blend

KF: Kalman Filter

LAI: Leaf Area Index

LC/LU: Land Cover/Land Use

MAF: Minimum/Maximum Autocorrelation Factors

MERIS: Medium Resolution Imaging Spectrometer

MLC: Maximum-Likelihood Classifier

MMT: Multisensor Multiresolution Technique

MNF: Minimum Noise Fraction

MODIS: Moderate Resolution Imaging Spectroradiometer

NDVI: Normalized Difference Vegetation Index. It is a vegetation index calculated by the reflectance of red band (ρ_{red}) and near infrared band (ρ_{nir}) of the remote sensing images:

$$NDVI = \frac{\rho_{nir} - \rho_{red}}{\rho_{nir} + \rho_{red}}$$

NDVI-LMGM: NDVI Linear Mixing Growth Model

NDVI-BSFM: NDVI-Bayesian Spatiotemporal Fusion Model

OA: Overall Accuracy

$$OA = \frac{\text{Total number of pixels assigned to correct classes}}{\text{Total number of pixels assessed}}$$

OOB: Out-Of-Bag

PA: Producer's Accuracy

$$PA = \frac{\text{Number of correct pixels in a class}}{\text{Total number of pixels of that class from the reference data}}$$

PAR: Photosynthetically Active Radiation

PCA: Principal Component Analysis.

PolInSAR: Polarimetric Interferometry Synthetic Aperture Radar

PolSAR: Polarimetric Synthetic Aperture Radar

RF: Random Forest

RMSE: Root Mean Square Error

RRMSE: Relative RMSE. $RRMSE = RMSE / \text{Average value of the measured data}$

SAFY: Simple Algorithm for Yield Estimates

SAR: Synthetic Aperture Radar

STARFM: Spatial and Temporal Adaptive Reflectance Fusion Model

STDFA: Spatial Temporal Data Fusion Approach

STNLFFM: Spatial and Temporal Nonlocal Filter-Based Data Fusion Method

STVIFM: Spatio-Temporal Vegetation Index image Fusion Model

SLA: Specific Leaf Area

SLC: Single Look Complex

SNR: Signal-to-Noise Ratio

SOS: Start of Season

SPSTFM: Sparse Representation-based Spatiotemporal Reflectance Fusion Model

SVM: Support Vector Machine

UA: User's Accuracy

$$UA = \frac{\text{Number of correct pixels in a class}}{\text{Total number of pixels that were actually classified in that class}}$$

USTARFM: STARFM with help of unmixing-based method

VI: Vegetation Index

VV: Vertical transmitting and Vertical receiving polarization

Chapter 1

1 Introduction

1.1 Background

Canada is a major agricultural production country and plays an important role in the global agricultural market (Shang, McNairn, Deschamps, Jiao, & Champagne, 2011). The agriculture sector employs 12.5% of Canadian employees. In 2016, the Canadian agriculture and agri-food system (AAFS) generated \$ 111.9 billion, accounting for 6.7% of Canada's gross domestic product (GDP) (Agriculture and Agri-Food Canada, 2017). Field crops in the agricultural sector are grown on 36.4 Mha (3.6% of Canada's total landmass) (Wood & Layzell, 2003). They not only provide food and fiber for human beings and livestock, but also have significant influence on climate change by contributing to the global carbon budget (Jones & Vaughan, 2010). To ensure the food security for the growing world population while maintaining environmental health, the need for agricultural land use assessment and crop monitoring is well recognized at the national, regional and global scale. Crop monitoring refers to the monitoring of crop biophysical variables such as crop height, vegetation cover, crop phenology and biomass at temporal scale and spatial scale. With these temporal and spatial biophysical variables, crop production can be estimated. Agriculture and Agri-food Canada has conducted a series of studies in crop monitoring, crop land cover mapping and crop yield estimation. Most of the studies focus on regional or national scale, and the results of these studies can provide products and guidance for better informed trading decisions and agri-environmental policy decisions (Liu, Shang, Vachon, & McNairn, 2013; Wiseman, McNairn, Homayouni, & Shang, 2014). The monitoring of crop growth and crop production forecasting at smaller scale (subfield scale) also enables agriculture companies or farmers to make timely decisions on crop management in order to maximize crop production and boost the agricultural economy. Crop type information is essential for crop monitoring, yield estimation and agriculture statistics reporting (Larrañaga, 2011). Therefore, crop type mapping is also an important topic in agricultural applications.

The use of Earth Observation (EO) technology has provided an efficient way for spatial and temporal monitoring of crops as well as the identification of crop types over large areas (Duveiller & Defourny, 2010). Optical satellites such as Aqua/Terra and Landsat-8 passively observe the earth surface and capture spatial and spectral information of objects on the earth surface. Vegetation indices (VIs), which are related to crop growth conditions, can be computed from the spectral information. Crop biophysical or biochemical variables such as Leaf Area Index (LAI) and chlorophyll content can be derived from the VIs (Rasmus Fensholt, Sandholt, & Rasmussen, 2004; Gutman & Ignatov, 1998; Muñoz-Huerta et al., 2013). The Normalized Difference Vegetation Index (NDVI) time series are widely used for crop phenology detection or crop production estimation (Claverie et al., 2012; Liu et al., 2010; Sakamoto et al., 2005, 2010). Multi-temporal and multi-spectral data are often used for crop classification (Tatsumi, Yamashiki, Canales Torres, & Taïpe, 2015; Wardlow, Egbert, & Kastens, 2007). However, the acquisition of optical data relies heavily on the weather condition as optical bands cannot penetrate cloud. Therefore, the number of cloud-free optical images will be limited if the presence of clouds are frequent.

Synthetic Aperture Radar (SAR) satellites such as the Advanced Land Observing Satellite (ALOS) and Radarsat-2 observe the earth surface in an active way by transmitting and receiving pulses of electromagnetic waves at wavelength from 1 mm to 1 m. They are less weather dependent and can provide crop structure information such as height, size, orientation of leaves, and water content of crop canopy, due to the ability to penetrate clouds, haze, light rain, and vegetation canopy (Berens, 2006). Two important parameters for SAR systems are frequency and polarization. The sensitivity of SAR backscatter depends on their wavelength, polarization, and incidence angle (Jiao, McNairn, Shang, & Liu, 2010). Generally, longer wavelengths such as L-band (15 to 30 cm) and P-band (30 - 100 cm) have better capability of penetrating through the crop canopy than shorter SAR wavelengths such as X-band (2.4 to 3.8 cm) and C-band (3.8 - 7.5 cm) (Lee & Pottier, 2009b). Shorter wavelengths are more sensitive to small surface structures (Huang, Wang, Shang, Liao, & Liu, 2017) and longer wavelengths will interact more with the soil surface instead of the crop canopy since they have a stronger ability to penetrate the crop canopy. Radarsat-2 polarimetric SAR (Appendix A) with four independent polarization channels (HH, HV, VH, VV) can provide more crop structure information than single polarization.

The SAR parameters acquired at a steeper (smaller) incidence angle are more sensitive to crop variables than the parameters acquired at a shallower (larger) incidence angle (Jiao et al., 2010). In many studies, multi-temporal SAR data are coupled with multi-temporal optical data for crop monitoring.

1.2 Research questions

Two of the most important parameters in the application of remote sensing data are spatial resolution, the ground size of an image pixel, and temporal resolution, the length of time it takes for a satellite to revisit the same area on the earth surface. In local-scale to subfield-scale crop monitoring research, not only is the high spatial resolution needed due to the spatial variations of the patchy distribution of different types of crop lands, but also high temporal resolution is needed to monitor the fast growth of crops through the growing season. However, for optical remote sensing data, the two requirements, high spatial resolution and high temporal resolution, generally cannot be met at the same time due to the trade-off in remote sensor designs that balance spatial detail and temporal coverage. For areas with frequent cloud cover, high temporal optical data are more difficult to acquire due to the interference of cloud cover. On the other hand, polarimetric SAR data have great potential in crop monitoring due to its capability of penetrating the clouds, haze, etc., but they are affected by speckle noise and soil background. Therefore, the research questions in this dissertation are:

- (1) What is the potential of multi-temporal Radarsat-2 polarimetric SAR in subfield-scale crop biophysical variable monitoring and crop type mapping?
- (2) How can a limited number of high spatial resolution optical images collected in an area with frequent cloud cover be used for subfield-scale crop growth monitoring and yield estimation?

1.3 Research objectives

The main objectives of the thesis are to monitor crop growth and estimate crop yield at a subfield scale in a cloudy area using different sources of remotely sensed data. To answer the research questions proposed above, the following four specific objectives are defined:

- (1) Investigate the sensitivity of polarimetric SAR parameters to crop biophysical variables and the potential of polarimetric SAR in crop monitoring.
- (2) Improve the crop classification accuracy using multi-temporal polarimetric SAR data, and examine the performance of different polarimetric SAR parameters in crop classification and the impact of the timing of the polarimetric SAR datasets on crop classification in southwestern Ontario.
- (3) Propose a spatio-temporal data fusion method that is suitable for crop monitoring in heterogeneous region to generate NDVI time series with a high temporal and spatial resolution.
- (4) Improve a crop phenology detection method and estimate the crop biomass and yield by calibrating the Simple Algorithm for Yield Estimation (SAFY) model using the spatio-temporal fusion of Landsat-8 and MODIS data.

1.4 Study areas

Ontario is the largest producer (about 63%) of corn in Canada and a major producer of soybean (Statistics Canada, 2015; Statistics Canada, 2018). Most of the field crops are located in southwestern Ontario due to the suitable water, soil and mild climate. The study site for Chapter 2 is the croplands area near Stratford, Ontario and study site for Chapter 3, Chapter 4 and Chapter 5 is near Komoka, Ontario. The study areas are located in the Mixedwood Plains Ecozone in southwestern Ontario, characterized by abundant water supply, relatively mild climate and productive soils for agriculture. It covers a 175 963 km² area bounded by the Great Lakes. Many types of crops are planted in this area such as corn, soybean, and winter wheat. It has a longer growing season than most of the rest of the country. However, it is difficult to obtain cloud-free high spatial resolution satellite images (e.g. Landsat, RapidEye) during the growing season.

The field data including soil moisture, crop height, LAI, phenology, and crop biomass (winter wheat, corn, and soybean) during the whole growing season have been collected in 2013 for the Stratford site and in 2015 for the Komoka site. The multi-temporal Radarsat-

2 polarimetric Synthetic Aperture Radar (SAR) data during the growing season over the two sites have been provided by Agriculture and Agri-Food Canada (AAFC).

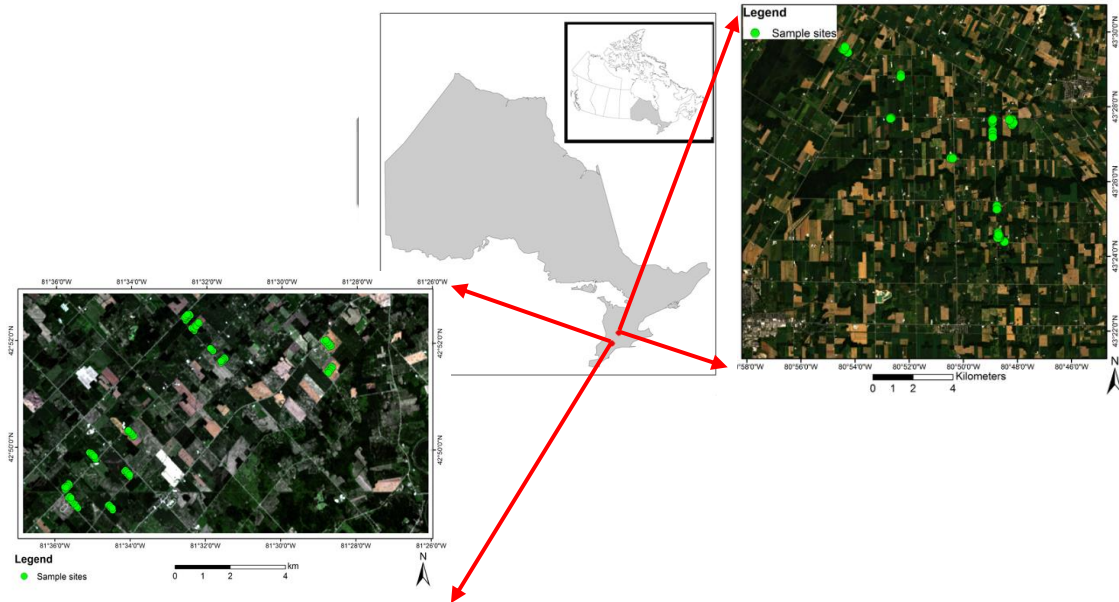


Figure 1-1: Overview of the study areas

1.5 Structure of the dissertation

This dissertation contains six chapters. Chapter 1 introduces the background of this research, and briefly reviews the remote sensing technology used in crop monitoring. It states the research questions, research objectives, and introduces the study areas and thesis structure. The next four chapters are standalone papers that have been published, are in press, or are in review. Chapter 2 presents a sensitivity study of Radarsat-2 polarimetric SAR to crop height and fractional vegetation cover of corn and wheat. Chapter 3 investigates the effects of the Minimum Noise Fraction (MNF) transformation of multi-temporal Radarsat-2 polarimetric SAR data on the performance of cropland classification. It discusses the performance of different polarimetric SAR parameter sets, and the impact of the timing of Radarsat-2 datasets in southwestern Ontario. Chapter 4 presents a new method to fuse Landsat and MODIS NDVI images. In this chapter, I proposed a spatio-temporal vegetation index image fusion method (STVIFM) to generate NDVI time series with both high spatial and high temporal resolution. Chapter 5 proposes an improved

phenology detection method based on the crop classification map generated from Chapter 3 and the STVIFM method proposed in Chapter 4. It estimates crop biomass by calibrating the SAFY model based on the phenology information and remotely sensed Green Leaf Area Index (GLAI). Chapter 6 concludes the dissertation and discusses possible future work. The overall relationships among Chapter 2, Chapter 3, Chapter 4 and Chapter 5 are illustrated in Figure 1-2.

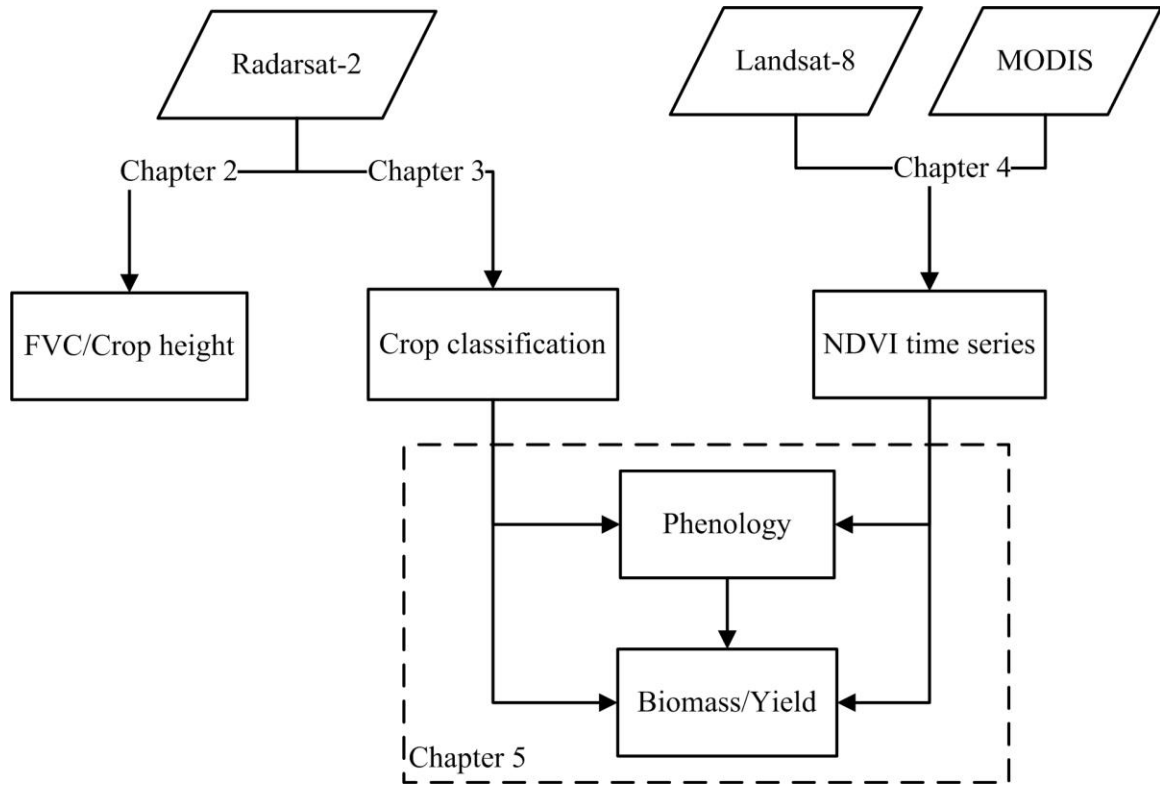


Figure 1-2: The relationships among Chapter 2, 3, 4 and 5

References

- Agriculture and Agri-Food Canada. (2017). *An Overview of the Canadian Agriculture and Agri-Food System 2017*. Retrieved from <http://www.agr.gc.ca/eng/about-us/publications/economic-publications/an-overview-of-the-canadian-agriculture-and-agri-food-system-2017/?id=1510326669269>
- Statistics Canada. (2015). *Corn: Canadian's third most valuable crop*. Retrieved from <http://www.statcan.gc.ca/pub/96-325-x/2014001/article/11913-eng.htm>
- Statistics Canada. (2018). *Soybean area as a proportion of total field crop area by census division (CD), 2016 Canada*. Retrieved from <http://www.statcan.gc.ca/pub/95-634-x/2017001/article/54904/catm-ctra-078-eng.htm>
- Berens, P. (2006). Introduction to synthetic aperture radar (SAR). In *Advanced Radar Signal and Data Processing* (pp. 3-13–14). Neuilly-sur-Seine, France: RTO. Retrieved from <http://oai.dtic.mil/oai/oai?verb=getRecord&metadataPrefix=html&identifier=ADA470686>
- Claverie, M., Demarez, V., Duchemin, B., Hagolle, O., Ducrot, D., Marais-sicre, C., ... Dedieu, G. (2012). Maize and sun flower biomass estimation in southwest France using high spatial and temporal resolution remote sensing data. *Remote Sensing of Environment*, *124*, 844–857. <http://doi.org/10.1016/j.rse.2012.04.005>
- Duveiller, G., & Defourny, P. (2010). A conceptual framework to define the spatial resolution requirements for agricultural monitoring using remote sensing. *Remote Sensing of Environment*, *114*(11), 2637–2650. <http://doi.org/10.1016/j.rse.2010.06.001>
- Fensholt, R., Sandholt, I., & Rasmussen, M. S. (2004). Evaluation of MODIS LAI, fAPAR and the relation between fAPAR and NDVI in a semi-arid environment using in situ measurements. *Remote Sensing of Environment*, *91*(3–4), 490–507. <http://doi.org/10.1016/j.rse.2004.04.009>
- Gutman, G., & Ignatov, A. (1998). The derivation of the green vegetation fraction from NOAA / AVHRR data for use in numerical weather prediction models. *International Journal of Remote Sensing*, *19*(8), 1533–1543. <http://doi.org/10.1080/014311698215333>
- Huang, X., Wang, J., Shang, J., Liao, C., & Liu, J. (2017). Application of polarization signature to land cover scattering mechanism analysis and classification using multi-temporal C-

- band polarimetric RADARSAT-2 imagery. *Remote Sensing of Environment*, 193, 11–28. <http://doi.org/10.1016/j.rse.2017.02.014>
- Jiao, X., McNairn, H., Shang, J., & Liu, J. (2010). The Sensitivity of multi-frequency (X, C and L-Band) radar backscatter signatures to bio-physical variables (LAI) over corn and soybean fields. *International Archives Photogrammetry Remote Sensing*, XXXVIII(Part B 7), 317–321. Retrieved from http://www.isprs.org/proceedings/XXXVIII/part7/b/pdf/317_XXXVIII-part7B.pdf
- Jones, H. G., & Vaughan, R. A. (2010). *Remote Sensing of Vegetation*. Oxford University Press.
- Lee, J.-S., & Pottier, E. (2009). *Polarimetric Radar Imaging: From Basics to Applications*. Boca Raton, FL, USA: CRC Press.
- Liu, C., Shang, J., Vachon, P. W., & McNairn, H. (2013). Multiyear crop monitoring using polarimetric RADARSAT-2 data. *IEEE Transactions on Geoscience and Remote Sensing*, 51(4), 2227–2240. <http://doi.org/10.1109/TGRS.2012.2208649>
- Liu, J., Pattey, E., Miller, J. R., McNairn, H., Smith, A., & Hu, B. (2010). Estimating crop stresses, aboveground dry biomass and yield of corn using multi-temporal optical data combined with a radiation use efficiency model. *Remote Sensing of Environment*, 114(6), 1167–1177. <http://doi.org/10.1016/j.rse.2010.01.004>
- Muñoz-Huerta, R. F., Guevara-Gonzalez, R. G., Contreras-Medina, L. M., Torres-Pacheco, I., Prado-Olivarez, J., & Ocampo-Velazquez, R. V. (2013). A review of methods for sensing the nitrogen status in plants: Advantages, disadvantages and recent advances. *Sensors (Switzerland)*, 13(8), 10823–10843. <http://doi.org/10.3390/s130810823>
- Sakamoto, T., Wardlow, B. D., Gitelson, A. A., Verma, S. B., Suyker, A. E., & Arkebauer, T. J. (2010). A Two-Step Filtering approach for detecting maize and soybean phenology with time-series MODIS data. *Remote Sensing of Environment*, 114(10), 2146–2159. <http://doi.org/10.1016/j.rse.2010.04.019>
- Sakamoto, T., Yokozawa, M., Toritani, H., Shibayama, M., Ishitsuka, N., & Ohno, H. (2005). A crop phenology detection method using time-series MODIS data. *Remote Sensing of Environment*, 96(3–4), 366–374. <http://doi.org/10.1016/j.rse.2005.03.008>
- Shang, J., McNairn, H., Deschamps, B., Jiao, X., & Champagne, C. (2011). Contribution of TerraSAR-X data to in-season crop mapping in Canada. *Proceedings of TerraSAR-X Science Team Meeting*, 14–16.
- Tatsumi, K., Yamashiki, Y., Canales Torres, M. A., & Taïpe, C. L. R. (2015). Crop classification of upland fields using random forest of time-series Landsat 7 ETM+ data. *Computers and Electronics in Agriculture*, 115, 171–179. <http://doi.org/10.1016/j.compag.2015.05.001>

- Wardlow, B. D., Egbert, S. L., & Kastens, J. H. (2007). Analysis of time-series MODIS 250 m vegetation index data for crop classification in the U.S. Central Great Plains. *Remote Sensing of Environment*, 108(3), 290–310. <http://doi.org/10.1016/j.rse.2006.11.021>
- Wiseman, G., McNairn, H., Homayouni, S., & Shang, J. (2014). RADARSAT-2 Polarimetric SAR Response to Crop Biomass for Agricultural Production Monitoring. *IEEE Journal of Selected Topics in Applied Earth Observations and Remote Sensing*, 7(11), 4461–4471.
- Wood, S., & Layzell, D. (2003). A Canadian biomass inventory: feedstocks for a bio-based economy\final report. *BIOCAP Canada Foundation*, 42 pp. <http://doi.org/citeulike-article-id:11656574>

Chapter 2

2 Sensitivity Study of Radarsat-2 Polarimetric SAR to Crop Height and Fractional Vegetation Cover of Corn and Wheat¹

2.1 Introduction

Corn and wheat are two different types of crops according to their leaf size (broad-leaf crop vs narrow-leaf crop). They are two of the most valuable crops in Canada and play an important role in the global agricultural trading market (Farm Credit Canada, 2013; Hamel & Dorff, 2014). The corn and wheat planted in Canada are used not only for grain but also for silage. Therefore, crop growth monitoring enables farmers to make timely decisions on crop management in order to maximize crop production. Crop height is closely related to crop biomass and phenology and is an important indicator for crop growth monitoring, crop discrimination and crop production estimation (McNairn & Brisco, 2004; Srivastava, Patel, & Navalgund, 2006). The fractional vegetation cover (FVC) is defined as the fraction of green vegetation area including leaves and stems projected on a flat surface in unit area. FVC is an important structural property of a plant canopy, and a key variable for describing the vegetation coverage. It was found that FVC has a linear relationship with the Fraction of Absorbed Photosynthetically Active Radiation ($fAPAR$) of crop canopies, which is an important variable for crop biomass estimation (Donghui Xie, Wang, Wang, Yan, & Song, 2013). Compared with Leaf Area Index (LAI), both the LAI and FVC can be calculated from the gap fractions derived from digital hemispherical photographs (DHP) (Mougin et al., 2014), whereas the uncertainties of FVC is lower than the effective LAI (Verger, Martínez, Camacho - de Coca, & García - Haro, 2009).

¹ A version of this chapter has been published (Chunhua Liao, Jinfei Wang, Jiali Shang, Xiaodong Huang, Jiangui Liu, Ted Huffman. Sensitivity Study of RADARSAT-2 Polarimetric SAR Parameters to Crop Height and Fractional Vegetation Cover of Corn and Winter Wheat in Southwest Ontario, Canada. *International Journal of Remote Sensing*. 2018, 39(5): 1475-1490).

The use of Earth Observation (EO) technology has provided an efficient way for various agricultural applications such as crop variable estimation, crop type inventory, and crop yield prediction due to its capability of providing timely and large spatial coverage of land surface information over a wide range of spatial and temporal scales. However, optical image acquisition relies heavily on the weather condition, and the crop variable estimation over regions with frequent cloud cover usually cannot meet the temporal requirement for agricultural applications during the growing season. Besides, the estimation of crop structure-related variables such as crop height is difficult using optical remote sensing (Srivastava et al., 2006). The multi-temporal polarimetric Synthetic Aperture Radar (SAR) data can be used to monitor the temporal variations of crop growth more continuously than optical data due to its capability of penetrating the clouds, haze, light rain, and vegetation canopy. Polarimetric SAR data have great potential in estimating crop variables because SAR parameters are sensitive to many vegetation biophysical variables such as plant structure, leaf size, stem density, biomass and plant water content (McNairn & Brisco, 2004; Srivastava et al., 2006). However, they are also sensitive to the parameters of the underlying soil such as soil moisture and surface roughness (Jiao et al., 2011; McNairn & Brisco, 2004), and the responses of SAR backscatter to crop biophysical characteristics vary with SAR frequency, incidence angle, and polarizations (Jiao et al., 2011), which makes the application of SAR in agriculture more complicated. Previous research has revealed that polarimetric SAR parameters are sensitive to crop leaf area index (LAI) (Jiao et al., 2011) and crop biomass (Mattia et al., 2003; Wiseman, McNairn, Homayouni, & Shang, 2014) which is related to crop phenological development (Shang et al., 2013). Jiao et al.(2010) investigated the sensitivity of X-band, C-band, and L-band polarimetric SAR backscatter signatures to corn and soybean LAI. High correlations were observed between L-band and C-band polarimetric SAR backscatter and corn and soybean LAI, whereas X-band backscatter was poorly correlated with both corn and soybean LAI. C-band SAR data have relatively longer wavelength than X-band SAR data but shorter wavelength than L-band SAR data, and thus they can penetrate into the crop canopy but are less affected by soil due to reduced penetration into the deep crop canopy (McNairn & Brisco, 2004). Therefore, the C-band polarimetric SAR data was regarded as a good candidate for biomass and LAI estimation of crops (Ferrazzoli et al., 1997; Lin, Chen, Pei, Zhang, & Hu, 2009).

Radarsat-2 is a C-band (5.3 GHz) polarimetric SAR system with the spatial resolutions varying from 3 to 100 meters (Appendix A). Although the orbit repeat cycle is 24 days, the flexibility of the steerable radar beam makes the revisit intervals shorter. With the available of quad-polarization data from satellites such as Radarsat-2, it is possible to study the sensitivity of more polarimetric SAR parameters including the four polarizations (HH, HV, VH, and VV) and several decompositions extracted from the quad polarization scattering matrix. Previous studies have investigated the sensitivity of SAR parameters to crop biophysical variables such as LAI and biomass, and it was observed that the responses of SAR backscatter to LAI or biomass of narrow-leaf crops such as wheat were different from the responses of SAR backscatter to the LAI or biomass of broad-leaf crops such as corn (Fontanelli, Paloscia, Zribi, & Chahbi, 2013; Macelloni, Paloscia, Pampaloni, Marliani, & Gai, 2001; Mattia et al., 2003; Smith et al., 2006; Wiseman et al., 2014). Besides LAI and biomass, crop height is an important crop variable in vegetation growth dynamics monitoring, and FVC has been used for crop biomass estimation and crop evapotranspiration modeling (Paruelo, Lauenroth, & Roset, 2000; Singh, Dutta, & Dharaiya, 2013). If these crop variables can be estimated from Radarsat-2 polarimetric SAR data, the high temporal frequency requirement can be met. However, the responses of Radarsat-2 polarimetric SAR backscatter to crop height and FVC were not well documented in the literature. In order to investigate the potential of Radarsat-2 polarimetric SAR in crop height and crop FVC estimation and monitoring, the objectives of this study are (1) to investigate the sensitivity of different Radarsat-2 polarimetric SAR parameters to crop height and FVC of corn and wheat, and (2) to explore the variations in SAR responses to crop height and FVC at different crop growth stage.

2.2 Methodology

2.2.1 Study site

The study site was selected near Stratford, Ontario, Canada (43.3° N, 80.8° W, Figure 2-1), a place located in the Mixedwood Plains Ecozone, and characterized by abundant water supply, ideal weather conditions and productive soil for agriculture. The study site's average elevation is about 350 m above sea level with a relatively flat terrain. Corn and winter wheat are two major crops grown in this area. Corn in our study area is generally

seeded in May and harvested in September or October, and winter wheat is seeded in October and harvested in July. Five corn fields and 4 winter wheat fields were selected for intensive field measurements and sampling throughout the growing season in 2013. The fields were within a 100 km² area.

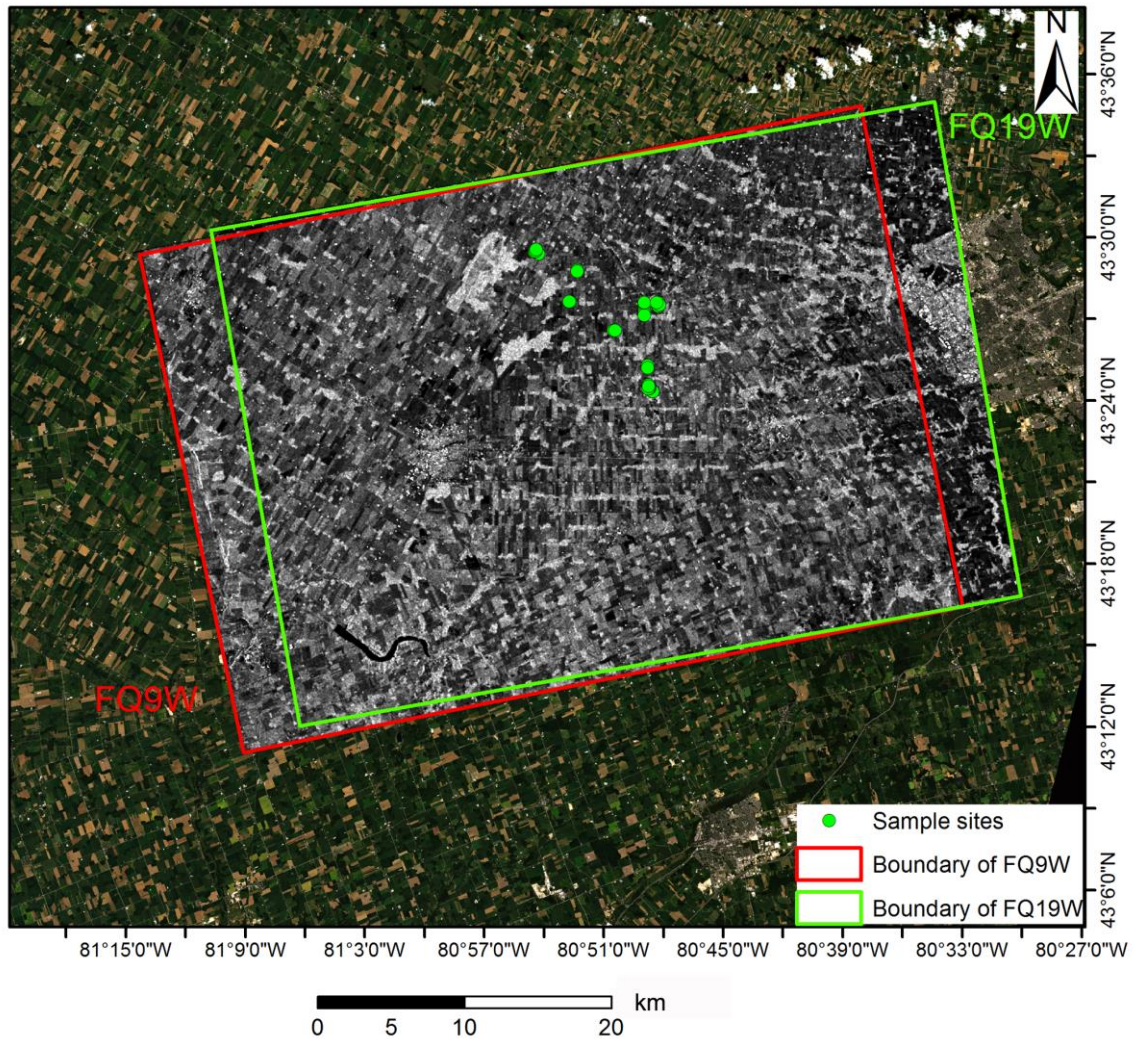


Figure 2-1: Map of study site and the sample sites

2.2.2 Field data collection and analysis

A total of 17 sample sites located in 5 corn fields and 18 sample sites in 4 winter wheat fields were deployed (Appendix D). The distance between two neighboring sample sites is between 30 - 120 meters. The Garmin GPS, with a maximum error of 3 meters, was used to navigate during each field work. Field data collected at each sample site within a 5 m by

5 m area include: (1) taking 14 hemispherical photographs for each sampling site (7 photographs along one row and then another 7 photographs along another row), (2) collecting 6 crop height measurements and recording crop phenological stages using the Biologische Bundesanstalt, Bundessortenamt and Chemical (BBCH) scale (AAFC, 2011) at each sample site. For corn fields, the photos were taken by the camera facing downward if the plant height of corn was less than 1.2 m, otherwise, the photos were taken upward. For wheat fields, the photos were all taken downwards. The FVC for each sample site was extracted from the 14 hemispherical photographs using CAN-EYE (Weiss & Baret, 2017). The mean crop height of the 6 measurements was calculated for each sample site. The fieldwork was conducted from April to August 2013, concurrently with Radarsat-2 satellite passing over. Figure 2-2 gives a synopsis of the corn and winter wheat at different growing stages during the period under study.

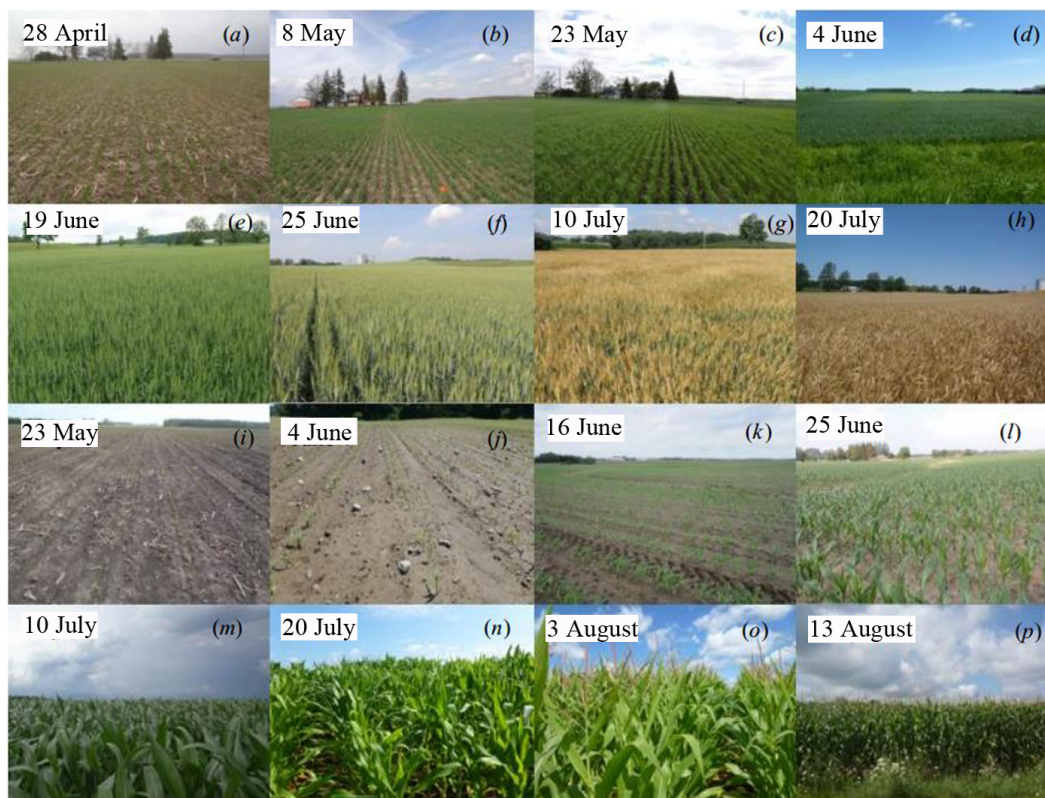


Figure 2-2: Photos of different growth stages of (a-h) wheat and (i-p) corn: (a) leaf development, (b) tillering (c) beginning of stem elongation, (d) middle of stem elongation, (e) end of heading, (f) development of fruit, (g) ripening (hard dough), (h) fully ripe; (i) leaf development (3 leaves), (j) leaf development (4 leaves), (k) Leaf development (6 leaves), (l) beginning of stem elongation, (m) end of stem elongation, (n) tassel emergence; (o) tassel in flower and stigmata fully emerged, (p) end of flowering and stigmata completely dry.

Crop height was related to crop phenology and crop biomass, especially at the early growing stage. According to the phenological stage survey, the relationship between the BBCH scale and the average crop height of each sample site is shown in Figure 2-3 (a) and Figure 2-3 (b). In this study site, when the corn height was around 150 cm, the BBCH scale was observed as 51, and the phenology of corn reached to the beginning of heading and tasselling. When the wheat height was greater than 65 cm, the BBCH scale was observed as 59, the end of heading. It was observed that different wheat height could have the same wheat BBCH. This may be because that the difference of wheat varieties and growth

conditions lead to the difference of wheat height even though they are at the same phenology. Experience in fields showed that plants canopy can have different heights or LAI values in the same field – with the same BBCH.

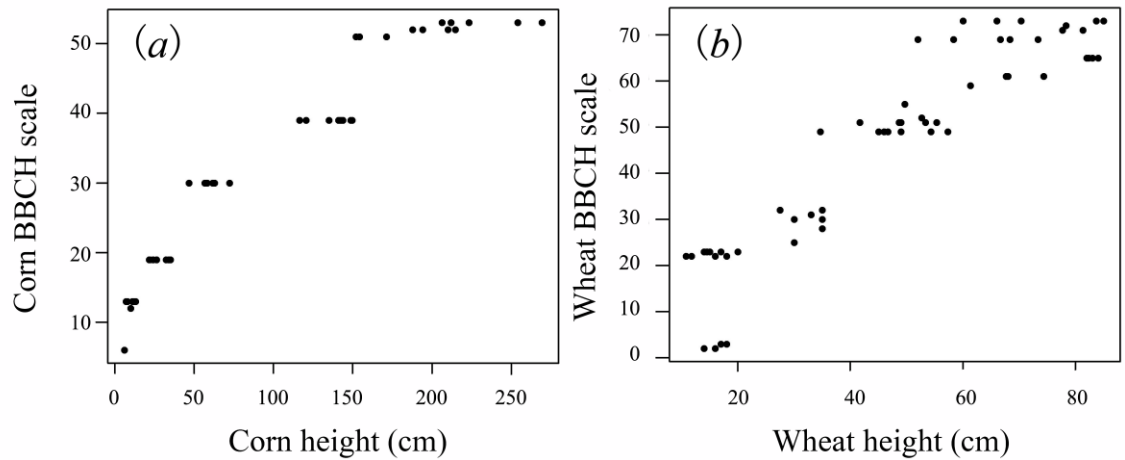


Figure 2-3: Relationship between crop height and BBCH scale for (a) corn and (b) winter wheat

Corn FVC showed a strong correlation with corn height at the early growing stages but became less responsive when the height was greater than 150 cm, as the plants continued growth in the vertical dimension after canopy reached closure. For wheat, FVC also showed a saturation phenomenon when wheat height was greater than 45 cm, and it varied from nearly 60% to 85% (Figure 2-4). According to the definition of FVC, this phenomenon for wheat may be because the dense plants and narrow leaves of wheat make the stems contribute a large percentage to the FVC, and accordingly lead to the saturation of FVC at the early stage. In addition, this large variation of FVC at the later stage may be caused by the difference of wheat varieties.

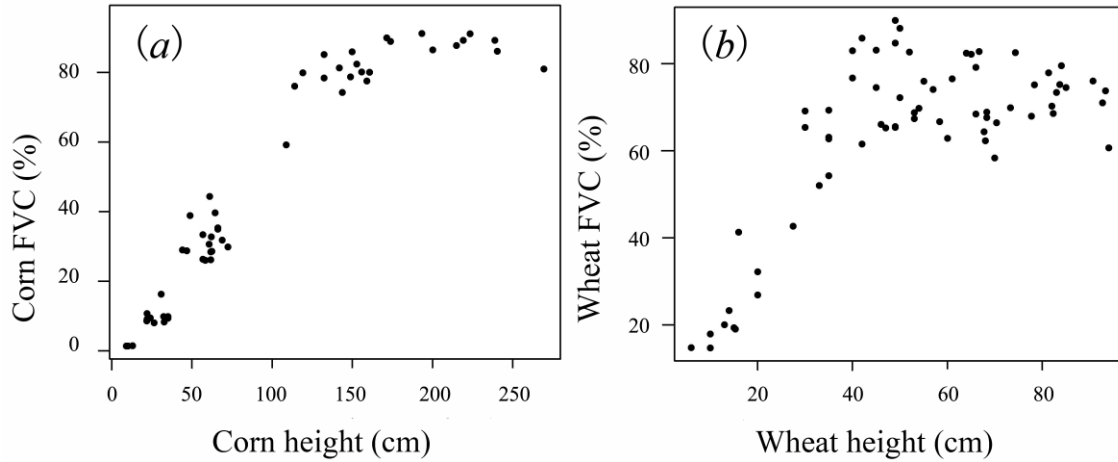


Figure 2-4: Correlation between FVC and (a) corn height and (b) wheat height

2.2.3 Radarsat-2 data acquisition and processing

The characteristics of the Radarsat-2 data used in this study and the phenology of the winter wheat and corn associated with each image were shown in Table 2-1. Radarsat-2 polarimetric SAR can provide full polarimetric data with its Wide Fine Quad-polarization mode (FQW) at different incidence angles. The temporal resolution for the same mode is 24 days. However, most of the crops such as corn in North America grow rapidly in the summer season. For example, during the 16-day period from June 25 to July 11, the average height of corn changed from 60 cm to 145 cm. So if only the polarimetric SAR images acquired at the same mode were used, there will be a lack of data at some important phenological stage. For this reason, 10 SAR images at two modes: FQ9W (incidence angle: 27.2°-30.5°) and FQ19W (incidence angle: 37.7°-40.4°) during the growing season from 29 April 2013 to 13 August 2013, were acquired and analysed together in this study, and the time intervals were shortened to 10-14 days. The difference of the two incidence angles is about 10°. Even though the backscatter will decrease slightly with the increase of incidence angle (McNairn, van der Sanden, Brown, & Ellis, 2000), the sensitivity will not change significantly when the difference of the two incidence angles is less or equal to 10° degrees if the data for each incidence angle could cover all phenological stages (Fontanelli et al., 2013).

Table 2-1: Characteristics of the acquired Radarsat-2 data and the phenology of crops associated with each image

Date	Sensor type	Incidence angle (°)	Beam	Crop type	Growing stage of most crops
29 April 2013	Radarsat-2	27.2-30.5	FQ9W	Wheat	Leaf development (5 leaves)
08 May 2013	Radarsat-2	37.7-40.4	FQ19W	Wheat	Beginning of tillering
23 May 2013	Radarsat-2	27.2-30.5	FQ9W	Wheat/corn	Beginning of stem elongation/Leaf development (3 leaves)
02 June 2013	Radarsat-2	37.7-40.4	FQ19W	Wheat/corn	Middle of stem elongation/ Leaf development (4 leaves)
16 June 2013	Radarsat-2	27.2-30.5	FQ9W	Wheat/corn	End of heading / Leaf development (6 leaves)
26 June 2013	Radarsat-2	37.7-40.4	FQ19W	Wheat/corn	Development of fruit/ Beginning of stem elongation
10 July 2013	Radarsat-2	27.2-30.5	FQ9W	Wheat/corn	Ripening (hard dough)/ End of stem elongation
20 July 2013	Radarsat-2	37.7-40.4	FQ19W	Wheat/corn	Fully ripe/ Tassel emergence
03 August 2013	Radarsat-2	27.2-30.5	FQ9W	Corn	Tassel in flower and stigmata fully emerged
13 August 2013	Radarsat-2	37.7-40.4	FQ19W	Corn	End of flowering and stigmata completely dry

Radarsat-2 data were processed using *PolSARPro 4.2* (López-Martínez, Ferro-Famil, and Pottier, 2005) and the final pixel size of the Radarsat-2 data was 12.5m. A 7×7 boxcar filter was applied to the data by averaging the speckle noise (Goodman, 1976) to suppress the speckle. Then, orthorectification was performed using *MapReady 3.2* (Alaska Satellite Facility, 2012). A variety of parameters can be extracted from the Radarsat-2 polarimetric SAR data. The covariance matrix (\mathbf{C}_3) and coherency matrix (\mathbf{T}_3) are convertible fundamental matrices, from which other decomposition parameters can be derived. The covariance matrix (\mathbf{C}_3) was extracted from the single look complex (SLC) format SAR data, which can be described by a scattering matrix \mathbf{S} (Equation (2-1)) (Lee and Pottier 2009):

$$\mathbf{S} = \begin{bmatrix} S_{HH} & S_{HV} \\ S_{VH} & S_{VV} \end{bmatrix} \quad (2-1)$$

The four elements of the \mathbf{S} matrix S_{HH} , S_{HV} , S_{VH} , and S_{VV} represent the four polarizations, with each polarization having a complex pair.

The covariance matrix \mathbf{C}_3 can be expressed as Equation (2-2):

$$\begin{aligned}
\mathbf{C}_3 &= \langle \mathbf{f}_{3L} \cdot \mathbf{f}_{3L}^{*T} \rangle = \begin{bmatrix} C_{11} & C_{12} & C_{13} \\ C_{21} & C_{22} & C_{23} \\ C_{31} & C_{32} & C_{33} \end{bmatrix} \\
&= \begin{bmatrix} \langle |S_{HH}|^2 \rangle & \langle \sqrt{2}S_{HH}S_{HV}^* \rangle & \langle S_{HH}S_{VV}^* \rangle \\ \langle \sqrt{2}S_{HV}S_{HH}^* \rangle & \langle 2|S_{HV}|^2 \rangle & \langle \sqrt{2}S_{HV}S_{VV}^* \rangle \\ \langle S_{VV}S_{HH}^* \rangle & \langle 2S_{HV}(S_{HH} - S_{VV})^* \rangle & \langle |S_{VV}|^2 \rangle \end{bmatrix} \quad (2-2)
\end{aligned}$$

where $\mathbf{f}_{3L} = [S_{HH} \ \sqrt{2}S_{HV} \ S_{VV}]^T$. For the monostatic case, $S_{HV} = S_{VH}$, * denotes the conjugate, || denotes the modulus, and $\langle \ \rangle$ denotes the average.

The coherency matrix \mathbf{T}_3 can be expressed as Equation (2-3):

$$\begin{aligned}
\mathbf{T}_3 &= \langle \mathbf{f}_{3P} \cdot \mathbf{f}_{3P}^{*T} \rangle = \begin{bmatrix} T_{11} & T_{12} & T_{13} \\ T_{21} & T_{22} & T_{23} \\ T_{31} & T_{32} & T_{33} \end{bmatrix} \\
&= \frac{1}{2} \begin{bmatrix} \langle |S_{HH} + S_{VV}|^2 \rangle & \langle (S_{HH} + S_{VV})(S_{HH} - S_{VV})^* \rangle & \langle 2(S_{HH} + S_{VV})S_{HV}^* \rangle \\ \langle (S_{HH} - S_{VV})(S_{HH} + S_{VV})^* \rangle & \langle |S_{HH} - S_{VV}|^2 \rangle & \langle 2(S_{HH} - S_{VV})S_{HV}^* \rangle \\ \langle 2S_{HV}(S_{HH} + S_{VV})^* \rangle & \langle 2S_{HV}(S_{HH} - S_{VV})^* \rangle & \langle 4|S_{HV}|^2 \rangle \end{bmatrix} \quad (2-3)
\end{aligned}$$

where $\mathbf{f}_{3P} = \frac{1}{\sqrt{2}} [S_{HH} + S_{VV} \ S_{HH} - S_{VV} \ S_{HV} + S_{VH}]^T$.

In the covariance matrix, the upper or lower triangular elements are complex numbers. The diagonal elements C_{11} , C_{22} , and C_{33} are used as the backscattering coefficients of the targets in horizontal polarization (HH), cross polarization (HV), and vertical polarization (VV) respectively ($C_{11} = \sigma_{HH}^0$, $C_{22} = \sigma_{HV}^0$, $C_{33} = \sigma_{VV}^0$) (Duguay, Bernier, Lévesque, & Tremblay, 2015), and they are associated with the structural characteristics of the targets. The three diagonal elements in the coherency matrix (\mathbf{T}_3) matrix, T_{11} ($|HH+VV|^2$), T_{22} ($|HH-VV|^2$), and T_{33} ($|HV|^2$) are Pauli decomposition parameters and are associated with single bounce scattering, double bounce scattering, and volume scattering respectively (Lee and Pottier 2009). It has been reported that the element T_{22} ($|HH-VV|^2$) of Radarsat-2 Pauli-basis decomposition is a good indicator of crop growth development since it represents double bounce and is related to crop canopy (Liu et al., 2013; Wiseman et al.,

2014). Because the element T_{33} is the same as C_{22} , which represents HV polarization, T_{33} is not analysed in this study.

The Cloude-Pottier decomposition, Yamaguchi 4-component decomposition, radar vegetation index (RVI), as well as the intensity ratio (HH/VV, HV/VV, HV/HH) were obtained from the covariance matrix. These polarimetric SAR parameters reflect the scattering characteristics associated with the structural information of targets, such as the dominant type of scattering, the randomness of the scattering. The Cloude-Pottier decomposition includes entropy (H), anisotropy (A), and alpha angle (α). Entropy (H) is the randomness of the scattering, which ranges between 0 and 1. The alpha angle identifies the type of scattering, which varies among surface scattering ($0^\circ - 40^\circ$), volume scattering ($40^\circ - 50^\circ$) and double-bounce scattering ($50^\circ - 90^\circ$). The anisotropy (A) represents how relatively important the second eigenvalue is in comparison to the third eigenvalue (Cloude & Pottier, 1996). The Yamaguchi 4-component decomposition is a modification of the Freeman-Durden decomposition. It decomposes covariance matrix into volume scattering, helix scattering, double bounce scattering and single bounce scattering. The surface scattering and double bounce components represent the same mechanisms as in Freeman-Durden decomposition. The helix component is added to interpret areas with sharp corners and edges over urban areas (Yamaguchi, Moriyama, Ishido, & Yamada, 2005).

The radar vegetation index (RVI) was proposed to monitor the vegetation growth condition (Kim & van Zyl, 2009), and it was found that RVI had a good correlation with different vegetation indices such as LAI and NDVI as well as the crop water content. The RVI was calculated by Equation (2-4).

$$RVI = \frac{8\sigma_{HV}^0}{\sigma_{HH}^0 + \sigma_{VV}^0 + 2\sigma_{HV}^0} \quad (2-4)$$

where σ_{HH}^0 , σ_{HV}^0 , and σ_{VV}^0 represent the backscatter at HH, HV, and VV polarization.

2.2.4 Correlation analysis

Correlation analysis between the crop variable observations at all the sample sites and their corresponding Radarsat-2 polarimetric SAR parameter values was conducted to evaluate the sensitivity of SAR parameters to crop variables through the course of the growth cycle.

The crop height and FVC were collected through fieldwork from April to August. The scatterplots of SAR response to crop height and FVC show different patterns or trends at different crop stages. Therefore, the correlation analysis between SAR parameters and crop variables was conducted separately at different growing stages for corn and wheat.

2.3 Results and Discussion

The SAR data obtained at two different incidence angles were combined in this study in order to shorten the revisit time and capture the important phenological changes of crops during the growing season. From the scatterplots between different Radarsat-2 polarimetric SAR parameters, including linear backscatter coefficients, Pauli decomposition, Cloude-Pottier decomposition, Yamaguchi four-component decomposition parameters, radar vegetation index and the intensity ratios ($|HH/VV|^2$, $|HV/VV|^2$, $|HV/HH|^2$), and crop variables (crop height and FVC), it was found that the responses of SAR parameters to the crop variables were different for corn and wheat, and the responses were also different at different growing stages. Corn and wheat are two distinct types of crops with different leaf size, orientation, and canopy structures. Corn has a much broader leaf size than wheat, and the contribution of corn leaves to backscattering dominates and the contribution of stems is attenuated for the broadleaf crop (Macelloni et al., 2001; Paloscia et al., 2014). Wheat leaf is narrow, and the contribution of the leaves and stems to backscattering is comparable (Macelloni et al., 2001; Paloscia et al., 2014). In addition, the soil below, the canopy and the change of crop physical structure can also affect the SAR backscatter, and the penetrating capability of C-band SAR signal can be weakened by the growing canopy volume and accumulation of biomass.

2.3.1 Correlation analysis between Radarsat-2 polarimetric SAR parameters and crop height

From the scatterplots between corn height and different SAR parameters, it was found that the corn height was correlated with most SAR parameters, especially $|HV|^2$, $|HH-VV|^2$, and $|HV/VV|^2$, when the height was less than 150 cm or before the heading of corn (hereafter we call it the early stage). When the corn grew taller than 150 cm (hereafter we call it the later stage), the sensitivity of most SAR parameters to the corn height was lost. From the

scatterplots between wheat height and different SAR parameters, three distinctive stages were observed for most SAR parameters. The two height thresholds for the three stages were 25 cm (middle of tillering) and 65 cm (end of heading) (hereafter we call the three stages the early stage, the middle stage, and the later stage).

Table 2-2 provides the correlation coefficients (r) between in-situ measured crop height and the Radarsat-2 polarimetric SAR parameters for corn and wheat at two different growing stages. The sensitivity of polarimetric SAR parameters to crop variables was higher for corn than for wheat, which is consistent with the finding by Wiseman et al. (2014) in their study over western Canada. It was also found that most polarimetric SAR parameters had negative relationship with wheat height, and the correlation was very weak. At the early stage when wheat height was less than 25 cm, SAR backscatter was not responsive to wheat height at all. This is probably due to the dominant influence of soil moisture caused by the melting of snow at the beginning of winter wheat growth. Therefore, the analysis at the early stage was not listed in Table 2-2.

Table 2-2: Correlation coefficients (r) between in situ measured crop height and Radarsat-2 polarimetric SAR parameters.

SAR parameters	Corn		Wheat	
	Height <150 cm	Height ≥150 cm	25 ≤ Height <65 cm	Height ≥65 cm
Linear polarization				
$ HH ^2(C_{11})$	0.87*	-0.52*	-0.28	-0.3
$ HV ^2(C_{22})$	0.94*	-0.44	-0.75*	-0.2
$ VV ^2(C_{33})$	0.53*	-0.14	-0.45*	-0.37*
Pauli decomposition				
$ HH+VV ^2(T_{11})$	0.58*	-0.14	-0.46*	-0.39*
$ HH-VV ^2(T_{22})$	0.92*	-0.77*	-0.1	-0.32*
Intensity ratio				
$ HH/VV ^2(C_{11}/C_{33})$	0.76*	-0.4	0.35	0.17
$ HV/HH ^2(C_{22}/C_{11})$	0.63*	0.2	-0.55*	0.1
$ HV/VV ^2(C_{22}/C_{33})$	0.89*	0.1	-0.14	0.36*
Radar vegetation index				
RVI	0.73*	0.36	-0.51*	0.26
Cloude-Pottier decomposition				
Entropy(H)	0.69*	-0.22	-0.46*	-0.1
Anisotropy(A)	-0.53*	-0.44	0.32	-0.1
Alpha(α)	-0.62*	0.41	-0.45*	-0.14
Yamaguchi 4-component decomposition				
Yamaguchi single bounce	0.39*	0.00	-0.33	-0.4
Yamaguchi double bounce	0.78*	-0.68*	0.3	0.00
Yamaguchi volume scattering	0.8*	-0.5*	-0.2	0.00
Yamaguchi helix scattering	0.81*	-0.3	-0.62*	-0.24

* p -value < 0.01

Figure 2-5 illustrates the relationships between the corn height and $|HV|^2$ (a) and $|HH-VV|^2$ (b) for the two modes (FQ9W and FQ19W). The HV polarization, representing volume scattering, was significantly correlated with the corn height at the early stage ($r=0.94$). At the later stage, the HV backscatter intensity decreased with the further increase of corn height, and the sensitive to the corn height became weak. This is because that HV is primarily representing the volume scattering at early growing stages, but once the corn grows taller and denser, the SAR penetration ability is limited. Therefore, L-band polarimetric SAR may be more useful for the corn height estimation for the later growing stage. The $|HH-VV|^2$ is strongly correlated with the corn height at the early stage ($r=0.92$), and a good negative correlation was also observed at the later stage ($r=-0.77$). This correlation was also supported by Liu's work addressing that $|HH-VV|^2$ was strongly correlated with corn LAI, and $|HH-VV|^2$ decreased as the LAI increased in the later stage

(Liu et al., 2013). The $|\text{HH-VV}|^2$ represents double-bounce scattering and it is related to the growth of stems. At different stages of corn, the dominant scattering may be different. If there is only one dominant scattering, the correlation with the height would be high. Otherwise, the correlation would be lower. The good correlations between $|\text{HH-VV}|^2$ and corn height at both stages, even though the trends of the correlations are opposite, indicate that the $|\text{HH-VV}|^2$ has a great potential in corn height monitoring and estimation through the whole growing season.

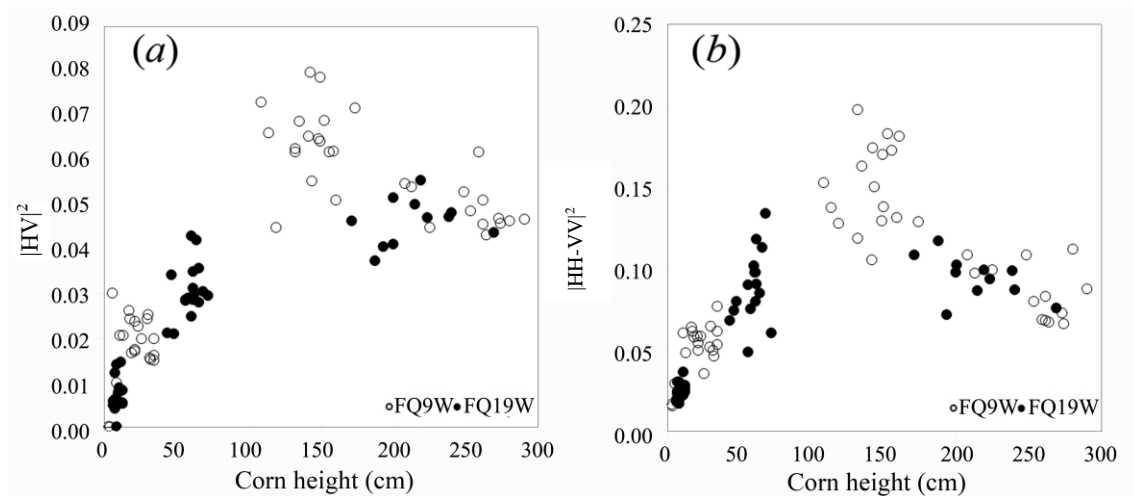


Figure 2-5: Scatterplots between (a) corn height and $|\text{HV}|^2$ (C_{22}), (b) corn height and $|\text{HH-VV}|^2$ (T_{22})

Table 2-2 shows that most SAR parameters except $|\text{HV}|^2$ and Yamaguchi helix scattering were not sensitive to wheat height in this study site. Figure 2-6 illustrates that the relationship between the wheat height and $|\text{HV}|^2$ (a) and Yamaguchi helix scattering (b) for the two modes (FQ9W and FQ19W). At the early stage when the wheat height was less than 25 cm, no SAR parameters were sensitive to wheat height. The HV backscatter from FQ9W (29 April) was much higher than that from FQ19W (8 May). This is perhaps due to the much higher soil moisture after the rain on 29 April when the FQ9W mode image was acquired (Baghdadi et al., 2007; Shoshany, Svoray, Curran, Foody, & Perevolotsky, 2000), the large soil roughness or crop residues (Huang, Wang, & Shang, 2016) at the early growing stage. It was also observed that wheat height was negatively correlated with $|\text{HV}|^2$ ($r=-0.75$) and Yamaguchi helix scattering ($r=-0.62$) at the middle stage. This may be

because that the dense vertical and hollow stems would absorb the backscatter (Fontanelli et al. 2013; Macelloni et al. 2001), hence it results in the decrease of backscatter with the growth of wheat during the stem elongation. At the later stage, the wheat was in its heading and ripening stage, the $|HV|^2$ and Yamaguchi helix scattering increased drastically and was no longer sensitive to wheat height. It is likely that the emergence of inflorescence led to the change of the wheat canopy and affected the responses of SAR parameters. In addition, as the wheat kernels developed, the inside of them changed from a liquid state to dough, and became denser in consistency and thus resulting in the increase in SAR backscatters (Wiseman et al., 2014). Due to the variations of $|HV|^2$ and Yamaguchi helix scattering before and after the heading stage, they may be applied to the wheat phenology detection.

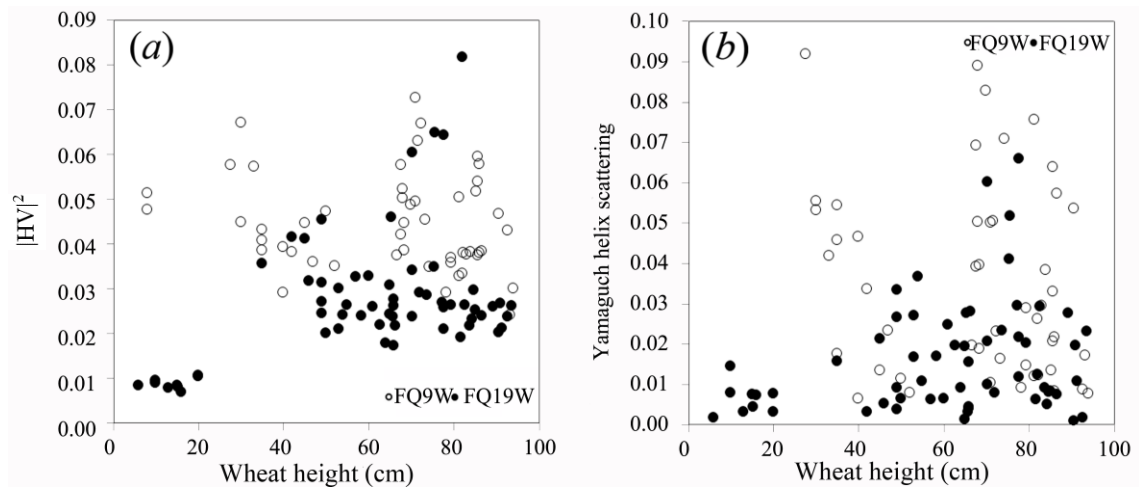


Figure 2-6: Scatterplots between (a) wheat height and $|HV|^2$ (C22), (b) wheat height and Yamaguchi Helix Scattering

2.3.2 Correlation analysis between Radarsat-2 polarimetric SAR parameters and FVC

Table 2-3 shows the correlation coefficients (r) between the in-situ measured FVC and Radarsat-2 polarimetric SAR parameters for corn and wheat at two different growing stages. Previous research has found that when crop (corn and soybean) LAI reached to a certain value ($LAI > 3$) (Jiao et al., 2011), the sensitivity of Radarsat-2 polarimetric SAR parameters to crop LAI decreased. A similar phenomenon also exists in the correlation analysis between SAR parameters and corn FVC. All SAR parameters were insensitive to

corn FVC when FVC was greater than 75% (the beginning of tassel emergence). For wheat FVC, because of the influence of soil at the early stage, and the saturation and the large variation of FVC at later stage (Figure 2-4), no SAR parameters were found sensitive to wheat FVC at any stage.

Table 2-3: Correlation coefficients (r) between in situ measured FVC and Radarsat-2 polarimetric SAR parameters.

SAR parameters	Corn		Wheat	
	FVC<75%	FVC≥75%	FVC<42%	FVC≥42%
Linear polarization				
$ HH ^2(C_{11})$	0.59*	0.55*	0.14	-0.35
$ HV ^2(C_{22})$	0.89*	0.35	0.1	-0.51*
$ VV ^2(C_{33})$	0.1	-0.24	-0.52*	-0.46*
Pauli decomposition				
$ HH+VV ^2(T_{11})$	0.14	-0.32	-0.51*	-0.37
$ HH-VV ^2(T_{22})$	0.82*	0.56*	0.41*	-0.35
Intensity ratio				
$ HH/VV ^2(C_{11}/C_{33})$	0.73*	0.35	0.5*	0.22
$ HV/HH ^2(C_{22}/C_{11})$	0.71*	0.32	0.00	-0.22
$ HV/VV ^2(C_{22}/C_{33})$	0.96*	0.00	0.35	0.1
Radar vegetation index				
RVI	0.75*	0.33	0.17	-0.14
Cloude-Pottier decomposition				
Entropy(H)	0.75*	0.00	0.51*	-0.00
Anisotropy (A)	-0.49*	0.00	0.39	-0.00
Alpha (α)	-0.54*	0.32	-0.42*	-0.24
Yamaguchi 4-component decomposition				
Yamaguchi single bounce	-0.1	-0.1	-0.41*	-0.24
Yamaguchi double bounce	0.66*	0.37	0.28	-0.1
Yamaguchi volume scattering	0.82*	0.41*	0.00	-0.17
Yamaguchi helix scattering	0.59*	0.1	0.00	-0.35

* p -value < 0.01

Among the three linear polarizations (HH, HV, VV), HV showed a good correlation with the corn FVC ($r=0.89$) when the FVC was below 75%. The VV barely showed any correlation with FVC at both stages. It suggests that the C-band VV polarization is not an effective parameter to monitor broadleaf plants. Similar results were also found in Moncelloni's study (Macelloni et al., 2001), which showed that the correlation between C-band VV polarization and LAI of broadleaf crops (corn and sunflower) was lower than the correlation between VV polarization and LAI of narrow leaf crops (wheat), and in Xu's study (Xu et al., 2014), which showed that the classification accuracy of peanut and woods

using Radarsat-2 VV polarization was the lowest among the three polarizations (HH, HV, VV). These findings indicate that the VV polarization is mainly dominated by surface scattering.

In Figure 2-7, the ratio $|HV/VV|^2$ is plotted against the corn FVC. The $|HV/VV|^2$ gave the best correlation with corn FVC ($r=0.96$) when the FVC was below 75%. When the corn FVC was greater than 75%, the sensitivity of $|HV/VV|^2$ to FVC decreased significantly ($r=0.00$). In addition to the weakened penetrating capability caused by accumulated biomass, this may also be caused by the saturation of FVC at the later growing stage.

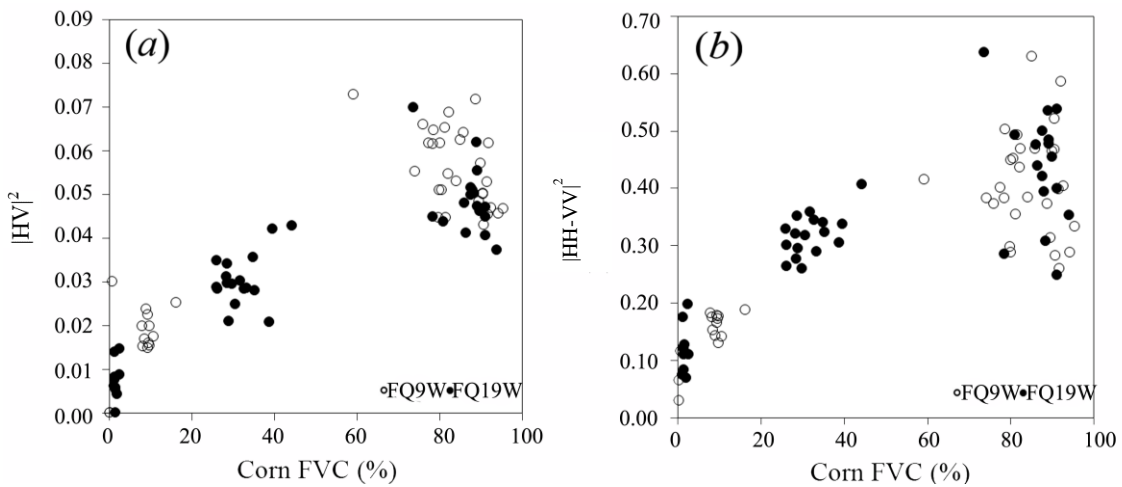


Figure 2-7: Scatterplots between (a) corn FVC and $|HV|^2$ (C_{22}), (b) corn FVC and $|HV/VV|^2$

Figure 2-8 shows the scatterplots between wheat FVC and $|VV|^2$ (a) and $|HV+VV|^2$ (b). No obvious correlation was observed between the Radarsat-2 polarimetric decompositions and the wheat FVC at any stage. It may be because of the two following factors. Firstly, the dense plants and narrow leaves of wheat make the stems contribute a large percentage to the FVC and accordingly lead to the saturation of FVC at an early stage. In addition, the SAR backscatter can easily penetrate the canopy and be affected by the stems and underlying soil due to the upright and narrow characteristics of wheat leaves and the small amount of biomass (Macelloni et al., 2001). In this view, C-band polarimetric SAR parameters are not good indicators for wheat FVC.

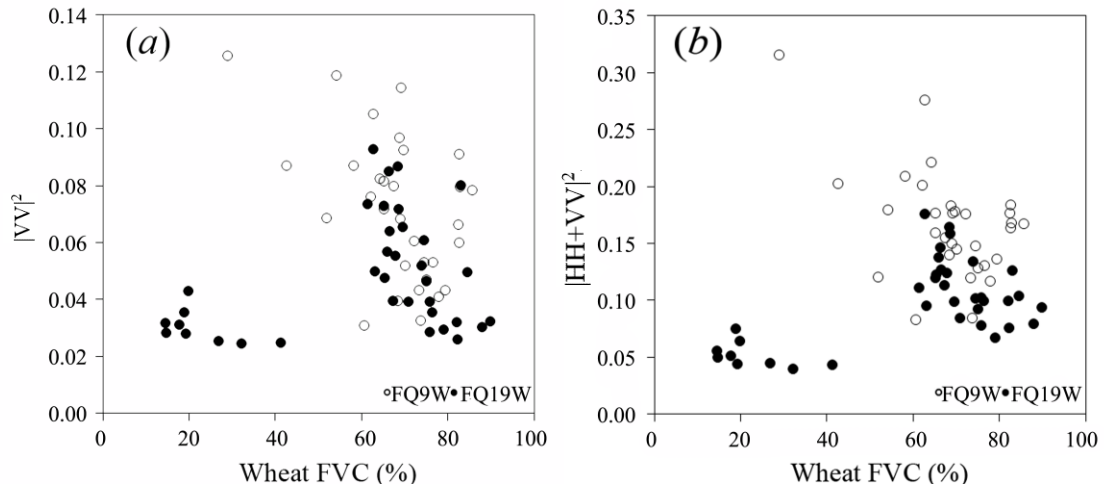


Figure 2-8: Scatterplots between (a) wheat FVC and $|VV|^2$ (C33), (b) wheat FVC and $|HH+VV|^2$ (T11)

The results indicated that the C-band Radarsat-2 polarimetric SAR has great potential in crop height and FVC estimation for broad-leaf crops (corn), and identifying the changes in crop canopy structures and phenology (corn and wheat) in cloudy areas.

2.4 Conclusions

This study investigated the sensitivity of different Radarsat-2 polarimetric SAR parameters to crop height and FVC of corn and wheat in southwestern Ontario, Canada. The results showed that the sensitivity of polarimetric SAR parameters to crop variables was higher for corn than for wheat. For corn, the $|HV|^2$, $|HH-VV|^2$, and $|HV/VV|^2$ were strongly and positively correlated with the corn height when it was below 150 cm (before the heading stage). The correlation between most of the SAR parameters and corn height became weaker and negative after the heading stage. Only the $|HH-VV|^2$ was observed to be strongly correlated with corn height at the later stage. The $|HV|^2$ and $|HV/VV|^2$ showed good sensitivity to corn FVC when corn FVC was below 75% (before the heading stage). Beyond this threshold, the sensitivity to corn FVC was lost. For wheat, the responses of polarimetric SAR parameters to wheat height were complex. The correlation between polarimetric SAR parameters and wheat height was very weak at the early and later growing stage. And then negative trends with weak correlations were observed between most polarimetric SAR parameters and wheat height during the stem elongation stage.

Among the SAR parameters studied, $|HV|^2$ and Yamaguchi helix scattering were negatively correlated with wheat height during this stage with relatively higher coefficients of determination ($r=0.75$ and $r=0.62$). Whereas, the wheat FVC was not correlated with any SAR parameters.

References

- Agriculture and Agri-food Canada. (2011). *Crop Identification and BBCH Staging Manual: SMAP-12 Field Campaign*. Retrieved from http://www.jecam.org/BBCH_STAGING_MANUAL_GENERAL_ALL_CROPS.pdf
- Alaska Satellite Facility. (2012). *ASF MapReady User Manual*. Retrieved from https://media.asf.alaska.edu/asfmainsite/documents/mapready_manual_3.1.22.pdf
- Baghdadi, N., Aubert, M., Cerdan, O., Franchistéguy, L., Viel, C., Eric, M., ... Desprats, J. F. (2007). Operational mapping of soil moisture using Synthetic Aperture Radar Data: application to the touch basin (France). *Sensors*, 7(10), 2458–2483. <http://doi.org/10.3390/s7102458>
- Cloude, S. R., & Pottier, E. (1996). A review of target decomposition theorems in radar polarimetry. *IEEE Transactions on Geoscience and Remote Sensing*, 34(2), 498–518. Retrieved from http://ieeexplore.ieee.org/xpls/abs_all.jsp?arnumber=485127
- Duguay, Y., Bernier, M., Lévesque, E., & Tremblay, B. (2015). Potential of C and X Band SAR for shrub growth monitoring in Sub-Arctic environments. *Remote Sensing*, 7(7), 9410–9430. <http://doi.org/10.3390/rs70709410>
- Farm Credit Canada. (2013). *Canadian Agriculture and Agri-Food in the Global Economy 2013-14*.
- Ferrazzoli, P., Paloscia, S., Pampaloni, P., Schiavon, G., Sigismondi, S., & Solimini, D. (1997). The potential of multifrequency polarimetric SAR in assessing agricultural and arboreous biomass. *IEEE Transactions on Geoscience and Remote Sensing*, 35(1), 5–17. <http://doi.org/10.1109/36.551929>
- Fontanelli, G., Paloscia, S., Zribi, M., & Chahbi, A. (2013). Sensitivity analysis of X-band SAR to wheat and barley leaf area index in the Merguellil Basin. *Remote Sensing Letters*, 4(11), 1107–1116. <http://doi.org/10.1080/2150704X.2013.842285>
- Goodman, J. W. (1976). Some fundamental properties of speckle. *Optical Society of America*, 66(11), 1145–1150.
- Hamel, M.-A., & Dorff, E. (2014). Corn: Canada's third most valuable crop.

- Huang, X., Wang, J., & Shang, J. (2016). An integrated surface parameter inversion scheme over agricultural fields at early growing stages by means of C-band polarimetric RADARSAT-2 imagery. *IEEE Transactions on Geoscience and Remote Sensing*, 54(5), 2510–2528.
- Jiao, X., McNairn, H., Shang, J., & Liu, J. (2010). The sensitivity of multi-frequency (X, C and L-Band) radar backscatter signatures to bio-physical variables (LAI) over corn and soybean fields. *International Archives Photogrammetry Remote Sensing*, XXXVIII(Part B 7), 317–321. Retrieved from http://www.isprs.org/proceedings/XXXVIII/part7/b/pdf/317_XXXVIII-part7B.pdf
- Jiao, X., McNairn, H., Shang, J., Pattey, E., Liu, J., & Champagne, C. (2011). The sensitivity of RADARSAT-2 polarimetric SAR data to corn and soybean leaf area index. *Canadian Journal of Remote Sensing*, 37(1), 69–81. <http://doi.org/10.5589/m11-023>
- Kim, Y., & van Zyl, J. (2009). A time-series approach to estimate soil moisture using polarimetric Radar data. *Geoscience and Remote Sensing, IEEE Transactions on*, 47(8), 2519–2527. <http://doi.org/10.1109/TGRS.2009.2014944>
- Lee, J.-S., & Pottier, E. (2009). H/A/ $\bar{\alpha}$ polarimetric decomposition theorem. In *Polarimetric Radar Imaging* (p. 237). CRC Press. <http://doi.org/doi:10.1201/9781420054989.ch7>
- Lee, J., & Pottier, E. (2009). Electromagnetic vector scattering operators. In *Polarimetric Radar Imaging: From Basics to Applications* (p. 66). New York: CRC Press. <http://doi.org/10.1201/9781420054989>
- Lin, H., Chen, J., Pei, Z., Zhang, S., & Hu, X. (2009). Monitoring sugarcane growth using ENVISAT ASAR data. *IEEE Transactions on Geoscience and Remote Sensing*, 47(8), 2572–2580. <http://doi.org/10.1109/TGRS.2009.2015769>
- Liu, C., Shang, J., Vachon, P. W., & McNairn, H. (2013). Multiyear crop monitoring using polarimetric RADARSAT-2 data. *IEEE Transactions on Geoscience and Remote Sensing*, 51(4), 2227–2240. <http://doi.org/10.1109/TGRS.2012.2208649>
- Macelloni, G., Paloscia, S., Pampaloni, P., Marliani, F., & Gai, M. (2001). The relationship between the backscattering coefficient and the biomass of narrow and

- broad leaf crops. *IEEE Transactions on Geoscience and Remote Sensing*, 39(4), 873–884. <http://doi.org/10.1109/36.917914>
- Mattia, F., Le Toan, T., Picard, G., Posa, F. I., D'Alessio, A., Notarnicola, C., ... Pasquariello, G. (2003). Multitemporal C-band radar measurements on wheat fields. *IEEE Transactions on Geoscience and Remote Sensing*, 41(7), 1551–1560. <http://doi.org/10.1109/TGRS.2003.813531>
- McNairn, H., & Brisco, B. (2004). The application of C-band polarimetric SAR for agriculture: A review. *Canadian Journal of Remote Sensing*. <http://doi.org/10.5589/m03-069>
- McNairn, H., van der Sanden, J. J., Brown, R. J., & Ellis, J. (2000). The potential of RADARSAT-2 for crop mapping and assessing crop condition. In *Proceedings of the 2nd International Conference on Geospatial Information in Agriculture and Forestry* (pp. 81–88). Lake Buena Vista, Florida, USA.: ERIM International, Inc.
- Mougin, E., Demarez, V., Diawara, M., Hiernaux, P., Soumaguel, N., & Berg, A. (2014). Estimation of LAI, fAPAR and fCover of Sahel rangelands (Gourma, Mali). *Agricultural and Forest Meteorology*, 198, 155–167. <http://doi.org/10.1016/j.agrformet.2014.08.006>
- Paloscia, S., Santi, E., Fontanelli, G., Montomoli, F., Brogioni, M., Macelloni, G., ... Pettinato, S. (2014). The sensitivity of cosmo-skymed backscatter to agricultural crop type and vegetation parameters. *IEEE Journal of Selected Topics in Applied Earth Observations and Remote Sensing*, 7(7), 2856–2868.
- Paruelo, J. M., Lauenroth, W. K., & Roset, P. A. (2000). Estimating aboveground plant biomass using a photographic technique. *Journal of Range Management*, 53(2), 190–193.
- Shang, J., Jiao, X., McNairn, H., Kovacs, J., Walters, D., Ma, B., & Geng, X. (2013). Tracking crop phenological development of spring wheat using synthetic Aperture Radar (SAR) in northern Ontario, Canada. *IEEE Proceedings of the 2nd International Conference on Agro-Geoinformatics*, 517–521.
- Shoshany, M., Svoray, T., Curran, P. J., Foody, G. M., & Perevolotsky, A. (2000). The relationship between ERS-2 SAR backscatter and soil moisture: generalization

- from a humid to semi-arid transect. *International Journal of Remote Sensing*, 21(11), 2337–2343. <http://doi.org/10.1080/01431160050029620>
- Singh, S. K., Dutta, S., & Dharaiya, N. (2013). Estimation of crop evapotranspiration of cotton using remote sensing technique. *International Journal of Environmental Engineering and Management*, 4(5), 523–528.
- Smith, A. M., Eddy, P. R., Bugden-Storie, J., Pattey, E., McNairn, H., Nolin, M., ... Haboudane, D. (2006). Multipolarized radar for delineating within-field variability in corn and wheat. *Canadian Journal of Remote Sensing*, 32(4), 300–313. <http://doi.org/10.5589/m06-026>
- Srivastava, H. S., Patel, P., & Navalgund, R. R. (2006). Application potentials of synthetic aperture radar interferometry for land-cover mapping and crop-height estimation. *Current Science*, 91(6), 783–788.
- Verger, a., Martínez, B., Camacho-de Coca, F., & García-Haro, F. J. (2009). Accuracy assessment of fraction of vegetation cover and leaf area index estimates from pragmatic methods in a cropland area. *International Journal of Remote Sensing*, 30(10), 2685–2704. <http://doi.org/10.1080/01431160802555804>
- Weiss, M., & Baret, F. (2017). *Can-eye version 6.4.91 user manual*. Retrieved from <https://www6.paca.inra.fr/can-eye/Documentation/Documentation>
- Wiseman, G., McNairn, H., Homayouni, S., & Shang, J. (2014). RADARSAT-2 Polarimetric SAR response to crop biomass for agricultural production monitoring. *IEEE Journal of Selected Topics in Applied Earth Observations and Remote Sensing*, 7(11), 4461–4471.
- Xie, D., Wang, Y., Wang, P., Yan, G., & Song, J. (2013). Analyzing the characteristics of FPAR from maize canopies measured in Northwest China. *International Geoscience and Remote Sensing Symposium (IGARSS)*, 1(1), 2802–2805. <http://doi.org/10.1109/IGARSS.2013.6723406>
- Xu, J., Li, Z., Tian, B., Huang, L., Chen, Q., & Fu, S. (2014). Polarimetric analysis of multi-temporal RADARSAT-2 SAR images for wheat monitoring and mapping. *International Journal of Remote Sensing*, 35(10), 3840–3858. <http://doi.org/10.1080/01431161.2014.919679>

Yamaguchi, Y., Moriyama, T., M. Ishido, & Yamada, H. (2005). Four-component scattering model for polarimetric SAR image decomposition. *IEEE Trans. Geosci. Remote Sensing*, 43(8), 1699–1706.

Chapter 3

3 Contribution of Minimum Noise Fraction Transformation of Multi-temporal Radarsat-2 Polarimetric SAR Data to Cropland Classification²

3.1 Introduction

Canada is a major exporter of agricultural products and plays an important role in the global agricultural market (Shang, McNairn, Deschamps, Jiao, & Champagne, 2011a). Annual crop inventories are required in many agriculture applications such as crop monitoring, crop biomass and yield estimation, scientific agriculture management and agriculture statistics reporting (Larrañaga, 2011). Compared with other vegetation land covers, crop fields are heavily influenced by human activities, and the crop types commonly change every year due to crop rotation, which makes an accurate and robust system for annual crop inventory delivery important.

Due to the different temporal change patterns or phenology associated with different crop types (Zhu, Woodcock, Rogan, & Kellndorfer, 2012), multi-temporal optical data have been widely used in crop classification to provide not only spectral information but also temporal information of different crops. Multi-temporal Advanced Very High Resolution Radiometer (AVHRR) and Moderate Resolution Imaging Spectroradiometer (MODIS) vegetation index data are generally used for large scale crop classification (Wardlow, Egbert, & Kastens, 2007). Landsat TM/ETM+, RapidEye, and Sentinel-2 data are generally used for detailed local-scale crop mapping (Tatsumi, Yamashiki, Canales Torres, & Taipe, 2015).

² A version of this chapter has been accepted for publication (Chunhua Liao, Jinfei Wang, Xiaodong Huang, Jiali Shang. Contribution of Minimum Noise Fraction transformation of multi-temporal RADARSAT-2 polarimetric SAR data to cropland classification. Canadian Journal of Remote Sensing. 2018, 44(4). (will be published in August 2018))

As frequent cloud contamination challenges the application of optical remote sensing imagery, the synthetic aperture radar (SAR) sensors show great potential in agriculture applications due to their capability of working day and night and penetrating the cloud cover (Zhu et al., 2012). Polarimetric SAR data with four polarization channels, which contain more information than the single polarization SAR data, can assist in crop discrimination by reflecting the structure and dielectric properties of the crop canopies (Forkuor, Conrad, Thiel, Ullmann, & Zoungrana, 2014; McNairn, Shang, Jiao, & Champagne, 2009a; Zhu et al., 2012). Different frequency polarimetric SAR systems such as the ASAR (C-band) (Tavakkoli & Lohmann, 2006), PALSAR (L-band) (Mishra, Singh, Yamaguchi, & Singh, 2011), TerraSAR-X (X-band) (Sonobe, Tani, Wang, Kobayashi, & Shimamura, 2014), Radarsat-1 (C-band), Radarsat-2 (C-band) (Deschamps, McNairn, Shang, & Jiao, 2012; Huang, Wang, Shang, Liao, & Liu, 2017; Shang, McNairn, Deschamps, & Jiao, 2011b), and the combination of different frequency SAR data (Shang et al., 2011b; Skriver, 2012) have been applied to crop classification with satisfactory accuracies. It has been reported that large biomass crops such as corn and soybean were well classified using the longer wavelength L-band SAR data, and the lower biomass crops such as cereals and hay pasture were better classified using C-band SAR data (McNairn et al., 2009a). The combination of multi-temporal SAR and optical data was also used for crop classification (McNairn, Champagne, Shang, Holmstrom, & Reichert, 2009b). Previous studies suggested that the integration of optical and SAR data was able to improve crop classification accuracy due to its ability to provide complementary information to better characterize crops. Optical images contain spectral (pigment) information of different crops, and SAR images provide the structure information of crop canopy (Zhu et al., 2012). Multi-temporal optical and SAR images capture the temporal change characteristics of different crop types. Integration of the spectral, polarimetric and temporal dimensions of features can produce higher accuracy in crop classification than using only one dimension of the features (Iannini, Molijn, & Hanssen, 2013; Larrañaga, 2011; McNairn et al., 2009a; Heather McNairn et al., 2009b; Shang et al., 2006; Zhu et al., 2012).

Many SAR decomposition methods have been developed to separate the SAR backscatter signals into surface scattering, double bounce, and volume scattering. A previous study conducted in an agricultural area over North-eastern Ontario, Canada (Jiao et al., 2014)

found that the Cloude–Pottier decomposition parameters have higher accuracy than both measured linear polarizations (HH, HV, VV) and parameters decomposed by the Freeman–Durden decomposition parameters using multi-temporal Radarsat-2 data using an object-oriented classification method. Similar findings were also reported in another study conducted in the Great Lakes–St. Lawrence Valley near Ottawa (McNairn et al., 2009b). The crop classification results using multi-temporal Phased Array type L-band Synthetic Aperture Radar (PALSAR) showed that the L-band parameters derived from three decomposition approaches (Cloude–Pottier, Freeman–Durden, and Krogager) produced superior crop classification accuracies relative to linear polarizations. However, few studies have focused on the potential of elements of the coherency matrix and covariance matrix of the fully-polarimetric Radarsat-2 data in crop classification.

Due to the cost and acquisition limitations of optical and SAR data, identifying the ideal timing of data acquisition during the growing season is also of great importance (McNairn et al., 2009a; Shang et al., 2006). For western Canada, where spring wheat is the main cereal crop, it is found that data acquired at the later growing season (late August and early September) are critical for crop classification, and early season data are less useful due to low vegetation cover (Jiao et al., 2014; McNairn et al., 2009a; Shang et al., 2006). However, the optimal acquisition dates of the datasets for crop classification may vary with regions due to the difference in crop type and complexity of crop mix. For regions where winter wheat is the main cereal crop, such as southwestern Ontario, earlier images may also be important. Therefore, it is necessary to study the impact of timing of polarimetric SAR data acquisition on crop classification, and provide guidance in data selection for crop classification in southwestern Ontario.

Due to the inherent speckle phenomenon, it is important to suppress the noise of the data. Generally, a speckle filter is applied for each band of the polarimetric SAR data, but the speckle noise is still not sufficiently reduced. The Minimum Noise Fraction (MNF) transformation was originally developed for hyperspectral image processing to produce principal components by maximizing the signal-to-noise ratio of the data (Green, Berman, Switzer, & Craig, 1988). The MNF transform was also applied to MODIS time series in order to reduce the noise (Couto Junior, de Carvalho Júnior, Martins, & Vasconcelos, 2013).

From our knowledge, however, the MNF transform has never been applied to multi-temporal polarimetric SAR data.

Therefore, the main objectives of this study are (1) to determine the performance of different polarimetric SAR parameter sets for crop classification using the random forest classifier, (2) to study the impact of the timing of the acquisition of SAR images on crop classification in southwestern Ontario, and (3) to investigate the effects of MNF transformation of SAR time series data on crop classification.

3.2 Methodology

3.2.1 Study site

The study site is a cropland area near Komoka, Ontario, which is located in the Mixedwood Plains Ecozone in southwestern Ontario (Figure 3-1). This region is characterized by abundant water supply, relatively mild climate, productive soils for agriculture, and a longer growing season than most of the country. The croplands in the study site are mixed with woods, and the dominant crops are winter wheat, corn, soybean, and forage including alfalfa and grass. These four crops accounted for more than 90% of the total planting area in the study site. Generally, the winter wheat in this study site is seeded in October the previous year and harvested in July, while the corn and soybean are seeded in May and harvested in September or October. Due to crop rotation, the type of crop planted in each field usually changed every year.

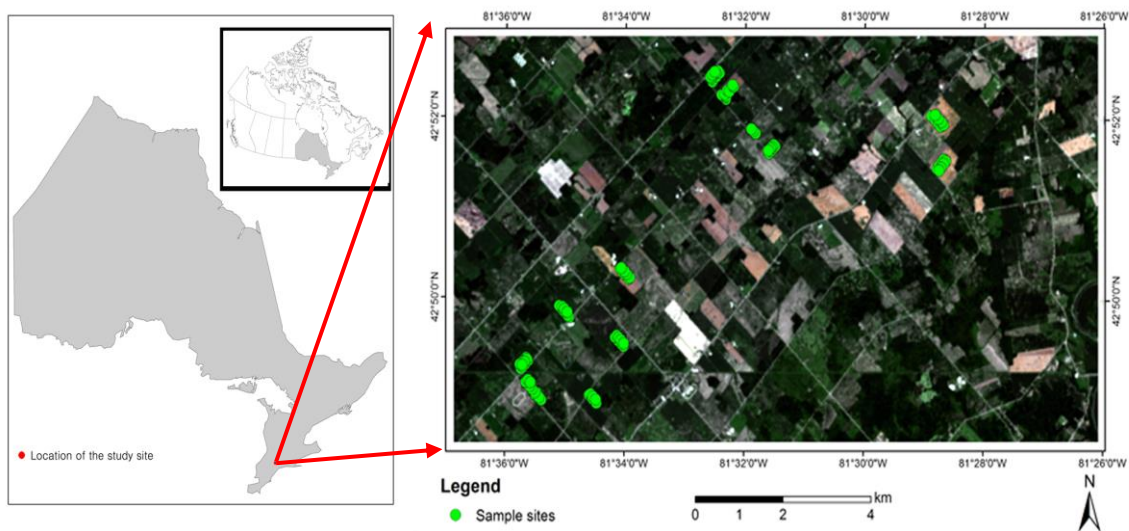


Figure 3-1: Location of the study site

3.2.2 Ground reference data collection

Field surveys were conducted in each month from April to September 2015. A total of 118 fields (Figure 3-2) including 35 corn fields, 22 winter wheat fields, 29 soybean fields, 18 forage fields, one bare soil field, one built-up field, one watermelon field, and two tobacco fields were visited. Nine forest patches were identified on Google Earth and Landsat images. For each crop type, about half of the ground truth data were selected as training samples from the ground reference fields, and the remaining ones were used as testing samples for the accuracy assessment (Table 3-1). There was no overlap between the training samples and testing samples.

Table 3-1: Field data collected in the field work and the number of pixels used for training and testing

LU/LC type	Number of Fields Surveyed	No. of training pixels	No. of test pixels	LU/LC type	Number of Fields Surveyed	No. of training pixels	No. of test pixels
Built-up	1	1267	1117	Winter wheat	22	6018	17723
Forest	9	5148	7292	Forage	18	3700	3615
Corn	35	6258	20246	Watermelon	1	310	309
Soybean	29	6505	15995	Tobacco	2	416	301
Soil	1	2331	1592				

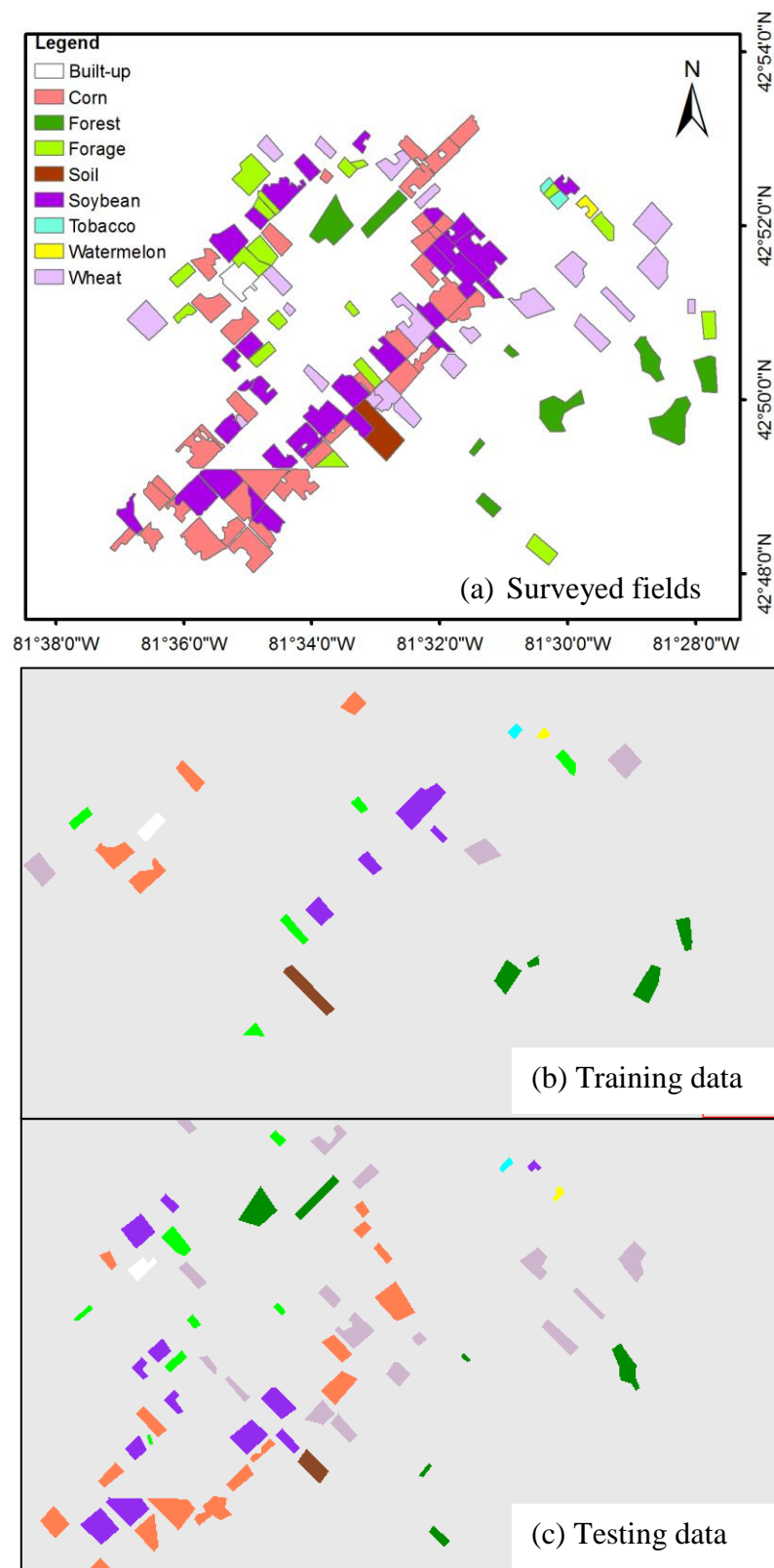


Figure 3-2: Map of the (a) surveyed fields, (b) training data and (c) testing data

3.2.3 Satellite data acquisition

A total of 15 fine-quad wide beam mode (FQW) Radarsat-2 polarimetric SAR images were acquired throughout the 2015 growing season over the study site. There was no precipitation during the time of the Radarsat-2 image acquisitions. The acquired Radarsat-2 data are single look complex (SLC) products, which contain four polarizations HH, HV, VH, and VV. The revisit time for the same FQW of Radarsat-2 data is 24 days. In order to shorten the revisit time and to achieve satisfactory classification accuracies (Shang et al., 2011b), SAR images acquired at different incidence angles (FQ1W, FQ9W, FQ10W, FQ14W, FQ15W, FQ20W) were also included. The incidence angle ranges from 20° to 40° (Table 3-2).

Table 3-2: The acquired Radarsat-2 data

Satellite	Date	Mode	Incidence angle (degree)	Nominal resolution (m) range
Radarsat-2	12 April 2015	FQ10W	28.4-31.6	9.9-10.9
	6 May 2015	FQ10W	28.4-31.6	9.9-10.9
	20 May 2015	FQ1W	17.5 21.2	14.4-17.3
	23 June 2015	FQ10W	28.4-31.6	9.9-10.9
	3 July 2015	FQ20W	38.6-41.3	7.9-8.3
	17 July 2015	FQ10W	28.4-31.6	9.9-10.9
	10 Aug. 2015	FQ10W	28.4-31.6	9.9-10.9
	3 Sep. 2015	FQ10W	28.4-31.6	9.9-10.9
	13 Sep. 2015	FQ20W	38.6-41.3	7.9-8.3
	17 Sep. 2015	FQ1W	17.5 21.2	14.4-17.3
	27 Sep. 2015	FQ10W	28.4-31.6	9.9-10.9
	1 Oct. 2015	FQ9W	27.2-30.5	10.2-11.4
	14 Oct. 2015	FQ15W	33.7-36.7	8.7-9.4
	1 Nov. 2015	FQ14W	32.7-35.7	8.9-9.6
	25 Nov. 2015	FQ14W	32.7-35.7	8.9-9.6

Three cloud-free Landsat-8 OLI surface reflectance products (path 19, row 30) were downloaded from the USGS Explorer (<https://earthexplorer.usgs.gov/>). The first cloud-free Landsat image was captured on 10 June 2015, when all crops were growing. The other two images were captured on 28 July 2015, when the winter wheat began to be harvested, and 14 September 2015, when corn and soybean began to senesce (Table 3-3).

Table 3-3: The acquired Landsat-8 data

Satellite	Date	Row	Path	Spatial resolution (m)
Landsat-8	10 June 2015	19	30	30
	28 July 2015	19	30	
	14 Sep. 2015	19	30	

3.2.4 Satellite image preprocessing

3.2.4.1 Polarimetric SAR parameter extraction

The Radarsat-2 data were filtered using a 9×9 Boxcar filter to suppress the inherent speckle noise. Even though the Boxcar filtered image shows blurred boundaries when compared with other filters such as the Gaussian, Lee Refined, and Lee Sigma filters, it looks much smoother and more uniform, which is very important in the agricultural classification where all pixels within an entire crop field are supposed to be classified as the same crop type. In addition, the Boxcar filter has a higher Equivalent Numbers of Looks (ENL) than other filters, a good indicator to evaluate the filter performance with a larger value corresponding to a better quantitative performance, than other filters (Huang et al., 2017). The 9 by 9 window size is chosen in order to preserve the sufficient ENL to reduce the speckle noise and to keep details as many as possible. A too small window size will lead to insufficient filtering and too large window size will not preserve the details (Huang et al., 2017). Then, orthorectification was performed using MapReady software with an external digital elevation model (DEM) of Ontario and an output cell resolution of 10 m by 10 m. The coherency matrix (\mathbf{T}_3) and covariance matrix (\mathbf{C}_3) are two fundamental matrices representing the information of the polarimetric SAR data, from which most decomposition parameters can be extracted (Lee & Pottier, 2009).

Linear polarizations (HH, HV, and VV) can be represented by the three diagonal elements (C_{11} , C_{22} , C_{33}) of the covariance matrix \mathbf{C}_3 , of which, C_{22} represents the volume scattering. The components of the Pauli decomposition can be represented by the three diagonal elements (T_{11} , T_{22} , T_{33}) of the coherency matrix \mathbf{T}_3 . T_{11} , T_{22} and T_{33} represent single bounce scattering, double bounce scattering, and volume scattering respectively. The typical examples of those three scattering mechanisms are bare soil, soil-stalk and crop canopies respectively (Lee & Pottier, 2009).

The Cloude-Pottier decomposition decomposes the coherency matrix into three eigenvectors and eigenvalues, and from which the entropy (H), anisotropy (A), and alpha angle (α) can be derived. Entropy (H) is a measure of the purity of scattering mechanism, which varies between 0 (a single pure mechanism) and 1 (equal contributions from all three basic mechanisms). The α corresponds to the average scattering mechanism of an extended target and varies between 0° and 90° , measuring the impotence between the surface and double-bounce scattering. It is segmented into surface scattering ($0^\circ - 40^\circ$), volume scattering ($40^\circ - 50^\circ$) and double-bounce scattering ($50^\circ - 90^\circ$). The anisotropy (A) is defined as the relative importance between the two smallest eigenvalues (Alvarez-Perez, 2011; Cloude & Pottier, 1996).

The Freeman-Durden decomposition is a model based decomposition. It decomposes each polarimetric SAR backscatter into three scattering components: surface scattering, double-bounce scattering, and volume scattering. The three components are modeled as the first-order Bragg surface scatter, the scattering from a dihedral corner reflector, and canopy scatters from randomly oriented dipoles respectively (Freeman & Durden, 1998). The Freeman-Durden decomposition has been widely used in LU/LC classification since it can provide useful features for distinguishing between different surface cover types.

Each of the upper and lower triangular elements of the coherency matrix (\mathbf{T}_3) and covariance matrix (\mathbf{C}_3) is a complex number. The nine parameters, including three diagonal elements and the real and imaginary parts of the three off-diagonal elements, were given as one type of input feature. For other parameters, all of the elements of each decomposition were stacked. Then all the Radarsat-2 images were clipped to the study area.

Due to the fact that a single image is usually not adequate for distinguishing different crop types, multi-temporal data are always required for successful LU/LC classification in agricultural areas as it provides temporal dimensional information, which can reflect the difference in crop change over time. In this study, a total of 14 scenarios of multi-temporal were prepared for the classification (Table 3-4). All the acquired data were used in Scenario 1, and then one image was removed each time from April to November for the following scenarios. This strategy was selected because the images acquired later in the growing

season are reported to be important for crop classification (Jiao et al., 2014; McNairn et al., 2009a; Shang et al., 2006). Even though nearly all the crops were generally harvested in November, the difference in crop residual features for different crop types such as residual height and density can still provide useful information for crop classification. For example, in our study area, the corn residuals will be left in the corn fields with a height of 20 cm to 30 cm after the harvest. Thus the corn fields will present different polarimetric SAR backscattering features due to the roughness caused by corn residuals. Therefore, the November images were kept in all scenarios.

Table 3-4: Different combination of multi-temporal Radarsat-2 data

Date	Scenarios													
	1	2	3	4	5	6	7	8	9	10	11	12	13	14
12 April 2015	√													
6 May 2015	√	√												
20 May 2015	√	√	√											
23 June 2015	√	√	√	√										
3 July 2015	√	√	√	√	√									
17 July 2015	√	√	√	√	√	√								
10 Aug. 2015	√	√	√	√	√	√	√							
3 Sep. 2015	√	√	√	√	√	√	√	√						
13 Sep. 2015	√	√	√	√	√	√	√	√	√					
17 Sep. 2015	√	√	√	√	√	√	√	√	√	√				
27 Sep. 2015	√	√	√	√	√	√	√	√	√	√	√			
1 Oct. 2015	√	√	√	√	√	√	√	√	√	√	√	√		
14 Oct. 2015	√	√	√	√	√	√	√	√	√	√	√	√	√	
1 Nov. 2015	√	√	√	√	√	√	√	√	√	√	√	√	√	√
25 Nov. 2015	√	√	√	√	√	√	√	√	√	√	√	√	√	√

3.2.4.2 MNF transformation

The multi-temporal Radarsat-2 images for each set of parameters were stacked as one file. Then the MNF transform was performed on the multi-temporal Radarsat-2 data using the MNF transform module in ENVI. The MNF transform can determine the inherent dimensionality of data by examining the final eigenvalues, and segregate noise in the data (Boardman & Kruse, 1994). The MNF transform contains two steps: (1) estimates the noise covariance matrix (Σ_N) to decorrelate and rescale the noise in the data (noise whitening),

and (2) performs two separate standard Principal Component Analysis (PCA) (Appendix B) transformation of the noise-whitened data to compute the signal covariance matrix (Σ_S). The MNF transform is an eigenvector procedure, and the output of MNF is a set of image bands that are ordered according to image information content (Green, Berman, Switzer, & Graig, 1988). Assuming that the multi-temporal data have m bands $A_i(x)$, $i=1, 2, \dots, m$, and $\mathbf{A}(\mathbf{x})=\{ A_1(x), A_2(x), \dots, A_m(x)\}^T$. It can be expressed as the sum of the uncorrelated signal ($\mathbf{S}(\mathbf{x})$) and noise ($\mathbf{N}(\mathbf{x})$) components:

$$\mathbf{A}(\mathbf{x}) = \mathbf{S}(\mathbf{x}) + \mathbf{N}(\mathbf{x}) \quad (3-1)$$

Hence,

$$Cov\{\mathbf{A}(\mathbf{x})\} = \Sigma = \Sigma_S + \Sigma_N \quad (3-2)$$

where $Cov\{\mathbf{A}(\mathbf{x})\}$ represents the covariance matrix of $\mathbf{A}(\mathbf{x})$. The signal covariance Σ_S is computed in the same way as is done for the PCA transform. The noise covariance Σ_N can be estimated using minimum/maximum autocorrelation factors (MAF) (Switzer & Green, 1984) (Appendix C). Compared with the PCA, MNF depends on the signal-to-noise ratio (SNR), and is better for signal-dependent noise (i.e. speckle) (Luo, Chen, Tian, Qin, & Qian, 2016).

The Landsat data were resampled to 10 m, and the reflectance was converted to a range from 0 to 1. Then the Landsat-8 OLI data were clipped to the study area, and the three optical images were stacked as one file.

3.2.5 Image classification

The classification methods such as Maximum-Likelihood Classifier (MLC), Decision Tree (DT), Artificial Neural Networks (ANN), Support Vector Machines (SVM), and the Random Forest (RF) classifier have been frequently used in crop classification (McNairn et al., 2009b; Sonobe et al., 2014). The RF classifier was selected in this study due to its excellent ability in crop classification. The RF classifier shows a compromise between the requirement of the large numbers of training samples and expensive cost of time, and has a good ability in crop classification (Deschamps et al., 2012; Jiao et al., 2014; Rodriguez-

Galiano, Ghimire, Rogan, Chica-Olmo, & Rigol-Sanchez, 2012; Sonobe et al., 2014; Tatsumi et al., 2015). Compared with other classification methods mentioned above, the RF classifier has several advantages: (i) overall and class-specific accuracies are generally higher, (ii) a supplementary variable importance measure can be provided, and (iii) the parameters that are needed to run the RF classifier show low sensitivity to classification accuracy (Deschamps et al., 2012). It has also been demonstrated that the RF classifier performs well even with a relatively small size of training samples (Banks et al., 2015).

The RF classifier consists of an ensemble of decision tree classifiers. Each tree is grown to the maximum depth independently using a random combination of features from the input features. An input vector is classified into a class according to the maximum number of votes from the collection of trees (Breiman, 1999). As the number of decision trees increases, classification results will not be affected by the problem of overfitting because of the Strong Law of Large Numbers (Breiman, 1999; Prasad, Iverson, & Liaw, 2006), and thus pruning is unnecessary. Each tree is grown using a certain percentage (two-thirds) of the training sample data (the “bag”). The remaining (one-third) training sample data (the “Out-Of-Bag”, OOB) are used to compute the error rate for the tree. Variable importance of the input image can be produced by the random forest algorithm to determine the predictive ability and importance of each input feature in the classification (Banks et al., 2015). The variable importance score can be calculated from the difference between the OOB error rate with variable j included and the OOB error rate variable j excluded. Usually, the classification accuracy increases as the number of trees increases. However, the improvement diminishes with an increase of the numbers of trees (Zhu et al., 2012). Optimal results can be achieved by defining the number of trees, and the number of split variables for each decision tree. According to previous studies, the error rate nearly reached stability when the number of trees is larger than 50 (Sonobe et al., 2014). In this study, a random forest classifier with a total of 100 trees was built, and the number of split variables was given as the default value, the square root of the total number of variables (Zhu et al., 2012).

The linear polarizations (HH, HV, VV), the elements of the coherency matrix, covariance matrix, the polarimetric parameters of the Pauli decomposition, Cloude-Pottier

decomposition and Freeman-Durden decomposition were extracted from all Radarsat-2 data. For comparison purposes, the classifications were firstly run on the 6 sets of parameters of the single-date RADARSAT-2 data. Then the classifications were also performed on 14 scenarios of multi-temporal RADARSAT-2 images and the MNF transformed multi-temporal images. The classifications were also run on the multi-temporal Landsat-8 data and the integration of Landsat-8 (resampled to 10 m and clipped to the study area) and Radarsat-2 data for comparisons. All the classifications were performed on a per-pixel basis, and the post-classification (clump classes) was performed to eliminate the “speckle” classes with a window size of 5 by 5. The producer’s accuracy (PA), user’s accuracy (UA), overall accuracy (OA) and the Kappa coefficient were generated using the testing samples. The PA represents the probability that a certain area is accurately classified as such on the map (omission error). The UA represents the probability of a pixel being labeled as a certain class on the map really is that class (commission error). Kappa represents the measure of agreement between the classification map and the reference data.

3.3 Results and discussion

Table 3-5 shows the overall accuracy using the 6 parameter sets of single-date Radarsat-2 data. The average accuracies of all dates were calculated for each SAR parameter, and the average overall accuracies of different polarimetric SAR parameter sets were calculated for each date (Table 3-5). The coherency matrix produced the highest overall classification accuracy and followed by the covariance matrix, Pauli decomposition, linear polarization, Freeman-Durden decomposition and Cloude-Pottier decomposition. The images acquired on 23 June, 3 July, 3 September, 13 September and 14 October produced higher overall accuracy than the images acquired on other dates.

Table 3-5: Overall classification accuracies (%) for different polarimetric SAR parameter sets using single-date Radarsat-2 data (T3: coherency matrix; C3: covariance matrix; F-D: Freeman-Durden decomposition; C-P: Cloude-Pottier decomposition; Pauli: Pauli decomposition; Linear: Linear polarization)

Date	T3	C3	F-D	C-P	Pauli	Linear	Average
12 April 2015	45.07	44.16	41.30	40.87	41.29	40.79	42.25
6 May 2015	53.04	47.73	44.55	41.49	43.08	39.74	44.94
20 May 2015	61.33	61.40	57.02	50.11	55.98	58.33	57.36
23 June 2015	70.44	69.73	61.15	58.92	68.75	64.99	65.66
3 July 2015	74.03	73.88	55.85	51.26	64.10	65.99	64.19
17 July 2015	58.10	59.13	43.36	48.05	44.59	51.97	50.87
10 Aug. 2015	52.77	53.00	46.86	36.44	45.57	48.48	47.19
3 Sep. 2015	72.62	71.52	61.40	45.92	63.11	63.82	63.07
13 Sep. 2015	76.54	76.65	61.28	58.52	68.07	67.04	68.02
17 Sep. 2015	49.71	49.5	43.34	35.39	44.17	44.26	44.4
27 Sep. 2015	68.73	67.41	61.55	46.74	64.25	53.44	60.35
1 Oct. 2015	64.12	62.72	59.80	43.91	61.59	56.12	58.04
14 Oct. 2015	76.98	75.00	72.60	59.98	74.04	71.22	71.64
1 Nov. 2015	61.37	61.23	51.02	43.29	54.07	52.25	53.87
25 Nov. 2015	54.26	51.74	52.17	48.75	51.96	51.55	51.74
Average	62.61	61.65	54.22	47.31	56.31	55.33	

Table 3-6 shows the overall classification accuracies for the individual set of polarimetric SAR parameters using the original and the MNF transformed multi-temporal Radarsat-2 images. The average overall accuracies of different scenarios for each polarimetric SAR parameter and the average overall accuracies of polarimetric SAR parameter sets for each scenario were calculated (Table 3-6).

Table 3-6: Overall classification accuracies (%) using the original and the MNF transformation of multi-temporal Radarsat-2 parameters for different scenarios

Scenarios	T3		C3		F-D		C-P		Pauli		Linear		Average	
	Orig	MNF	Orig	MNF	Orig	MNF								
Scenario 1	92.6	94.51	91.71	92.04	91.86	89.74	91.36	91.31	91.08	91.08	90.98	90.84	91.6	91.32
Scenario 2	94.41	95.23	93.4	94.52	93.74	93.31	91.65	91.63	94.29	93.47	91.93	92.05	93.24	93.18
Scenario 3	94.05	95.28	93.59	94.78	92.96	93.97	91.12	91.45	93.49	94.86	92.56	93.65	92.96	93.8
Scenario 4	94.65	95.88	93.66	95.57	92.64	95.54	90.79	90.09	93.59	94.77	93.09	95.87	93.07	94.47
Scenario 5	94.38	95.89	93.59	95.35	92.84	95.09	90.35	88.94	93.3	95.21	94.02	95.47	93.08	94.4
Scenario 6	93.39	94.81	93.37	94.62	92.65	94.55	89.95	87.49	93.49	93.82	94.06	94.08	92.82	93.33
Scenario 7	93.14	95.05	92.93	95.12	91.57	93.97	88.65	85.98	92.68	94.7	92.58	94.13	91.93	93.2
Scenario 8	91.92	94.76	91.27	94.2	90.72	93.53	88.55	84.5	90.89	92.57	89.52	93.23	90.48	92.56
Scenario 9	90.27	93.02	89.41	92.62	88.8	92.1	86.59	85.39	89.1	91.31	88.41	91.87	88.76	91.13
Scenario 10	86.65	88.92	85.68	89.54	83.14	86.64	83.8	79.85	85.15	86.06	83.74	85.19	84.69	86.18
Scenario 11	85.98	86.88	84.17	88.33	82.41	83.7	80.55	76.8	83.43	84.34	82.21	83.56	83.13	83.96
Scenario 12	84.37	85.35	81.72	85.77	82.8	82.17	76.48	77.3	83.15	83.9	82.28	82.73	81.8	82.75
Scenario 13	84.79	81.97	82.61	82.36	80.38	76.15	76.23	76.45	81.97	78.21	81.04	81.17	81.17	79.39
Scenario 14	72.61	72.58	70.89	72.68	61.29	68.17	61.58	61.92	68.1	69.19	69.69	70.29	67.36	69.14
Average	89.52	90.72	88.43	90.54	86.99	88.47	84.83	83.51	88.12	88.82	87.58	88.87		

The MNF transformation improved the overall accuracy for most of the parameters and most of the scenarios, and the improvement ranges from 0 to 6.88%. The overall classification accuracy using the MNF transformation of the coherency matrix for Scenario 5 was the highest (95.89%), and increased by 1.51% when compared with the overall accuracy using the data without MNF transformation.

The MNF transformed bands were ordered according to the amount of information in the image. Figure 3-3 shows the first two bands and the last band of the MNF transformation of the multi-temporal Radarsat-2 coherency matrix for Scenario 5. The first two bands of the MNF transformed data show spatially coherent texture and clear field boundaries, and the last band contains almost noise, whereas the original images showed obvious noise.

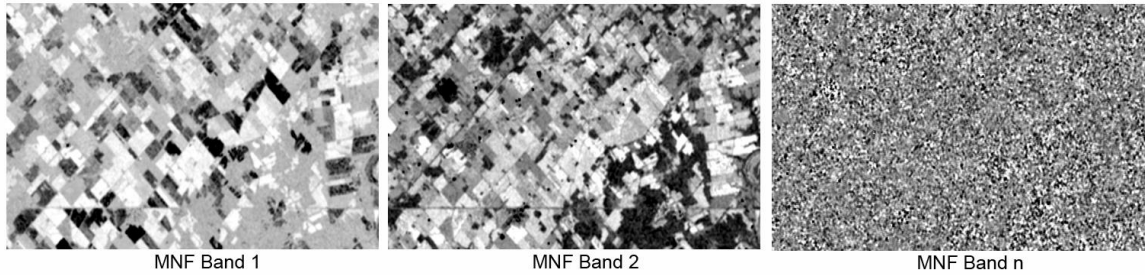


Figure 3-3: The first two bands and the last band of the MNF transformation of multi-temporal coherency matrix of Radarsat-2 data

As revealed in the MNF eigenvalue plot (Figure 3-4), the eigenvalue for the first band of the MNF transformed SAR time series was the largest, which means most of the information was contained in band 1. Information content decreased gradually in the subsequent bands.

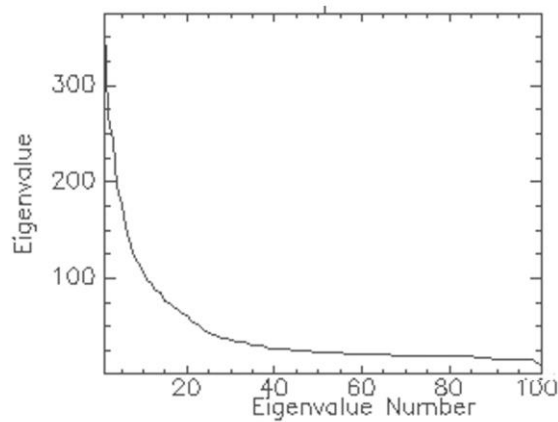


Figure 3-4: Eigenvalues of the MNF transformation of the multi-temporal Radarsat-2 coherency matrix for Scenario 5. Eigenvalues of the MNF transformation of the multi-temporal Radarsat-2 coherency matrix for Scenario 5.

3.3.1 Effects of MNF transformation on cropland classification in terms of different polarimetric SAR parameter sets

3.3.1.1 Overall classification accuracies and the effects of MNF transformation

When the classifications were run on the 6 sets of parameters of single-date Radarsat-2 data, the overall accuracies of all parameters were below 80%. The highest overall accuracy (76.98%) was achieved by the coherency matrix using the data acquired later in the growing season (Table 3-5). Figure 3-5 illustrates that the average overall accuracy for coherency matrix reaches the highest (89.52%), followed by the covariance matrix (88.43%), Pauli decomposition (88.12%), linear polarization (87.58%), Freeman-Durden decomposition (86.99%) and the Cloude-Pottier decomposition (84.83%). The difference among classifications using different SAR parameters can vary by as high as 20%.

The coherency matrix outperformed the covariance matrix in classification because it is a more appropriate representation of underlying physical scattering mechanisms, as it considered the phase of different combinations of polarizations (Gao & Ban, 2008). The overall accuracy for the Cloude-Pottier decomposition was the lowest, which agreed with previous findings (Alberga, 2007). This is possibly due to the following two causes: Firstly, as the entropy and anisotropy are derived from eigenvalues, they do not contain any span (intensity) information. The eigenvalue analysis compressed the original information into fewer dominant components and reduced the detailed information. Secondly, the Cloude-Pottier decomposition only senses the scattering mechanism without taking the crop types into consideration. All crops might show a dominant volume scattering with high Entropy and medium Alpha value (Alberga, 2007; Cao & Hong, 2005).

However, Jiao et al. (2014) reported that the Cloude-Pottier decomposition performed better than linear polarizations and Freeman-Durden decomposition for wheat classification using an object-oriented method. It may be because that the object-oriented classification was able to reduce the noise inherent in the SAR data. It is also probably because the crop (especially corn) residual left from previous year existed in many fields in our study site before the soybean and corn were seeded, and the Cloude-Pottier

decomposition parameters may be sensitive to crop residual, so that it was difficult to classify between wheat and crop residual.

The MNF transformation of the coherency matrix and covariance matrix gave competitive average overall accuracies (90.72% vs 90.54%). The performance of the Pauli decomposition, linear polarizations and Freeman-Durden decomposition are comparable (88.82% vs 88.87% vs 88.47%). The average overall accuracies for the coherency matrix, covariance matrix, Pauli decomposition, linear polarization and Freeman-Durden decomposition were increased by 1.20%, 2.11%, 0.70%, 1.29%, and 1.48% respectively when compared with the average overall accuracies using the data without MNF transformation. It seems that the MNF transformation can reduce the differences of overall accuracies between SAR parameter sets. However, the MNF transformation of the Cloude-Pottier decomposition reduced the classification accuracy by 1.32%.

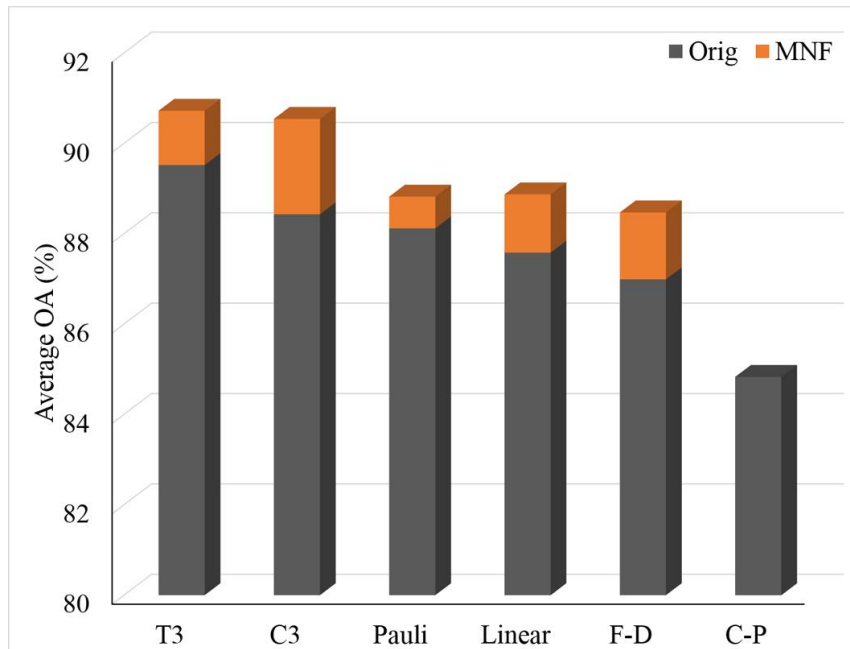


Figure 3-5: The average overall accuracy before and after the MNF transformation for different polarimetric SAR parameter sets

3.3.1.2 Individual land cover classification accuracies and the effects of MNF transform

To examine the classification performance of different parameters for individual land covers, the average accuracies of all scenarios for the five dominant land cover types (forest, corn, winter wheat, soybean, and forage) were calculated using the multi-temporal data before and after the MNF transformation (Figure 3-6). As tobacco and watermelon were rare crop types in this area, and the sample size for the two crop types was small, these two crops were out of our discussion.

The coherency matrix was the best for corn and winter wheat classification, and the highest producer's accuracies were 94.26% for corn at Scenario 3 and 93.87% for winter wheat at Scenario 5. The Cloude-Pottier decomposition was the best for soybean classification and the highest producer's and user's accuracy were 99.44% and 91.52 % at Scenario 1. Linear polarization was the best for forage classification with the highest producer's accuracy of 95.44% at Scenario 1. All the parameters had similar performance for forest classification. However, the Cloude-Pottier decomposition was slightly better than other parameters with a producer's accuracy of 99.97% at Scenario 1.

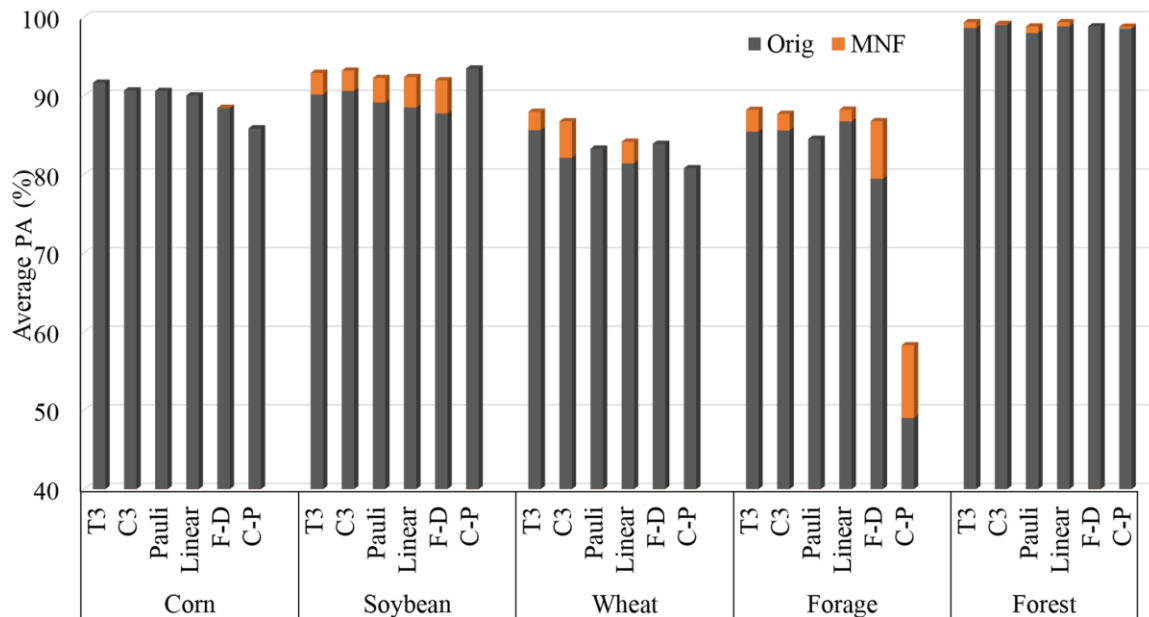


Figure 3-6: The average producer's accuracies of all scenarios for 5 dominant land cover types using different SAR parameter sets

Among the five dominant land cover types, forest was classified with the highest accuracy. The MNF transformation of the original Radarsat-2 data for all the parameters showing only minor differences in forest classification accuracies. For corn, an average producer's accuracy of 89.6% was produced, and the coherency matrix can give a slightly higher producer's accuracy. However, the MNF transformation of multi-temporal Radarsat-2 parameters except for the Freeman-Durden decomposition decreased the producer's accuracy by about 1% to 3%. For soybean, the average producer's accuracy is approximately 90%. The MNF transformation of the parameter sets except for the Cloude-Pottier decomposition improved the producer's accuracy by about 2% to 4% and reduced the differences in the producer's accuracy between different parameter sets. However, the MNF transformation of the Cloude-Pottier decomposition decreased the producer's accuracy. For winter wheat, the MNF transformation of the coherency matrix, covariance matrix, and linear decomposition improved the producer's accuracies by about 3% to 5%. For forage, the Cloude-Pottier decomposition gave the lowest accuracy, but the MNF transformation of the Cloude-Pottier decomposition improved the average producer's accuracy by 10.76%. The MNF transformation of the coherency decomposition, covariance decomposition, linear polarizations, and Freeman-Durden decomposition gave similar producer's accuracies.

The results of this study indicated that different parameters were sensitive to different land cover types. For instance, the coherency matrix is sensitive to most crops, and the Cloude-Pottier decomposition has the lowest sensitivity for most crops but has the highest sensitivity for soybean. This difference in classifications can be caused by the spatial difference in the canopy structures as well as the temporal difference in planting and harvesting dates. The MNF transformation can improve the producer's accuracy for soybean, winter wheat and forage, and can reduce the differences in the producer's accuracy between different parameter sets.

3.3.2 Effects of MNF transform on cropland classification in terms of the timing of Radarsat-2 datasets

3.3.2.1 Overall classification accuracies and the effects of MNF transformation

When the classifications were run on the six parameters of single-date Radarsat-2 data, the Radarsat-2 data acquired in the middle of October gave the best average overall accuracy (71.64%), while the data acquired early in September, and from the end of June to the beginning of July, gave average accuracies of more than 60%. The Radarsat-2 images acquired in April, early in May and later in September gave the average classification accuracy as low as 40% (Table 3-4). This is probably because in the middle of October the main crops especially soybean and corn have the largest separability as the soybean and corn show the largest difference in the vertical structure after they have been senescent and before harvested.

When the classifications were run on the original multi-temporal polarimetric SAR data, the average overall accuracies of all polarimetric SAR parameter sets for each scenario (Figure 3-7) illustrated that the inclusion of the image acquired in April reduced the accuracy of the classification using the multi-temporal data. The MNF transformation nearly gave the same overall accuracy as the original data. This is likely caused by the fact that the corn and soybean fields were presented as bare soil in April, and thus larger misclassification was introduced.

The best average overall classification accuracy was produced at Scenario 5, when the image acquired in the end of June was included. The changes in average overall accuracy were small (less than 0.3%) when the data acquired in May, June, and early July were eliminated respectively, and the average overall accuracy reached a maximum when the images acquired before early July were removed, while the MNF transformation of these scenarios improved the average overall accuracies and the average overall accuracy reached a maximum when the images acquired before June were eliminated. Generally, corn and soybean were planted later in May, therefore, the soil could still affect the classification when the images acquired in May were used.

It is worth noting that there were two large overall accuracy decreases (4.07% and 14.43%) at Scenario 10 and Scenario 14, when the images acquired on 13 September and 14 October were eliminated respectively. It means that the images acquired on these two dates were important in crop classification, which agreed with the results using single-date images. When the SAR image acquired on other dates were eliminated, the average overall accuracy decreased by about 1% each time. The MNF transformation improved the average overall accuracy for most scenarios. Scenario 4 and Scenario 5 showed similar overall accuracy before and after the MNF transformation. From Scenario 6 to Scenario 9, it is likely that the MNF transformation made the differences of overall accuracies between scenarios smaller (Figure 3-7).

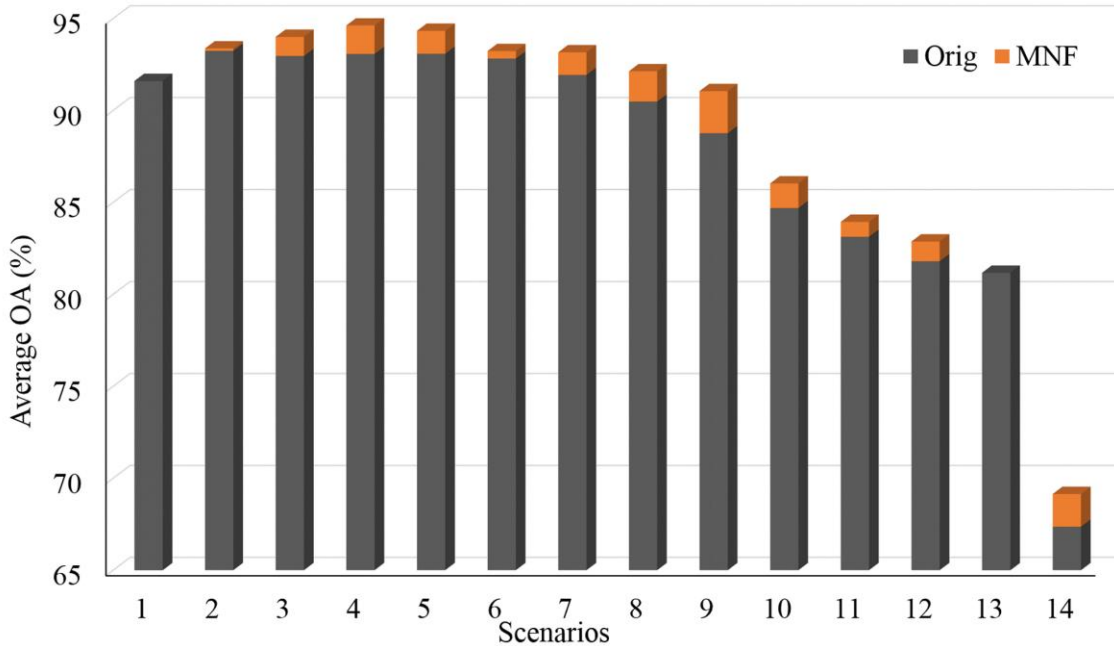


Figure 3-7: The average overall accuracy before and after the MNF transformation for different scenarios

As the coherency matrix outperforms other parameter sets for the classifications, the overall classification accuracy decreases after the elimination of each image were calculated for coherency matrix. As shown in Table 3-6, the best classification was produced at Scenario 4 for original multi-temporal coherency matrix, while the best classification was produced at Scenario 5 for the MNF transformation of the multi-

temporal coherency matrix. According to Table 3-6, the overall accuracy decreased by 12.18% when the image acquired on 14 October was removed, and the overall accuracy decreased by 3.62% when the image acquired on 13 September was removed. According to Table 3-5, the single-date images acquired on 14 October can produce the best classification accuracy and followed by the image acquired on 13 September. This indicates that the images acquired on 14 October and 13 September are two import images for the classification in this study site. In order to explore the best classification accuracies using different numbers of images, the classifications were performed using random combinations of the images acquired from July to November based on the principle that the images should be acquired at different growth stages of crops as much as possible.

Table 3-7 presents the overall accuracies of the classifications using different combinations of coherency matrix datasets acquired on different dates and the MNF transformation of the datasets. Figure 3-8 shows the maximum overall classification accuracies using different numbers of dates of coherency matrix datasets and the MNF transformation of the datasets presented in Table 3-7. It illustrates that an overall accuracy of more than 90% can be achieved using two-date images (14 October and 13 September), and similar overall accuracy was achieved using the MNF transformation of the images. The overall accuracy for three-date images acquired on 10 August, 13 September and 14 October was 92.25% and the MNF transformation of three-date images also showed a similar overall accuracy (92.76%). The overall accuracy of four-date images acquired on 10 August, 3 September, 13 September and 14 October can be 92.98%. An overall accuracy of 94.57% can be achieved using the MNF transformation of images acquired on 3 July, 3 September, 13 September and 14 October. With the increase of numbers of images, the average of the overall accuracy basically increased accordingly. The MNF transformation can improve the overall accuracy by 1% to 3% for most combinations using 4 or more images. A maximum overall accuracy of 95.46% can be achieved using the MNF transformation of six-date datasets. Then with the increase of numbers of images, the improvement of the overall accuracy was limited.

Table 3-7: Overall classification accuracies using different combinations of coherency matrix datasets acquired on different dates and the MNF transformation of the datasets. The coloured cells mean the dates when the RADARSA-2 data were used for the classification (Red: two-date; Orange: three-date; Yellow: four-date; Green: five-date; Blue: six-date; Purple: seven-date; Cyan: eight-date; Pink: nine-date; Gray: Ten-date).

	03 July	17 July	10 Aug.	03 Sep.	13 Sep.	17 Sep.	27 Sep.	01 Oct.	14 Oct.	01 Nov.	Orig OA (%)	MNF OA(%)
2											90.27	90.54
											88.85	90.09
											84.29	83.48
											82.96	83.54
											85.16	84.52
3											91.31	91.54
											91.08	91.45
											92.25	92.76
											91.72	91.34
											89.26	92.16
											91.95	91.46
											89.07	90.69
4											90.92	91.28
											92.13	93.47
											92.98	92.66
											92.03	94.57
											90.88	94.09
5											93.82	94.44
											93.53	94.69
											93.79	94.72
											93.19	94.47
6											93.78	95.03
											93.56	94.82
											92.95	95.46
											94.01	95.17
7											94.00	94.87
											93.47	95.51
8											94.68	95.24
											93.27	94.85
9											94.75	94.95
											94.85	95.78
10											94.10	95.48

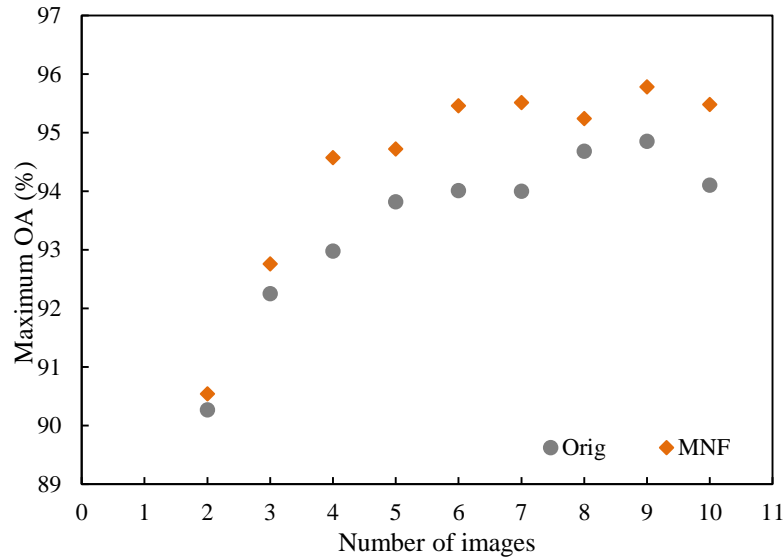


Figure 3-8: Maximum OA using original and MNF transformation of two-date to seven-date coherency matrix datasets

3.3.2.2 Individual land cover classification accuracies and the effects of MNF transformation

In order to investigate the impact of timing of the Radarsat-2 data on individual land cover classification, we examined the average producer's accuracies of all SAR parameter sets for 5 dominant land cover types in the study site at different scenarios (Figure 3-9).

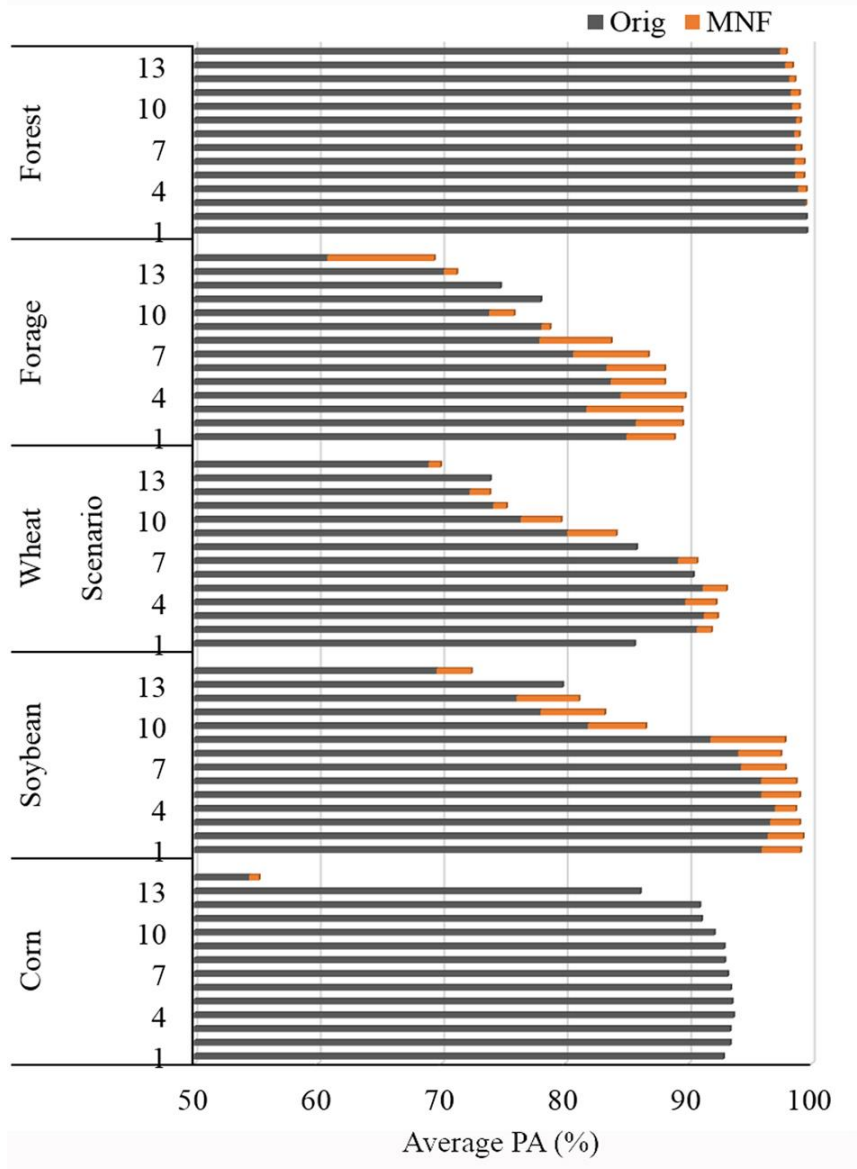


Figure 3-9: The average producer’s accuracies of all SAR parameter sets for 5 dominant land cover types at different scenarios

It was found that, the average producer’s accuracy for soybean was the highest (97.03%) when the data acquired in April and May were excluded (Scenario 4). Before and after the elimination of the image acquired on 13 September, the producer’s accuracy decreased by nearly 10%. According to the photos and phenology information collected during the fieldwork, we found that there was an obvious senescence process for the soybean plants during this period of time. In late September, most soybean fields were in the late stage of

senescence (basically there are two types of soybean within this study site). On 13 September, the soybean was still green or green-to-yellow. But on 17 September, the leaves of some soybean fields were senescent and had dried up. Therefore, the SAR backscatter was mainly affected by the stems of soybean and the soil surface. The maximum difference of average producer's accuracies between different scenarios was 2.14% for forest. Therefore the producer's accuracies for forest were barely influenced by the timing of Radarsat-2 data. For wheat, the producer's accuracy of more than 90% was produced when the images acquired in May, June and July were included (Scenario 2 to Scenario 6). As wheat was harvested early in August, an obvious decrease in producer's accuracy was observed after the image acquired in August was eliminated. The highest producer's accuracy for corn was observed when the data acquired before June were excluded, and the difference of average producer's accuracies between different scenarios for corn was less than 3 % when the SAR data acquired before November were included (Scenario 1 to Scenario 13). However, after the SAR data acquired in October were eliminated and only images acquired in November were retained, the average overall accuracy for corn decreased by 31.65%. It turned out that the corn was harvested in November, and thus the separability between corn fields and other fields became small. For forage, the highest accuracy was produced when the April data were eliminated (85.76%), and the average producer's accuracy decreased the most (9.44%) when the data acquired before November was excluded.

The MNF transformation obviously improved the average producer's accuracy for all the scenarios for soybean except Scenario 13, and the maximum improvement was 6.02%. The MNF transformation also improved most scenarios for wheat (the maximum improvement is 3.94%) and forage (the maximum improvement is 8.65%). For forest, MNF transformation had little influence on the producer's accuracy. For corn, however, the MNF transformation slightly reduced the producer's accuracy for all scenarios except Scenario 14, and more pixels were misclassified into soybean, forage or winter wheat. A possible reason for the decrease of producer's accuracy for corn when using the MNF transformation of the multi-temporal data is that the corn has a larger space between individual plants and a larger leaf inclination angle than soybean, forage and wheat. Due to these spatial and temporal differences in different land cover types, the MNF

transformation of the multi-temporal data cannot extract spatial and temporal features from corn that are helpful for distinguishing corn fields, so that the classification accuracies are not improved.

According to the classification results using single-date and multi-temporal SAR images, the SAR backscatters were mainly affected by the soil roughness due to the low vegetation cover in April and May (McNairn et al., 2009b; Shang et al., 2006). Therefore the data acquired early in the growing season (April and May) are not suitable for crop classification. The senescence or harvesting of crops can also affect the classification of the crops due to the loss of volume scattering information of these crops. Generally, the images acquired during the time when the crop was growing with distinguishable structure and a large amount of biomass was of great importance to crop classification. So the images acquired before the senescence or harvesting of the crops were of great importance. In this study area, the SAR data acquired during the time from June to the end of July, June to the middle of September and June to the end of October are important for wheat, soybean and corn classification respectively. During these periods, the greater the number of SAR images, the higher the classification accuracy. In November, even though the crops were harvested and the forest was senescent, the crop residual can provide special features for crops.

3.3.3 Assessment of the best classification result and the random forest classifier

As the best classification was obtained using the MNF transformation of multi-temporal coherency matrix at Scenario 5, the classification map and the confusion matrix were presented in Figure 3-10 and Table 3-8.

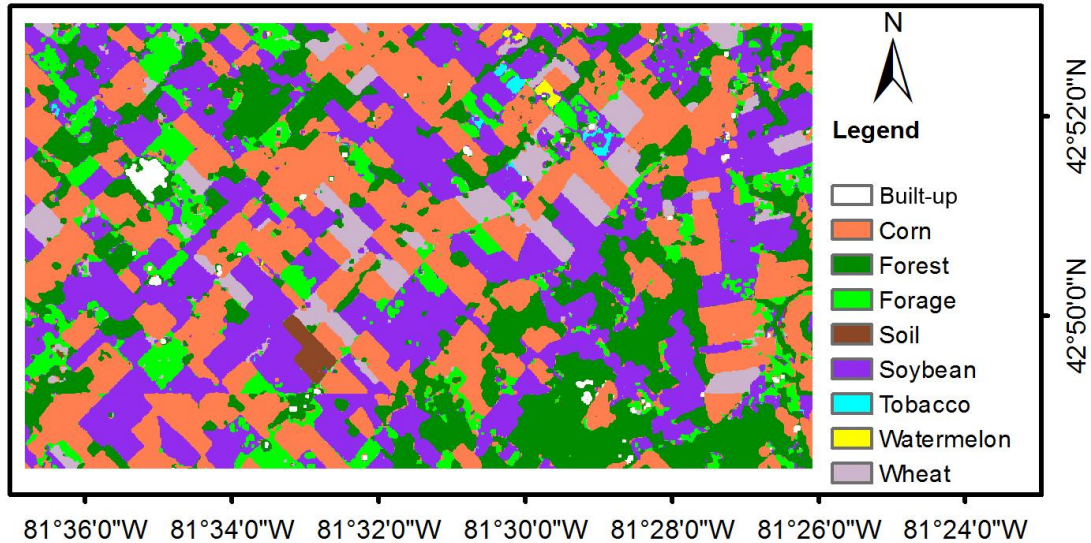


Figure 3-10: The land cover mapping using the MNF transformation of the coherency matrix at Scenario 5

The confusion matrix (Table 3-8) shows that the user’s accuracies for most of the land cover types were high (97.72% in average) with an exception of the forage class (85.95%). Higher producer’s accuracies were achieved for forest (99.67%) and soybean (99.54%). Lower producer’s accuracies were produced for tobacco (72.4%) and watermelon (75.73%), which may be because that the tobacco and watermelon were rare crop types in this area, and the training sample size for the two crop types was limited. The misclassification mainly occurred between soybean and corn classes, which are both summer crops with broad leaves. Confusion also occurred between winter wheat and forage. This is likely caused by the reasons that the wheat shows similar canopy features with grass in the early growing stage, and the grass or alfalfa sometimes was planted after the harvesting of winter wheat.

Table 3-8: Confusion matrix for the land cover mapping obtained using the MNF transformation of the coherency matrix at Scenario 5 (B=Built-up, C=Corn, F=Forest, FG=Forage, S=Soil, SB=Soybean, T=Tobacco, WM=Watermelon, W=Wheat)

Class	Ground truth										
	B	C	F	FG	S	SB	T	WM	W	Tol.	UA (%)
B	945	0	0	0	0	0	0	0	0	945	100.00
C	8	19022	24	97	0	16	4	2	198	19371	98.20
F	152	70	7268	0	27	43	2	0	4	7566	96.06
FG	12	18	0	3309	0	11	16	13	471	3850	85.95
S	0	0	0	0	1537	0	0	0	0	1537	100.00
SB	0	872	0	7	25	15922	37	60	120	17043	93.42
T	0	5	0	0	0	2	218	0	0	225	96.89
WM	0	0	0	0	0	0	0	234	0	234	100.00
W	0	259	0	202	3	1	24	0	16930	17419	97.19
Tol.	1117	20246	7292	3615	1592	15995	301	309	17723	68190	
PA (%)	84.60	93.95	99.67	91.54	96.55	99.54	72.43	75.73	95.53		
OA (%)	95.89										
Kappa	0.95										

The random forest classifier uses all the features simultaneously to classify a pixel (Rodriguez-Galiano et al., 2012). Figure 3-11 illustrates the variable importance generated from the random forest classifier before and after the MNF transformation of the coherency matrix at Scenario 5. Before the MNF transformation, the most important image was acquired on 13 September (T_{22}), and then the image acquired on 3 July (T_{22}). It is apparent that the imaginary part of the T_{12} on 13 September has a high variable importance (5.32). After the MNF transformation, the MNF eigenvalue plot which plots the eigenvalue of each band will be generated by ENVI. The larger the eigenvalue of a band is, the more information it contains. According to the eigenvalue plot, more than 95% of useful information was kept in the first 60 bands (Figure 3-4). As a result, the features with high variable importance were distributed in the first 60 bands.

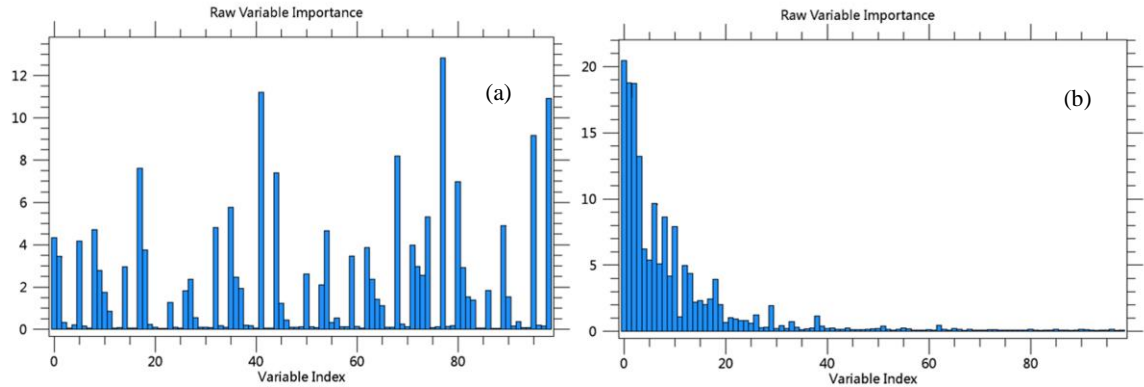


Figure 3-11: The variable importance of different input features (a) before and (b) after the MNF transformation

Figure 3-12 shows the relationship between the number of trees and the Out-Of-Bag (OOB) accuracy for different land cover types. The accuracy became stable when the number of trees reached 20. It indicates that a random forest classifier with 100 trees, which was used in this study is stable enough for crop classification.

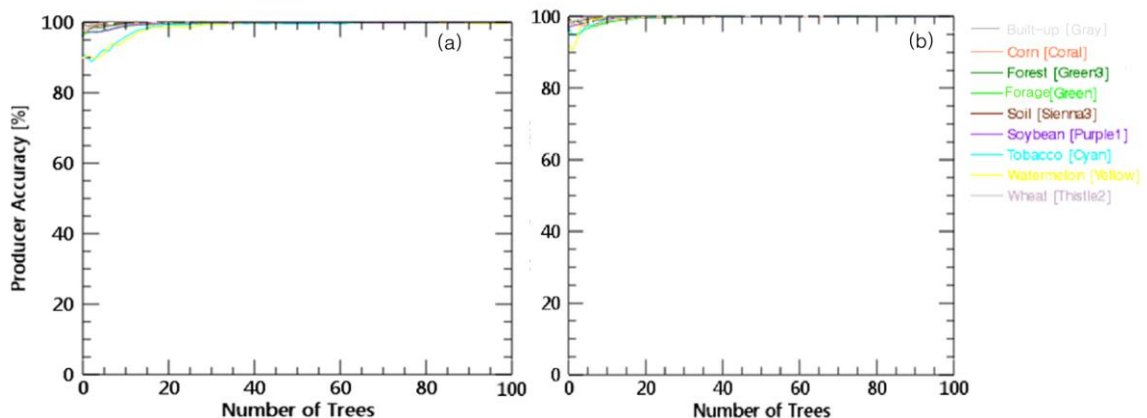


Figure 3-12: Learning curve (OOB accuracy) of the random forest classifier with different numbers of trees (a) original image, (b) MNF transformed image

3.3.4 Comparison of the classification accuracies using the MNF transformation of multi-temporal Radarsat-2 polarimetric SAR data with the accuracies using other strategies

Among the machine learning approaches, the neural network-based approach faces the problems such as slow convergence and the possibility of falling in local minima (Ghamisi,

Plaza, Chen, Li, & Plaza, 2017). The support vector machine (SVM) classifier is a kernel-based technique which aims to find the optimal separating hyperplane between classes (Soliman, Mahmoud, & Hassan, 2012). In this study, the SVM classifier with a second-order kernel polynomial was used for comparison. We also compared the classification accuracies using Landsat-8 data, the original multi-temporal coherency matrix at Scenario 5, the MNF transformation of the coherency matrix, the first 60 bands of the MNF transformation and the integration of Landsat-8 and Radarsat-2 data (Table 3-9).

Table 3-9: Comparison of the classification accuracies using the MNF transformation of multi-temporal Radarsat-2 polarimetric SAR data with the accuracies using other strategies at Scenario 5 based on RF and SVM classifier (B=Built-up, C=Corn, F=Forest, FG=Forage, S=Soil, SB=Soybean, T=Tobacco, WM=Watermelon, W=Wheat)

RF											
	OA (%)	Kappa	B	C	F	FG	S	SB	T	WM	W
I	93.26	0.91	98.84	85.04	99.20	83.57	96.23	99.33	78.74	68.28	96.76
II	94.38	0.93	76.90	94.14	98.68	88.96	96.67	96.42	80.07	60.84	93.87
III	95.89	0.95	84.60	93.95	99.67	91.54	96.55	99.54	72.43	75.73	95.53
IV	92.42	0.90	76.1	93.11	99.38	91.65	95.92	95.78	67.77	55.99	87.67
V	96.03	0.95	83.17	93.89	99.66	90.48	97.11	99.64	77.74	78.96	96.17
VI	95.13	0.94	90.15	89.42	99.01	96.07	97.68	99.74	84.72	63.75	96.52
VII	94.73	0.93	99.91	87.82	99.37	88.82	97.99	99.92	85.38	75.73	97.09
SVM											
	OA (%)	Kappa	B	C	F	FG	S	SB	T	WM	W
I	91.20	0.89	99.37	86.76	99.73	88.96	97.30	92.00	76.41	94.82	91.62
II	92.23	0.90	69.11	90.02	99.74	91.48	97.74	98.99	75.42	63.43	87.49
III	92.48	0.90	68.85	85.19	99.55	92.34	97.42	98.87	73.75	75.40	93.84
IV	93.25	0.91	67.68	89.76	99.37	84.98	96.92	99.17	72.76	75.08	93.03
V	92.56	0.90	71.26	84.35	99.41	94.55	97.24	98.95	76.74	79.61	94.38
VI	94.89	0.93	84.51	88.62	99.84	89.82	97.55	99.47	84.39	83.82	97.70
VII	94.58	0.93	98.66	86.74	99.74	91.40	96.17	99.31	83.39	84.14	97.77
Note: I: multi-temporal Landsat-8 data; II: multi-temporal coherency matrix; III: MNF transformation of multi-temporal coherency matrix; IV: PCA transformation of multi-temporal coherency matrix; V: first 60 bands of the MNF transformed data; VI: multi-temporal Landsat-8 and coherency matrix; VII: multi-temporal Landsat-8 and MNF transformation of coherency matrix)											

The overall accuracies and kappa coefficients illustrated that the RF classifier outperformed the SVM classifier, and higher producer's accuracies were achieved for bare soil, corn, tobacco, and winter wheat using the RF classifier. The MNF transformation of the multi-temporal data improved the overall accuracy more using the RF classifier than using the SVM classifier. As a comparison, the classification was conducted using the PCA transformation of multi-temporal polarimetric SAR data. With the RF, the MNF transformation shows higher classification accuracy than the PCA transformation. The producer's accuracy for winter wheat using the MNF transformation is 8% higher than the producer's accuracy using the PCA transformation. Since the most information was contained in the first 60 bands, the last 39 bands (noise bands) of the MNF transformation can be removed in order to improve the computational efficiency. The overall classification accuracy improved slightly after removing the noise bands using both classifier. The accuracies for the main land cover types were comparable with the accuracies using all bands of the MNF transformed data based on both classifiers.

The optical data can provide spectral information that the polarimetric SAR data cannot provide, while the temporal changes in the spectral information of the optical data will be limited due to the lower temporal resolution and frequent cloud cover. Compared with the classification results obtained using the three Landsat-8 reflectance images, the overall accuracy using multi-temporal Radarsat-2 coherency matrix was improved based on both classifiers, and the producer's accuracies for corn and forage were improved by approximately 9% and 5% respectively. The overall classification accuracies obtained using the MNF transformation of multi-temporal Radarsat-2 data and using the integration of multi-temporal Landsat-8 and Radarsat-2 data were competitive, and the producer's accuracy for corn was obviously higher using the MNF transformation of the multi-temporal coherency matrix than using the integration of the two datasets based on the RF classifier.

3.4 Conclusions

This study investigated the effects of MNF transformation of multi-temporal Radarsat-2 polarimetric SAR data using a random forest classifier on cropland classification in southwestern Ontario. The research is performed through a discussion of the performance

of different polarimetric SAR parameters sets and the impact of timing of Radarsat-2 datasets on cropland classification.

Among the six polarimetric SAR parameter sets, coherency matrix gave the best overall accuracy when the random forest classification was applied, followed by the covariance matrix, Pauli decomposition, linear polarization, Freeman-Durden decomposition and Cloude-Pottier decomposition. The data acquired later in the growing season were important for the crop classification. Specifically, the multi-temporal SAR data acquired during the time between June and the end of July, July and the middle of September, and July and the end of October were important for wheat, soybean and corn classification respectively. The November SAR data are also helpful to achieve a higher accuracy. An overall accuracy of 90% can be achieved using two images acquired in the middle of September and October, and an accuracy of 94% can be achieved using four datasets acquired between July and October.

The MNF transformation of the multi-temporal polarimetric SAR parameter sets can improve the overall classification accuracy when random forest classifier was used. In addition, the difference between different polarimetric SAR parameter sets or between different scenarios can be reduced through the MNF transformation. A maximum overall accuracy of 95.89% was achieved using the MNF transformation of the multi-temporal (July to November) coherency matrix, and the accuracy was further improved by removing the last few bands which mainly contained noise. The maximum improvement of the MNF transformation was 3.94% for wheat, 6.02% for soybean, and 8.65% for forage. For forest, the accuracies before and after the MNF transformation showed minor differences, and the classification accuracies were similar between different polarimetric SAR parameter sets. However, for corn, the MNF transformation slightly reduced its producer's accuracy. The overall accuracy of the MNF transformation of the multi-temporal coherency matrix data was competitive with the overall accuracy of the integration of multi-temporal optical images and the coherency matrix data. The SVM classifier performed worse than the RF classifier, and the MNF transformation of the multi-temporal SAR data had a minor influence on the classification accuracy when the SVM classifier was used.

References

- Alberga, V. (2007). A study of land cover classification using polarimetric SAR parameters. *International Journal of Remote Sensing*, 28(17), 3851–3870. <http://doi.org/10.1080/01431160601075541>
- Alvarez-Perez, J. L. (2011). Coherence, polarization, and statistical independence in Cloude-Pottier's radar polarimetry. *IEEE Transactions on Geoscience and Remote Sensing*, 49(1), 426–441. <http://doi.org/10.1109/TGRS.2010.2056375>
- Banks, S., Millard, K., Pasher, J., Richardson, M., Wang, H., & Duffe, J. (2015). Assessing the potential to operationalize shoreline sensitivity mapping: Classifying multiple wide fine quadrature polarized RADARSAT-2 and Landsat 5 scenes with a single random forest model. *Remote Sensing*, 7(10), 13528–13563. <http://doi.org/10.3390/rs71013528>
- Boardman, J. W., & Kruse, F. A. (1994). Automatic spectral analysis: A geological example using AVIRIS data, North Grapevine Mountain, Nevada. In *10th Thematic Conference on Geologic Remote Sensing* (pp. 407–418). Ann Arbor.
- Breiman, L. (1999). Random Forests, 1–29. Retrieved from <http://www.stat.berkeley.edu/~breiman/random-forests.pdf>
- Cao, F., & Hong, W. (2005). A new classification method based on Cloude Pottier eigenvalue/eigenvector decomposition. *Geoscience and Remote Sensing Symposium, 2005. IGARSS '05. Proceedings. 2005 IEEE International*, 1(1), 4. <http://doi.org/10.1109/IGARSS.2005.1526166>
- Cloude, S. R., & Pottier, E. (1996). A review of target decomposition theorems in radar polarimetry. *IEEE Transactions on Geoscience and Remote Sensing*, 34(2), 498–518. Retrieved from http://ieeexplore.ieee.org/xpls/abs_all.jsp?arnumber=485127
- Couto Junior, A. F., de Carvalho Júnior, O. A., Martins, É. de S., & Vasconcelos, V. (2013). Characterization of the agriculture occupation in the cerrado biome using modis time-series. *Revista Brasileira de Geofísica*, 31(3), 393–402.
- Deschamps, B., McNairn, H., Shang, J., & Jiao, X. (2012). Towards operational radar-only crop type classification: Comparison of a traditional decision tree with a random forest classifier. *Canadian Journal of Remote Sensing*, 38(1), 60–68. <http://doi.org/10.5589/m12-012>

- Forkuor, G., Conrad, C., Thiel, M., Ullmann, T., & Zoungrana, E. (2014). Integration of optical and synthetic aperture radar imagery for improving crop mapping in northwestern Benin, West Africa. *Remote Sensing*, 6(7), 6472–6499. <http://doi.org/10.3390/rs6076472>
- Freeman, A., & Durden, S. L. (1998). A three-component scattering model for polarimetric SAR data. *IEEE Transactions on Geoscience and Remote Sensing*, 36(3), 963–973. <http://doi.org/10.1109/36.673687>
- Gao, L., & Ban, Y. (2008). Investigating the performance of SAR polarimetric features in land-cover classification. *The International Archives of the Photogrammetry, Remote Sensing and Spatial Information Sciences. Vol. XXXVII. Part B6b*, (1), 317–322.
- Ghamisi, P., Plaza, J., Chen, Y., Li, J., & Plaza, A. J. (2017). Advanced spectral classifiers for hyperspectral images: A review. *IEEE Geoscience and Remote Sensing Magazine*, 5(1), 8–32. <http://doi.org/10.1109/MGRS.2016.2616418>
- Green, A. A., Berman, M., Switzer, P., & Craig, M. D. (1988). A transformation for ordering multispectral data in terms of image quality with implications for noise removal. *IEEE Transactions on Geoscience and Remote Sensing*, 26(1), 65–74. <http://doi.org/10.1109/36.3001>
- Huang, X., Wang, J., Shang, J., Liao, C., & Liu, J. (2017). Application of polarization signature to land cover scattering mechanism analysis and classification using multi-temporal C-band polarimetric RADARSAT-2 imagery. *Remote Sensing of Environment*, 193, 11–28. <http://doi.org/10.1016/j.rse.2017.02.014>
- Iannini, L., Molijn, R. A., & Hanssen, R. F. (2013). Integration of multispectral and C-band SAR data for crop classification. *Conference on Remote Sensing for Agriculture, Ecosystems, and Hydrology*, 8887, 1–8. <http://doi.org/10.1117/12.2029330>
- Jiao, X., Kovacs, J. M., Shang, J., McNairn, H., Walters, D., Ma, B., & Geng, X. (2014). Object-oriented crop mapping and monitoring using multi-temporal polarimetric RADARSAT-2 data. *ISPRS Journal of Photogrammetry and Remote Sensing*, 96, 38–46. <http://doi.org/10.1016/j.isprsjprs.2014.06.014>

- Larrañaga, A. (2011). Crop classification in rain-fed and irrigated agricultural areas using Landsat TM and ALOS / PALSAR data, *37*(1). <http://doi.org/10.5589/m11-022>
- Lee, J.-S., & Pottier, E. (2009). H/A/ $\bar{\alpha}$ polarimetric decomposition theorem. In *Polarimetric Radar Imaging* (p. 237). CRC Press.
<http://doi.org/doi:10.1201/9781420054989.ch7>
- Luo, G., Chen, G., Tian, L., Qin, K., & Qian, S. (2016). Minimum noise fraction versus principal component analysis as a preprocessing step for hyperspectral imagery denoising. *Canadian Journal of Remote Sensing*, *42*(2), 106-116.
<https://doi.org/10.1080/07038992.2016.1160772>
- McNairn, H., Champagne, C., Shang, J., Holmstrom, D., & Reichert, G. (2009a). Integration of optical and Synthetic Aperture Radar (SAR) imagery for delivering operational annual crop inventories. *ISPRS Journal of Photogrammetry and Remote Sensing*, *64*(5), 434–449. <http://doi.org/10.1016/j.isprsjprs.2008.07.006>
- McNairn, H., Shang, J., Jiao, X., & Champagne, C. (2009b). The contribution of ALOS PALSAR multipolarization and polarimetric data to crop classification. *IEEE Transactions on Geoscience and Remote Sensing*, *47*(12), 3981–3992.
<http://doi.org/10.1109/TGRS.2009.2026052>
- Mishra, P., Singh, D., Yamaguchi, Y., & Singh, D. (2011). Land cover classification of PALSAR images by knowledge based decision tree classifier and supervised classifiers based on SAR observables. *Progress In Electromagnetics Research B*, *30*(January), 47–70. <http://doi.org/10.2528/PIERB11011405>
- Prasad, A. M., Iverson, L. R., & Liaw, A. (2006). Newer classification and regression tree techniques: Bagging and random forests for ecological prediction. *Ecosystems*, *9*(2), 181–199. <http://doi.org/10.1007/s10021-005-0054-1>
- Rodriguez-Galiano, V. F., Ghimire, B., Rogan, J., Chica-Olmo, M., & Rigol-Sanchez, J. P. (2012). An assessment of the effectiveness of a random forest classifier for land-cover classification. *ISPRS Journal of Photogrammetry and Remote Sensing*, *67*(1), 93–104. <http://doi.org/10.1016/j.isprsjprs.2011.11.002>
- Shang, J., Champagne, C., & McNairn, H. (2006). Agriculture land use mapping using multi-sensor and multi-temporal Earth Observation data. *Proceedings of the MAPPs/ASPRS 2006 Fall Conference, 6-10 November, 2006, San Antonio, USA*,

- 1–12. Retrieved from
<http://www.asprs.org/a/publications/proceedings/fall2006/0044.pdf>
- Shang, J., McNairn, H., Deschamps, B., Jiao, X., & Champagne, C. (2011a). Contribution of TerraSAR-X data to in-season crop mapping in Canada. *Proceedings of TerraSAR-X Science Team Meeting*, (Figure 1), 2–10.
- Shang, J., McNairn, H., Deschamps, J., & Jiao, X. (2011b). In-season crop inventory using multi-angle and multi-pass RADARSAT-2 SAR data over the Canadian prairies. *Proceedings of SPIE - The International Society for Optical Engineering*, 8156, 815604–815604. <http://doi.org/10.1117/12.894211>
- Skriver, H. (2012). Crop classification by multitemporal C- and L-band single- and dual-polarization and fully polarimetric SAR. *IEEE Transactions on Geoscience and Remote Sensing*, 50(6), 2138–2149. <http://doi.org/10.1109/TGRS.2011.2172994>
- Soliman, O. S., Mahmoud, A. S., & Hassan, S. M. (2012). Remote sensing satellite images classification using support vector machine and particle swarm optimization. *2012 Third International Conference on Innovations in Bio-Inspired Computing and Applications*, 280–285. <http://doi.org/10.1109/IBICA.2012.61>
- Sonobe, R., Tani, H., Wang, X., Kobayashi, N., & Shimamura, H. (2014). Random forest classification of crop type using multi-temporal TerraSAR-X dual-polarimetric data. *Remote Sensing Letters*, 5(2), 157–164.
<http://doi.org/10.1080/2150704X.2014.889863>
- Switzer, P., & Green, A. A. (1984). *Min/max autocorrelation factors for multivariate spatial imagery*.
- Tatsumi, K., Yamashiki, Y., Canales Torres, M. A., & Taïpe, C. L. R. (2015). Crop classification of upland fields using random forest of time-series Landsat 7 ETM+ data. *Computers and Electronics in Agriculture*, 115, 171–179.
<http://doi.org/10.1016/j.compag.2015.05.001>
- Tavakkoli, M., & Lohmann, P. (2006, May). *Multi-Temporal classification of ASAR images in agricultural areas*, ISPRS May 2006.
- Wardlow, B. D., Egbert, S. L., & Kastens, J. H. (2007). Analysis of time-series MODIS 250 m vegetation index data for crop classification in the U.S. Central Great

Plains. *Remote Sensing of Environment*, 108(3), 290–310.

<http://doi.org/10.1016/j.rse.2006.11.021>

Zhu, Z., Woodcock, C. E., Rogan, J., & Kellndorfer, J. (2012). Assessment of spectral, polarimetric, temporal, and spatial dimensions for urban and peri-urban land cover classification using Landsat and SAR data. *Remote Sensing of Environment*, 117, 72–82. <http://doi.org/10.1016/j.rse.2011.07.020>

Chapter 4

4 A Spatio-Temporal Data Fusion Model for Generating NDVI Time Series in Heterogeneous Regions³

4.1 Introduction

The Normalized Difference Vegetation Index (NDVI) is a widely used vegetation index (VI) derived from optical remote-sensing data to evaluate the biophysical or biochemical information related to vegetation growth (Busetto, Meroni, & Colombo, 2008; Fensholt, 2004; Hilker et al., 2009; Jönsson & Eklundh, 2002; Kang et al., 2003). Large scale time series NDVI is generally used for assessment and monitoring of forest (Bhandari, Phinn, & Gill, 2012; Walker, De Beurs, Wynne, & Gao, 2012), grassland (Olexa & Lawrence, 2014; Schmidt, Udelhoven, Gill, & Röder, 2012; Tewes et al., 2015), ecological environment (Tian et al., 2013; Watts, Powell, Lawrence, & Hilker, 2011), wildlife habitat disturbance (Gaulton, Hilker, Wulder, Coops, & Stenhouse, 2011), and to estimate gross primary productivity (Chen et al., 2010), biomass (Dong et al., 2016; Meng, Du, & Wu, 2011), and evapotranspiration (Anderson et al., 2011). It can be calculated from the images acquired by sensors such as the Advanced Very High Resolution Radiometer (AVHRR), Moderate Resolution Imaging Spectroradiometer (MODIS), Medium Resolution Imaging Spectrometer (MERIS), Sea-Viewing Wide Field-of-View Sensor (SEAWIFS), or VEGETATION, with spatial resolution ranging from 250 m to a few kilometers (Busetto et al., 2008). In applications such as crop monitoring, time series images acquired by high spatial-resolution sensors such as Landsat-OLI (30 m) and RapidEye (5 m) are required to provide spatial and temporal details. However, due to cost and technical limitations (trade-off between pixel spatial resolution and satellite temporal revisiting cycle) (Zhu, Chen, Gao, Chen, & Masek, 2010) and cloud cover problems, it is difficult to acquire images with both

³ A version of this chapter has been published (Chunhua Liao, Jinfei Wang, Ian Pritchard, Jianguo Liu, Jiali Shang. A spatio-temporal vegetation index image fusion model for generating high spatial and temporal resolution NDVI images in cropland areas. *Remote Sensing*. 2017, 9(11):1125)

high spatial resolution and high temporal frequency. Thus, spatio-temporal data fusion techniques have been developed as a feasible and less expensive way to acquire remote sensing time series data for land surface dynamics monitoring (Gao, Masek, Schwaller, & Hall, 2006; Hazaymeh & Hassan, 2015; Marfai, Almohammad, Dey, Susanto, & King, 2008; Zhu et al., 2016).

In general, generating fine-resolution NDVI time series images through spatio-temporal data fusion can be conducted in two ways (Jarihani et al., 2014): (i) conduct fusion of reflectance first and then calculate the NDVI (Blend-then-Index, BI); and (ii) calculate the NDVI first and then conduct fusion (Index-then-Blend, IB). The theoretical basis of the two ways are essentially the same, and some of the methods developed for reflectance images can also be used for NDVI images. However, the IB is preferred over BI due to less error propagation and fewer computational steps (blending one index band versus multiple reflectance bands) (Jarihani et al., 2014).

A few categories of spatio-temporal data fusion approaches have been originally proposed to blend reflectance images including data-assimilation based algorithms, unmixing based methods, dictionary-pair learning based methods, and weighted function based methods (Zhu et al., 2016). The data-assimilation based algorithms incorporate observation data with models and their uncertainties to minimize the residual errors (Mathieu & O'Neill, 2008). The advantage of data-assimilation based algorithms is that a complete time series of fine-resolution images, rather than single synthetic image, can be synthesized in the implementation. A recursive Kalman filter algorithm (KF) was implemented to produce frequent fine-resolution NDVI time series using available fine-resolution images and a time series of coarse-resolution NDVI images in previous studies (Kempeneers, Sedano, Piccard, & Eerens, 2016; Sedano, Kempeneers, & Hurtt, 2014). The uncertainty of these algorithms is correlated to the number of available fine-resolution observations, and these algorithms suffer large uncertainties when the available fine-resolution images are limited in heterogeneous areas.

The unmixing based methods include the Multisensor Multiresolution Technique (MMT) (Zhukov, Oertel, & Lanzl, 1999), the spatial temporal data fusion approach (STDFA) (Wu,

Wang, Niu, Zhao, & Wang, 2012), and the spatial and temporal reflectance unmixing model (STRUM) (Gevaert & García-Haro, 2015). These methods assume that remote sensing signal of coarse-resolution pixels is the weighted average of the mean reflectance of each class and a residual error. The weight of each class is its fractional cover within one coarse-resolution pixel, which can be calculated from a fine-resolution land-cover map. The mean reflectance of each land cover is estimated by solving a number of spectral unmixing model equations of coarse-resolution pixels, and the mean reflectance of each land cover is assigned to the fine-resolution pixels. The unmixing based concept can also be used for spatio-temporal fusion of NDVI images. Busetto et al. (2008) proposed an approach for the estimation of sub-pixel NDVI time series by combining fine- and coarse-resolution NDVI images based on an unmixing approach. This approach aims to estimate the mean NDVI of each land cover within one coarse-resolution pixel from daily MODIS data by solving the linear weighted equations using manually selected coarse-resolution pixels, and disaggregate MODIS NDVI using weights calculated by Gaussian functions of MODIS spectral dissimilarity index and the Euclidean spatial distance between the target and each pixel. Rao et al. (2015) proposed the NDVI Linear Mixing Growth Model (NDVI-LMGM) to produce high spatial resolution NDVI time-series data by using MODIS NDVI time series data and Landsat NDVI images. The NDVI-LMGM combines the NDVI linear mixing model with the NDVI linear growth model. It assumes that the short-term changes in NDVI can be interpreted as linear, and long-term NDVI changes can only be predicted reliably by several short-term predictions. The change rate of each land cover during the two dates on the TM/ETM+ pixel scale within the corresponding MODIS pixel can be estimated by solving the linear weighted equations. Another method, NDVI-Bayesian spatiotemporal fusion model (NDVI-BSFM) (Liao, Song, Wang, Xiao, & Wang, 2016), employed the Bayesian pixel unmixing process through incorporating the prior multi-year average MODIS NDVI from the first day of the year to the last day of the year for each land cover type, and it can predict a single Landsat-like NDVI image as well as build a Landsat-like NDVI time-series dataset. However, these methods are computationally intensive and rely heavily on the quality of MODIS NDVI data. Furthermore, the performance of these methods will be affected by the classification accuracies (Zurita-Milla, Kaiser, Clevers, Schneider, & Schaepman, 2009), especially when there are land

cover changes within a year. These methods are not applicable when reliable Land cover/Land use (LC/LU) ancillary information is not available. For example, in some cropland area, the crop types change every year due to the annual rotation of the crops. Thus, the LC/LU data are generally produced at the end of the growing season.

The dictionary-pair learning based methods, such as the sparse representation-based spatio-temporal reflectance fusion model (SPSTFM) (Huang & Song, 2012; Song & Huang, 2013) and the error-bound-regularized semi-coupled dictionary learning (EBSCDL) (Wu, Huang, Zhang, & Member, 2015), need one or two pairs of fine- and coarse-resolution images and one coarse-resolution image as input data. It builds relationships (dictionaries) between the features of fine-resolution images and their corresponding coarse-resolution images through dictionary-pair learning (Chen, Huang, & Xu, 2015; Yang, Wright, Huang, & Ma, 2010), and then applies the relationship (dictionary) to predict a fine-resolution image on the prediction date. The dictionary-pair learning based methods performed well in phenology change, but they still face challenges in heterogeneous regions with abrupt land cover type changes (Zhu et al., 2016), and they are computationally complex (Huang & Song, 2012; Zhu et al., 2016).

The weighted function based methods include the spatial and temporal adaptive reflectance fusion model (STARFM) (Gao et al., 2006), and the enhanced spatial and temporal adaptive reflectance fusion model (ESTARFM) (Zhu et al., 2010). Due to simple input requirements (no ancillary land cover data or classification data required) and robustness, they are widely used in many applications (Bisquert et al., 2015; Jarihani et al., 2014; Knauer, Gessner, Fensholt, & Kuenzer, 2016; Meng et al., 2011; Tian et al., 2013). The input data of the STARFM algorithm are one or two pairs of fine- and coarse-resolution images acquired at the same time and one coarse-resolution image acquired at the prediction time. This algorithm assumes that the reflectance of a given coarse-resolution pixel can be aggregated from fine-resolution homogeneous pixels. The STARFM attempts to search neighboring spectral similar fine-resolution pixels within a moving window and endows the weights of these similar pixels calculated according to the spectral difference between coarse-resolution and fine-resolution data, the temporal difference between the input MODIS data, and the distance to the central pixel. The reflectance of the central fine-

resolution pixel is estimated from the neighboring similar homogeneous pixels. However, the STARFM algorithm is not applicable to heterogeneous areas such as croplands (Zhu et al., 2010). Due to this limitation, an improved STARFM with help of unmixing-based method (USTARFM) was proposed (Xie et al., 2016). However, it still subjects the problem of land cover changes. The ESTARFM was proposed by Zhu et al. (Zhu et al., 2010) to enhance the ability of STARFM through the use of two pairs of fine-resolution and coarse-resolution images obtained on two dates. It is able to minimize the system biases between the sensors and is more suitable for heterogeneous areas by using two pairs of fine- and coarse-resolution images to detect land cover changes and it keeps more spatial details (Zhu et al., 2010). However, the ESTARFM method assumes that there is no temporal variation in change rate of the vegetation during a period, which is not reasonable if it is long a period between the input images. Furthermore, the ESTARFM neglects the variation of the relationship between the fine- and coarse-resolution images caused by different acquisition dates. The spatial and temporal nonlocal filter-based data fusion method (STNLFFM) (Cheng, Liu, Shen, Wu, & Zhang, 2017) is a recently proposed method that can predict the fine-resolution reflectance accurately and robustly by introducing the idea of nonlocal filtering, for both heterogeneous landscapes and temporally dynamic areas. However, it is based on the assumption that the reflectance change rate is linear, which is not accurate over a long period. The flexible spatiotemporal data fusion (FSDAF) model (Zhu et al., 2016) is a method using one pair of fine- and coarse-resolution images and one coarse-resolution image acquired on the prediction date. This method integrates the unmixing-based methods, spatial interpolation, and STARFM into one framework. It performs better in predicting abrupt land cover changes than other methods that use only one pair of fine- and coarse-resolution images. However, this method is computationally expensive and the prediction accuracy greatly depends on the extent of land cover changes between the two dates of the input images.

In this study, a spatio-temporal vegetation index image fusion model (STVIFM) is proposed to generate NDVI time series images with high spatial and high temporal resolution in heterogeneous regions such as croplands more accurately and robustly. Different from the methods mentioned above, we aim to predict the NDVI change for each fine-resolution pixel by using a weighting system to disaggregate the total NDVI change

within a moving window, which can be calculated from the coarse-resolution NDVI images acquired on two different dates. The proposed model employed: (1) a new weighting system; (2) a new method to obtain the relationship between the two resolution images; and (3) more reasonable assumptions on the NDVI change rate of non-evergreen vegetation, which considers the change rate variations at both spatial scale and temporal scale. This algorithm is tested by Landsat-OLI and MODIS data acquired in three study sites. The results generated by the STARFM, ESTARFM and FSDAF methods are validated by the real Landsat NDVI images or field measurements for three study sites and different growth stages of a cropland area.

4.2 Methodology

4.2.1 Theoretical Basis

Most of the spatio-temporal data fusion methods are based on the linear mixture model, which assumes that the reflectance of a coarse-resolution pixel (mixed pixel) can be modeled as the sum of the reflectance of different land cover endmembers (pure pixels) within the pixel, weighted by the corresponding fractional cover of each component (Busetto et al., 2008; Settle & Drake, 1993). This assumption can also be used for NDVI values, and it was demonstrated that this linear assumption for NDVI only led to minor inaccuracies (Kerdiles & Grondona, 1995). The linear mixture model can be written as in Equation (4-1):

$$\text{NDVI} = \sum_{c=1}^k (f_c \times \text{NDVI}_c) + \varepsilon \quad (4-1)$$

where k is the number of classes. f_c represents the fractional cover of land cover class c in this pixel and $\sum_{c=1}^k f_c = 1$. NDVI_c is the NDVI of endmember of land cover class c . ε is the residual error term. This model can be applied to both fine- and coarse-resolution pixels.

The difference in NDVI between a single coarse-resolution pixel and a fine-resolution pixel results from the heterogeneity of the observed area and the systematic biases caused by the difference in sensor systems (Zhu et al., 2010). For heterogeneous areas, there may be great changes of fine-resolution pixels within one original coarse-resolution pixel, so it is

inappropriate to build relationships between the individual fine-resolution pixels and coarse-resolution pixels with a linear regression method. The relationship between NDVI of a pure coarse-resolution pixel ($NDVI'_c$) and NDVI of a pure fine-resolution pixel ($NDVI_c$) for a given class c can be described with a linear model:

$$NDVI_c = a \times NDVI'_c + b \quad (c = 1, 2, \dots, k) \quad (4-2)$$

where a and b are the coefficients of the linear regression model between the coarse- and fine-resolution NDVI of pure pixels.

For fine-resolution pixels contained by a coarse resolution pixel, if we neglect the residual error, NDVI of the i th fine-resolution pixel can be calculated from Equations (4-1) and (4-2):

$$NDVI_i = \sum_{c=1}^k (f_{ci} \times (a \times NDVI'_c + b)) = a \times \left(\sum_{c=1}^k f_{ci} \times NDVI'_c \right) + b \quad (4-3)$$

The average fractional cover of class c of all the fine-resolution pixels within one coarse-resolution image is equal to the fractional cover of the coarse-resolution image. Therefore, the average NDVI of fine-resolution pixels can be obtained using Equation (4-4):

$$\overline{NDVI} = a \times NDVI' + b \quad (4-4)$$

where $NDVI'$ is the NDVI of one coarse-resolution pixel. If the coarse-resolution image is resampled to the same spatial resolution as the fine-resolution image using the nearest neighbor method (the value of each resampled pixel is the same within a coarse-resolution pixel), the NDVI value of each original coarse-resolution pixel is equal to the mean value of the resampled pixels within the original pixel. If there are three pairs of fine- and coarse-resolution images acquired on date m (t_m), date n (t_n), and the prediction date p (t_p), which is between t_m and t_n ($t_m < t_p < t_n$), the mean NDVI of the N fine-resolution image pixels on the three dates ($\overline{NDVI}_m, \overline{NDVI}_n, \overline{NDVI}_p$) have linear relationships with the mean NDVI of the corresponding N resampled coarse-resolution image pixels ($\overline{NDVI}'_m, \overline{NDVI}'_n, \overline{NDVI}'_p$) respectively. The relationships can be expressed as Equation (4-5):

$$\overline{\text{NDVI}}_k = a_k \times \overline{\text{NDVI}}'_k + b_k \quad (k = m, p, n) \quad (4-5)$$

where a_m, a_n and b_m, b_n can be obtained through the regression of the two pairs of images, respectively. As there is no available fine-resolution image at t_p , the correlation cannot be achieved through regression. a_p and b_p may be different from a_m, b_m or a_n, b_n ; thus, the total NDVI difference between the prediction date (t_p) and the date before (t_m) or after (t_n) of the fine-resolution pixels within the moving window can be obtained by Equation (4-6):

$$\begin{aligned} \sum_{i=1}^N (\Delta \text{NDVI}_{pki}) &= (\overline{\text{NDVI}}_p - \overline{\text{NDVI}}_k) \times N \\ &= (a_p \times \overline{\text{NDVI}}'_p - a_k \times \overline{\text{NDVI}}'_k + b_p - b_k) \times N \quad (k \\ &= m, n) \end{aligned} \quad (4-6)$$

To obtain each fine-resolution pixel's NDVI change between t_m (or t_n) and t_p , a disaggregation weighting system can be adopted to describe the contribution of each pixel to the total NDVI changes calculated from the coarse-resolution pixels within the moving window. Then, the NDVI for each pixel can be obtained from the image acquired at t_m or the image acquired at t_n by adding the predicted NDVI change of each fine-resolution pixel (Equation (4-7)):

$$\text{NDVI}_{pki} = \text{NDVI}_{ki} + W_{ki} \times \sum_{i=1}^N (\Delta \text{NDVI}_{pki}) \quad (k = m, n) \quad (4-7)$$

Theoretically, the NDVI at t_p can be predicted using the fine-resolution NDVI at t_m or t_n . In heterogeneous regions, local land cover changes may cause large inaccuracies if only one fine-resolution image is used as the base image. To reduce the inaccuracy caused by local land cover changes, the two estimations based on the two fine-resolution images can be combined according to the local similarity between the two coarse-resolution images to obtain a more robust result.

$$\text{NDVI}_{pi} = S_{lpm} \times \text{NDVI}_{pmi} + S_{lpn} \times \text{NDVI}_{pni} \quad (4-8)$$

where S_{lpm} and S_{lpn} represent the local similarity weights, $S_{lpm} + S_{lpn} = 1$. The calculation of S_{lpm} and S_{lpn} will be given in Section 4.2.3.

4.2.2 Weighting System

To predict fine-resolution NDVI at t_p , the accurate calculation of weights, which aim to disaggregate the total NDVI change to each fine-resolution pixel within a moving window, is an important part of this algorithm. The traditional approach to calculate the NDVI change is to solve a system of linear mixture equations based on a prior classification map. However, this process is time consuming and the results ignored the difference of growth status in the same land cover type. Another approach is to calculate the change rate using the two fine-resolution images, which is adopted in the ESTARFM method (Zhu et al., 2010). The ESTARFM assumes that the change rate is stable during the period between t_m and t_n . This assumption is reasonable if the period between t_m and t_n is short enough (e.g., a few days), but if the period is not short enough (e.g., 20 days), the change rate will vary during this period. In this study, we attempt to estimate the NDVI change based on the two acquired fine-resolution images by addressing the variations of NDVI change rate at spatial and temporal scale.

According to the NDVI time series profile of pure vegetation pixels generated from MODIS NDVI time series data acquired in a growing season shown in previous studies (Liao et al., 2016; Rao et al., 2015) or the simulated NDVI time-series profile modeled by a double logistic function (Sun & Schulz, 2017), the NDVI change rate increases with the increase of NDVI at the beginning of the growing stage, then reaches a maximum, and then decreases at the growing stage. The same trend is shown at the senescent stage. Theoretically, at the early growing stage, the growth rate, which is related to the NDVI change rate of healthy vegetation, is low due to the limited photosynthesis process caused by many factors such as temperature and chlorophyll content (Lambers, Chapin III, & Pons, 2008). Then, the growth rate increases due to the optimal temperature, increasing chlorophyll content and other factors. At the later growing stage, the growth rate decreases due to the deficiency of nitrogen, water, and the change of temperature, etc. (Lambers et al., 2008). For heterogeneous regions, the NDVI change rates of different pixels may vary

within a moving window. This variation may be caused by the difference of vegetation types or the difference in growth stages of the same vegetation type. Therefore, the spatial variation of fine-resolution NDVI change (spatial weight) varies with the prediction time t_p . For better understanding the variation of NDVI change rate at the temporal scale and spatial scale, we simulated the NDVI time series profiles for three pure crop pixels within a moving window according to the NDVI time series profile of vegetation pixel generated from MODIS NDVI time series data in previous studies (Liao et al., 2016; Rao et al., 2015) (Figure 4-1).

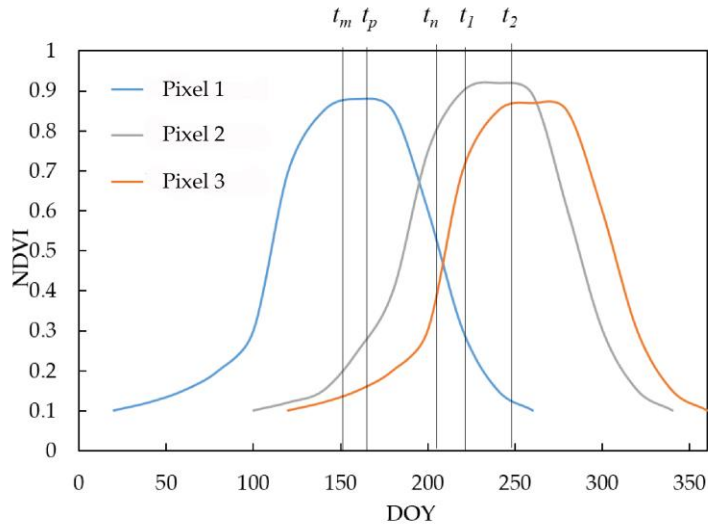


Figure 4-1: Diagram of simulated Normalized Difference Vegetation Index (NDVI) profiles for different crop pixels.

When image acquired at t_m is used as the base image, if Δt_{np} ($t_n - t_p$) is short enough, the spatial variation of NDVI change from t_m to t_p can be determined by the spatial variation of the fine-resolution NDVI change from t_m to t_n . If Δt_{mp} ($t_p - t_m$) is short enough (e.g., one day), the spatial variation of NDVI change from t_m to t_p cannot be accurately calculated using the spatial variation of the fine-resolution NDVI change from t_m to t_n due to the spatial and temporal variations of NDVI change rate. However, the spatial variation of fine-resolution NDVI change from t_m to t_p is closely related to the spatial variation of NDVI change rate at t_m . When t_p moves from t_m to t_n , the NDVI change between t_m and t_p becomes more and more related to the NDVI change between t_m and t_n . The idea is the same when image acquired at t_n is used as the base image. Thus, for any time t_p between t_m and t_n , we

propose to calculate the final spatial weight for NDVI changes by combining the NDVI change rate calculated from the image acquired at t_m or t_n , and the temporal NDVI change between t_m and t_n using a temporal weight. Since two estimations can be calculated from the two base images, and there may be abrupt changes, a more robust final prediction can be achieved by combining the two predictions using a local similarity weight (Equation (4-8)). However, if there are peaks (growing stage to senescence stage) or valleys (senescence stage to growing stage) for the vegetation NDVI profile between t_m and t_n , and t_p is neither close to t_m nor to t_n , large inaccuracy would be produced. The detailed idea of the weighting system is illustrated in Sections 4.2.2.1–4.2.2.3.

4.2.2.1 Weight Calculation Based on Temporal NDVI Change

As mentioned above, if t_p is very close to t_n , the variation of NDVI change from t_m to t_p can be determined by the variation of the fine-resolution NDVI change from t_m to t_n (Equation (4-9)).

$$D = \text{NDVI}_n - \text{NDVI}_m \quad (4-9)$$

In heterogeneous regions, for example when increasing NDVI pixels may be mixed with decreasing NDVI pixels caused by harvesting, flooding or re-planting areas and unchanged NDVI pixels such as bare soil within the moving window, the weight calculation based on temporal NDVI change is complex. To keep the same sign of the weight calculated from temporal NDVI change, the three types of pixels should be processed separately. The land covers were classified into three categories according to the NDVI change from t_m to t_n (Equation (4-10)). Even though it is an unvegetated area such as bare soil, the NDVI may have minor temporal changes due to the slight variation of its spectral characteristics over time. Therefore, ± 0.1 are selected as the thresholds for the classification. The selection of the thresholds is also supported by the finding that the NDVI threshold for bare soil was 0.1 (Gandhi, Parthiban, Thummalu, & Christy, 2015). The weight of each pixel within the moving window was calculated separately according to their categories.

$$\begin{cases} D_i > 0.1 & \text{Category 1, growing vegetation} \\ D_i < -0.1 & \text{Category 2, senescent vegetation/ disturbance} \\ -0.1 \leq D_i \leq 0.1 & \text{Category 3, unchanged area/short term changes} \end{cases} \quad (4-10)$$

where D_i is the NDVI difference of the i th pixel in the moving window. If D_i is greater than 0.1 ($D_i > 0.1$), the i th pixels is marked as growing vegetation. If D_i is less than -0.1 ($D_i < -0.1$), it is marked as a disturbance or senescent vegetation. If D_i is less than or equal to -0.1 and greater than or equal to 0.1 ($-0.1 \leq D_i \leq 0.1$), it is regarded as unchanged area or short-term changes that were not recorded in the two fine-resolution images. For Categories 1 and 2, the weight related to the temporal NDVI change between t_m and t_n for each pixel can be obtained by and Equation (4-11).

$$w_{tji} = D_i / \sum_{i=1}^{N_j} D_i \quad (j = 1, 2) \quad (4-11)$$

where w_{tji} is the weight calculated from temporal NDVI change for the i th pixel that belongs to the j th category. N_j is the number of the pixels that belong to category j within the moving window. However, for areas where there is no temporal NDVI change between t_m and t_p (Category 3), this calculation is not applicable.

4.2.2.2 Weight Calculation Based on NDVI Change Rate

If Δt_{mp} ($t_p - t_m$) is short enough (e.g., 1 day), the variation of fine-resolution NDVI change from t_m to t_p is closely related to the variation of NDVI change rate at t_m . Under this circumstance, we believe that the NDVI value of the fine-resolution image acquired at any time is related to the NDVI change rate at that time according to Figure 4-1 and the physiological characteristics of plants described in (Lambers, Chapin III, & Pons, 2008). For heterogeneous regions, the spatial variation of NDVI values at t_m causes the spatial variation of the NDVI change rate, and accordingly the NDVI change between t_m and t_p . From the simulated NDVI profile shown in Figure 4-1 or the NDVI profile generated from remote sensing time series images (Liao et al., 2016; Rao et al., 2015), it can be assumed that for different types of vegetation or the same type of vegetation with different growth stages, the pixels with low or high NDVI values have lower NDVI change rate and the pixels with median NDVI values should have higher change rate at that time. The spatial variation of the NDVI change rate can be interpreted using a change rate index (CRI)

calculated by an exponential function (Equation (4-12)) based on one acquired fine-resolution NDVI image.

$$CRI_k = e^{-\frac{(NDVI_k-d)^2}{\sigma^2}} \quad (k = m, n) \quad (4-12)$$

where σ^2 is the variance of the transformed values, and d represents the NDVI value where the change rate is maximum. Since the theoretical NDVI values for vegetation pixels range from 0 to 1, the median value 0.5 was selected as the value of d in this study. σ^2 was set to 0.1 to obtain the change rate index with a dynamic range from 0 to 1.

The weight calculated from the NDVI change rate for the i th pixel that belongs to category j at t_m (w_{mji}) or t_n (w_{nji}) can be calculated by Equation (4-13).

$$w_{kji} = \frac{CRI_{ki}}{\sum_{i=1}^{N_j} CRI_{ki}} \quad (k = m, n; j = 1, 2, 3) \quad (4-13)$$

4.2.2.3 Final Weight Calculation

For heterogeneous vegetated areas, the more similar the land cover on the base date (t_m or t_n) is to the land cover on the prediction date, the more accurate is the predicted image. The time interval can be an indicator for the similarity of land cover but there are exceptions. For example, in Figure 4-1, the NDVI change is larger from t_n to t_1 than from t_1 to t_2 for pixel 2 even though $t_1 - t_n$ is less than $t_2 - t_1$. To avoid the manual input of dates for the acquired images, and the circumstance that the NDVI change is larger in a shorter period, the correlation coefficient (r_w) (Equation (4-14)) between two coarse-resolution images for the whole region is selected to calculate the temporal weight (T) (Equation (4-15)). Compared with other statistical indices, the correlation coefficient is more suitable for indicating land cover similarity in heterogeneous regions as it reflects the similarity in the trend of differences associated with each pixel.

$$r_{wpk} = \frac{\sum_{i=1}^N (NDVI'_{ki} - \overline{NDVI'_k})(NDVI'_{pi} - \overline{NDVI'_p})}{\sqrt{\sum_{i=1}^N (NDVI'_{ki} - \overline{NDVI'_k})^2} \times \sqrt{\sum_{i=1}^N (NDVI'_{pi} - \overline{NDVI'_p})^2}} \quad (k = m, n) \quad (4-14)$$

$$T_{pk} = \frac{r_{wpk}^2}{r_{wpm}^2 + r_{wpn}^2} \quad (k = m, n) \quad (4-15)$$

where r_{wpk} is the correlation coefficient of the whole image at t_p and t_k ($k = m, n$). N is the number of pixels in the whole region. T_{pk} represents the temporal weight between image t_p and t_k ($k = m, n$).

For any prediction time between t_m and t_n , the final weight for vegetated areas (Category 1,2) can be calculated using the temporal weighted average of the weight calculated from the spatial NDVI variation and the temporal NDVI change (Equation (4-16)).

$$\begin{cases} W_{mji} = T_{pm} \times w_{mji} + T_{pn} \times w_{tji} \\ W_{nji} = T_{pn} \times w_{nji} + T_{pm} \times w_{tji} \end{cases} \quad (j = 1,2) \quad (4-16)$$

where W_{mji} or W_{nji} is the final weight for the i th pixel calculated based on the fine-resolution image acquired at t_m or t_n for the j th category. For areas where there is no temporal NDVI change (Category 3) between t_m and t_p , the final weight is the same as the weight calculated based on the NDVI change rate (Equation (4-17)).

$$\begin{cases} W_{mji} = w_{mji} \\ W_{nji} = w_{nji} \end{cases} \quad (j = 3) \quad (4-17)$$

4.2.3 Implementation of the STVIFM

The STVIFM requires two pairs of fine- and coarse-resolution images acquired on the same date and one coarse-resolution image on the prediction date. All of the input images need to be preprocessed (re-projection, geometric correction, and NDVI calculation). A moving window is adopted for implementing the STVIFM. The step of the moving window is one fine-resolution pixel and each step calculates the NDVI of the center pixel in the moving window.

The flowchart for the STVIFM algorithm is shown in Figure 4-2. There are four main steps for the STVIFM implementation. The first step is to detect NDVI changes according to the two input fine-resolution NDVI images and classify the land cover into three categories.

The second step is to calculate the correlation coefficient between the coarse-resolution images for the whole region and within the moving window, and then the weights. The third step is to determine the coefficients a and b through a linear regression between the two fine-resolution and coarse-resolution image pairs. The last step is to calculate the final weight and the NDVI value of the center pixel on the prediction date for its category. As the weight calculations have been introduced in Section 4.2.2, this section mainly illustrates the last two steps.

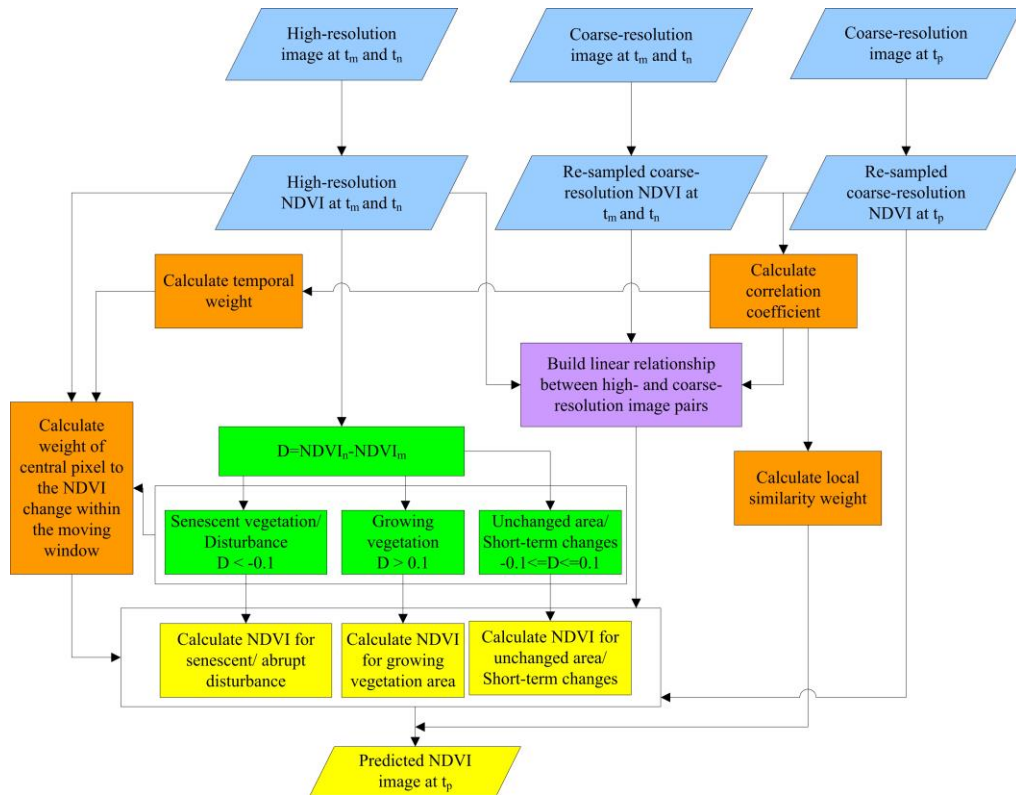


Figure 4-2: Flowchart of the spatio-temporal vegetation index image fusion model (STVIFM) algorithm. The steps are shaded by different colors (blue: satellite data preprocessing; green: NDVI change detection; orange: weight calculation; purple: coefficients determination; yellow: NDVI prediction).

4.2.3.1 Determination of Coefficients between the Fine- and Coarse-Resolution Images

Due to differences in remote sensor systems, systematic biases exist between different sensor imagery. In addition, directional effects and weather conditions can also lead to biases between different sensor images on different dates. In this study, the coefficients

between the fine-resolution and coarse-resolution images on different dates were acquired through regression analyses. For the two pairs of fine-resolution and coarse-resolution images, a moving window was used to calculate the mean NDVI of the fine- and coarse-resolution images within this window, then the linear regression with the mean NDVI values was conducted to obtain the coefficients a_m , b_m and a_n , b_n . The window size should be the odd number which is near to the integer multiple of the ratio between the coarse resolution and fine resolution to accommodate the original coarse-resolution pixel. The step of the moving window is the same as the window size (rather than one-pixel step) so as to avoid self-correlation with the mean values of the NDVI. For example, if the window size is 9 by 9, the step will be 9. It is difficult to determine a_p and b_p due to the unavailability of the fine-resolution image at t_p . The coefficients a_p and b_p were calculated by the temporal weighted average of a_m , a_n and b_m , b_n respectively (Equations (4-18) and (4-19)), with the assumption that the more similar the two coarse-resolution images, the greater the weight:

$$a_p = T_{pm} \times a_m + T_{pn} \times a_n \quad (4-18)$$

$$b_p = T_{pm} \times b_m + T_{pn} \times b_n \quad (4-19)$$

4.2.3.2 Local Similarity Weight Calculation and NDVI Prediction for the Central Pixel

There may be local land cover changes caused by harvesting or flooding for heterogeneous regions such as croplands with crops growing in different seasons. The correlation coefficient of the local area within the moving window (r_l) is used to calculate the local similarity weight (S_l), which is mentioned in Section 4.2.1 for local heterogeneous area, whereas the mean absolute difference within the moving window (MAD_l) (Equation (4-20)) is used to calculate local similarity weight for local homogeneous area (Equation (4-21)).

$$MAD_{tpk} = \frac{1}{N_l} \sum_{i=1}^{N_l} abs(NDVI'_{ki} - NDVI'_{pi}) \quad (k = m, n) \quad (4-20)$$

$$\left\{ \begin{array}{l} S_{lpk} = \frac{r_{lpk}^2}{r_{lpm}^2 + r_{lpn}^2} \text{ (} k = m, n \text{) heterogeneous area} \\ S_{lpm} = \frac{MAD_{lpn}}{MAD_{lpm} + MAD_{lpn}} \text{ homogeneous area} \\ S_{lpn} = \frac{MAD_{lpm}}{MAD_{lpm} + MAD_{lpn}} \text{ homogeneous area} \end{array} \right. \quad (4-21)$$

where MAD_{lpk} is the local mean absolute difference between coarse-resolution image at t_k ($k = m, n$) and t_p . N_l is the number of pixels within the local moving window. S_{lpk} is the local similarity weight between coarse-resolution image at t_k ($k = m, n$) and t_p . If $MAD_{lpm} = MAD_{lpn} = 0$, $S_{lpm} = S_{lpn} = 0.5$.

To determine the heterogeneous area and homogeneous area, the standard deviation (SD) was calculated for all three coarse-resolution images (Equation (4-22)). If the SD for the three images satisfies Equation (4-23), the area within the moving window is determined as homogeneous, otherwise heterogeneous.

$$SD_k = \sqrt{\frac{\sum_{i=1}^{N_l} (NDVI'_{ki} - \overline{NDVI'_k})^2}{N_l - 1}} \quad (k = m, n, p) \quad (4-22)$$

$$\begin{aligned} SD_m < 0.002 \times NDVI'_{maxm} \text{ and } SD_n < 0.002 \times NDVI'_{maxn} \text{ and} \\ SD_p < 0.002 \times NDVI'_{maxp} \end{aligned} \quad (4-23)$$

where N_l is the number of pixels in the local moving window, and $NDVI'_{maxk}$ means the maximum NDVI of the whole coarse image acquired on date k ($k = m, n, p$). $NDVI'_{ki}$ and $\overline{NDVI'_k}$ represent NDVI of the i th pixel and mean NDVI within the moving window on the coarse-resolution image acquired on date k ($k = m, n, p$) respectively.

In the moving window, the weight was calculated within each category (Equations (4-16) and (4-17)), and the final NDVI for the central pixel on the prediction date can be predicted by Equations (4-7) and (4-8) using the pixels which have the same category as the central pixel.

4.3 Results of Data Fusion

4.3.1 Test Sites and Data

Three test sites of distinct geographic locations and climate zones were chosen to test the STVIFM algorithm. The first site (42°53'N 81°35'W, 12 km × 12 km) is located in the Mixedwood Plains Ecozone in southwestern Ontario, Canada, near the city of London. This area is constantly contaminated by cloud cover during the growing season. For example, from April to October, about 57% of Landsat-8 images contain cloud cover greater than 35%. The dominant crops are winter wheat, corn, and soybean. The winter wheat is generally seeded in October in the previous year and harvested in late July, whereas the corn and soybean are generally seeded in May and harvested in September or October. The second site (37°01'N 99°07'W, 24 km × 24 km) is located near Dodge City in Kansas, United States. This study site contains a large area of grassland as well as crops such as winter wheat. This area receives around 532 mm of rainfall with annual average temperature of 13.3 °C, and altitude between 700 and 800 m above sea level. The third site (44°13'N 87°53'E, 45 km × 45 km) is situated in the south of the Junggar Basin in Xinjiang, China, bordered by the Gurbantunggut Desert in the north. The dominant crop types in this area are cotton, corn, and winter wheat. The cotton and corn are planted in April and harvested in September, whereas wheat is generally seeded in October in the previous year and harvested in May. This area receives scarce rainfall and has long and cold winters with short and hot summer with sharp contrast between daytime and night temperature (Zhang, Liao, Li, & Sun, 2013).

Landsat-8 OLI data and Moderate Resolution Imaging Spectroradiometer (MODIS) surface reflectance products (MOD09GQ and MOD09Q1) were obtained. The Landsat-8 images, with 9 spectral bands, 16-day temporal frequency, and 30 m spatial resolution, were downloaded from the United States Geological Survey (USGS) (<http://landsat.usgs.gov/landsat8.php>). MOD09GQ is a daily reflectance product and MOD09Q1 is a level-3 eight-day composite product of MOD09GQ, which provides surface reflectance of Band 1 and Band 2 at 250 m resolution. Each MOD09Q1 pixel represents the best observation during an eight-day period (Vermote, Kotchenova, & Ray, 2011). The eight-day MODIS reflectance products (MOD09Q1) were downloaded from

the National Aeronautics and Space Administration (NASA) Reverb portal (<http://reverb.echo.nasa.gov/reverb/>) for the Ontario site due to the frequent cloud contamination of the daily reflectance products. The daily MODIS reflectance products MOD09GQ were downloaded for Kansas and Xinjiang sites. The MODIS data were re-projected and mosaicked using the MODIS re-projection tool (MRT). They were then resampled to 30 m resolution using the nearest neighbor method and geo-rectified to the corresponding Landsat images. To avoid the influence of clouds, the MODIS and Landsat-8 images were then clipped to the areas where there was no cloud presence. Finally, the NDVI was calculated.

The dates of cloud-free Landsat-8 OLI and the corresponding MODIS images acquired near the dates of the Landsat acquisitions are shown in Table 4-1. The two pairs of MODIS and Landsat-8 NDVI images acquired before and after the prediction date, and one MODIS NDVI image acquired on the prediction date were used to predict the synthetic Landsat-like NDVI image. The Landsat-8 images acquired on the prediction date at each study site were used to validate the synthetic Landsat-like NDVI images.

Table 4-1: Dates of MODIS and Landsat-8 OLI images.

	Composite Period (Date) of Obtained MODIS Images	Date of Obtained Landsat OLI Images
Ontario, Canada	15 April 2014–22 April 2014 (DOY: 105–112)	20 April 2014 (DOY: 110)
	1 May 2014–8 May 2014 (DOY: 121–128)	6 May 2014 (DOY: 126) (validation)
	2 June 2014–9 June 2014 (DOY: 153–160)	7 June 2014 (DOY: 158)
Kansas, U.S.	3 May 2014 (DOY: 123)	3 May 2014 (DOY: 123)
	19 May 2014 (DOY: 139)	19 May 2014 (DOY: 139) (validation)
	20 June 2014 (DOY: 171)	20 June 2014 (DOY: 171)
Xinjiang, China	27 May 2014 (DOY: 147)	27 May 2014 (DOY: 147)
	12 June 2014 (DOY: 163)	12 June 2014 (DOY: 163) (validation)
	28 June 2014 (DOY: 179)	28 June 2014 (DOY: 179)

Figure 4-3–Figure 4-5 show the NDVI images obtained on three dates over three study sites. The sub-images (30 m resolution, 400 × 400 pixels) at the upper rows are Landsat-8 NDVI images (fine-resolution, 30 m) and lower rows are MODIS NDVI images (coarse-resolution, 250 m resampled to 30 m).

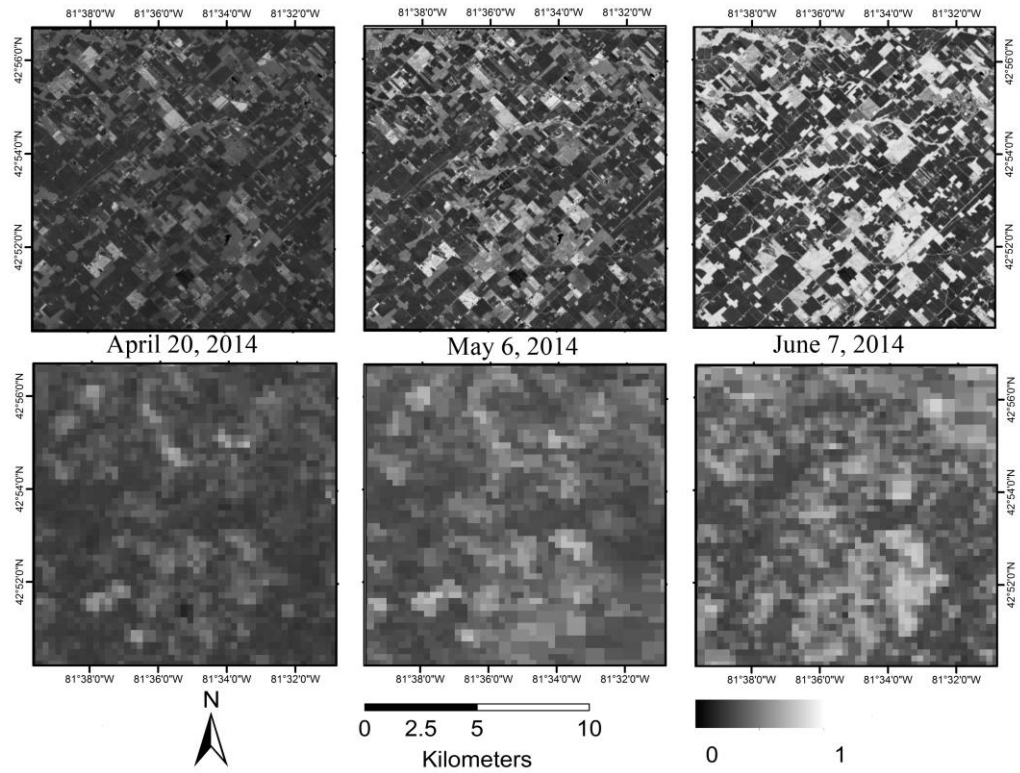


Figure 4-3: Landsat (upper row); and MODIS (lower row) NDVI images from three dates in 2014 over a cropland area in Ontario, Canada.

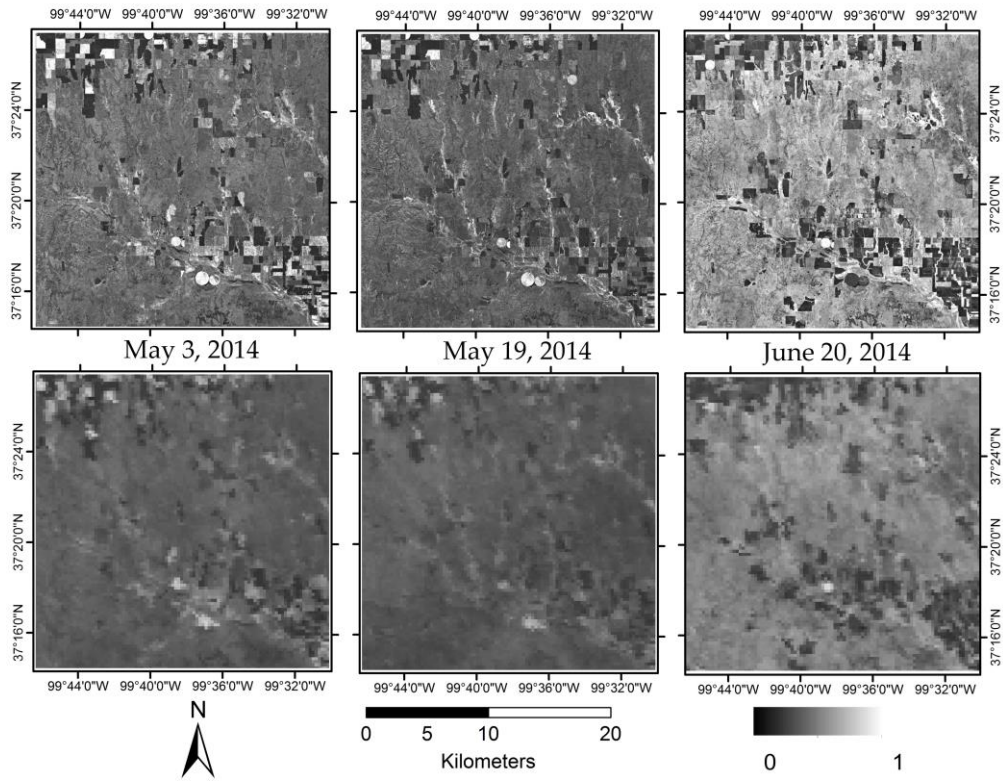


Figure 4-4: Landsat (upper row) and MODIS (lower row) NDVI images from three dates in 2014 over a mixed crop and grassland area in Kansas, U.S.

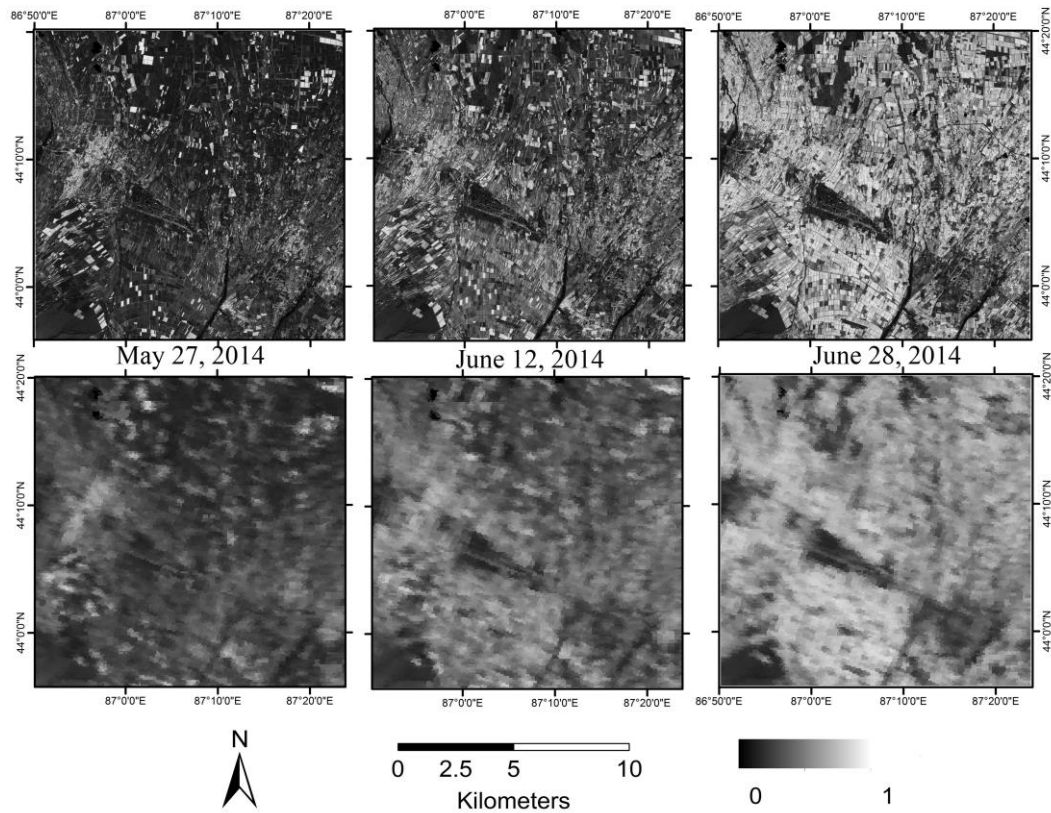


Figure 4-5: Landsat (upper row) and MODIS (lower row) NDVI images from three dates in 2014 over a cropland area in Xinjiang, China.

To assess the application of the proposed algorithm on time series data, a total of 18 cloud-free MODIS MOD09Q1 data and six Landsat-8 OLI data were acquired over London, Ontario throughout the growing season in 2014 (Figure 4-6). Figure 4-7 shows the six cloud-free NDVI images and corresponding MODIS NDVI images. The sub-images at the upper row are Landsat-8 NDVI images (fine-resolution, 30 m). The sub-images at the lower row are the eight-day MODIS NDVI images. From 6 May to 7 June, as the winter wheat grew, the NDVI increased greatly. On 10 August, the winter wheat had been harvested, and most of the land was covered by corn and soybean. Thus, there were great land cover changes from 7 June to 10 August. From 10 August to 26 August, a few winter wheat fields were covered by alfalfa, and the NDVI increased again. On 27 September, most corn and soybean were senescent and the NDVI decreased.

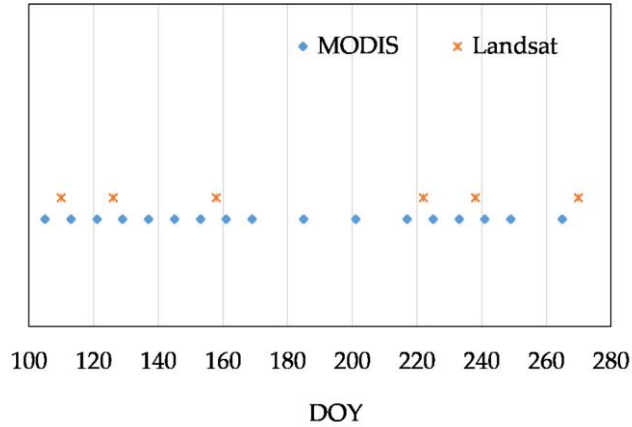


Figure 4-6: The dates for the available cloud free Landsat imagery and the MODIS time series data for the Ontario site.

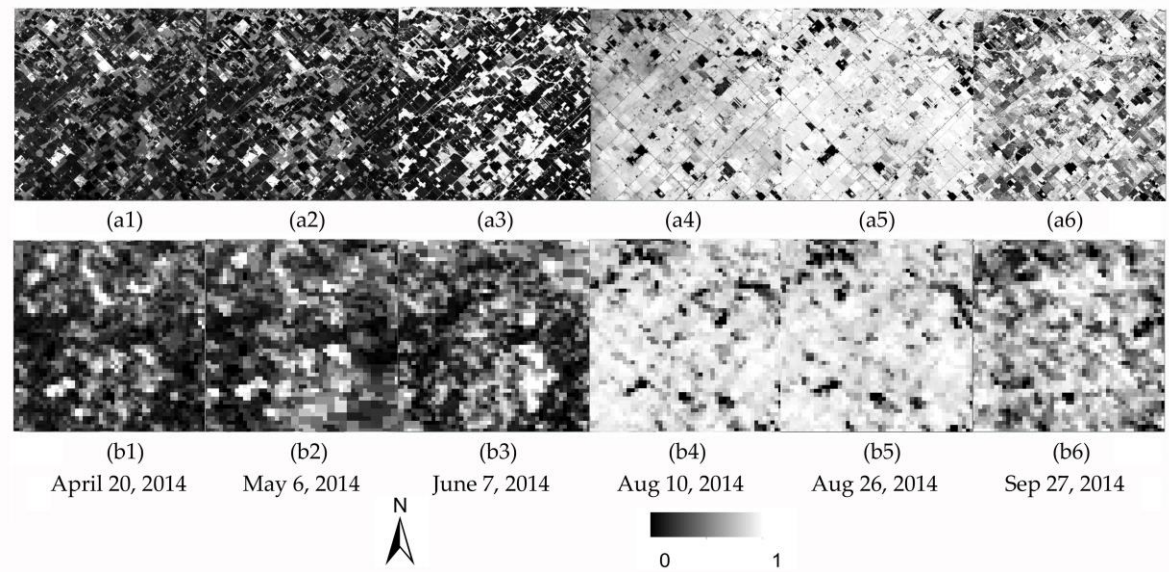


Figure 4-7: The Landsat and MODIS NDVI image pairs acquired throughout the growing season in Ontario, Canada.

4.3.2 Selection of Window Size for Deriving the Coefficients

Linear regression analysis was conducted between the fine- and coarse-resolution image pairs (Section 4.2.3.1) for different study sites using different sizes of moving window. The variations of the coefficient of determination (R^2), a and b with the increasing window size are shown in Figure 4-8. It was illustrated that when 9 (the approximate size of one coarse-resolution pixel) was adopted as the window size, the correlation was much lower than for

other choices. The reason for this is likely that there are errors introduced by rounding and the geometric correction process between fine-resolution and coarse-resolution images. In this way, the fine-resolution pixels may not be the pixels that are supposed to be within the original coarse-resolution pixel. With the increase of window size, the R^2 values increased for most image pairs and plateaued when the window size is 17, which contains 4 MODIS pixels. This should be impacted by the MODIS point spread function (SPF) (Amorós-López et al., 2013). The value of a ranges from 0.9 to 1.5 for different study sites, and b ranges from -0.15 to 0.05 for different study sites. Even for the same study site, a and b vary on different dates. With the increase of the window size, the variations of a and b are slight and smooth. It can be believed that both a and b are not sensitive to the change of window size. However, with a larger window, the increase rate of R^2 becomes smaller, the sample points become less, and the significance of the correlation will be reduced. Accordingly, a 33×33 moving window (4×4 coarse-resolution pixels) was used to obtain the coefficients.

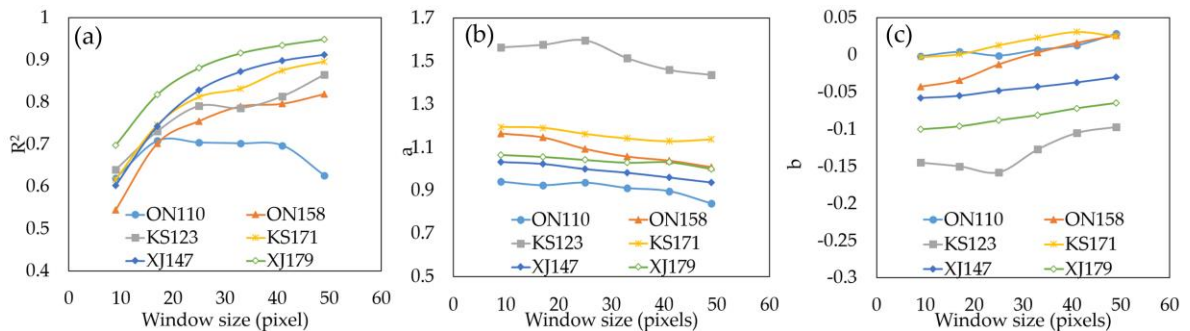


Figure 4-8: The variations of: R^2 (a); a (b); and b (c) with the increasing window size for fine- and coarse-resolution NDVI pairs over different study sites.

Besides the proposed method, the STARFM, ESTARFM and FSDAF methods were also used for comparison purposes. To select a reasonable window size for the algorithm implementation, the data fusion was conducted with different window sizes based on the STARFM, ESTARFM, FSDAF and STVIFM methods. Take the Ontario site as an example (Table 4-2). For the STVIFM, the accuracy is the highest when the window size is 25, and the computation time increases with the increase of window size. For the ESTARFM, the accuracy is the highest when the window size is 33. For the STARFM and the FSDAF, the larger window size gives higher accuracy (higher R^2 and lower RMSE),

but the increase of accuracy is very small. Therefore, we chose 33 as the window size (the same as the window size used in coefficients calculation) for the fusion models, after analyzing the R^2 , RMSE, and computational efficiency of these algorithms using different window sizes.

Table 4-2: Correlation analysis between Landsat-8 NDVI image and correspondent synthetic NDVI image based on different algorithm using different window size at the Ontario site.

Window Size	STARFM			ESTARFM			FSDAF			STVIFM		
	R^2	RMS E	Time (s)	R^2	RMS E	Time (s)	R^2	RMS E	Time (s)	R^2	RMS E	Time (s)
9	0.668	0.099	2.08	0.673	0.120	34.67	0.782	0.081	52.04	0.739	0.099	13.6
17	0.661	0.098	4.07	0.704	0.116	40.57	0.804	0.077	55.56	0.824	0.071	20.69
25	0.659	0.096	7.21	0.717	0.113	46.71	0.816	0.076	58.68	0.83	0.070	31.5
33	0.659	0.096	11.52	0.723	0.112	52.2	0.824	0.075	68.6	0.826	0.071	46.4
41	0.659	0.095	16.31	0.722	0.112	62.01	0.828	0.075	67.45	0.818	0.074	64.18
49	0.659	0.094	22.8	0.721	0.113	73.59	0.832	0.074	78.7	0.811	0.076	87.08

$p < 0.01$.

4.3.3 Algorithm Tests in Regions with Different Landscapes

As the FSDAF only needs one pair of fine- and coarse-resolution images, the pair of images acquired on the date before and after the prediction date were used, respectively, for all three sites, and FSDAF_m and FSDAF_n were used to represent the two predictions hereafter. The performances of the four algorithms were assessed by visual comparison and correlation analyses. The coefficient of determination, Mean Absolute Difference (MAD) and Mean Difference (MD) between the observed NDVI and predicted NDVI images were also calculated to assess the accuracies of the four algorithms.

Figure 4-9 to Figure 4-14 show the original Landsat-8 OLI NDVI image and the synthetic NDVI images predicted by the four algorithms, and the scatter plots between the synthetic and the original NDVI values of Landsat OLI image acquired at t_p at the three study sites. Table 4-3 shows the R^2 , RMSE, MAD, MD and computation time of the four algorithms at different test sites. The performance of the STVIFM is better than the STARFM and ESTARFM methods, and similar with the best prediction of the FSDAF at all the three study sites according to R^2 , RMSE, and MAD. In addition, the STVIFM is more

computationally efficient than the ESTARFM and FSDAF when a window of 33×33 pixels was adopted.

The Ontario site has many small-area croplands (the width of the fields is less than 250 m), which resulted in many mixed pixels in the coarse-resolution image. Figure 4-10 shows that the predicted NDVI images generated by the FSDAF_m and STVIFM are more similar to the original image. However, the small-area land cover changes shown in the red boxes in Figure 4-10 were not accurately predicted by the FSDAF. Actually, the predicted NDVI image obtained by the FSDAF is more similar to the input fine-resolution image. As there are less land cover changes between 20 April and 6 May than between 6 May and 7 June at this site, the predicted result using the FSDAF (FSDAF_m) is more similar to the observed NDVI. The STARFM, ESTARFM, and STVIFM are all able to predict the land cover change by making use of two image pairs, whereas the ESTARFM overestimated the NDVI.

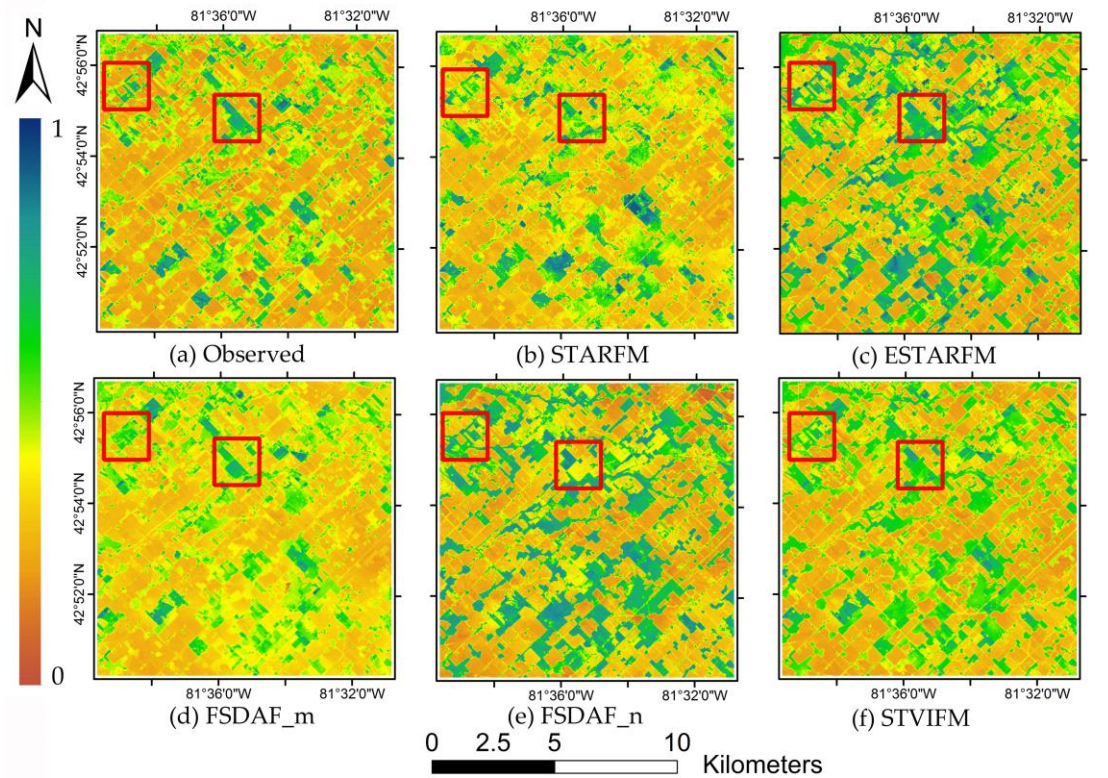


Figure 4-9: Comparison of the (a) observed Landsat image; and the synthetic images based on: (b) spatial and temporal adaptive reflectance fusion model (STARFM); (c) enhanced spatial and temporal adaptive reflectance fusion model (ESTARFM); (d, e)flexible spatiotemporal data fusion (FSDAF); and (f) spatio-temporal vegetation index image fusion model (STVIFM), in Ontario, Canada. Red boxes show small-area land cover changes occurred on Landsat-8 images acquired at t_p (6 May 2014) and t_n (7 June 2014).

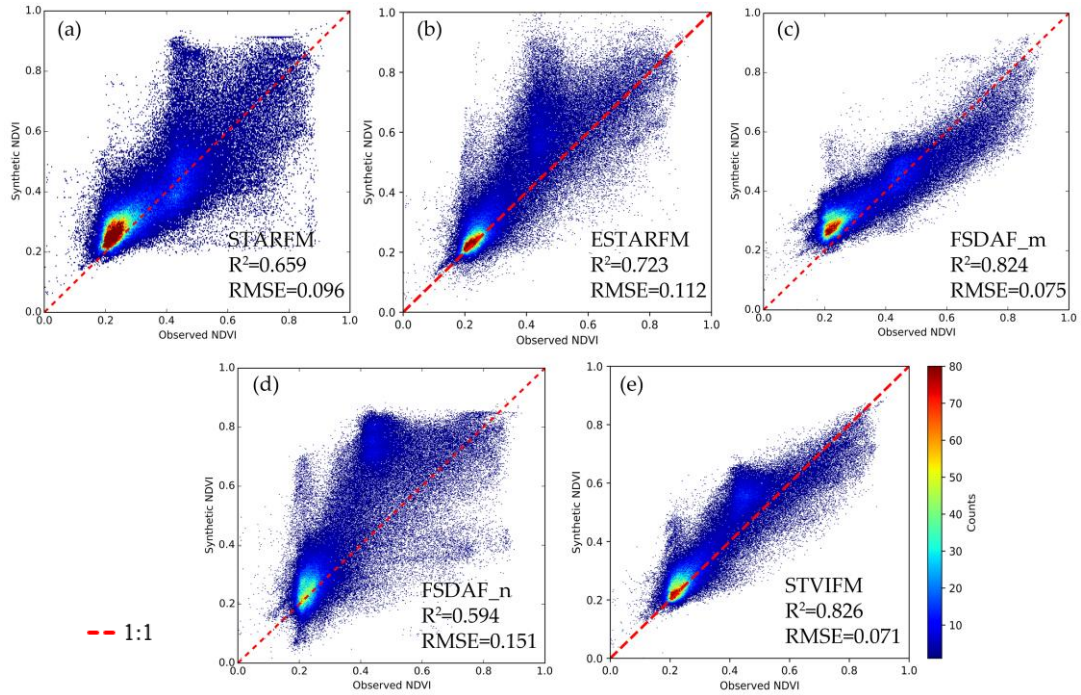


Figure 4-10: Scatter plots of the observed and synthetic Landsat NDVI produced by: (a) STARFM; (b) ESTARFM; (c) FSDAF_m; (d) FSDAF_n; and (e) STVIFM in Ontario, Canada.

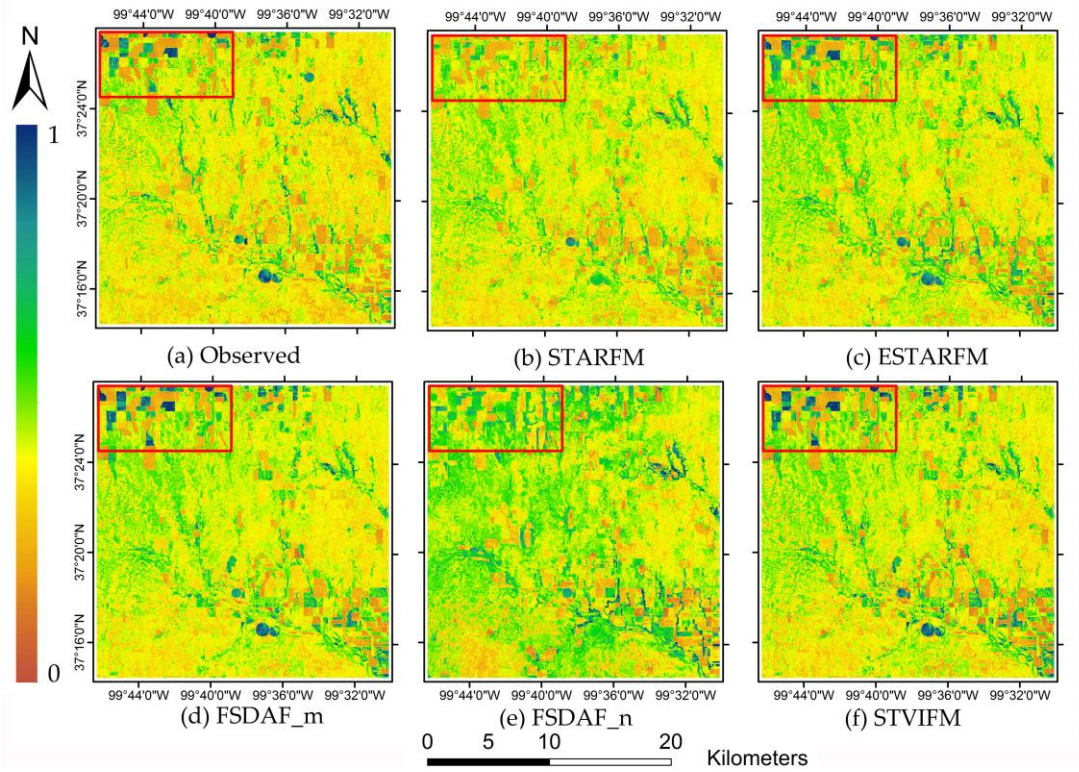


Figure 4-11: Comparison of the (a) observed Landsat image; and the synthetic images based on: (b) STARFM; (c) ESTARFM; (d, e) FSDAF; and (f) STVIFM, in Kansas, U.S. Red boxes show that the harvesting of crops appeared in Landsat-8 images acquired at t_n (20 June 2014) are accurately predicted in the synthetic NDVI image based on the STVIFM and ESTARFM.

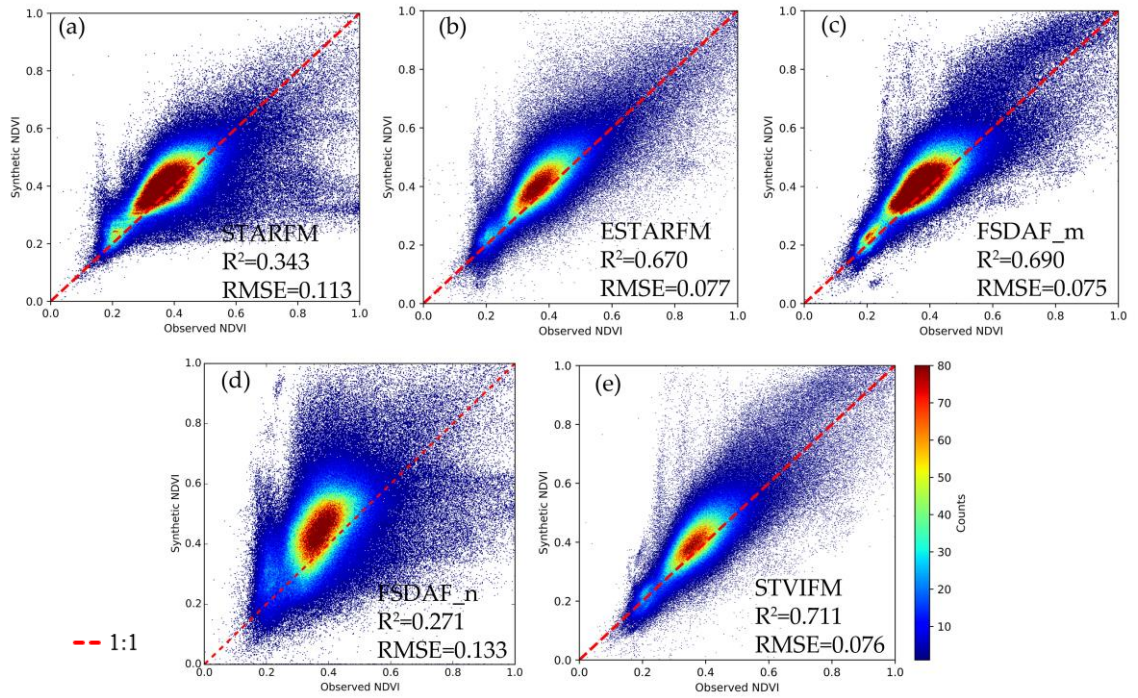


Figure 4-12: Scatter plots of observed and synthetic Landsat NDVI by: (a) STARFM; (b) ESTARFM; (c) FSDAF_m; (d) FSDAF_n; and (e) STVIFM in Kansas, U.S.

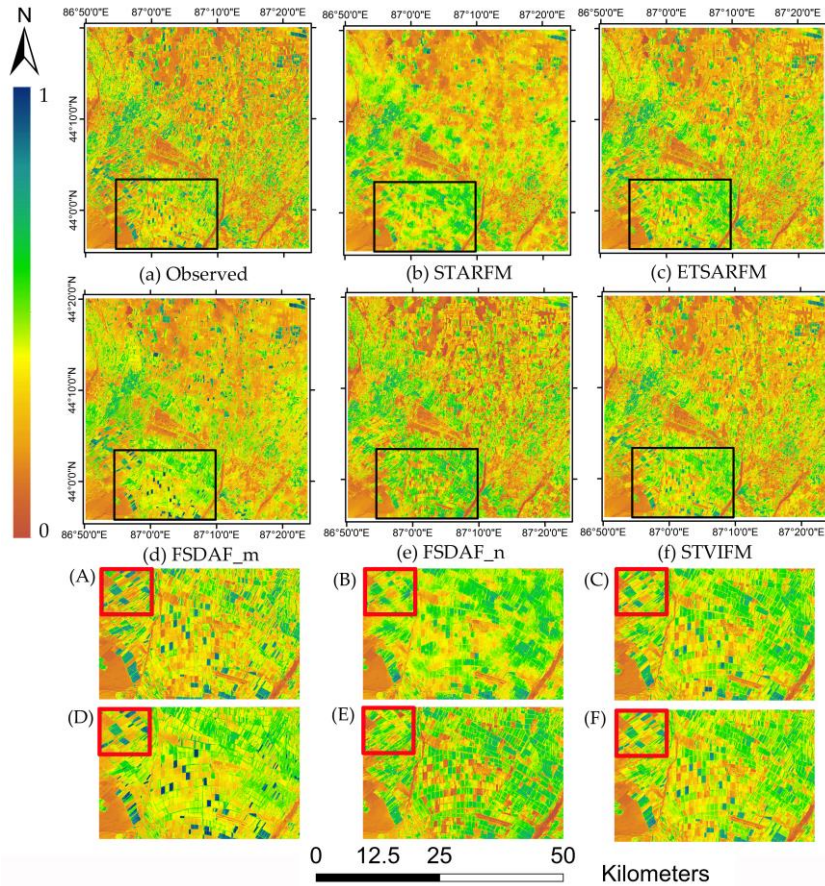


Figure 4-13: Comparison of the (a) observed Landsat image; and the synthetic images based on: (b) STARFM; (c) ESTARFM; (d) FSDAF_m; (e) FSDAF_n; and (f) STVIFM in Xinjiang, China. (A–F) Zoom-in images shown in the black boxes on the original NDVI and the all the results generated by the four methods. Red boxes show the senescent fields.

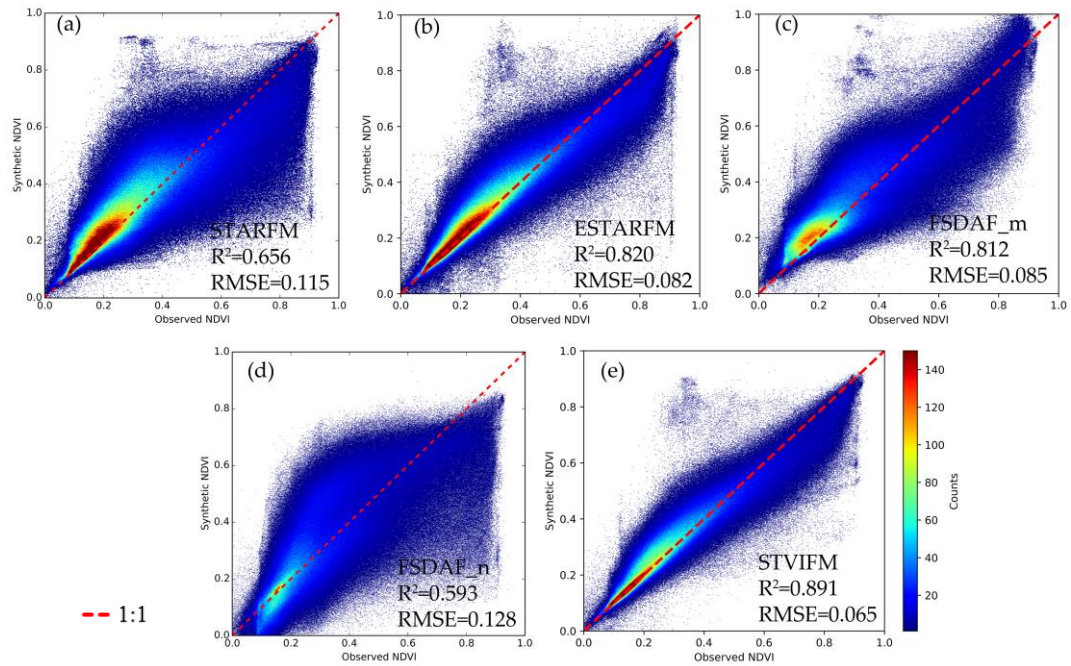


Figure 4-14: Scatter plot of observed and synthetic Landsat NDVI by: (a) STARFM; (b) ESTARFM; (c) FSDAF_m; (d) FSDAF_n; and (e) STVIFM in Xinjiang, China.

Table 4-3: Statistical parameters of the correlation analysis between synthetic and original Landsat NDVI image.

Study Site	Image Size	Methods	R ²	RMSE	MAD	MD	Time
Ontario, Canada	400 × 400 (12 km × 12 km)	STARFM	0.659	0.096	0.066	0.020	12 s
		ESTARFM	0.723	0.112	0.075	0.052	52 s
		FSDAF_m	0.824	0.075	0.061	0.026	69 s
		FSDAF_n	0.594	0.151	0.109	0.072	65 s
		STVIFM	0.826	0.071	0.052	0.026	46 s
Kansas, United States	800 × 800 (24 km × 24 km)	STARFM	0.343	0.113	0.073	0.005	40 s
		ESTARFM	0.67	0.077	0.057	0.031	3 min 25 s
		FSDAF_m	0.69	0.075	0.056	0.032	9 min 21 s
		FSDAF_n	0.271	0.133	0.102	0.059	9 min
		STVIFM	0.711	0.076	0.055	0.028	3 min 9 s
Xinjiang, China	1500 × 1500 (45 km × 45 km)	STARFM	0.656	0.115	0.072	-0.02	2 min 42 s
		ESTARFM	0.82	0.082	0.048	0	12 min 29 s
		FSDAF_m	0.812	0.085	0.060	0.010	41 min 57 s
		FSDAF_n	0.593	0.128	0.095	0.001	40 min 16 s
		STVIFM	0.891	0.065	0.045	0.006	11 min 15 s

$p < 0.01$.

As indicated by the scatter plots shown in Figure 4-11 and the assessment indices shown in Table 4-3, the accuracy of the predicted NDVI image using the STVIFM is the best (R²: 0.826, RMSE: 0.071) and slightly better than the accuracy of the predicted NDVI image using FSDAF_m (R²: 0.824, RMSE: 0.075). The STARFM performed better than the ESTARFM and FSDAF_n in terms of the RMSE and MAD. Most NDVI values were overestimated by the ESTARFM and FSDAF_n. From the perspective of computational efficiency, the STVIFM consumed less time than the ESTARFM and the FSDAF. For the sub-image of 400 × 400 pixels, the ESTARFM and FSDAF consumed 52 s and 69 s, respectively, and the STVIFM consumed about 46 s.

The Kansas site is mostly covered by grassland and it is more homogeneous than the other two sites. The overall accuracy using the proposed STVIFM method (R²: 0.711, RMSE: 0.076) is the best when compared with the STARFM and ESTARFM. The RMSE and MAD of the result produced by the STVIFM are comparable with that of the result produced by the FSDAF_m, but the R² of the former result is higher than the later one. Figure 4-12 reveals that the ESTARFM, FSDAF_m, and STVIFM performed better in the cropland area shown in the red box, while all the methods seem to overestimate the NDVI in the grassland area. The RMSEs for these three methods are similar (RMSE: 0.077 vs.

0.075 vs. 0.076) but the R^2 for the STVIFM is the highest (R^2 : 0.711). As the land cover for most areas barely changed from the date of the first image pair (3 May 2014) to the prediction date (19 May 2014), the NDVI predicted by the FSDAF_m shows higher accuracy than the NDVI predicted by the FSDAF_n. In terms of computational efficiency, the ESTARFM and FSDAF consumed 3 min 29 s and 9 min, respectively, whereas the STVIFM consumed 3 min 9 s for an image of 800×800 pixels.

At the Xinjiang site, the predicted NDVI image produced by the STVIFM shows good agreement with the observed NDVI (R^2 : 0.891, RMSE: 0.065). Most of the fields were in the growing stage during this period and a few fields were in the senescent stage. The accuracy of the synthetic NDVI images produced by the ESTARFM and FSDAF_m are comparable but lower than that of the STVIFM (R^2 : 0.820 vs. 0.812, RMSE: 0.082 vs. 0.085). As shown in the zoom-in area in the black box, the predicted NDVI image obtained by the STARFM shows “blurred” field boundaries, and the overall accuracy is much lower than the ESTARFM. The temporal NDVI changes of the senescent fields shown in the red box in Figure 4-14 were more accurately captured using the STVIFM when compared with the STARFM and ESTARFM. For the FSDAF, the predicted NDVI image is more accurate using the image pair acquired on 27 May than using the image pair acquired on 28 June. Even though the time intervals between the prediction date (12 June 2014) and dates of the two base image pairs were the same, the land cover changed significantly from 12 June to 28 June. Therefore, the NDVI prediction using the image pair acquired on 27 May is more accurate than using the image pair acquired on 28 June. In terms of the computational efficiency, the ESTARFM and FSDAF consumed about 12 min and 40 min respectively for an image of 1500×1500 pixels, whereas the STVIFM consumed about 11 min.

When we compare the accuracies for the three study sites, it is obvious that both the Ontario site and Xinjiang site are more heterogeneous than the Kansas site and there are many crop fields with small areas. This is possibly the reason that the STARFM and ESTARFM performed better at Kansas site than Ontario site and Xinjiang site in terms of the RMSE and MAD. However, the STVIFM performed better for Ontario site and Xinjiang site than Kansas site. Therefore, it can be concluded that the STVIFM performs better than the

STARFM and ESTARFM not only in homogeneous regions but also in heterogeneous regions.

4.3.4 Tests with Time Series Data

In this test, all six available Landsat NDVI images and the corresponding MODIS NDVI images acquired throughout the whole growing season over Ontario site were tested using the four methods for the four predictions shown in Table 4-4. For the FSDAF, both the image pairs before and after the prediction date were used to implement this method. (a1)–(a6) and (b1)–(b6) are the images shown in Figure 4-7.

Table 4-4: Images used for the four methods in the four experiments.

Prediction Date (DOY)	Input Images	Images for Validation
121	FSDAF_m: b1, a1, b2	a2
	FSDAF_n: b3, a3, b2	
	STARFM: b1, a1, b3, a3, b2	
	ESTARFM: b1, a1, b3, a3, b2	
	STVIFM: b1, a1, b3, a3, b2	
158	FSDAF_m: b2, a2, b3	a3
	FSDAF_n: b4, a4, b3	
	STARFM: b2, a3, b4, a4, b3	
	ESTARFM: b2, a3, b4, a4, b3	
	STVIFM: b2, a3, b4, a4, b3	
222	FSDAF_m: b3, a3, b4	a4
	FSDAF_n: b5, a5, b4	
	STARFM: b3, a3, b5, a5, b4	
	ESTARFM: b3, a3, b5, a5, b4	
	STVIFM: b3, a3, b5, a5, b4	
238	FSDAF_m: b4, a4, b5	a5
	FSDAF_n: b6, a6, b5	
	STARFM: a4, b4, a6, b6, a5	
	ESTARFM: a4, b4, a6, b6, a5	
	STVIFM: a4, b4, a6, b6, a5	

The results were validated with the original Landsat NDVI images, and the assessment indices including R^2 , RMSE, MAD, and AD for different methods were shown in Figure 4-15. For the first prediction, the two Landsat images were acquired on 20 April and 7 June. The main crop was winter wheat, which was growing steadily during this period. There were some small-area land cover changes in images acquired on 6 May and 7 June (Figure 4-7 (a3)). As presented in Section 4.3.3 (Ontario site), the STVIFM performed the best when compared with the other three methods during this period.

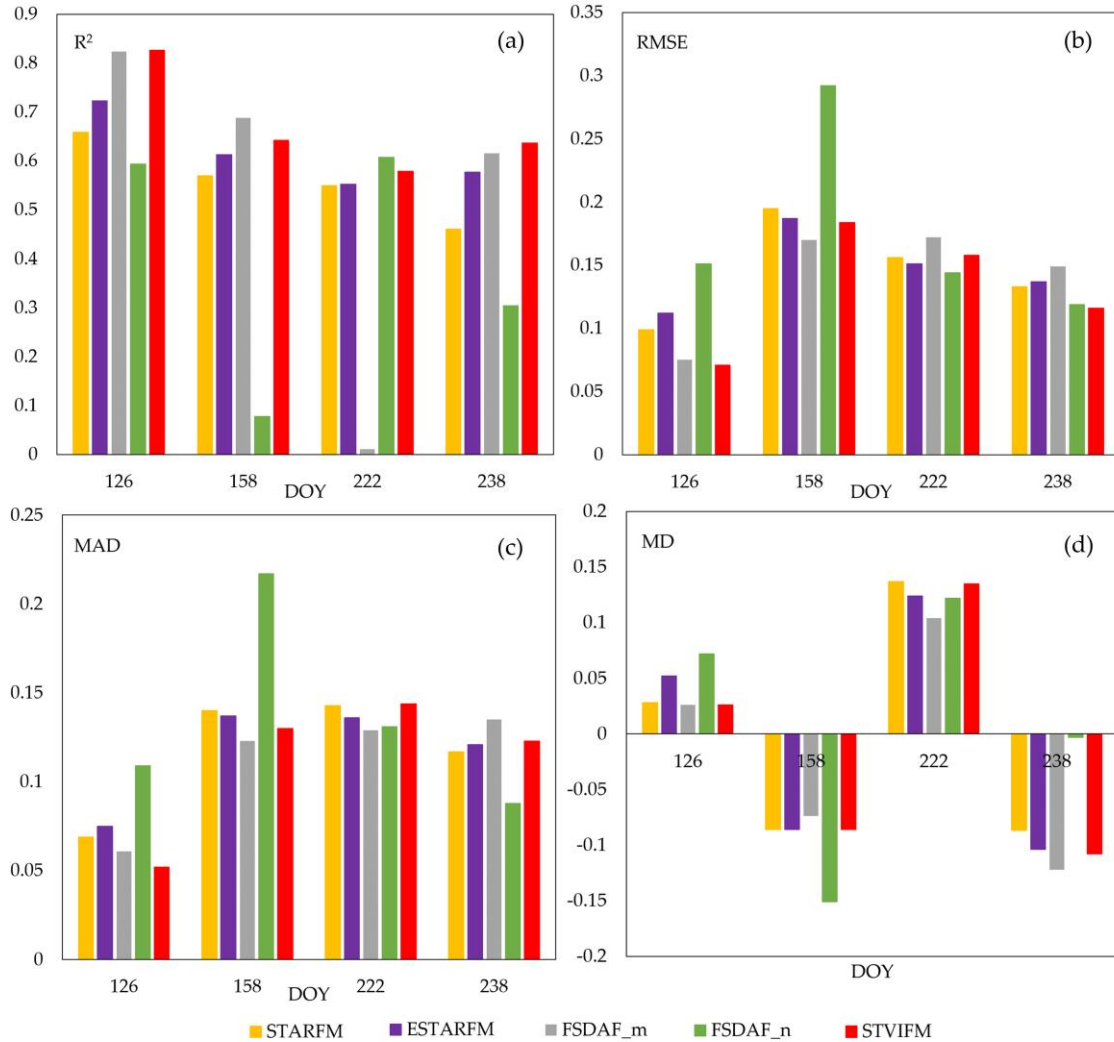


Figure 4-15: The accuracy of predicted NDVI obtained by different methods on four different dates in Ontario site during the growing season: (a) R^2 ; (b) RMSE; (c) MAD; and (d) MD.

For the second prediction, the two Landsat images were acquired on 6 May and 10 August and the prediction date was 7 June. From 6 May to 7 June, corn and soybeans were planted, then wheat was harvested and alfalfa was planted in the harvested wheat fields from 7 June to 10 August. The STVIFM performed better than the STARFM and ESTARFM (RMSE: 0.184 vs. 0.195 vs. 187). The predicted NDVI image generated by the FSDAF using the image pair acquired on 6 May shows much higher accuracy than using the image acquired on 10 August and the predicted NDVI generated by the other two methods.

For the third prediction, the two Landsat images were acquired on 6 June and 26 August and the prediction date was 10 August. As mentioned above, the wheat fields changed greatly from 6 June to 10 August, whereas the land cover seldom changed from 10 August to 26 August. The correlation of determination of the predicted NDVI using the STVIFM is higher than the STARFM and ESTARFM (R^2 : 0.579 vs. 0.550 vs. 0.552), whereas the RMSE is higher than the STARFM and ESTARFM (RMSE: 0.158 vs. 0.151 vs. 0.156). This may be because of the large land cover changes for wheat fields from 6 June to 26 August, and the NDVI for wheat field is near the valley of the NDVI profile on 10 August. As mentioned earlier, larger inaccuracy would be produced by the STVIFM if the peak or valley in the NDVI profile between the two dates of acquired Landsat images needs to be predicted, and the NDVI change is not captured by the NDVI difference of the two Landsat images. This inaccuracy can be reduced if more fine-resolution images can be acquired during this period. The prediction of the FSDAF using the image pair acquired on 26 August shows a higher accuracy than using the image pair acquired on the 6 June.

For the fourth prediction, the two Landsat images were acquired on 10 August and 27 September, and the prediction date was 26 August. Corn and soybeans were senescent during this period. The STVIFM performed better than the STARFM and ESTARFM (RMSE: 0.116 vs. 0.133 vs. 0.137). The accuracy of the image predicted by the FSDAF using image acquired on 27 September is higher than the accuracy of the NDVI predicted by the FSDAF using image acquired on 10 August in terms of the RMSE and MAD.

In addition, a total of 12 Landsat-like NDVI images were predicted using the six acquired Landsat and MODIS image pairs. By using more Landsat images, the prediction accuracy would be improved. However, there was no more available Landsat image to assess the prediction results. The NDVI time series were assessed by analyzing the temporal variations over the cornfield and winter wheat field and compare with the phenology information and photos collected in the field work. For the STARFM, ESTARFM and STVIFM, two temporally closest Landsat and MODIS NDVI image pairs and one MODIS NDVI image acquired between the two dates were used to predict the Landsat-like NDVI image each time. For the FSDAF, the MODIS NDVI image on the prediction date and one

Landsat and MODIS NDVI image pair acquired closer to the prediction date was used to predict the Landsat-like NDVI image each time.

Figure 4-16 shows the temporal profiles of the average NDVI of an area (360 m × 360 m) from a healthy cornfield and an area (360 m × 360 m) from a healthy winter wheat field between DOY 113 and DOY 249, which were generated by the STARFM, ESTARFM, FSDAF, and the STVIFM. These two fields were surrounded by different crop types; therefore, the MODIS pixels contain mixed Landsat pixels. The average NDVI extracted from the original MODIS NDVI time series images and five Landsat-8 NDVI images are also presented as comparisons.

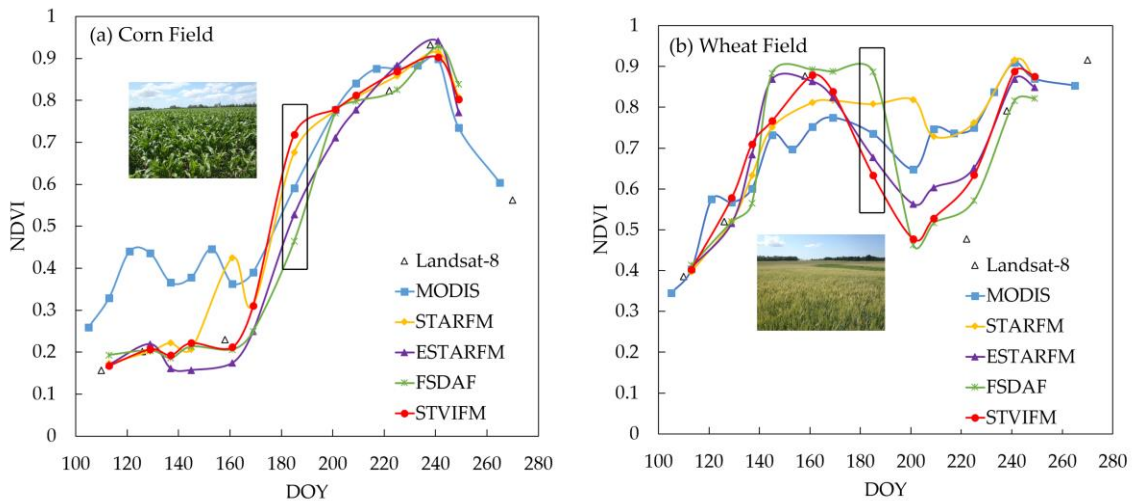


Figure 4-16: Time series of the average NDVI of: (a) the cornfield; and (b) the wheat field, generated by the STARFM, ESTARFM, FSDAF, and STVIFM algorithms. The predictions shown in the black box (DOY 185) present large difference between the FSDAF and STVIFM. The pictures were collected two days before that date (DOY 183).

The corn and winter wheat show two distinct temporal patterns due to the difference of their growing seasons. The corn was generally seeded in May and harvested in October. The winter wheat was generally seeded in October of the previous year, started to ripen from the beginning of July and was harvested by the end of July, then alfalfa was planted. Before the emergence of corn, the MODIS NDVI shows higher and fluctuated values in the cornfield due to the influence of neighboring wheat fields. All the methods can generate

reasonable predictions during this period. Between 7 June and 10 August, only two Landsat images were acquired, and the predictions of the STVIFM and FSDAF show large difference on 4 July (DOY 185). As the image pair closer to the prediction date was always used, the profile generated by the FSDAF shows peak and valley, but large inaccuracy was still produced on some dates when the land cover changed greatly. During this period, corn was in its growing stage whereas winter wheat was harvested and alfalfa was planted. From the general survey pictures collected in 2014, corn had reached to the stem elongation stage (BBCH-scale 33) and most fields were covered by corn leaves, whereas the color of wheat started to turn yellow (BBCH-scale 79). Therefore, the STVIFM seems to generate more reasonable temporal profiles for corn and winter wheat. The ESTARFM also shows reasonable temporal profiles for the two types of crops, however, the prediction of the land cover change for the wheat field is less accurate than the prediction produced by the STVIFM when compared with the nearby Landsat NDVI values.

4.4 Discussion

4.4.1 Advantages of the STVIFM

The algorithm tests at three study sites illustrated that the STVIFM algorithm performed better than the STARFM, ESTARFM and FSDAF at the three study sites. According to the results of the above tests, the performance of the FSDAF greatly depends on the degree of land cover change between the two dates of the input data as it uses only one pair of fine- and coarse-resolution images as input, which agrees with the findings stated in (Liao et al., 2016). It performs better than other methods which use one image pair and it is flexible when only one fine-resolution image can be acquired. However, it is less robust than methods using two fine-resolution images as inputs in the land cover change prediction. Even though the FSDAF can predict NDVI with higher accuracy when the time interval between the two dates of the input images are close enough or land covers are similar enough, the STVIFM still performs better than the FSDAF during the growing stage or senescent stage. In addition, the STVIFM is more computationally efficient and performs about three times faster than the FSDAF at Kansas site and Xinjiang site, where the sizes are $24 \text{ km} \times 24 \text{ km}$ and $45 \text{ km} \times 45 \text{ km}$, respectively.

Since the inputs of the STVIFM are same as the inputs of the STARFM and ESTARFM, the theoretical comparisons are made between the three methods. Compared with the STARFM and ESTARFM algorithm, the STVIFM has made several improvements. Firstly, the STVIFM builds a relationship between the mean NDVI change of fine-resolution pixels and mean NDVI change of coarse-resolution pixels within a moving window. It attempts to detect the mean fine-resolution NDVI change calculated from the coarse-resolution NDVI images and to seek each fine-resolution pixel's contribution to the total NDVI change by calculating the weight of each fine-resolution pixel. In contrast, the STARFM and ESTARFM build a relationship between the NDVI change of single fine-resolution pixels and single coarse-resolution pixels, therefore accurate geometric correction between the fine- and coarse-resolution images is required in order to achieve more accurate results (Chen et al., 2015).

Secondly, the ESTARFM assumes that the relationships between the fine-resolution and coarse-resolution image pairs are the same on all dates. However, due to the difference of weather conditions, the relationship between the two images may be different on different dates. The STVIFM attempts to obtain the coefficients between the fine-resolution and coarse-resolution image pairs on different dates using linear regression analyses. However, it is difficult to obtain the coefficients between the images on the prediction date, due to the unavailability of the fine-resolution image. The STVIFM adopts the weights calculated from the correlation coefficients between the coarse-resolution images to obtain the coefficients between the fine- and coarse-resolution images on the prediction date.

Thirdly, each of the STVIFM, STARFM and ESTARFM applied a weighting system to calculate the NDVI of the central pixel, but the meanings of the weighting system for STVIFM and the weighting system for STARFM and ESTARFM are different. The weight in the STARFM or ESTARFM means the similarity between the central pixel and the surrounding similar pixels within the moving window, whereas the weight in the STVIFM means the variation in contributions of fine-resolution pixels to the total NDVI change within the moving window. The STVIFM considers the change rate variation at both spatial scale and temporal scale, which is more reasonable for non-evergreen vegetation. It attempts to calculate the spatial variation of NDVI change (spatial weight) of each fine-

resolution pixel at any prediction date by incorporating the weights calculated based on one base fine-resolution image and the temporal NDVI change of the two fine-resolution images. These two elements are incorporated according to the land cover similarity between the prediction date and the two base dates. However, the ESTARFM assumes that the change rate is stable during a short period. This assumption is reasonable if the vegetation is evergreen or if the period between the two input image pairs is short enough (e.g., one day), but it would be unreasonable if the period is longer (e.g., more than 10 days) (Zhu et al., 2010).

Lastly, the two predictions obtained from the two base dates are combined using a temporal weight for the ESTARFM and a similarity weight for the STVIFM. The ESTARFM calculated the temporal weight using the mean absolute difference between two coarse-resolution pixels within the moving window (Zhu et al., 2010). However, this is not the best selection to determine the land cover similarity in heterogeneous region. For instance, the mean absolute difference may be the same for area where has large land cover change (NDVI decrease mixed with NDVI increase), and area where has the same land cover but with NDVI decrease or increase. Therefore, the STVIFM adopts the correlation of determination for heterogeneous areas and the mean absolute difference for homogeneous areas to calculate the similarity weight.

Due to the advantages mentioned above, the STVIFM can make more accurate NDVI predictions in heterogeneous regions than the STARFM and ESTARFM when the land cover or NDVI changes were captured by the two pairs of fine- and coarse-resolution images. The accuracy improvements of the STVIFM are more obvious for Ontario site and Xinjiang site, which are characterized by heterogeneous cropland areas. Accordingly, the STVIFM can generate more reasonable NDVI time series for winter wheat and corn, which have different growing seasons.

4.4.2 Limitations and Uncertainties of the STVIFM

In addition to the advantages mentioned above, it is worth noting that the STVIFM has its limitations. The following three aspects are the theoretical limitations of the STVIFM algorithm. Firstly, the STVIFM algorithm assumes that the NDVI is spatially additive. This

linear assumption for the NDVI may lead to minor inaccuracies since the NDVI is not a linear combination of reflectance. Secondly, the relationship between the fine-resolution and coarse-resolution images acquired at t_p is calculated from the relationship between the two input image pairs. The result obtained in this way may be slightly different from the real relationship. Additionally, the STVIFM adopts the same coefficients for the whole image, but the coefficients may vary at different locations. More efforts should be made in further work to obtain the coefficients using a more accurate way.

There are some practical limitations with the STVIFM. Firstly, the small-area (width or length is less than one coarse-resolution pixel) abrupt disturbances that occurred between t_m and t_p or between t_p and t_n , may not be accurately detected because the influence of other land covers in one coarse-resolution pixel. Secondly, if the dates t_m and t_n are in the growing and senescent period of the vegetation, respectively, and the NDVI change at t_p is not captured by the images acquired at t_m and t_n , the performance of the STVIFM is slightly worse than the other methods since the NDVI change from t_m to t_n cannot reflect the NDVI change from t_m to t_p . In this case, more frequent high spatial resolution images that can cover the important vegetation phenology will be helpful. Another possible way to improve the prediction accuracy is to integrate the fusion model with a vegetation growth model for different types of vegetation.

4.4.3 Applications of the STVIFM

The STVIFM uses two pairs of Landsat-8 OLI and MODIS images acquired before and after the prediction date and one coarse-resolution image on the prediction date as inputs, to predict the fine-resolution NDVI image on the prediction date. This algorithm can be applied to regions with different landscapes such as grassland, forest and cropland areas. It can also be applied to other vegetation indices, but the thresholds may need to be adjusted accordingly. Besides the Landsat-8 OLI and MODIS data, other high spatial resolution data such as the SPOT, RapidEye, Sentinel-2, and high temporal frequency data such as AVHRR, MERIS can also be used. There are four parameters that could be set in the STVIFM, the window size for coefficients deriving and the window size for STVIFM implementation, the NDVI value for the maximum change rate of vegetation and the variance of the change rate index. The window size should be the odd rounding value of

the integer multiple of the resolution ratio between the coarse- and fine-resolution images. The suggested window size for coefficients deriving and algorithm implementation is 25 or 33 for Landsat and MODIS data. However, for images with different spatial scales, the window size may need to be adjusted. Since the theoretical NDVI values for vegetation pixels range from 0 to 1, the median value 0.5 is suggested as the value of d , but the value can be adjusted according to the actual NDVI range of vegetation for special vegetation cover types. The suggested value for σ^2 is 0.1–0.2 to obtain the change rate index with a dynamic range from 0 to 1. For the NDVI time series generation, different spatio-temporal data fusion methods may need to be incorporated to improve accuracy.

4.5 Conclusions

In this study, a spatio-temporal vegetation index image fusion model (STVIFM) was developed to fuse high spatial resolution and high temporal frequency NDVI images. The STVIFM algorithm considers the differences between fine-resolution and coarse-resolution pixel values on different dates. It also considers the variations of change rate at the spatial scale and temporal scale by using a temporal weight calculated from the correlation coefficients between two temporally adjacent coarse-resolution images. The STVIFM outperforms in NDVI prediction compared to the STARFM and ESTARFM when the land cover or NDVI changes are captured by two pairs of fine- and coarse-resolution images. For the results predicted by STVIFM, the R^2 varied between 0.711 and 0.891 and the RMSE varied between 0.065 and 0.76 for three study sites with different landscapes, which shows a higher NDVI prediction accuracy than the STARFM and ESTARFM. The STVIFM is more robust than the FSDAF when there are large land cover changes between the prediction date and the date of the image pairs. In addition, the STVIFM is more computationally efficient than the FSDAF. The STVIFM enhances the capability for generating both high spatial resolution and high temporal frequency NDVI images in heterogeneous regions. More efforts are needed in the future for the calculation of coefficients between different sensor images obtained under different weather conditions and geographic locations, and for the prediction of land cover changes that are not captured in the two fine-resolution images.

References

- Amorós-López, J., Gómez-Chova, L., Alonso, L., Guanter, L., Zurita-Milla, R., Moreno, J., & Camps-Valls, G. (2013). Multitemporal fusion of Landsat/TM and ENVISAT/MERIS for crop monitoring. *International Journal of Applied Earth Observation and Geoinformation*, 23(1), 132–141. <http://doi.org/10.1016/j.jag.2012.12.004>
- Anderson, M. C., Kustas, W. P., Norman, J. M., Hain, C. R., Mecikalski, J. R., Schultz, L., ... Gao, F. (2011). Mapping daily evapotranspiration at field to continental scales using geostationary and polar orbiting satellite imagery. *Hydrology and Earth System Sciences*, 15(1), 223–239. <http://doi.org/10.5194/hess-15-223-2011>
- Bhandari, S., Phinn, S., & Gill, T. (2012). Preparing landsat image time series (LITS) for monitoring changes in vegetation phenology in Queensland, Australia. *Remote Sensing*, 4(12), 1856–1886. <http://doi.org/10.3390/rs4061856>
- Bisquert, M., Bordogna, G., Bégué, A., Candiani, G., Teisseire, M., & Poncelet, P. (2015). A simple fusion method for image time series based on the estimation of image temporal validity. *Remote Sensing*, 7(1), 704–724. <http://doi.org/10.3390/rs70100704>
- Busetto, L., Meroni, M., & Colombo, R. (2008). Combining medium and coarse spatial resolution satellite data to improve the estimation of sub-pixel NDVI time series. *Remote Sensing of Environment*, 112(1), 118–131. <http://doi.org/10.1016/j.rse.2007.04.004>
- Chen, B., Ge, Q., Fu, D., Yu, G., Sun, X., Wang, S., & Wang, H. (2010). A data-model fusion approach for upscaling gross ecosystem productivity to the landscape scale based on remote sensing and flux footprint modelling. *Biogeosciences*, 7(9), 2943–2958. <http://doi.org/10.5194/bg-7-2943-2010>
- Chen, B., Huang, B., & Xu, B. (2015). Comparison of spatiotemporal fusion models: A review. *Remote Sensing*, 7(2), 1798–1835. <http://doi.org/10.3390/rs70201798>
- Cheng, Q., Liu, H., Shen, H., Wu, P., & Zhang, L. (2017). A spatial and temporal nonlocal filter-based data fusion method. *IEEE Transactions on Geoscience and Remote Sensing*, 55(8), 4476–4488. <http://doi.org/10.1109/TGRS.2017.2692802>

- Dong, T., Liu, J., Qian, B., Zhao, T., Jing, Q., Geng, X., ... Shang, J. (2016). Estimating winter wheat biomass by assimilating leaf area index derived from fusion of Landsat-8 and MODIS data. *International Journal of Applied Earth Observation and Geoinformation*, 49, 63–74. <http://doi.org/10.1016/j.jag.2016.02.001>
- Fensholt, R. (2004). Earth observation of vegetation status in the Sahelian and Sudanian West Africa: comparison of terra MODIS and NOAA AVHRR satellite data. *International Journal of Remote Sensing*, 25(9), 1641–1659. <http://doi.org/10.1080/01431160310001598999>
- Gandhi, G. M., Parthiban, S., Thummalu, N., & Christy, A. (2015). NDVI : Vegetation change detection using remote sensing and gis – A case study of Vellore District. *Procedia - Procedia Computer Science*, 57, 1199–1210. <http://doi.org/10.1016/j.procs.2015.07.415>
- Gao, F., Masek, J., Schwaller, M., & Hall, F. (2006). On the blending of the MODIS and Landsat ETM + surface reflectance. *IEEE Transactions on Geoscience and Remote Sensing*, 44(8), 2207–2218.
- Gaulton, R., Hilker, T., Wulder, M. A., Coops, N. C., & Stenhouse, G. (2011). Characterizing stand-replacing disturbance in western Alberta grizzly bear habitat, using a satellite-derived high temporal and spatial resolution change sequence. *Forest Ecology and Management*, 261(4), 865–877. <http://doi.org/10.1016/j.foreco.2010.12.020>
- Gevaert, C. M., & García-Haro, F. J. (2015). A comparison of STARFM and an unmixing-based algorithm for Landsat and MODIS data fusion. *Remote Sensing of Environment*, 156, 34–44. <http://doi.org/10.1016/j.rse.2014.09.012>
- Hazaymeh, K., & Hassan, Q. K. (2015). Spatiotemporal image-fusion model for enhancing the temporal resolution of Landsat-8 surface reflectance images using MODIS images. *Journal of Applied Remote Sensing*, 9(1), 96095. <http://doi.org/10.1117/1.JRS.9.096095>
- Hilker, T., Wulder, M. A., Coops, N. C., Linke, J., McDermid, G., Masek, J. G., ... White, J. C. (2009). A new data fusion model for high spatial- and temporal-resolution mapping of forest disturbance based on Landsat and MODIS. *Remote*

- Sensing of Environment*, 113(8), 1613–1627.
<http://doi.org/10.1016/j.rse.2009.03.007>
- Huang, B., & Song, H. (2012). Spatiotemporal reflectance fusion via sparse representation. *IEEE Transactions on Geoscience and Remote Sensing*, 50(10 PART1), 3707–3716. <http://doi.org/10.1109/TGRS.2012.2186638>
- Jarihani, A., McVicar, T., Van Niel, T., Emelyanova, I., Callow, J., & Johansen, K. (2014). Blending Landsat and MODIS Data to Generate Multispectral Indices: A comparison of “Index-then-Blend” and “Blend-then-Index” approaches. *Remote Sensing*, 6(10), 9213–9238. <http://doi.org/10.3390/rs6109213>
- Jönsson, P., & Eklundh, L. (2002). Seasonality extraction by function fitting to time-series of satellite sensor data. *IEEE Transactions on Geoscience and Remote Sensing*, 40(8), 1824–1832. <http://doi.org/10.1109/TGRS.2002.802519>
- Kang, S., Running, S. W., Lim, J. H., Zhao, M., Park, C. R., & Loehman, R. (2003). A regional phenology model for detecting onset of greenness in temperate mixed forests, Korea: An application of MODIS leaf area index. *Remote Sensing of Environment*, 86(2), 232–242. [http://doi.org/10.1016/S0034-4257\(03\)00103-2](http://doi.org/10.1016/S0034-4257(03)00103-2)
- Kempeneers, P., Sedano, F., Piccard, I., & Eerens, H. (2016). Data Assimilation of PROBA-V 100 and 300 m. *IEEE Journal of Selected Topics in Applied Earth Observations and Remote Sensing*, 9(7), 3314–3325.
<http://doi.org/10.1109/JSTARS.2016.2527922>
- Kerdiles, H., & Grondona, M. O. (1995). NOAA-AVHRR NDVI decomposition and subpixel classification using linear mixing in the Argentinean Pampa. *International Journal of Remote Sensing*, 16(7), 1303–1325.
<http://doi.org/10.1080/01431169508954478>
- Knauer, K., Gessner, U., Fensholt, R., & Kuenzer, C. (2016). An ESTARFM fusion framework for the generation of large-scale time series in cloud-prone and heterogeneous landscapes. *Remote Sensing*, 8(5).
<http://doi.org/10.3390/rs8050425>
- Lambers, H., Chapin III, F. S., & Pons, T. L. (2008). Ecosystem and global processes: ecophysiological controls. In *Plant Physiological Ecology* (p. 559).

- Liao, L., Song, J., Wang, J., Xiao, Z., & Wang, J. (2016). Bayesian method for building frequent landsat-like NDVI datasets by integrating MODIS and landsat NDVI. *Remote Sensing*, 8(6), 452-. <http://doi.org/10.3390/rs8060452>
- Marfai, M. A., Almohammad, H., Dey, S., Susanto, B., & King, L. (2008). Coastal dynamic and shoreline mapping: Multi-sources spatial data analysis in Semarang Indonesia. *Environmental Monitoring and Assessment*, 142(1–3), 297–308. <http://doi.org/10.1007/s10661-007-9929-2>
- Mathieu, P. P., & O’Neill, A. (2008). Data assimilation: From photon counts to Earth System forecasts. *Remote Sensing of Environment*, 112(4), 1258–1267. <http://doi.org/10.1016/j.rse.2007.02.040>
- Meng, J., Du, X., & Wu, B. (2011). Generation of high spatial and temporal resolution NDVI and its application in crop biomass estimation. *International Journal of Digital Earth*, 6(3), 203–218. <http://doi.org/10.1080/17538947.2011.623189>
- Olexa, E. M., & Lawrence, R. L. (2014). Performance and effects of land cover type on synthetic surface reflectance data and NDVI estimates for assessment and monitoring of semi-arid rangeland. *International Journal of Applied Earth Observation and Geoinformation*, 30(1), 30–41. <http://doi.org/10.1016/j.jag.2014.01.008>
- Rao, Y., Zhu, X., Chen, J., & Wang, J. (2015). An improved method for producing high spatial-resolution NDVI time series datasets with multi-temporal MODIS NDVI data and Landsat TM/ETM+ images. *Remote Sensing*, 7(6), 7865–7891. <http://doi.org/10.3390/rs70607865>
- Schmidt, M., Udelhoven, T., Gill, T., & Röder, A. (2012). Long term data fusion for a dense time series analysis with MODIS and Landsat imagery in an Australian Savanna. *Journal of Applied Remote Sensing*, 6(1), 63512. <http://doi.org/10.1117/1.JRS.6.063512>
- Sedano, F., Kempeneers, P., & Hurtt, G. (2014). A kalman filter-based method to generate continuous time series of medium-resolution NDVI images. *Remote Sensing*, 6(12), 12381–12408. <http://doi.org/10.3390/rs61212381>

- Settle, J. J., & Drake, N. A. (1993). Linear mixing and the estimation of ground cover proportions. *International Journal of Remote Sensing*, *14*(6), 1159–1177.
<http://doi.org/10.1080/01431169308904402>
- Song, H., & Huang, B. (2013). Spatiotemporal satellite image fusion through one-pair image learning. *IEEE Transactions on Geoscience and Remote Sensing*, *51*(4), 1883–1896. <http://doi.org/10.1109/TGRS.2012.2213095>
- Sun, L., & Schulz, K. (2017). Spatio-temporal LAI modelling by integrating climate and MODIS LAI data in a mesoscale catchment. *Remote Sensing*, *9*(2).
<http://doi.org/10.3390/rs9020144>
- Tewes, A., Thonfeld, F., Schmidt, M., Oomen, R., Zhu, X., Dubovyk, O., ... Schellberg, J. (2015). Using RapidEye and MODIS Data Fusion to Monitor Vegetation Dynamics in Semi-Arid Rangelands in South Africa. *Remote Sensing*, *7*(6), 6510–6534. <http://doi.org/10.3390/rs70606510>
- Tian, F., Wang, Y., Fensholt, R., Wang, K., Zhang, L., & Huang, Y. (2013). Mapping and evaluation of NDVI trends from synthetic time series obtained by blending landsat and MODIS data around a coalfield on the loess plateau. *Remote Sensing*, *5*(9), 4255–4279. <http://doi.org/10.3390/rs5094255>
- Vermote, E. F., Kotchenova, S. Y., & Ray, J. P. (2011). *MODIS Surface Reflectance User's Guide*.
- Walker, J. J., De Beurs, K. M., Wynne, R. H., & Gao, F. (2012). Evaluation of Landsat and MODIS data fusion products for analysis of dryland forest phenology. *Remote Sensing of Environment*, *117*, 381–393.
<http://doi.org/10.1016/j.rse.2011.10.014>
- Watts, J. D., Powell, S. L., Lawrence, R. L., & Hilker, T. (2011). Improved classification of conservation tillage adoption using high temporal and synthetic satellite imagery. *Remote Sensing of Environment*, *115*(1), 66–75.
<http://doi.org/10.1016/j.rse.2010.08.005>
- Wu, B., Huang, B., Zhang, L., & Member, S. (2015). An error-bound-regularized sparse coding for spatiotemporal reflectance fusion, *53*(12), 6791–6803.

- Wu, M., Wang, H., Niu, Z., Zhao, Y., & Wang, C. (2012). A model for spatial and temporal data fusion. *Journal of Infrared Millim. Waves (In Chinese)*, 31(1), 80–84.
- Xie, D., Zhang, J., Zhu, X., Pan, Y., Liu, H., Yuan, Z., & Yun, Y. (2016). An improved STARFM with help of an unmixing-based method to generate high spatial and temporal resolution remote sensing data in complex heterogeneous regions. *Sensors (Switzerland)*, 16(2). <http://doi.org/10.3390/s16020207>
- Yang, J., Wright, J., Huang, T. S., & Ma, Y. (2010). Image super-resolution via sparse representation. *IEEE Transactions on Image Processing*, 19(11), 2861–2873. <http://doi.org/10.1109/TIP.2010.2050625>
- Zhang, X., Liao, C., Li, J., & Sun, Q. (2013). Fractional vegetation cover estimation in arid and semi-arid environments using: HJ-1 satellite hyperspectral data. *International Journal of Applied Earth Observation and Geoinformation*, 21(1), 506–512. <http://doi.org/10.1016/j.jag.2012.07.003>
- Zhu, X., Chen, J., Gao, F., Chen, X., & Masek, J. G. (2010). An enhanced spatial and temporal adaptive reflectance fusion model for complex heterogeneous regions. *Remote Sensing of Environment*, 114(11), 2610–2623. <http://doi.org/10.1016/j.rse.2010.05.032>
- Zhu, X., Helmer, E. H., Gao, F., Liu, D., Chen, J., & Lefsky, M. A. (2016). A flexible spatiotemporal method for fusing satellite images with different resolutions. *Remote Sensing of Environment*, 172, 165–177. <http://doi.org/10.1016/j.rse.2015.11.016>
- Zhukov, B., Oertel, D., & Lanzl, F. (1999). Unmixing-based multisensor multiresolution image fusion. *IEEE Transactions on Geoscience and Remote Sensing*, 37(3), 1212–1226.
- Zurita-Milla, R., Kaiser, G., Clevers, J. G. P. W., Schneider, W., & Schaepman, M. E. (2009). Downscaling time series of MERIS full resolution data to monitor vegetation seasonal dynamics. *Remote Sensing of Environment*, 113(9), 1874–1885. <http://doi.org/10.1016/j.rse.2009.04.011>

Chapter 5

5 Phenology, Biomass and Yield Estimation for Corn and Soybean Using Spatio-Temporal Fusion of Landsat-8 and MODIS Data⁴

5.1 Introduction

To ensure food security for the growing world population, crop growth needs to be monitored and crop production needs to be estimated. The phenological information of a crop is an indicator to understand agricultural response to environment conditions and essential to estimate crop production (Sakamoto, 2010). Crop production is also a key indicator to understand the seasonal ecosystem carbon dioxide exchange and the contributions of agriculture to environmental change (Marshall & Thenkabail 2015; Paruelo et al. 2000).

Crop production can be estimated using empirical models, process-based models or semi-empirical models. Traditionally, empirical models have been adopted for crop production estimation by building relationships between the remotely sensed vegetation index and in situ measurements. However, they may be only applicable to specific crop growth stages or specific regions (Cheng, Meng, & Wang, 2016) and the accuracy of this method varies with the heterogeneity of environmental conditions (Kuwata & Shibasaki, 2016). Process-based models, such as the AquaCrop (Steduto, Hsiao, Raes, & Fereres, 2009), CERES-Maize (Dyke, Kiniry, & Jones, 1986), STICS (Brisson et al., 2003), and WOFOST (van Dopen et al. 1989) have been developed to simulate crop production. These models simulate the key physical and physiological processes of the plant-soil-atmosphere system to obtain daily dry above-ground biomass, defined as the dry weight of the total above-ground matter

⁴ A version of this chapter has been submitted for publication (Chunhua Liao, Jinfei Wang, Taifeng Dong, Jiali Shang, Jiangui Liu, Yang Song. Phenology, biomass and yield estimation for corn and soybean using spatio-temporal fusion of Landsat-8 and MODIS data. International Journal of Applied Earth Observation and Geoinformation. (*Under review*)).

of crops (Marshall & Thenkabail, 2015; Sellers, 1985), and then calculate crop yield using a harvest index (HI). But these process-based models need a large set of agro-environment variables, which may not be all available or difficult to obtain over large areas (Battude et al., 2016; Betbeder, Fieuzal, & Baup, 2016; Claverie et al., 2012).

Simpler process models based on the light use efficiency (LUE) theory (Monteith, 1972) have been widely used for regional biomass estimation by coupling with remote sensing data. The LUE refers to the efficiency of converting the Absorbed Photosynthetic Active Radiation (APAR) into aboveground dry matter in plants. In this model, the daily photosynthetic active radiation (PAR), fraction of PAR absorbed by green canopy ($fAPAR$), and LUE of the crops are the input parameters. The daily $fAPAR$ can be obtained from daily optical remote sensing data or by fitting a crop growth model using in situ or satellite observations acquired at key stages of crops during the growing season (Dong et al., 2017; Liu et al., 2010). Generally, the LUE is a function of the maximum LUE (LUE_{max}) limited by the temperature stress or water stress (Monteith, 1977; Potter et al., 1993). However, temperature or water stress alone may not always elucidate the variations in LUE for croplands, as crop management practices such as fertilizer application and irrigation rates also affect the LUE (Bradford, Hicke, & Lauenroth, 2005; Claverie et al., 2012).

A semi-empirical model, the Simple Algorithm for Yield Estimates (SAFY) model (Duchemin, Maisongrande, Boulet, & Benhadj, 2008), simulates the daily Green Leaf Area Index (GLAI) and Dry Aboveground Mass (DAM) (i.e. dry aboveground biomass) from the date of emergence by combining Monteith's LUE theory (Monteith, 1972) and Maas's leaf partitioning function (Maas, 1990). Claverie et al. (2012) demonstrated that the SAFY model could well estimate corn and sunflower biomass when the model parameters were calibrated by the high spatial and temporal resolution remotely sensed GLAI. To improve the corn biomass and yield, Battude et al. (2016) proposed a new version of the SAFY model by considering the seasonal dynamic of specific leaf area (SLA) and effective light use efficiency (ELUE), which is the LUE under all the environmental stresses excluding the temperature stress. The result demonstrated that the new model could accurately estimate crop biomass and yield by taking the interrelationship among parameters. The SAFY model coupled with time series remote sensing data was also applied to estimate

biomass and yield of other crops such as wheat (Dong et al., 2016) and soybean (Betbeder et al., 2016). In general, the time series GLAI data acquired at the key stages of the growing season are needed to calibrate the SAFY model. However, high spatial resolution data such as Formosat-2, SPOT-4, and Deimos-1 are costly, and free high spatial resolution data such as Landsat images may be unavailable on important dates due to low temporal resolution and frequent cloud contamination over the study site. Thus, how the biomass can be accurately estimated with a limited number of high spatial resolution remote sensing images is worth studying.

Crop phenology information is needed when running the SAFY model as many parameters are linked with crop phenological events. Therefore an accurate crop phenology detection algorithm is essential. The common steps for crop phenology detection includes (1) obtaining satellite-based vegetation parameter (e.g., Normalized Difference Vegetation Index (NDVI), LAI and $fAPAR$) time series, (2) reconstructing daily observation using a filter (Chen et al. 2004; Hird & McDermid 2009; Atkinson et al. 2012; Beck et al. 2006) or a mathematical function such as the asymmetric Gaussian function (Roerink, Menenti, Soepboer, & Su, 2003), and the double logistic function (Atkinson et al., 2012; Beck et al., 2006; Hird & McDermid, 2009; Xiaoyang Zhang et al., 2003) to reduce the high-frequency noise, (3) determining specific phenological events based on the reconstructed daily observations. The traditional crop phenology detection methods basically estimate phenological dates of natural vegetation and crops by detecting preliminary-defined metrics such as fixed threshold value, seasonal midpoint, maximum point and inflection point on the remotely sensed vegetation index time series. For example, the dates when the NDVI is greater than a specific threshold are defined as key phenological stages (Sakamoto et al., 2005), or the inflection point (minimum/maximum value of first derivative) of the NDVI curve to determine the start of season (SOS) and end of season (EOS) (Jeong, Ho, Gim, & Brown, 2011). However, the commonly used phenology detection methods are sensitive to satellite data noise caused by atmospheric constituents, and rely on the number of satellite images acquired at key phenological stages (Sakamoto et al. 2010).

The objective of this study is to propose a strategy to estimate subfield-scale crop phenology and crop production using the spatio-temporal fusion of Landsat-8 and MODIS

images. Firstly a recently proposed spatio-temporal vegetation index image fusion method (STVIFM) developed by Liao, Wang, Pritchard, Liu, and Shang (2017) will be applied to generate the NDVI time series with both high spatial resolution and high temporal resolution in this study. Then the *f*APAR will be derived from the NDVI data and an improved Two-Step Filtering (TSF) method incorporated with the canopy structure dynamics model (CSDM) will be applied to simulate daily *f*APAR and to detect major phenological events. Finally the phenology information will be linked to the parameters of the SAFY and the GLAI calculated from the remotely sensed data will be used to calibrate the SAFY model in order to estimate pixel-based biomass and ELUE.

5.2 Materials

5.2.1 Study site

The study area is located in the Mixedwood Plains Ecozone in southwestern Ontario, characterized by abundant water supply, a relatively mild climate during the growing season and harsh winter, productive soils for agriculture, and a longer growing season than most of the rest of the country. The common practice in this region is one harvest per year for field crops. The croplands in the study site are mixed with woods and the dominant crops are winter wheat, corn and soybean. Generally, the winter wheat in this study site is seeded in October of the previous year and harvested in July while the corn and soybean are seeded in May and harvested in September or October. An area of about 14 km by 8 km near the city of London, Ontario was selected as a study site (Figure 5-1).

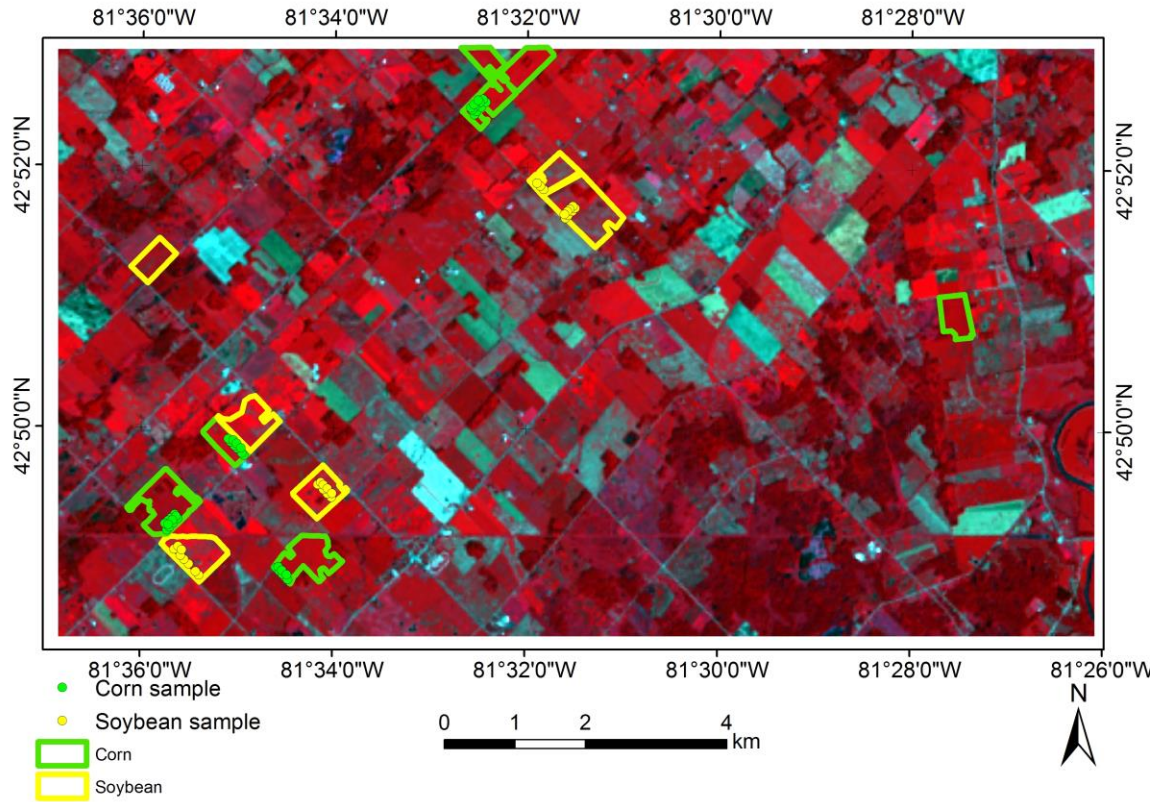


Figure 5-1: The study site observed on Landsat-8 image in July 2015 (Nir-Red-Green band). The green and yellow polygons are corn fields and soybean fields where the field data were collected; Green and yellow points are the sample sites for corn and soybean.

5.2.2 Field data collection

Intensive field work was conducted weekly from 23 May to 21 September in 2015 (Appendix D). A general survey including the digital hemispherical photos (DHP), crop phenology, crop height was collected for a total of 27 soybean samples and 6 corn samples each time. For each sample site, 7 photographs were taken along one transect and then another 7 photographs along another transect (Shang et al., 2014). The effective LAI and $fAPAR$ were derived from the photographs using the CAN-EYE software (Weiss & Baret, 2017).

Crop inventory information was also collected in September 2015. Crop biomass was collected on 25 September and 2 October using a destructive method in relatively

homogeneous locations for soybean (17 samples) and corn (15 samples). For corn sampling, 5 plants were randomly selected within a 5 m by 5 m area and manually harvested. The number of corn plants was counted within this area, and accordingly, the corn density was derived. For soybean sampling, two sample sites were selected within a 5 m by 5 m area. For each sample site, the plants were harvested within a 0.25 m by 0.25 m area. The number of soybean plants was counted within this area, and accordingly, the soybean density was derived. Then the two measurements within the 5 m by 5 m area were averaged. The harvested plants were cut and placed in large plastic bags and transferred back to the lab. The plants were separated into stems, leaves and seeds and were weighed separately to obtain the fresh mass by organ. These samples were then oven dried at 40 °C for 4 d to obtain the DAM. Table 5-1 shows the dates the field work was conducted on and the data collected in the field work.

Table 5-1: The dates for field work and crop types

Dates when the field work was conducted	Data collected in the field work
23 May 2015	Corn/soybean, Phenology
29 May 2015	Corn/soybean, Phenology
9 June 2015	Corn/soybean, Phenology
19 June 2015	Corn/soybean, Phenology
23 June 2015	Corn, general survey*
2 July 2015	Corn/soybean, general survey
9 July 2015	Soybean, general survey
16 July 2015	Soybean, general survey
23 July 2015	Corn, general survey
27 July 2015	Soybean, general survey
3 August 2015	Corn/soybean, general survey
11 August 2015	Corn/soybean, general survey
20 August 2015	Corn/soybean, general survey
3 September 2015	Corn/soybean, general survey
13 September 2015	Corn/soybean, general survey
21 September 2015	Corn/soybean, crop inventory
25 September 2015	Corn/soybean, biomass
27 September 2015	Corn/soybean, crop inventory
2 October 2015	Corn/soybean, biomass
* General survey include fisheye photos (LAI, fAPAR), phenology, crop type.	

5.2.3 Regional weather data

Both the daily shortwave solar radiation and mean temperature are required in this study. The radiation data were acquired from the Modern-Era Retrospective Analysis for

Research and Applications (MERRA) product (<http://disc.sci.gsfc.nasa.gov/>) (Rienecker et al., 2011). The spatial resolution of the MERRA radiation product is 0.5° latitude by 0.67° longitude. The radiation from this product was in good agreement with that of the meteorological stations in Canada (Kross, Seaquist, & Roulet, 2016). The daily shortwave solar radiation in 2015 at the study site was extracted centered to the site and calculated as the sum of hourly radiation (Figure 5-2(a)). The PAR ($0.4\text{--}0.7\ \mu\text{m}$) is part of the short wave solar radiation ($0.3\text{--}3.0\ \mu\text{m}$) that is absorbed by chlorophyll for photosynthesis in the plants (Bastiaanssen & Ali, 2003). The daily temperature data were obtained from the historical climate data website (<http://climate.weather.gc.ca/>) for the nearest London weather station (Figure 5-2(b)).

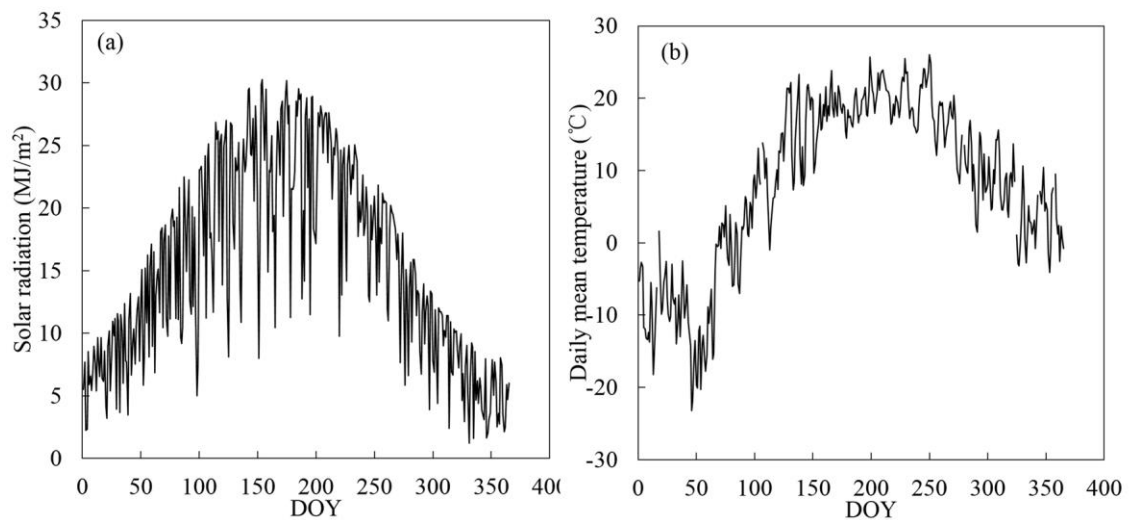


Figure 5-2: Annual time series of (a) daily shortwave solar radiation and (b) daily mean temperature

5.2.4 Crop classification data

In this study, the crop classification obtained from the minimum noise fraction (MNF) transformation of multitemporal Radarsat-2 data based on random forest classifier (Liao, Wang, Huang, & Shang, 2018) was used. The overall classification accuracy is 95.89% over this study area, and the producer's accuracy is 93.95% for corn and 99.54% for soybean. The corn and soybean fields were extracted separately based on this classification result.

5.2.5 Remote sensing data

In this study, only three cloud-free Landsat-8 OLI reflectance images were acquired from the United States Geological Survey (USGS) (<http://landsat.usgs.gov/landsat8.php>) over the study site during the 2015 growing season. Due to the influence of cloud contamination on the daily reflectance products, 10 cloud-free Moderate Resolution Imaging Spectroradiometer (MODIS) 8-day surface reflectance products (MOD09Q1, V6.0) with a spatial resolution of 250 m were downloaded from the National Aeronautics and Space Administration (NASA) Reverb portal (<http://reverb.echo.nasa.gov/reverb/>) (Table 5-2). Each MOD09Q1 pixel represents the best observation during an 8-day period (Vermote et al., 2011). The NDVI was calculated from the Landsat-8 and MODIS reflectance data.

Table 5-2: The acquired dates for remote sensing data.

Sensor	Landsat-8 OLI	MODIS
Date	10 June 2015	10 June 2015
		4 July 2015
		12 July 2015
		20 July 2015
	28 July 2015	28 July 2015
		13 August 2015
		21 August 2015
		29 August 2015
		6 September 2015
		14 September 2015
Spatial resolution	30 m	250 m

5.3 Methodology

Figure 5-3 is the flowchart showing the processing steps of this study. First of all, the Landsat-8 images and MODIS images were used to generate 10 Landsat-like NDVI images throughout the growing season by using a spatio-temporal vegetation index image fusion model (STVIFM) (Liao, Wang, Pritchard, Liu, & Shang, 2017). For the second step, an improved TSF method was proposed to detect phenology based on the 10 Landsat-like NDVI images and the pixel-based daily $fAPAR$ was generated at the same time. Lastly, the SAFY model was run using the GLAI computed from the remote sensing data, crop classification map, the phenology map, and the daily weather data.

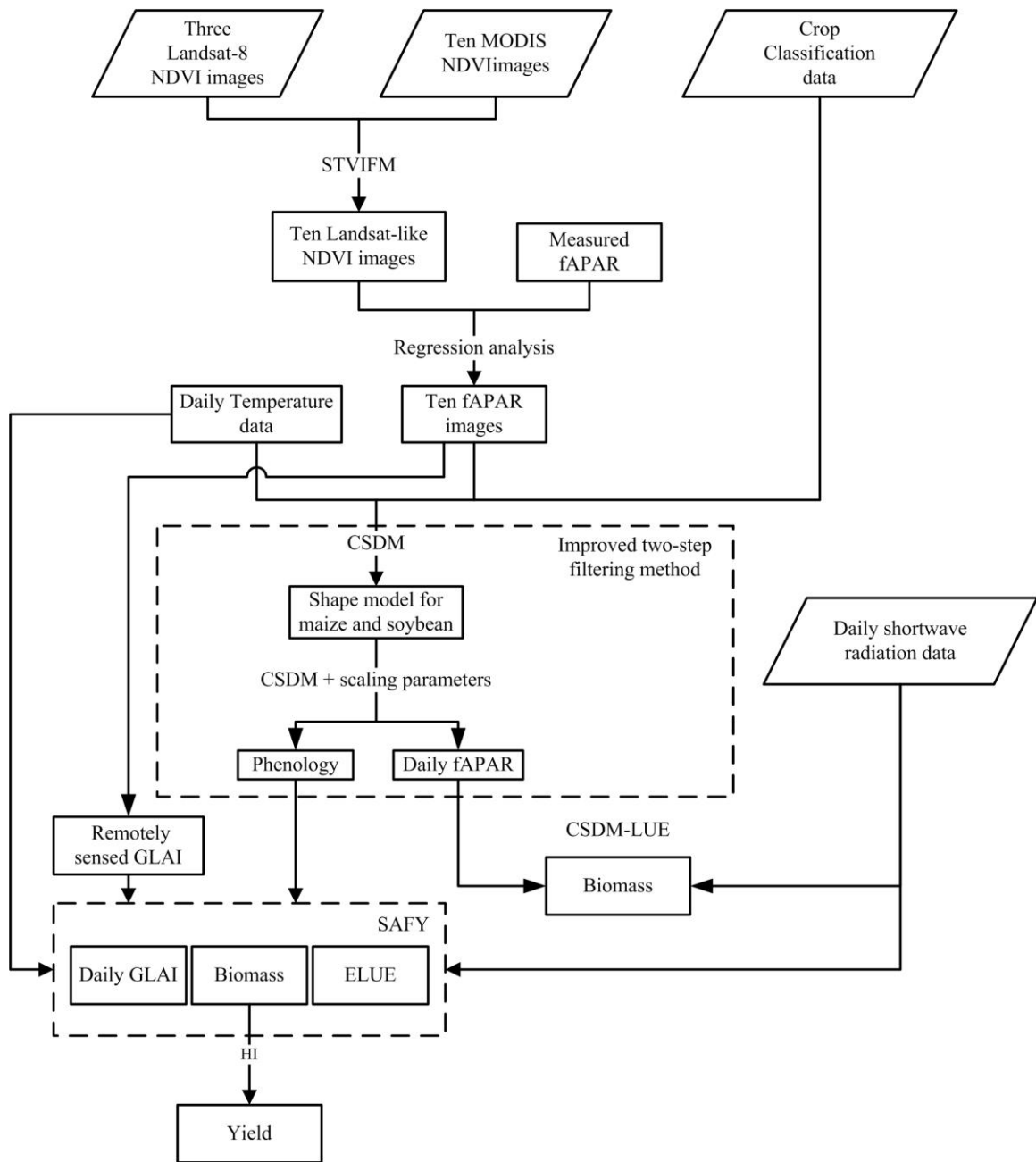


Figure 5-3: Flowchart for crop phenology, biomass, and yield estimation

5.3.1 Spatio-temporal data fusion

In 2015, only three cloud-free high spatial resolution Landsat-8 OLI images were acquired during the growing season over the study site. High temporal resolution images such as MODIS, however, have a lower spatial resolution of 250 m, which is not spatially sufficient for subfield agricultural studies. The spatio-temporal image fusion methods such as the

Spatial and Temporal Adaptive Reflectance Fusion Model (STARFM) (Gao et al., 2006) and the Enhanced Spatial and Temporal Adaptive Reflectance Fusion Model (ESTARFM) (Zhu et al., 2010) provide a way to generate time series images with both high spatial and temporal resolution. However, a previous study showed that the STVIFM performs superior to the STARFM and ESTARFM methods in generating NDVI time series in cropland area when the number of high spatial resolution images are limited (Liao et al., 2017). This is because the STVIFM considers the temporal variation of the NDVI change rate when the time interval between two adjacent high spatial resolution images is large (Liao et al., 2017).

In this study, seven other NDVI images with a spatial resolution of 30 m were generated using the three Landsat-8 OLI images and 10 MODIS images by the STVIFM. Two pairs of high spatial resolution and high temporal spatial resolution data, and the data acquired on the prediction dates were needed as inputs. The Landsat-8 and MODIS data acquired on 10 June and 28 July were used to generate the Landsat-like NDVI image for 4 July, 12 July, and 20 July. The Landsat-8 and MODIS data acquired on 28 July and 14 September were used to generate the Landsat-like NDVI images on 13 August, 21 August, 29 August and 6 September.

5.3.2 Crop phenology detection based on an improved TSF approach

5.3.2.1 Description of the improved TSF approach

The TSF method, firstly proposed by Sakamoto et al. (2010), incorporates the “shape-model fitting” concept to detect major phenological stages of corn and soybean from the time-series MODIS Wide Dynamic Range Vegetation Index (WDRVI) data. This method firstly adopts a shape model, which is a crop-specific WDRVI curve with typical phenological features generated by using the 8-day MODIS data with a spatial resolution of 250 m. Then it derives the optimum scaling parameters from shape-model fitting procedure. This approach relies on the number of satellite images acquired during the growing season. However, in areas with constant cloud presence, the number of high spatial resolution satellite images will be limited. To solve this problem, this approach will

be improved by using the shape model generated from the canopy structure dynamics model (CSDM) (Equation (5-2)) instead of the WDRVI time series filtered by the wavelet-based filter, and deriving three scaling parameters, which consider both growing and senescence stages, from the shape model through the optimizing procedure to obtain the daily $fAPAR$ for the entire region and detect the phenology (Equation (5-4)).

5.3.2.2 Deriving $fAPAR$ from remote sensing images

To implement the improved TSF approach, the remotely sensed $fAPAR$ should be derived firstly. The remote sensing data acquired simultaneously (or one or two days apart) (Table 5-3) with the field work were selected to conduct the regression analysis between the NDVI and the in situ measured $fAPAR$. To avoid the error caused by the different spatial scale between the collected data and the remote sensing data, the average values within the same crop fields were calculated. According to the relationship between the average NDVI and average $fAPAR$ collected in the fields (Figure 5-4), the $fAPAR$ can be calculated from the remotely sensed NDVI by Equation (5-1):

$$fAPAR = 1.55 \times NDVI - 0.48 \quad (5-1)$$

Table 5-3: The data used for regression analysis between NDVI and $fAPAR$

	Dates for field work	Dates for original and synthetic Landsat-8 images
Corn/soybean	2 July 2015	4 July 2015
Corn	23 July 2015	20 July 2015
Soybean	27 July 2015	28 July 2015
Corn/soybean	11 August 2015	13 August 2015
Corn/soybean	20 August 2015	21 August 2015
Corn/soybean	13 September 2015	14 September 2015

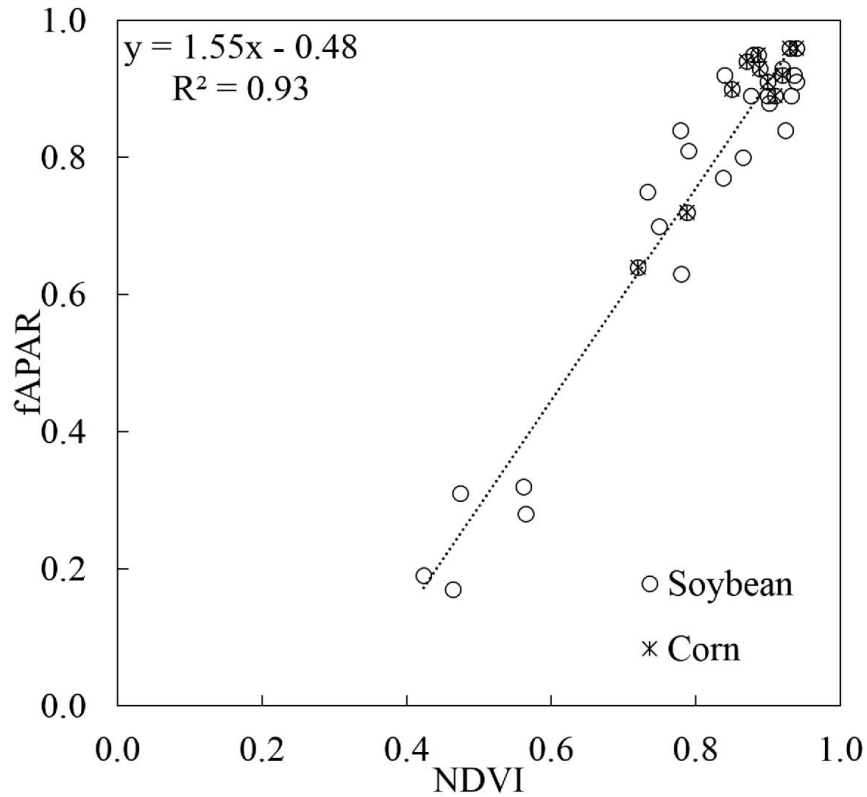


Figure 5-4: Relationship between average NDVI and average $fAPAR$ of the samples collected within each field

5.3.2.3 Shape model

The CSDM can be used for daily LAI or daily $fAPAR$ simulation (Dong et al., 2017; Koetz, Baret, Poilvé, & Hill, 2005; J. Liu et al., 2010). The daily $fAPAR$ is selected because it will be used in the simple LUE model for the biomass estimation.

$$fAPAR(T) = fAPAR_{max} [1/(1 + e^{-a(T-T_i)}) - e^{-b(T-T_s)}] \quad (5-2)$$

where T is the cumulative daily mean temperature for crops to grow starting from sowing date (Dong et al., 2017). As the corn and soybean were sowed between 5 May and 10 May, the cumulative temperature was calculated starting from 10 May. T_i is the cumulative temperature corresponding to the inflection point during the growth phase; T_s is the cumulative temperature at which $fAPAR$ decreases to 0 due to senescence. In this model, the five parameters $fAPAR_{max}$, a , b , T_i , and T_s vary with crop type and the crop growing

condition and they are optimized using the $fAPAR$ obtained from the 10 remote sensing images.

To generate the shape models, the 10 $fAPAR$ values generated from the Landsat or synthetic Landsat images were used for the optimization of the five parameters in the CSDM (Equation (5-2)) of the corn sample site C05-02 and the soybean sample site S09-02 respectively by a nonlinear least-squares solver method (i.e. lsqnonlin). The cost function is the Root Mean Square Error (RMSE) between the estimated $fAPAR$ and the $fAPAR$ derived from the remote sensing images (Equation (5-3)).

$$RMSE = \left[\frac{1}{N} \sum_{i=1}^N (fAPAR_i - fAPAR_{rsi})^2 \right]^{\frac{1}{2}} \quad (5-3)$$

where N is the number of remote sensing observations; $fAPAR_i$ is the estimated $fAPAR$; $fAPAR_{rsi}$ is the remotely sensed $fAPAR$.

The range and the optimized value of each parameter are shown in Table 5-4. The daily $fAPAR$ for the two sites are shown in Figure 5-5. It illustrates that corn has a longer growing season than soybean. As the phenology information for the two sample points was observed throughout the growing season, the phenological stages were defined on the shape models according to the observation from the field (Figure 5-5). The SOS, which is the time when vegetation growth begins to rapidly increase (Zheng, Wu, Zhang, & Zeng, 2016), the DOS and the end of season were identified according to the shape of the $fAPAR$ time course and the characteristic of crops at each Biologische Bundesanstalt, Bundessortenamt and Chemische (BBCH) scale (Zheng et al., 2016).

Table 5-4: The optimized parameters in CSDM obtained for soybean and corn

	Range	Corn	Soybean
$fAPAR_{max}$	0-1	0.99	0.99
a	0-0.01	0.0037	0.0068
b	-0.01-0	-0.0043	-0.0058
T_i	500-2000	742.5	1017.3
T_s	2000-3000	2694.2	2580.0

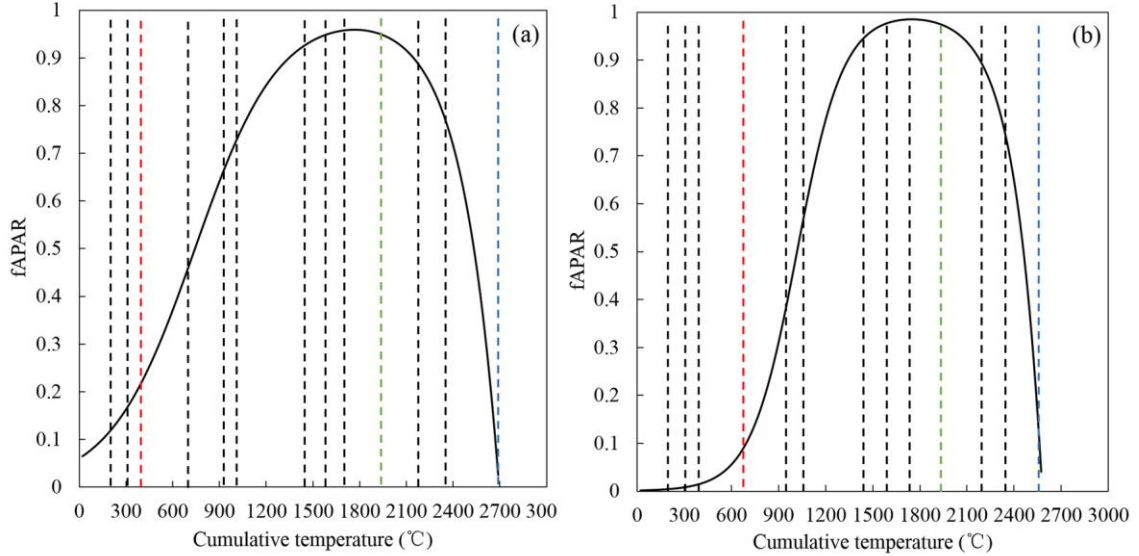


Figure 5-5: The shape model for (a) corn (BBCH=13, 16, 19, 31, 33, 37, 66, 67, 69, 75, 85, 87, 97) and (b) soybean (BBCH=9, 10, 12, 14, 25, 29, 65, 67, 70, 75, 85, 95, 97). The red lines represent the SOS. The green lines represent the DOS and the blue lines represent EOS.

5.3.2.4 Phenology detection

The TSF method does not consider the variation of the length of season (LOS) within the same crop type. In this study, the TSF model was improved by introducing three scaling parameters $yscale$, $xshift_1$ and $xshift_2$ to the shape models (Equation (5-2)) for corn and soybean (Equation (5-4)), so that the variation of LOS can also be addressed.

$$fAPAR(T) = yscale * fAPAR_{max} [1 / (1 + e^{-a(T+xshift_1-T_i)}) - e^{-b*(T+xshift_2-T_s)}] \quad (5-4)$$

where $yscale$ represents the scale for $fAPAR_{max}$, $xshift_1$ represents the temperature shift for the same phenology at the vegetative stage, and $xshift_2$ represents the temperature shift at the reproductive stage. The ranges for the three parameters are: $0.5 < yscale < 1.5$, $0.5 < xshift_1 < 1.5$, $-1000 < xshift_1 < 1000$ °C, $-1000 < xshift_2 < 1000$ °C. The three parameters were optimized for corn and soybean pixels respectively using the $fAPAR$ time series acquired from the NDVI images.

Then the scaling parameters were optimized for the entire region using the 10 remotely sensed $fAPAR$ images based on the same optimization procedure described above. Finally, the $fAPAR$ course can be obtained based on Equation (5-4) and the phenology for each pixel can be obtained based on the following steps.

As the phenological stages have been defined on the shape models, the cumulative temperature of different phenological stages for the unknown pixels can be estimated using the following strategy. The CSDM describes the vegetative stage and reproductive stage of the crops separately. Therefore, the growth stages need to be considered when calculating the phenological dates of the unknown pixels. In this study, a weighting system was adopted to differentiate the two stages as follows:

$$w_1 = 1/(1 + e^{-a*(T(k)-T_i)}) \quad (5-5)$$

$$w_2 = e^{-b*(T(k)-T_s)} \quad (5-6)$$

where $T(k)$ represents the cumulative temperature at phenology k . The cumulative temperature at phenology k for each unknown pixel ($T'(k)$) was calculated as follows:

$$T'(k) = w_1/(w_1 + w_2) * (T(k) - xshift_1) + w_2/(w_1 + w_2) * (T(k) - xshift_2) \quad (5-7)$$

As a specific cumulative temperature has a corresponding day of year (DOY), a lookup table was built between DOY and cumulative temperature. Then, the DOY of each phenological stage and the daily $fAPAR$ for each pixel were obtained based on the lookup table.

5.3.3 Dry aboveground biomass and yield estimation based on the SAFY model

5.3.3.1 Description of the SAFY model

The basic idea of the SAFY (Duchemin et al., 2008) is that during the plant growth, a fraction of daily plant DAM is partitioned to dry leaf mass production at the vegetative growth phase, and daily new GLAI is thus obtained by converting daily leaf biomass into

daily leaf area growth (Δ_{LAI}^+) using the specific leaf area (SLA). The simulation begins on the day of plant emergence (D_0) to the day D_j . Leaf senescence begins when the sum of temperature (SMT) reaches a given threshold (Stt). The GLAI decrease (Δ_{LAI}^-) is simply modeled based on the rate of senescence coefficient (Rs) controlled by temperature. The DAM is calculated based on the daily PAR absorbed by green plants (APAR), effective LUE (ELUE) and the temperature stress factor ($F_T(T_a)$). The SAFY only considers the temperature stress on crop condition, and the ELUE is the result of the interaction between nitrogen, water and other environmental stresses excluding the temperature stress. T_a is the daily average temperature. The T_{min} , T_{max} , T_{opt} are the minimum, maximum, and optimum temperature for crop growth.

$$\Delta_{DAM} = ELUE \times F_T(T_a) \times APAR \quad (5-8)$$

$$F_T(T_a) = \begin{cases} 1 - \left[\frac{T_{opt} - T_a}{T_{opt} - T_{min}} \right]^\beta & T_{min} < T_a < T_{opt} \\ 1 - \left[\frac{T_a - T_{opt}}{T_{max} - T_{opt}} \right]^\beta & T_{opt} < T_a < T_{max} \\ 0 & T_a < T_{min} \text{ or } T_a > T_{max} \end{cases} \quad (5-9)$$

The APAR is calculated using the daily incoming global radiation (R_g), the climate efficiency (ε_c), which defines the ratio of the PAR to the incoming global radiation, and the fraction of daily photosynthetically active radiation absorbed by plants (Equation (5-10)). The $fAPAR$ is estimated using Beer's law, and k_{ext} represents the light-extinction coefficient (Equation (5-11))

$$APAR = \varepsilon_c \times R_g \times fAPAR \quad (5-10)$$

$$fAPAR = 1 - e^{-k_{ext} \times LAI} \quad (5-11)$$

The partition-to-leaf (Pl) is a function of the sum of temperature (SMT) and two parameters Pl_a and Pl_b :

$$Pl = 1 - Pl_a e^{Pl_b \times SMT} \quad (5-12)$$

$$\text{SMT} = \sum_{t=D_0}^{D_j} (T_{a,t} - T_{min}) \quad (5-13)$$

$$\text{If } Pl > 0, \Delta_{LAI}^+ = \Delta_{DAM} \times Pl \times SLA \quad (5-14)$$

$$\text{If } \text{SMT} > Stt, \Delta_{LAI}^- = LAI_t \frac{\text{SMT} - Stt}{R_s} \quad (5-15)$$

$$LAI_t = LAI_{t-1} + \Delta_{LAI}^+ - \Delta_{LAI}^- \quad (5-16)$$

Crop yield is generally estimated by multiplying the final biomass with a harvest index (HI), which is defined as the ratio of final grain yield over the final DAM (Equation (5-17)).

$$\text{Yield} = \text{DAM} \times \text{HI} \quad (5-17)$$

As a comparison, the SAFY model with no phenology-related information was performed. The three phenology-related parameters were ingested as free parameters and determined in the second calibration phase. The simple LUE model was also performed as a comparison to the SAFY model. With the daily *f*APAR and daily solar radiation data, the daily APAR can be calculated based on Equation (5-10), and the DAM on date *t* can be computed using the ELUE, temperature stress and cumulative APAR by Equation (5-18). As the daily *f*APAR is simulated by the CSDM, this simple LUE model is referred as CSDM-LUE hereafter.

$$\text{DAM}_t = \text{ELUE} \times \sum_{t=D_0}^{D_j} (F_T(T_a) \times \text{APAR}_t) \quad (5-18)$$

5.3.3.2 Calibration of the SAFY model

The SAFY model requires 12 parameters. In this study, five parameters (ε_c , T , β , DAM_0 , k_{ext}) were fixed according to the literature and in situ measurements. Three parameters (D_0 , Stt , R_s) related to the phenological stages were determined from the remotely sensed

phenological map and the daily regional weather data. The four remaining parameters (SLA, Pl_a , Pl_b , ELUE) were calibrated using the original remotely sensed GLAI time series on two phases.

Generally, the common value of 0.48 was used for the ε_c (Battude et al., 2016; Britton & Dodd, 1976; Claverie et al., 2012; Varlet-Grancher, Bonhomme, Chartier, & Artis, 1982). A value of 4.2 g/m² was used for the initial dry above biomass (DAM₀) (Claverie et al., 2012; Dong et al., 2016, 2017). The T_{min} , T_{max} , T_{opt} for summer crops such as corn and soybean in Canada are reported as (10, 35, 30 °C) with slight difference among different species (Qian, Zhang, Chen, Feng, & O'Brien, 2010; Sánchez, Rasmussen, & Porter, 2014). Considering the facts that the corn in the study site generally emerged earlier than the soybean, the minimal temperature for corn was adjusted to 8 °C according to the literature (Battude et al., 2016; Claverie et al., 2012). The polynomial degree (β) in the temperature stress function is usually set as 2. The k_{ext} was computed by inverting Beer's law (Equation (5-11)) between the measured $fAPAR$ and the effective GLAI obtained from CAN-EYE software (Weiss & Baret, 2017) (Figure 5-6).

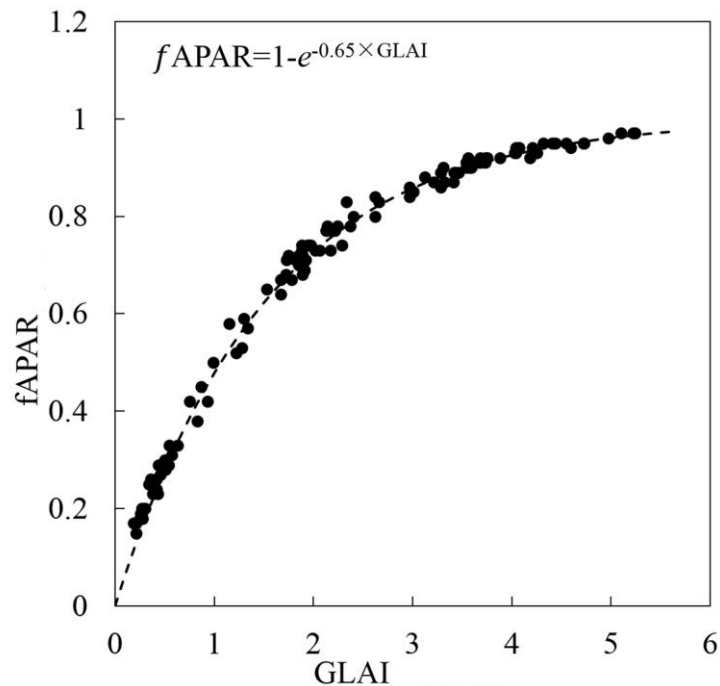


Figure 5-6: Relationship between $fAPAR$ and effective GLAI

The D_0 in the SAFY model was an important parameter. As in the SAFY, the remotely sensed GLAI on D_0 is usually about $0.1 \text{ m}^2/\text{m}^2$ (Duchemin et al., 2008), D_0 in the SAFY model was not exactly the day of emergence of the crops in the observation. In this study, D_0 was replaced by the SOS generated from the remote sensing images in the phenology detection process.

The Stt was the sum of temperature (SMT) from SOS to DOS (Equation (5-13)). As Figure 5-5 shows, the senescence rate for corn and soybean are similar, the Rs was calculated using the SMT difference between the EOS and the DOS (Equation(5-19)) (Battude et al., 2016).

$$Rs = 1725.7 \times e^{0.002 \times (SMT_{EOS} - Stt)} \quad (5-19)$$

The remotely sensed GLAI time series were required to calibrate the remaining parameters of the SAFY model. The $fAPAR$ data obtained from the three original Landsat-8 data and the seven synthetic Landsat-like data were used to compute the GLAI based on the inversion of Equation (5-11).

In the remaining parameters, a good relationship was reported between Pl_a and Pl_b for corn in a previous study (Battude et al., 2016). As the phenology-related parameters were forced into the SAFY model, and the soybean was also studied, the reported relationship between Pl_a and Pl_b may be not suitable. Therefore, the remaining three parameters ELUE, Pl_a and Pl_b were calibrated through two phases. The optimization procedure was based on the Shuffled Complex Evolution-University of Arizona (SCE-UA) algorithm (Duan, Sorooshian, & Gupta, 1994). The RMSE between the simulated GLAI and the remotely sensed GLAI was used as the cost function of the calibration.

$$RMSE = \left[\frac{1}{N} \sum_{i=1}^N (GLAI_i - GLAI_{rsi})^2 \right]^{\frac{1}{2}} \quad (5-20)$$

where N is the number of remote sensing observations; $GLAI_i$ is the estimated GLAI; $GLAI_{rsi}$ is the remotely sensed GLAI.

Before the calibration, the range of each parameter needs to be defined. The SLA represents the leaf area that the unit leaf biomass was converted to. It is related to the thickness of leaves (Battude et al., 2016). The SLA was reported as 0.023 m²/g and 0.024 m²/g for corn (Battude et al., 2016; Claverie et al., 2012; Dong et al., 2017) while the SLA for soybean was reported ranging between 0.021 m²/g and 0.029 m²/g (Pierozan Junior & Kawakami, 2013). Therefore, the range for SLA was defined as between 0.02 m²/g to 0.032 m²/g in this paper. $1 - Pl_a$ defines the percentage of biomass that was partitioned to the leaf of the plants at the D_0 . In previous study (Battude et al., 2016), the Pl_a was defined as between 0.05 and 0.5 for corn and soybean, and Pl_b is between 10^{-5} and 10^{-2} . The ELUE was assumed as field-specific parameters in a few previous studies (Battude et al., 2016; Claverie et al., 2012), but due to the agricultural management (seeding date) and field scale agro-environmental stresses such as water stress or nitrogen stress, the actual ELUE may vary within the fields (Dong et al., 2016). Table 5-5 lists the LUE (considered stresses) or LUE_{max} (under no stresses) values for corn and soybean reported in literature. Therefore, the range of ELUE for corn is 2-5 g/MJ and for soybean is 1-2 g/MJ.

Table 5-5: LUE or LUE_{max} for corn and soybean reported in literature

Corn	LUE (g MJ-1)	Source
Corn	3.9	(Liu et al., 2010)
Corn	3.3	(Claverie et al., 2012)
Corn	4.26	(Daughtry, Gallo, Goward, Prince, & Kustas, 1992)
Corn	3.4	(Bastiaanssen & Ali, 2003; Sinclair & Horie, 1989)
Corn	3.74, 3.84	(Lindquist, Arkebauer, Walters, Cassman, & Dobermann, 2005)
Corn	3.42-3.9	(Gallo, Daughtry, & Wiegand, 1993)
Soybean	1.14-1.91	(Jorge, Ponte, Ribeiro, & José, 2009)
Soybean	1.59, 2.34	(Daughtry et al., 1992)
Soybean	1.67-1.86	(Rochette, Desjardins, Pattey, & Lessard, 1995)

On the first phase, the four free parameters were optimized at the same time. The calibration was performed by minimizing the RMSE between the GLAI simulated by SAFY and the GLAI obtained from the three Landsat-8 data and seven synthetic Landsat-like data. 100 random pixels were selected from the corn fields and soybean fields respectively to conduct the optimization procedure. Each pixel was run 10 times to avoid the local minimum, and the one with the least RMSE was kept for analysing. We tried to analyze the correlation between Pl_a and Pl_b for both corn and soybean, and a good exponential relationship was found between Pl_a and Pl_b for soybean and corn respectively

(Figure 5-7). The mean value of SLA and Pl_a were calculated, and Pl_b was computed from the relationship between Pl_a and Pl_b (Equation (5-21)). The values and sources of the twelve parameters are listed in Table 5-6.

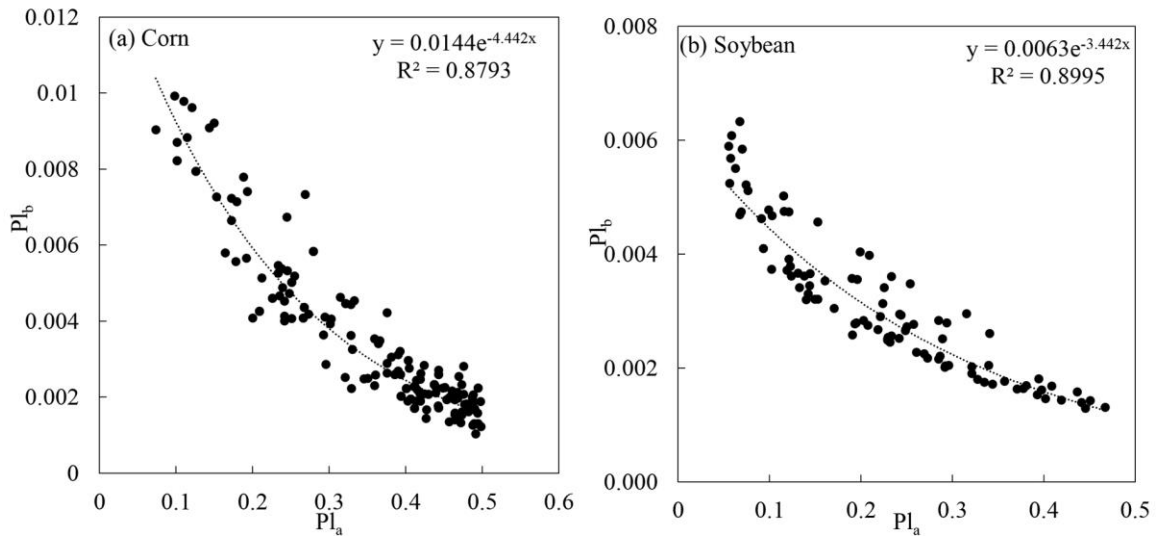


Figure 5-7: Relationship between Pl_a and Pl_b for (a) corn and (b) soybean

$$\begin{cases} Pl_b = 0.0144 \times e^{-4.442 \times Pl_a} & \text{Corn} \\ Pl_b = 0.0063 \times e^{-3.442 \times Pl_a} & \text{Soybean} \end{cases} \quad (5-21)$$

On the second phase, the crop-specific parameters obtained on the first phase were fixed, and the ELUE was optimized for each pixel and the biomass was estimated at the same time.

Table 5-6: The twelve SAFY parameters

Parameter name	Notation	Unit	Range	Corn	Soybean	Source
Fixed parameters						
Climatic efficiency	ε_c	-		0.48	0.48	Literature (Battude et al., 2016; Britton & Dodd, 1976; Claverie et al., 2012; Varlet-Grancher et al., 1982)
Temperature for growth	$T_{min}, T_{opt}, T_{max}$	°C		[8, 30, 35]	[10, 30, 35]	Literature (Battude et al., 2016; Claverie et al., 2012; Qian et al., 2010)
Polynomial degree	β	-		2	2	Literature (c Claverie et al. 2012)
Initial dry above ground mass	DAM ₀	g/m ²		4.2	4.2	Literature (Claverie et al., 2012; Dong et al., 2017)
Light-interception coefficient	k_{ext}			0.65	0.65	in situ measurements
Phenology-related parameters						
The day of emergence	D_0	DOY				SOS derived from the improved TSF model
Sum of temperature for senescence	Stt	°C				SOS, DOS and daily mean temperature
Rate of Senescence	Rs	°C day	[0-10 ⁵]	Linked to Stt and EOS	Linked to Stt and EOS	SOS, DOS, EOS and daily mean temperature (Battude et al. 2016)
Optimized parameters using remotely sensed GLAI						
Specific leaf area	SLA	M ² .g-1	[0.02-0.032]	0.0245	0.027	First phase of calibration
Partition to leaf function: par a	Pl_a	-	[0.05-0.5]	0.5	0.19	First phase of calibration
Partition to leaf function: par b	Pl_b	-	[10 ⁻⁵ -10 ⁻²]	Linked to Pl_a	Linked to Pl_a	Linked to Pl_a
Effective light use efficiency	ELUE	g/MJ	Corn [2-5], soybean [0.5-2]	Pixel specific	Pixel specific	Second phase of calibration

5.4 Results

5.4.1 Evaluation of fitted $fAPAR$ based on the CSDM

As the CSDM is optimized by the remotely sensed $fAPAR$, the accuracy of the fitted $fAPAR$ depends on the accuracy of the data fusion. Figure 5-8 shows that the fitted $fAPAR$ based on the CSDM agrees perfectly with the $fAPAR$ derived from the original Landsat-8 images and the synthetic Landsat-like images at different sample sites. However, the simulated $fAPAR$ is slightly underestimated compared with the in situ measured $fAPAR$.

The three cloud-free Landsat images were acquired at the beginning of the season, the time before the maximum $fAPAR$ and in the senescence stage. The three observations are not sufficient for optimizing the CSDM, but the synthetic images provided important observations (e.g. $fAPAR_{max}$) between the DOY 209 and DOY 257 in characterizing the time course of the $fAPAR$. The $fAPAR$ obtained from the synthetic Landsat data also agrees with the field measured $fAPAR$ at the vegetative stage (Figure 5-8). It indicates that the STVIFM has a great potential in spatio-temporal NDVI fusion for crops, and the CSDM, optimized by sufficient remotely sensed $fAPAR$, has a great potential in daily $fAPAR$ simulation.

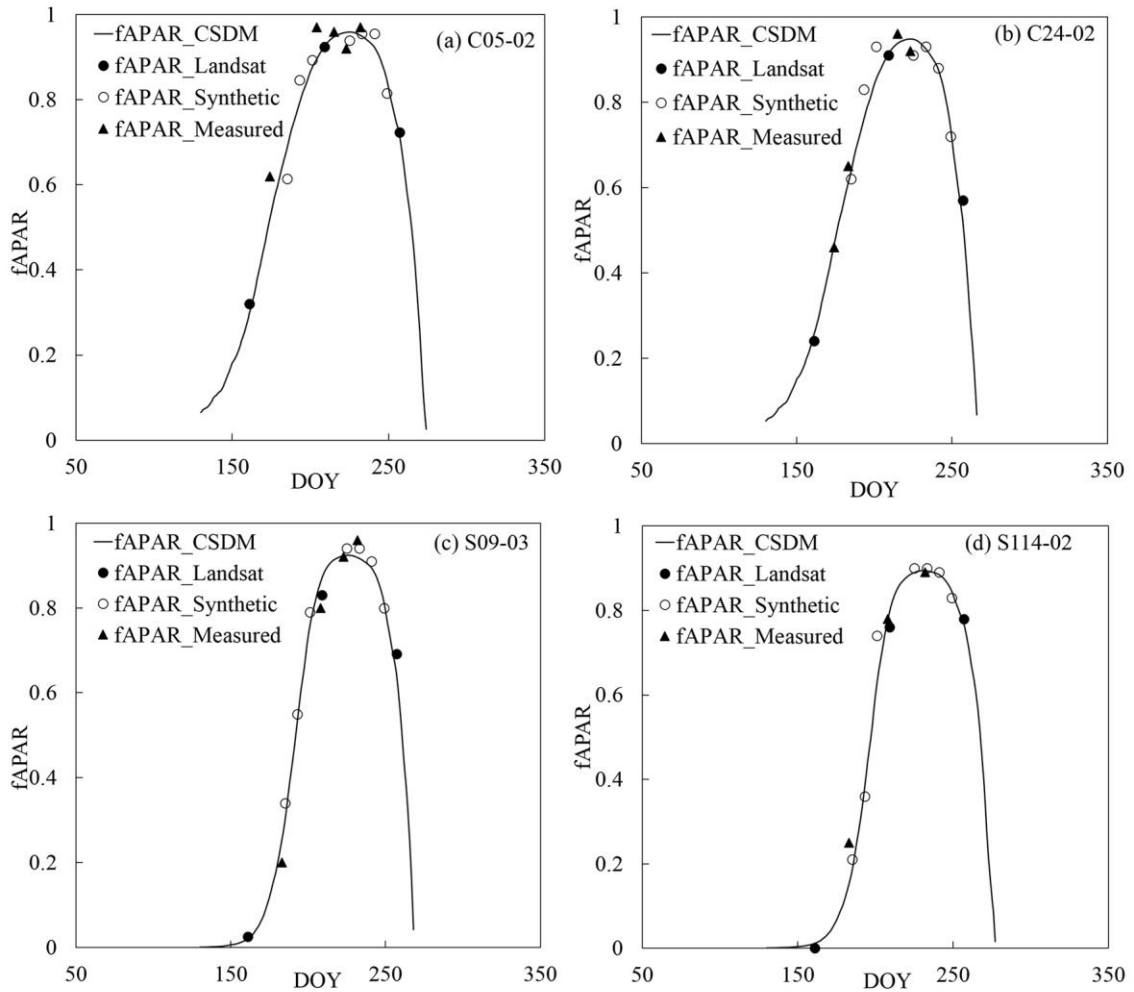


Figure 5-8: Comparison of the $fAPAR$ derived from the remotely sensed images, fitted by the CSDM, and measured in the field for different sample sites: (a) C05-02; (b) C24-02; (c) S09-03; (d) S114-02.

5.4.2 Verification of detected phenology with ground-based observations

Figure 5-9 shows the comparison of phenological dates between ground-based observations and the remotely sensed estimations for corn and soybean throughout the entire growing season. Most of the detected phenological dates are within an error of 5 days with corn (RMSE=3.3 days) showing a lower accuracy than soybean (RMSE =2.7 days). Larger errors are mainly found at the beginning of the growth for soybean.

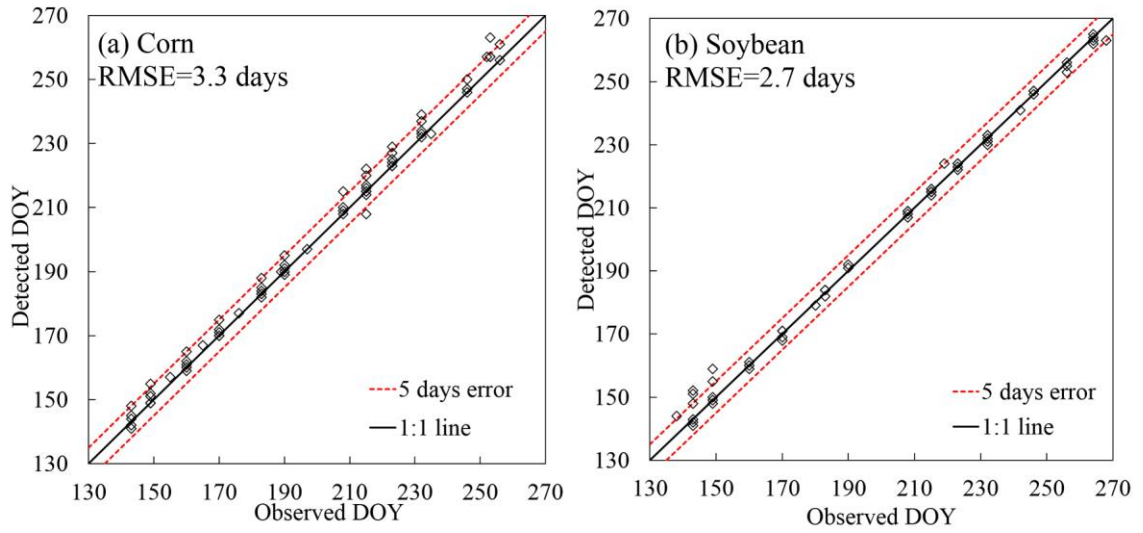


Figure 5-9: Comparison of phenological dates between the ground-based observations and estimations, (a) corn, (b) soybean

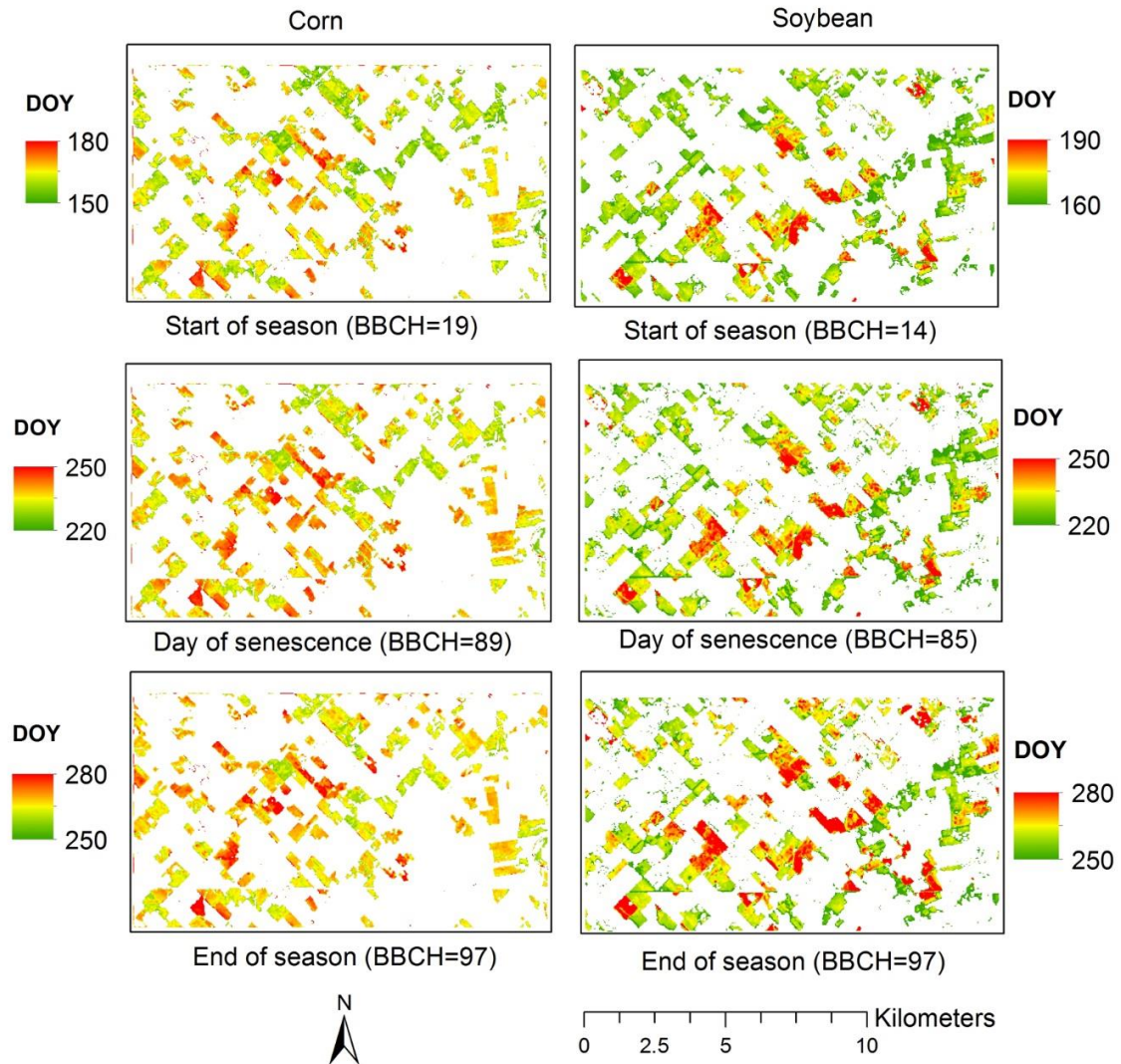


Figure 5-10: The spatial patterns of the dates of key phenological events (SOS, DOS, EOS) in the study area in 2015

The dates of the three key phenological events (SOS, DOS, EOS) of corn and soybean were mapped for the study area. Figure 5-10 shows that the range of phenology difference within the study area is about 0 to 30 days. A few corn and soybean fields show relatively late phenological dates. This is probably caused by the late seeding activities.

5.4.3 Performance of the SAFY model

5.4.3.1 Analysis of the pixel-based ELUE

The SAFY model is able to obtain the pixel-based ELUE in the final calibration step. In this study, the ELUE maps were generated for corn and soybean with the estimated biomass (Figure 5-11). The mean ELUE is 3.53 g/m^2 for corn and 1.22 g/m^2 for soybean. Due to the speckle noise of the polarimetric SAR data, the pixels with very low ELUE values at the field boundaries are most likely to be misclassifications. While other pixels with low ELUE values in the fields may be caused by low plant density or stressed growth condition.

Strong correlations were observed between the ELUE and $fAPAR_{max}$ of the daily $fAPAR$ fitted by the CSDM for corn ($R^2=0.91$), and soybean ($R^2=0.96$) (Figure 5-12). Thus, the ELUE for corn and soybean can be easily computed from the $fAPAR_{max}$, and the simple LUE model can be used directly for biomass estimation.

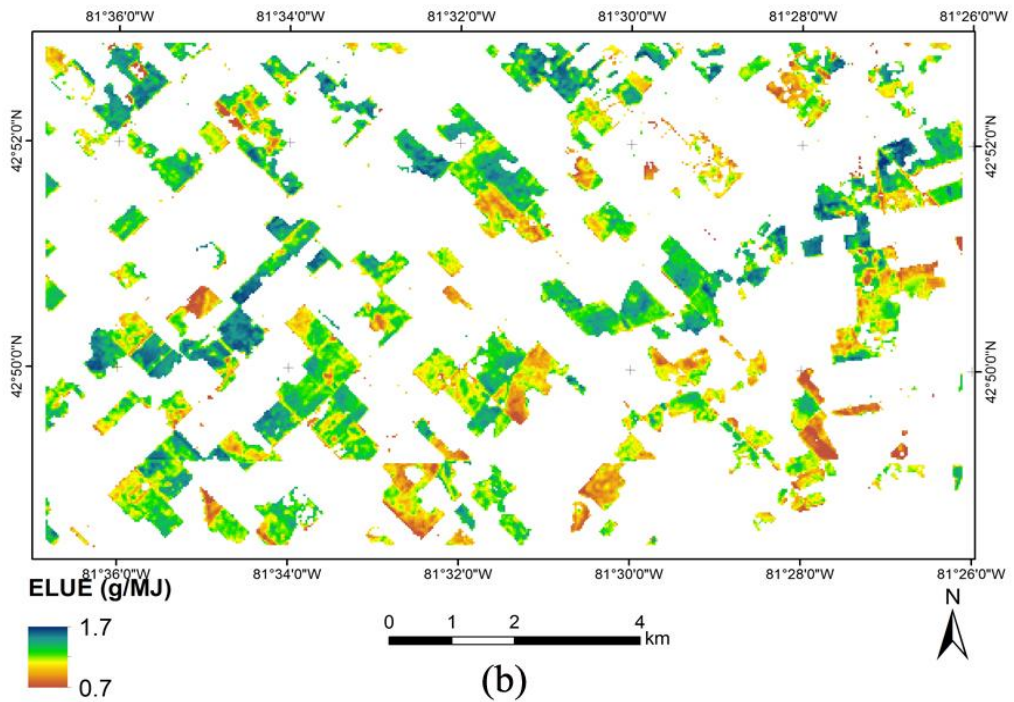
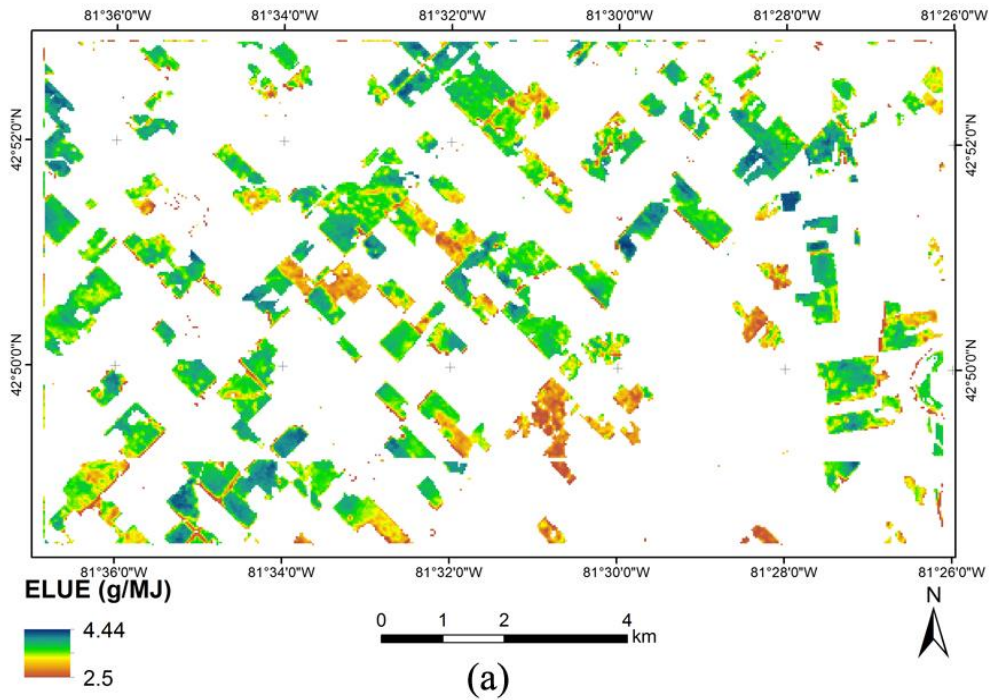


Figure 5-11: Pixel-based ELUE for (a) corn and (b) soybean generated from the SAFY

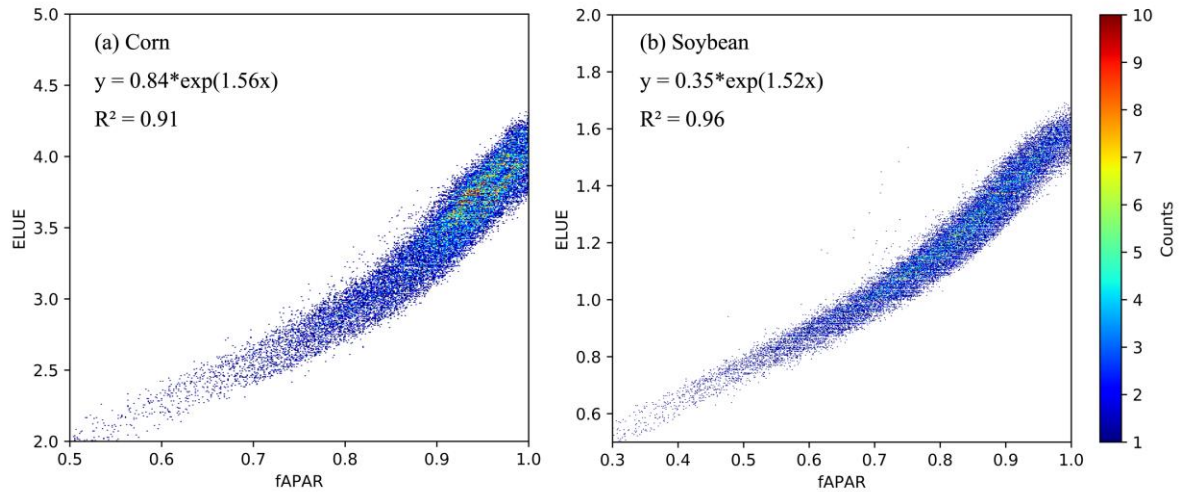


Figure 5-12: Scatter plots showing the relationship between the ELUE derived from SAFY and $fAPAR_{max}$ derived from the CSDM: (a) corn, (b) soybean

5.4.3.2 Evaluation of GLAI simulation

To evaluate the performance of the SAFY model, the GLAI values simulated by the SAFY were compared with the GLAI derived from the remotely sensed images and the in situ measured GLAI for two corn sites (C05-02, C24-02) and two soybean sites (S09-03, S114-02). As illustrated in Figure 5-13, the GLAI simulated by the SAFY model shows good agreements with the GLAI derived from the remote sensing images and the measured GLAI at the vegetative stage and the senescence stage. Discrepancies mainly exist at the peak GLAI stage, especially for corn, and the simulated GLAI is generally underestimated. As the photos were taken upward facing using the fisheye camera in the reproductive stage for corn, the in situ measured GLAI was not able to be obtained due to the difficulties in classification between green leaves and the yellow leaves. For sample site C05-02, the GLAI values derived from the synthetic Landsat images are slightly underestimated when compared with the field-measured GLAI, but the GLAI simulated by the SAFY show good agreements with the measured GLAI. This suggests that forcing the phenology information into the SAFY model is able to reduce the bias caused by the remotely sensed GLAI.

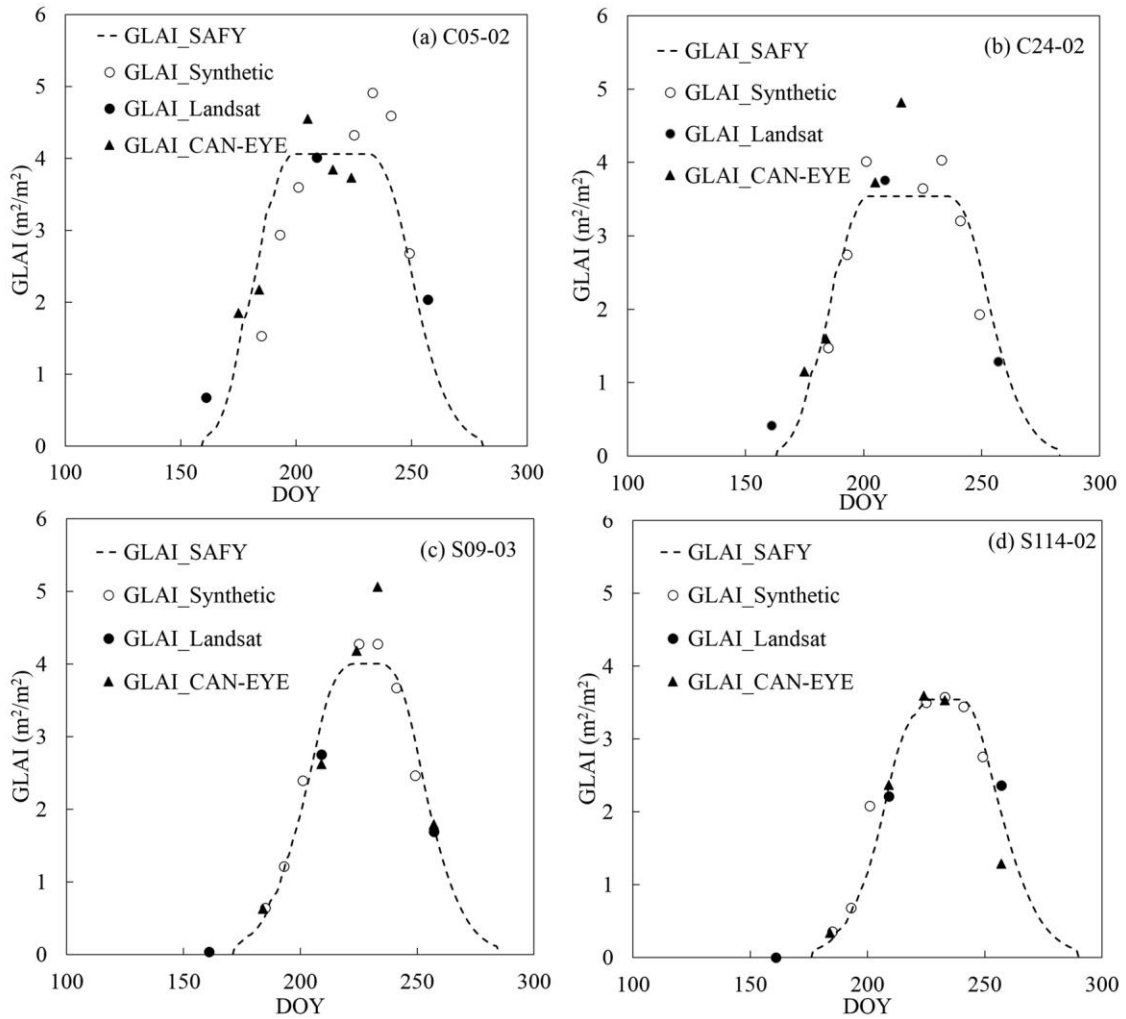


Figure 5-13: Comparison of GLAI simulated by the SAFY (GLAI_SAFY), the remotely sensed GLAI based on the original Landsat data (GLAI_Landsat), and the synthetic GLAI (GLAI_Synthetic) and the in situ measured GLAI (GLAI_CAN-EYE) for sample site (a) C05-02, (b) C24-02, (c) S09-03, (d) S114-02.

5.4.3.3 Evaluation of DAM estimation

Figure 5-14 illustrates the biomass map of corn and soybean generated by SAFY. The biomass varies not only among different fields but also within each field. The biomass of corn ranges from 1000 g/m² to 3131 g/m², with a mean value of 2128.16 g/m². The biomass for soybean ranges from 100 g/m² to 1003 g/m², with a mean value of 564.58 g/m². A few fields show extremely low biomass estimations. It is likely that they have lower plant density or have a shorter growing season due to the late sowing date.

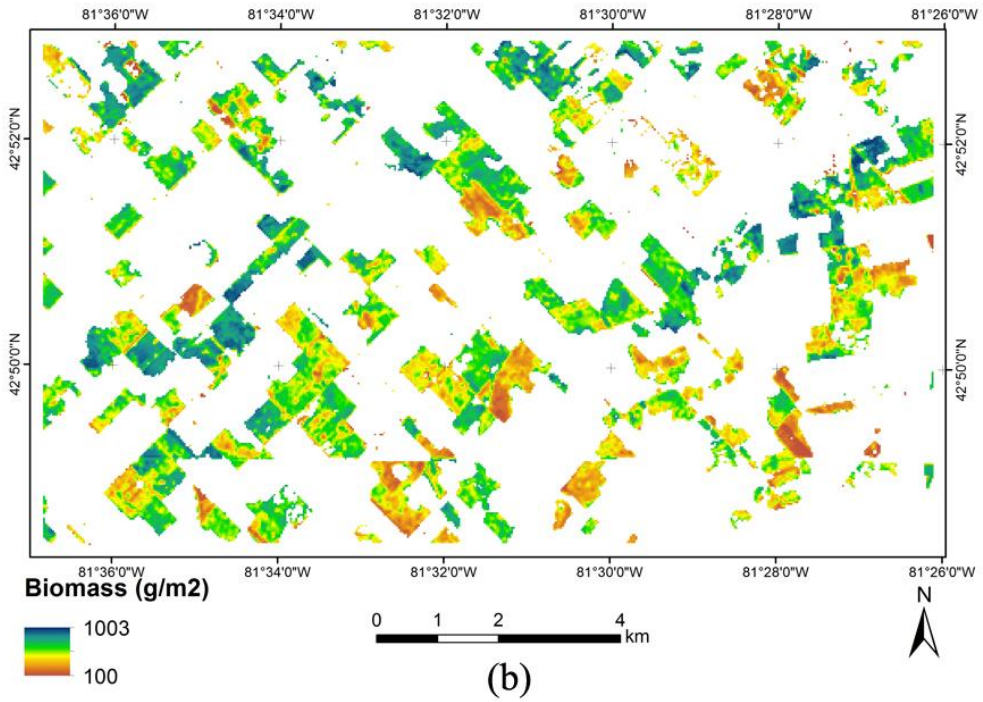
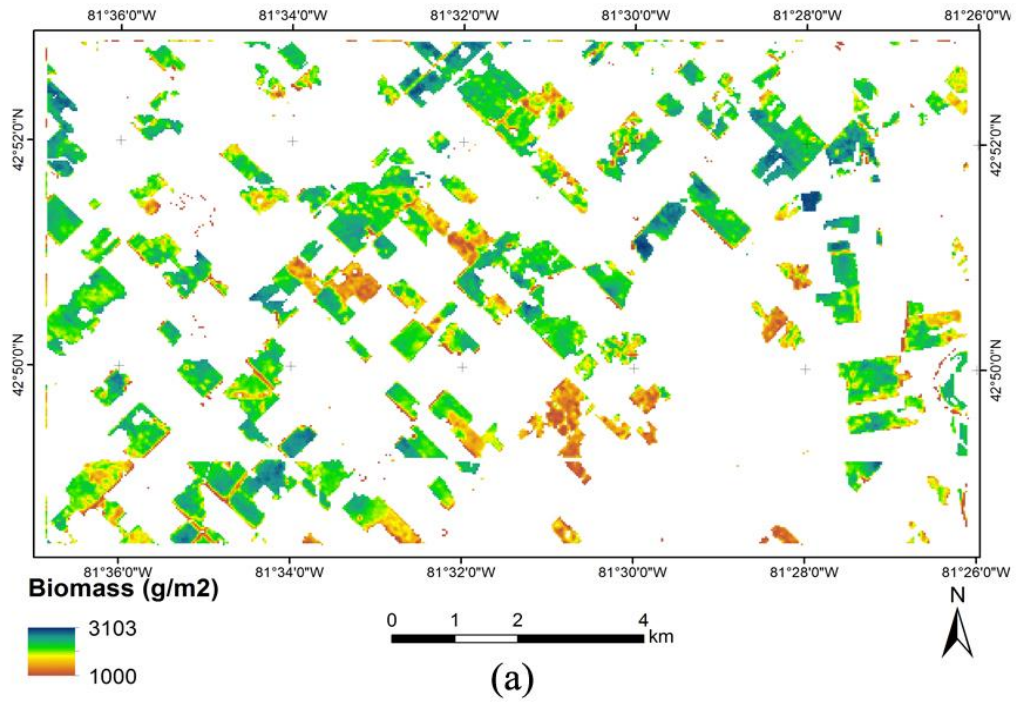


Figure 5-14: Spatial map of estimated total biomass using the SAFY model for (a) corn and (b) soybean

The estimated annual DAM values were compared with the destructive DAM measurements collected in three soybean fields and four corn fields. A total of 17 soybean measurements and 15 corn measurements collected at the end of the growing season were used for the evaluation. As comparisons, the DAM estimated by the SAFY model with no phenology information as input, the DAM estimated by the CSDM-LUE with fixed ELUE and the DAM estimated by the CSDM with varied ELUE were also compared with the in situ measurements. The accuracy of each method were listed in Table 5-7.

The results show that the SAFY model, after the calibration using the remotely sensed GLAI, is able to estimate the field-scale biomass for corn and soybean. . The accuracy of biomass estimation is higher for corn ($R^2=0.92$, RRMSE=5.91%) than for soybean ($R^2=0.49$, RRMSE: 18.29%) (Figure 5-15). This is likely due to fallen leaves for some soybean sample at the end of growing season. The result simulated by the SAFY without the phenology information shows a lower accuracy for both corn ($R^2=0.76$, RMSE=245.41 g/m^2 , RRMSE=9.82%) and soybean ($R^2=0.35$, RMSE=146.73 g/m^2 , RRMSE=22.32%).

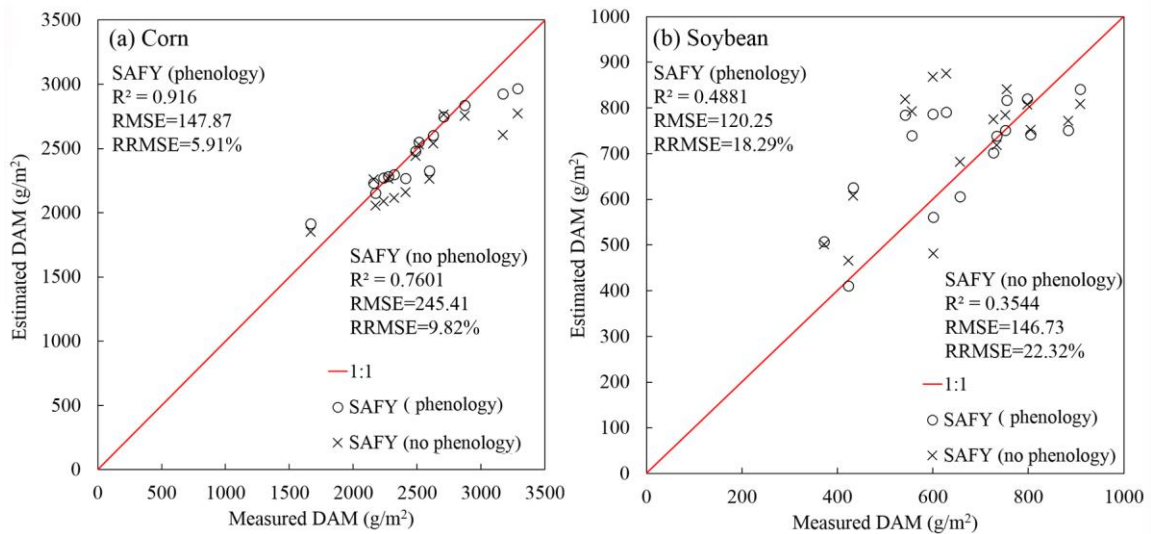


Figure 5-15: Comparison between measured biomass and the estimated biomass by the SAFY with and without forcing the phenology information for (a) corn, (b) soybean

In the traditional method, the ELUE was set as a fixed value for each crop type. As the pixel-based ELUE can be obtained from the $fAPAR$ data, the CSDM-LUE model can be

improved by addressing the spatial difference of the ELUE. In this study, the CSDM-LUE model with both fixed ELUE (the mean ELUE generated from the SAFY model) and varied ELUE (calculated from the $fAPAR_{max}$) was also performed for comparisons. The accuracy of the CSDM-LUE with varied ELUE (Corn: $R^2=0.82$, $RMSE=230.57$ g/m^2 , $RRMSE=9.22\%$; Soybean: $R^2=0.47$, $RMSE=123.88$ g/m^2 , $RRMSE=18.84\%$) is lower than the accuracy of SAFY, but is higher than the accuracy of the CSDM-LUE with fixed ELUE (Corn: $R^2=0.80$, $RMSE=357.64$ g/m^2 , $RRMSE=14.31\%$; Soybean: $R^2=0.39$, $RMSE=141.48$ g/m^2 , $RRMSE=21.52\%$) (Figure 5-16).

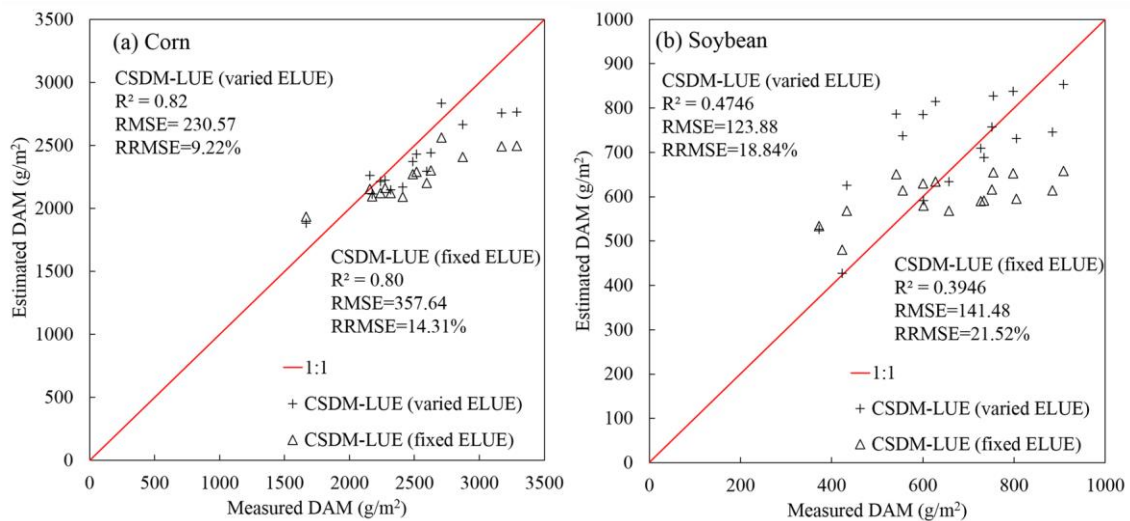


Figure 5-16: Comparison between measured biomass and estimated biomass by the CSDM-LUE model for (a) corn, (b) soybean

Table 5-7: The accuracy of the biomass estimation using different strategies

	Corn				Soybean			
	SAFY (phenology)	SAFY (No phenology)	CSDM-LUE (varied ELUE)	CSDM-LUE (fixed ELUE)	SAFY (phenology)	SAFY (No phenology)	CSDM-LUE (varied ELUE)	CSDM-LUE (fixed ELUE)
R^2	0.92	0.76	0.82	0.80	0.49	0.35	0.47	0.39
RMSE (g/m^2)	147.87	245.41	230.57	357.64	120.25	146.73	123.88	141.48
RRMSE (%)	5.91	9.82	9.22	14.31	18.29	22.32	18.84	21.52

5.4.3.4 Evaluation of crop yield

The ratio between the yield and in situ measured final DAM was calculated for corn and soybean. The ratio is 0.55 for corn and 0.58 for soybean, and they are used as the HI values. The obtained HI for corn agrees with the HI found in the literature (Battude et al. 2016). But the HI for soybean is higher than the HI found in the literature (0.54 and 0.50) (Spaeth et al. 1984). This is probably because that most of soybean leaves were fallen at the end of growing season. The crop yield was estimated using the two HI values, and it was compared with the field measurements (Figure 5-17). The overall RMSE is 116.98 g/m², and the RMSE is 146.34 g/m² for corn and 82.86 g/m² for soybean.

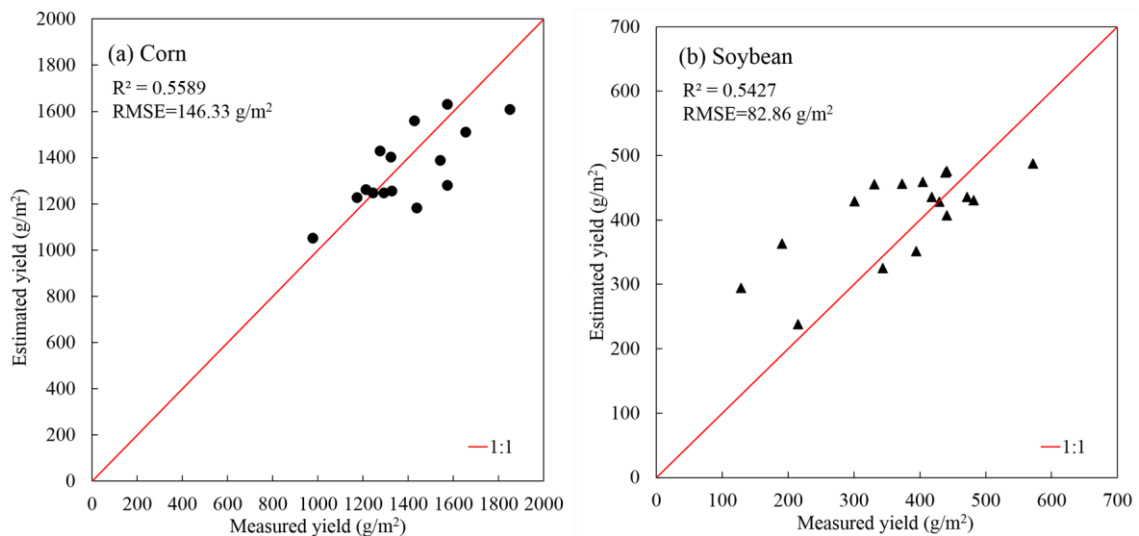


Figure 5-17: Comparison between measured and estimated yield for (a) corn and (b) soybean

5.5 Discussion

5.5.1 Factors that affect the crop biomass and yield

As the crop yield is closely related to crop biomass, the factors that affect crop biomass also affect crop yield. According to the LUE model, the biomass is affected by ELUE and APAR. ELUE is affected by LUE_{max} and all environmental stresses except temperature, such as nitrogen stress and water stress. By using the satellite remote sensing data, the plant density also matters as the spatial resolution is between meters to hundreds of meters. All of these stresses or plant density will finally affect the GLAI or $fAPAR$ of the crops in one

pixel. In this study, strong correlations were found between the ELUE and the maximum $fAPAR$ of each pixel during the growing season for corn and soybean respectively. Therefore, the pixel-based ELUE can be calculated from the daily $fAPAR$ fitted by the CSDM using remote sensing images if no remote sensing image was obtained at the peak $fAPAR$ stage.

APAR is affected by $fAPAR$ and PAR. As the $fAPAR$ is linearly correlated with NDVI, the $fAPAR$ is also related to the crop growth status (vegetation cover, chlorophyll content, etc.). Generally, the spatial variation of PAR is less for a local area, but the temporal variation of PAR significantly affect the APAR and accordingly the biomass. This temporal variation is caused by the variation of phenological events as well as the variation of LOS. By comparing the phenology map and the biomass map, the pixels that have a later phenological dates have a lower biomass, even though they have similar LOS (LOS=EOS-SOS). This is probably because the maximum shortwave solar radiation is between the end of May and the end of June (Figure 5-2). Therefore, the crops which were grown before the end of May received more PAR than crops which were grown later.

5.5.2 Uncertainties of the estimated crop biomass and yield

In this study, only three cloud-free high spatial resolution remote sensing images were acquired. To estimate crop biomass, daily LAI or $fAPAR$ is generally needed. The CSDM shows a great potential in simulating daily $fAPAR$ by using daily temperature. As there are 5 parameters in the CSDM, at least five remotely sensed values are needed to optimize it. Therefore, the spatio-temporal data fusion method STVIFM was adopted to generate more Landsat-like images using the three Landsat and the MODIS image pairs. The daily $fAPAR$ is able to be used for phenology detection for the SAFY model, and calculate ELUE directly for the simple LUE model, and itself is a parameter in the simple LUE model. Even though a good accuracy was achieved to estimate corn and soybean biomass, uncertainties still exist, especially in the fields with very low biomass production, because of the following aspects: (1) the discrepancy between the actual NDVI and the synthetic NDVI using the STVIFM; (2) the discrepancy between the actual $fAPAR$ and the fitted $fAPAR$ based on the CSDM approach; (3) the discrepancy between the actual LAI and the remotely

sensed LAI; (4) the errors of the crop classification; (5) the bias of the harvest index; (6) the limitations of the SAFY model.

Specifically, larger discrepancy may exist at the peak NDVI stage, and when the two adjacent Landsat images before and after this date are acquired far from this date. The remotely sensed $fAPAR$ which was calculated from NDVI through a linear regression method, and the daily $fAPAR$ which was fitted based on the CSDM and the remotely sensed $fAPAR$, may have discrepancy compared with the actual $fAPAR$. The first two discrepancies may be cancelled off to some degree. The LAI is calculated from the $fAPAR$ through the Beer's law, which may cause discrepancy compared to the actual LAI. The crop classification result has a high overall and producer's and user's accuracy, but a small part of pixels were still misclassified, especially at the boundaries of the crop fields. The D_0 in the SAFY model is not exactly the day of emergence observed in the field work. This may be caused by the assumption that the ELUE is fixed through the entire growing season. In fact, the ELUE may vary at different growing stages (Battude et al., 2016). This constant assumption leads to the bias of D_0 , Δ_{DAM} , and accordingly the bias of Δ_{LAI}^+ and maximum GLAI. In order to generate the ELUE map, which can be regarded as the mean ELUE through the whole season for each pixel, we did not consider the temporal variation of ELUE in this study.

5.5.3 Application of this study in crop production forecasting

This framework is also able to predict crop production by using empirical values for parameters and adjust these parameters by adding the real-time remote sensing observations. For example, for the phenology detection, the shape model defined for the previous year can be used as an initial shape model, and the remotely sensed $fAPAR$ obtained at the early stage (at least one observation) can be used to optimize the scaling parameter $xshift_1$, and the other two scaling parameters can be fixed using empirical values. Therefore the real-time SOS can be obtained. Then the real-time SOS and the empirical DOS and EOS can be forced into the SAFY model, and the initial pixel-specific ELUE can be calibrated by the acquired remote sensing GLAI (at least one observation). This process can be repeated and the pixel-specific parameters can be updated once new remotely sensed observations are acquired. Therefore the crop production can be forecasted using the

remote sensing observations acquired at the early stage and adjusted using new remote sensing observations.

5.5.4 Contributions and limitations of this study

The phenology information is significant to the SAFY model. The parameters that are related to crop phenology are D_0 , Stt , Rs . Accurate detection of crop phenology is important to the biomass estimation using the SAFY model. The improved two-step filtering approach defined the shape models, the time courses of $fAPAR$ generated by CSDM with the phenological dates observed in the field work, for corn and soybean, and then detect the phenological dates for each pixel using the shape models. By using empirical values, forcing the phenology information into the SAFY, and analyzing the relationships between different parameters in the SAFY, the number of free parameters can be reduced, and the efficiency of the SAFY model will be improved accordingly. The contributions of this study include: (1) an improved phenology detection approach was developed, and a subfield scale crop phenology map can be produced; (2) a guidance was provided in parameters determination when complementing the SAFY model for corn and soybean yield estimation in southwestern Ontario and the biomass and yield can be estimated accurately at a subfield scale; (3) good correlations were found between ELUE and $fAPAR_{max}$ for corn and soybean, so that the simple LUE model can be performed directly. The accuracy of the LUE model was improved after the spatial variation of ELUE was addressed. This study can be applied to crop production forecasting and it will be tested in the future.

The application of this framework would be limited if only two high spatial resolution images were acquired at the growing stage and the senescent stage respectively. Thus the fusion results would be inaccurate and the accuracy of the following procedure would be affected. We recommend that at least three images acquired at the growing, senescence, and peak stages and at least five MODIS images are needed. The relationship between ELUE and $fAPAR_{max}$ may vary with the study areas and the remotely sensed datasets. As the pixel-based optimization procedure is time consuming, this framework is more applicable for local-scale or field-scale phenology detection and biomass estimation.

5.6 Conclusions

In this study, we improved the TSF method to detect crop phenology and estimated biomass and yield for corn and soybean at subfield scale based on the SAFY model using the spatio-temporal fusion of three Landsat-8 images and 10 MODIS images. The results show that the spatio-temporal vegetation index image fusion method has a great potential in generating high spatial resolution images and interpolating temporal NDVI changes for crops during the growing season. The high spatial resolution of the fusion products are able to capture crop growth variability within the fields, and determine the parameters in a crop growth model. The improved two-step filtering approach, by the integration of the CSDM, shows a good ability in simulating daily $fAPAR$ and detecting crop phenology at pixel scale with an RMSE less than 5 days. The SAFY model, calibrated by the remotely sensed GLAI, shows a good performance in pixel-based GLAI simulation and biomass estimation. The accuracy of biomass estimation was improved by about 4% in RRMSE for corn and soybean by forcing the phenological information derived from remote sensing images. In addition, the SAFY model is able to obtain the ELUE for each pixel though the calibration and good correlations were found between ELUE and $fAPAR_{max}$. Therefore, the ELUE can be estimated from the $fAPAR_{max}$ and used for CSDM-LUE model.

References

- Atkinson, P. M., Jeganathan, C., Dash, J., & Atzberger, C. (2012). Inter-comparison of four models for smoothing satellite sensor time-series data to estimate vegetation phenology. *Remote Sensing of Environment*, *123*, 400–417. <http://doi.org/10.1016/j.rse.2012.04.001>
- Bastiaanssen, W. G. M., & Ali, S. (2003). A new crop yield forecasting model based on satellite measurements applied across the Indus Basin, Pakistan. *Agriculture, Ecosystems and Environment*, *94*, 321–340. [http://doi.org/10.1016/S0167-8809\(02\)00034-8](http://doi.org/10.1016/S0167-8809(02)00034-8)
- Battude, M., Al Bitar, A., Morin, D., Cros, J., Huc, M., Marais Sicre, C., Demarez, V. (2016). Estimating maize biomass and yield over large areas using high spatial and temporal resolution Sentinel-2 like remote sensing data. *Remote Sensing of Environment*, *184*, 668–681. <http://doi.org/10.1016/j.rse.2016.07.030>
- Beck, P. S. A., Atzberger, C., Høgda, K. A., Johansen, B., & Skidmore, A. K. (2006). Improved monitoring of vegetation dynamics at very high latitudes: A new method using MODIS NDVI. *Remote Sensing of Environment*, *100*(3), 321–334. <http://doi.org/10.1016/j.rse.2005.10.021>
- Betbeder, J., Fieuzal, R., & Baup, F. (2016). Assimilation of LAI and dry biomass data from optical and SAR images into an agro-meteorological model to estimate soybean yield. *IEEE Journal of Selected Topics in Applied Earth Observations and Remote Sensing*, *9*(6), 2540–2553. <http://doi.org/10.1109/JSTARS.2016.2541169>
- Bradford, J. B., Hicke, J. A., & Lauenroth, W. K. (2005). The relative importance of light-use efficiency modifications from environmental conditions and cultivation for estimation of large-scale net primary productivity. *Remote Sensing of Environment*, *96*(2), 246–255. <http://doi.org/10.1016/j.rse.2005.02.013>
- Brisson, N., Gary, C., Justes, E., Roche, R., Mary, B., Ripoche, D., Sinoquet, H. (2003). An overview of the crop model stics. *European Journal of Agronomy*, *18*(3), 309–332. [http://doi.org/https://doi.org/10.1016/S1161-0301\(02\)00110-7](http://doi.org/https://doi.org/10.1016/S1161-0301(02)00110-7)
- Britton, C. M., & Dodd, J. D. (1976). Relationships of photosynthetically active radiation and shortwave irradiance. *Agricultural Meteorology*, *17*, 1–7.

- Chen, J., Jönsson, P., Tamura, M., Gu, Z., Matsushita, B., & Eklundh, L. (2004). A simple method for reconstructing a high-quality NDVI time-series data set based on the Savitzky-Golay filter. *Remote Sensing of Environment*, *91*(3–4), 332–344. <http://doi.org/10.1016/j.rse.2004.03.014>
- Cheng, Z., Meng, J., & Wang, Y. (2016). Improving spring maize yield estimation at field scale by assimilating time-series HJ-1 CCD data into the WOFOST model using a new method with fast algorithms. *Remote Sensing*, *8*(4), 1–22. <http://doi.org/10.3390/rs8040303>
- Claverie, M., Demarez, V., Duchemin, B., Hagolle, O., Ducrot, D., Marais-sicre, C., ... Dedieu, G. (2012). Maize and sun flower biomass estimation in southwest France using high spatial and temporal resolution remote sensing data. *Remote Sensing of Environment*, *124*, 844–857. <http://doi.org/10.1016/j.rse.2012.04.005>
- Daughtry, C. S. T., Gallo, K. P., Goward, S. N., Prince, S. D., & Kustas, W. P. (1992). Spectral estimates of absorbed radiation and phytomass production in corn and soybean canopies. *Remote Sensing of Environment*, *39*, 141–152.
- Dong, T., Liu, J., Qian, B., Jing, Q., Croft, H., Chen, J., Chen, P. (2017). Deriving maximum light use efficiency from crop growth model and satellite data to improve crop biomass estimation. *IEEE Journal of Selected Topics in Applied Earth Observations and Remote Sensing*, *10*(1), 104–117. <http://doi.org/10.1109/JSTARS.2016.2605303>
- Dong, T., Liu, J., Qian, B., Zhao, T., Jing, Q., Geng, X., Shang, J. (2016). Estimating winter wheat biomass by assimilating leaf area index derived from fusion of Landsat-8 and MODIS data. *International Journal of Applied Earth Observation and Geoinformation*, *49*, 63–74. <http://doi.org/10.1016/j.jag.2016.02.001>
- Duan, Q., Sorooshian, S., & Gupta, V. K. (1994). Optimal use of the SCE-UA global optimization method for calibrating watershed models. *Journal of Hydrology*, *158*(3–4), 265–284. [http://doi.org/10.1016/0022-1694\(94\)90057-4](http://doi.org/10.1016/0022-1694(94)90057-4)
- Duchemin, B., Maisongrande, P., Boulet, G., & Benhadj, I. (2008). A simple algorithm for yield estimates: Evaluation for semi-arid irrigated winter wheat monitored with green leaf area index. *Environmental Modelling and Software*, *23*(7), 876–892. <http://doi.org/10.1016/j.envsoft.2007.10.003>

- Dyke, P. T., Kiniry, J. R., & Jones, C. A. (1986). CERES-Maize: a simulation model of maize growth and development. College Station: Texas A&M University Press. Retrieved from file://catalog.hathitrust.org/Record/000810137
- Gallo, K. P., Daughtry, C. S. T., & Wiegand, C. L. (1993). Errors in measuring absorbed radiation and computing crop radiation use efficiency. *Agronomy Journal*.
- Gao, F., Masek, J., Schwaller, M., & Hall, F. (2006). On the blending of the MODIS and Landsat ETM + surface reflectance. *IEEE Transactions on Geoscience and Remote Sensing*, 44(8), 2207–2218.
- Hird, J. N., & McDermid, G. J. (2009). Noise reduction of NDVI time series: An empirical comparison of selected techniques. *Remote Sensing of Environment*, 113(1), 248–258. <http://doi.org/10.1016/j.rse.2008.09.003>
- Jeong, S. J., Ho, C. H., Gim, H. J., & Brown, M. E. (2011). Phenology shifts at start vs. end of growing season in temperate vegetation over the Northern Hemisphere for the period 1982-2008. *Global Change Biology*, 17(7), 2385–2399. <http://doi.org/10.1111/j.1365-2486.2011.02397>.
- Jorge, P., Ponte, D. O., Ribeiro, A., & José, E. (2009). Solar radiation use efficiency by soybean under field conditions in the Amazon region, (1), 1211–1218.
- Koetz, B., Baret, F., Poilvé, H., & Hill, J. (2005). Use of coupled canopy structure dynamic and radiative transfer models to estimate biophysical canopy characteristics. *Remote Sensing of Environment*, 95(1), 115–124. <http://doi.org/10.1016/j.rse.2004.11.017>
- Kross, A., Seaquist, J. W., & Roulet, N. T. (2016). Light use efficiency of peatlands: Variability and suitability for modeling ecosystem production. *Remote Sensing of Environment*, 183, 239–249. <http://doi.org/10.1016/j.rse.2016.05.004>
- Kuwata, K., & Shibasaki, R. (2016). Estimating corn yield in the united states with modis EVI and machine learning methods. *ISPRS Annals of Photogrammetry, Remote Sensing and Spatial Information Sciences*, III-8(July), 131–136. <http://doi.org/10.5194/isprsannals-III-8-131-2016>
- Liao, C., Wang, J., Huang, X., & Shang, J. (2018). Contribution of minimum noise fraction transformation of multi-temporal RADARSAT-2 polarimetric SAR data

- to cropland classification. *Canadian Journal of Remote Sensing*.
<http://doi.org/10.1080/07038992.2018.1481737>
- Liao, C., Wang, J., Pritchard, I., Liu, J., & Shang, J. (2017). A spatio-temporal data fusion model for generating NDVI time series in heterogeneous regions. *Remote Sensing*, 9(11), 1–28. <http://doi.org/10.3390/rs9111125>
- Lindquist, J. L., Arkebauer, T. J., Walters, D. T., Cassman, K. G., & Dobermann, A. (2005). Maize Radiation Use Efficiency under Optimal Growth Conditions. *Agronomy Journal*, 97, 72–78. <http://doi.org/10.2134/agronj2005.0072>
- Liu, J., Pattey, E., Miller, J. R., McNairn, H., Smith, A., & Hu, B. (2010). Estimating crop stresses, aboveground dry biomass and yield of corn using multi-temporal optical data combined with a radiation use efficiency model. *Remote Sensing of Environment*, 114(6), 1167–1177. <http://doi.org/10.1016/j.rse.2010.01.004>
- Maas, S. J. (1990). Parameterized model of gramineous crop growth. I. Leaf area and dry mass simulation. *Agronomy Journal (USA)*.
- Marshall, M., & Thenkabail, P. (2015). Developing in situ non-destructive estimates of crop biomass to address issues of scale in remote sensing. *Remote Sensing*, 7(1), 808–835. <http://doi.org/10.3390/rs70100808>
- Monteith, J. L. (1972). Solar radiation and productivity in tropical ecosystems. *Journal Of Applied Ecology*. <http://doi.org/10.2307/2401901>
- Monteith, J. L. (1977). Climate and the efficiency of crop production in Britain. *Philosophical Transactions of the Royal Society of London. Series B: Biological Sciences*, 281, 277–294.
- Paruelo, J. M., Lauenroth, W. K., Roset, P. A., Journal, S., Mar, N., Paruelo, J. M., Roset, P. A. (2000). Estimating Aboveground Plant Biomass Using a Photographic Technique. *Journal of Range Management*, 53(2), 190–193.
- Pierozan Junior, C., & Kawakami, J. (2013). Efficiency of the leaf disc method for estimating the leaf area index of soybean plants. *Acta Scientiarum. Agronomy*, 35(4), 487–493. <http://doi.org/10.4025/actasciagron.v35i4.16290>
- Potter, C. S., Randerson, J. T., Field, C. B., Matson, P. A., Vitousek, P. M., Mooney, H. A., & Klooster, S. A. (1993). Terrestrial ecosystem production: A process model

- based on global satellite and surface data. *Global Biogeochemical Cycles*, 7(4), 811–841. <http://doi.org/http://dx.doi.org/10.1029/93GB02725>
- Qian, B., Zhang, X., Chen, K., Feng, Y., & O'Brien, T. (2010). Observed long-term trends for agroclimatic conditions in Canada. *Journal of Applied Meteorology and Climatology*, 49(4), 604–618. <http://doi.org/10.1175/2009JAMC2275.1>
- Rienecker, M. M., Suarez, M. J., Gelaro, R., Todling, R., Bacmeister, J., Liu, E., Woollen, J. (2011). MERRA: NASA's modern-era retrospective analysis for research and applications. *Journal of Climate*, 24(14), 3624–3648. <http://doi.org/10.1175/JCLI-D-11-00015.1>
- Rochette, P., Desjardins, R. L., Pattey, E., & Lessard, R. (1995). Crop net carbon dioxide exchange rate and radiation use efficiency in soybean. *Agronomy Journal (USA)*.
- Roerink, G. J., Menenti, M., Soepboer, W., & Su, Z. (2003). Assessment of climate impact on vegetation dynamics by using remote sensing. *Physics and Chemistry of the Earth*, 28(1–3), 103–109. [http://doi.org/10.1016/S1474-7065\(03\)00011-1](http://doi.org/10.1016/S1474-7065(03)00011-1)
- Sakamoto, T., Wardlow, B. D., Gitelson, A. A., Verma, S. B., Suyker, A. E., & Arkebauer, T. J. (2010). A Two-Step Filtering approach for detecting maize and soybean phenology with time-series MODIS data. *Remote Sensing of Environment*, 114(10), 2146–2159. <http://doi.org/10.1016/j.rse.2010.04.019>
- Sakamoto, T., Yokozawa, M., Toritani, H., Shibayama, M., Ishitsuka, N., & Ohno, H. (2005). A crop phenology detection method using time-series MODIS data. *Remote Sensing of Environment*, 96(3–4), 366–374. <http://doi.org/10.1016/j.rse.2005.03.008>
- Sánchez, B., Rasmussen, A., & Porter, J. R. (2014). Temperatures and the growth and development of maize and rice: A review. *Global Change Biology*, 20(2), 408–417. <http://doi.org/10.1111/gcb.12389>
- Sellers, P. J. (1985). Canopy reflectance, photosynthesis and transpiration. *International Journal of Remote Sensing*, 6(8), 1335–1372. <http://doi.org/10.1080/01431168508948283>
- Shang, J., Liu, J., Huffman, T., Qian, B., Pattey, E., Wang, J., Lantz, N. (2014). Estimating plant area index for monitoring crop growth dynamics using Landsat-8

- and RapidEye images. *Journal of Applied Remote Sensing*, 8(1), 85196.
<http://doi.org/10.1117/1.JRS.8.085196>
- Sinclair, T. R., & Horie, T. (1989). Leaf Nitrogen, Photosynthesis, and Crop Radiation Use Efficiency: A Review. *Crop Science*, 29, 90–98.
<http://doi.org/10.2135/cropsci1989.0011183X002900010023x>
- Spaeth, S. C., Randall, H. C., Sinclair, T. R., & Vendeland, J. S. (1984). Stability of soybean harvest index. *Agronomy Journal*, 76(3), 482–486.
- Steduto, P., Hsiao, T. C., Raes, D., & Fereres, E. (2009). Aquacrop-the FAO crop model to simulate yield response to water: I. concepts and underlying principles. *Agronomy Journal*, 101(3), 426–437. <http://doi.org/10.2134/agronj2008.0139s>
- van Dijen, C. A., Wolf, J., van Keulen, H., & Rappoldt, C. (1989). WOFOST-A Simulation Model of Crop Production. *Soil Use and Management*, 5(1), 16–24.
- Varlet-Grancher, C., Bonhomme, R., Chartier, M., & Artis, P. (1982). Efficiency of a plant cover of converting solar energy. *Acta Oecologica. Oecologia plantarum*.
- Vermote, E. F., Kotchenova, S. Y., & Ray, J. P. (2011). *MODIS Surface Reflectance User's Guide*.
- Weiss, M., & Baret, F. (2017). *Can-eye version 6.4.91 user manual*. Retrieved from <https://www6.paca.inra.fr/can-eye/Documentation/Documentation>
- Zhang, X., Friedl, M. A., Schaaf, C. B., Strahler, A. H., Hodges, J. C. F., Gao, F., Huete, A. (2003). Monitoring vegetation phenology using MODIS. *Remote Sensing of Environment*, 84(3), 471–475. [http://doi.org/10.1016/S0034-4257\(02\)00135-9](http://doi.org/10.1016/S0034-4257(02)00135-9)
- Zheng, Y., Wu, B., Zhang, M., & Zeng, H. (2016). Crop phenology detection using high spatio-temporal resolution data fused from SPOT5 and MODIS products. *Sensors*, 16(12), 2099. <http://doi.org/10.3390/s16122099>
- Zhu, X., Chen, J., Gao, F., Chen, X., & Masek, J. G. (2010). An enhanced spatial and temporal adaptive reflectance fusion model for complex heterogeneous regions. *Remote Sensing of Environment*, 114(11), 2610–2623.
<http://doi.org/10.1016/j.rse.2010.05.032>

Chapter 6

6 Discussion and Conclusions

6.1 Summary

Earth Observation (EO) technology has provided an efficient and effective way for spatial and temporal monitoring of crops. Multi-temporal optical satellite remote sensing data have been widely used in crop monitoring and crop yield estimation. For sub-field scale agriculture applications, both high spatial resolution and high temporal resolution are important. However, due to technical limitations and cloud contamination, it is difficult to obtain optical remote sensing data with both high spatial and temporal resolution. One alternative is to make use of multi-temporal high spatial resolution Synthetic Aperture Radar (SAR) data, which are less dependent on the weather condition. Another approach is to fuse high spatial resolution data and high temporal resolution data. This thesis mainly focuses on the application of multi-temporal polarimetric SAR data and optical remote sensing data in crop monitoring at a sub-field scale when the number of high spatial resolution optical remote sensing images is limited.

First, I investigated the sensitivity of Radarsat-2 polarimetric SAR parameters to crop biophysical variables. Next, I examined the contribution of Minimum Noise Fraction (MNF) transformation of multi-temporal Radarsat-2 polarimetric SAR on crop classification. Then, I proposed a spatio-temporal data fusion method that is suitable for crop monitoring in a heterogeneous region to generate time series images with a high temporal and high spatial resolution. Finally, I improved a crop phenology detection method and estimated the crop biomass for corn and soybean using the SAFY method based on the phenology information.

Chapter 2 presents the sensitivity study of 16 polarimetric SAR parameters derived from 10 C-band Radarsat-2 polarimetric SAR data to crop height and fractional vegetation cover (FVC) of corn and wheat. The 16 polarimetric SAR parameters include Linear polarizations (HH, VV, HV), Pauli decompositions (HH+VV, HH-VV), intensity ratios (HH/VV, HV/HH, HV/VV), Radar Vegetation Index (RVI), Cloude-Pottier

decompositions (Entropy, Anisotropy, Alpha angle) and Yamaguchi 4-component decompositions (Yamaguchi single bounce, Yamaguchi double bounce, Yamaguchi volume scattering, Yamaguchi helix scattering). Correlation analysis was conducted between these parameters and two crop variables (FVC, height). It was observed that at the early growing stage, the corn height was strongly correlated with the SAR parameters including HV, HH-VV, and HV/VV, and the corn FVC was significantly correlated with HV and HV/VV, but the correlation became weaker at the later growing stage. The sensitivity of the SAR parameters to wheat variables was very low and only HV and Yamaguchi helix scattering showed relatively good but negative correlations with wheat height at the middle growing stage.

Multi-temporal polarimetric SAR data are a necessary source for crop classification when there are insufficient optical remote sensing images. In Chapter 3, I investigated the contributions of MNF transformation of multi-temporal Radarsat-2 polarimetric SAR data on cropland classification in southwestern Ontario based on random forest classifier. The research is performed through a discussion of the performance of different polarimetric SAR parameters sets and the impact of timing of Radarsat-2 datasets on cropland classification..

The results illustrate that the coherency matrix gave the best overall accuracy. The multi-temporal polarimetric SAR data acquired between June and the end of July, July and the middle of September, and July and the end of October were important for wheat, soybean and corn classification respectively. An overall accuracy of 90% can be achieved using two images acquired in the middle of September and October, and an accuracy of 94% can be achieved using four datasets acquired between July and October. The MNF transformation was originally developed for hyperspectral image processing to produce principal components by maximizing the signal-to-noise ratio of the data. The MNF transformation of the multi-temporal polarimetric SAR parameter sets can improve the overall classification accuracy by segregating noise in the data. A maximum overall accuracy of 95.89% was achieved based on random forest classifier using the MNF transformation of the multi-temporal (July to November) coherency matrix, and the accuracy was further improved by removing the last few bands which mainly contained noise. The maximum

improvement of the MNF transformation was 3.94% for wheat, 6.02% for soybean, and 8.65% for forage. Compared with the Support Vector Machine (SVM) classifier, the Random Forest (RF) classifier performs better.

The retrieval of subfield-scale crop biophysical variables using polarimetric SAR data is limited due to the speckle noise, the influence of soil on SAR backscatters in the early growing stage of crops, and the saturation phenomenon of polarimetric SAR data in the later growing stage. To make use of the high spatial resolution characteristics and the high temporal resolution characteristics of difference optical satellite sources, in Chapter 4, I developed a spatio-temporal vegetation index image fusion model (STVIFM) to blend MODIS and Landsat NDVI images for generating NDVI time series in a heterogeneous region. Similar to most spatio-temporal data fusion methods, the STVIFM assumes that the NDVI is additive. The NDVI change of each fine-resolution pixel is obtained by a disaggregation weighting system, which describes the contribution of each fine-resolution pixel to the total NDVI changes calculated from the coarse-resolution pixels. The weighting system considers the differences between fine-resolution and coarse-resolution pixel values on different dates. It also considers the variations of change rate at both spatial scale and temporal scale. The spatial variation of NDVI change of each fine-resolution pixel at any prediction date is calculated by incorporating the weights calculated based on one base fine-resolution image and the temporal NDVI change of the two fine-resolution images. These two elements are incorporated according to the land cover similarity between the prediction date and the two base dates. The STVIFM outperforms in NDVI prediction compared to the STARFM and ESTARFM when the land cover or NDVI changes are captured by the two pairs of fine- and coarse-resolution images. In addition, the STVIFM is more computationally efficient and more robust than the FSDAF. The STVIFM enhances the capability for generating both high spatial resolution and high temporal frequency NDVI time series in heterogeneous regions.

With a more accurate spatio-temporal data fusion method, the high spatial resolution NDVI images at key stages of crops can be more accurately generated. In Chapter 5, I improved the two-step filtering method to detect crop phenology and estimated crop biomass and yield at subfield scale based on the SAFY model using the spatio-temporal fusion of three

Landsat-8 images and ten MODIS images. First, the STVIFM was applied to generate high spatial resolution time series images by integrating Landsat-8 and MODIS images. Second, the two-step filtering approach was improved by using the daily $fAPAR$ fitted by the CSDM to detect corn and soybean phenology at subfield scale: (1) the crop growth model CSDM was adopted to simulate daily $fAPAR$ for a known corn sample site and a known soybean sample site based on the daily mean temperature and the seven $fAPAR$ values calculated from the original and generated remote sensing images. (2) Based on the simulated shape model of corn and soybean with known phenological dates, the phenological dates for the remaining pixels of the image were obtained by introducing another three parameters to the CSDM function and the spatial maps of the phenological dates for SOS, DOS and EOS over the study site were produced. The parameters in the SAFY model were determined through the literature, forcing the SOS, DOS and EOS information integrated with the daily mean temperature and calibrating using the 10 remotely sensed GLAI values. The results show that the improved two-step filtering approach, by the integration of the CSDM, has a good ability in simulating daily $fAPAR$ and detecting crop phenology at pixel scale. The accuracy of biomass estimation was improved by about 4% in RRMSE for corn and soybean by forcing the phenological information derived from remote sensing images into the SAFY model. The SAFY model is able to obtain the ELUE for each pixel through the calibration and can accurately reflect the spatial variation of crop biomass. In addition, good correlations were found between ELUE and the $fAPAR_{max}$ during the growing season for corn and soybean.

6.2 Conclusions and research contributions

This thesis accomplished four specific objectives and answered the two research questions raised in Section 1.3. The following conclusions can be drawn from this thesis:

- (1) Multi-temporal Radarsat-2 polarimetric SAR data have potential in crop biophysical variable monitoring and show excellent performance in crop type mapping as demonstrated by the following two findings.
 - (a) This thesis suggests that Radarsat-2 polarimetric SAR parameters are sensitive to biophysical variables such as crop height and FVC. The degree of sensitivity

varies with crop types, growing stages, and the polarimetric SAR parameters. The multi-temporal Radasat-2 polarimetric SAR parameters such as C_{22} and T_{22} are sensitive to corn height and FVC at the early growing stages with R^2 of more than 0.8. But there is a large uncertainty in the later growing stage due to the influence of speckle noise in the SAR image, soil background at the early growing stage and weak capability of penetrating a large crop canopy at the later growing stage. However, the Radasat-2 polarimetric SAR data provide a good alternative for crop variables monitoring in areas where the cloud-free optical images are not available.

- (b) The multi-temporal coherency matrix of Radarsat-2 polarimetric SAR data acquired between June and November has excellent performance in crop classification using the random forest classifier with the highest OA of 94.65%. The MNF transformation of multi-temporal coherency matrix can improve the accuracy of soybean by about 6% and winter wheat by about 4%.
- (2) A limited number of high spatial resolution optical images can be used for crop growth monitoring and yield estimation by integrating high temporal but lower spatial resolution images using a spatio-temporal data fusion model and fitting a crop growth model.
- (a) The temporal resolution of high spatial resolution optical data can be improved by using a spatio-temporal data fusion method. The proposed STVIFM algorithm in this thesis improved the accuracy of the synthetic Landsat-like NDVI in heterogeneous regions using Landsat-8 and MODIS data compared to the existing methods such as STARFM and ESTARFM.
 - (b) The fusion of high spatial and high temporal resolution optical remote sensing images and the CSDM were used to generate daily $fAPAR$ and improve the TSF phenology detection model. The crop yield was estimated by calibrating the SAFY model using the phenology information and GLAI calculated from the original and synthetic NDVI images. The accuracy of biomass estimation was improved by about 4% in relative RMSE (RRMSE) compared with the SAFY model without forcing the remotely sensed phenology and a simple light use efficiency (LUE)

model.

The contributions of this thesis are summarized as follows:

- (1) The sensitivity of different Radarsat-2 polarimetric SAR parameters to crop FVC of corn and wheat was analyzed for the first time. Compared with most similar studies, this study was conducted on a per-pixel basis instead of the segmented polygon basis. The results indicated that the C-band Radarsat-2 polarimetric SAR has great potential in crop height and FVC estimation for broad-leaf crops (corn), and for identifying the changes in crop canopy structures and phenology (corn and wheat) in cloudy areas.
- (2) For the first time, the MNF transformation was applied to multi-temporal Radarsat-2 polarimetric SAR parameters. The results show that the MNF helps to segregate speckle noise when it is applied to multi-temporal polarimetric SAR. With the random forest classifier, the MNF transformation of most polarimetric SAR parameter sets improved the crop type classification accuracy.
- (3) I proposed a spatio-temporal vegetation index image fusion model (STVIFM) to blend high spatial resolution images and high temporal resolution images for generating high resolution NDVI time series. This algorithm performs better than the existing widely used algorithms especially in crop land areas. It can be applied to other vegetation indices with appropriate adjustment of the thresholds, and other sources of satellite images.
- (4) I proposed an improved TSF approach to detect crop phenology based on daily $fAPAR$ simulated from the CSDM model instead of the NDVI time series generated from the remote sensing images. The phenology information was forced into the SAFY model and a framework to calibrate the SAFY was introduced for both corn and soybean. In addition, a good relationship was found between the ELUE and the $fAPAR_{max}$. Subfield-scale crop biomass and yield estimation provide important information and practical tools for farmers, traders and agricultural companies for precision agriculture and crop production management.

6.3 Future research

6.3.1 Crop height estimation using PolInSAR

Crop height is closely related to crop biomass and phenology and is an important indicator for crop growth monitoring, crop discrimination and crop production estimation (H. McNairn & Brisco, 2004; Srivastava et al., 2006). Chapter 2 demonstrates that HV backscatter shows the best correlation with corn height at the early growing season. However, there is a saturation issue later in the growing season for crop height estimation. Polarimetric SAR interferometry (PolInSAR) may overcome the limitations of PolSAR because it combines the advantages of Polarimetric SAR and Interferometry (Kumar & Khati, 2010) and yields information not only about the dielectric properties, shape and orientation of the whole plant constituents (as PolSAR does), but also about the vertical structure of the plant (Hutt, Tilly, Schiedung, & Bareth, 2016). However, the potential of Radarsat-2 PolInSAR was limited due to the low-coherence caused by the 24-day repeat period. The Radarsat-2 PolInSAR was used for crop change detection through a coherence optimization (Li et al., 2014).

Therefore, future work may attempt to investigate the potential of Radarsat-2 in crop height estimation. Firstly, the crop height change between two dates (24-day interval) will be estimated using UAV point cloud data. Then Radarsat-2 PolInSAR and coherency optimization will be conducted. By analyzing the relationship between the coherency optimized Radarsat-2 PolInSAR information and crop height changes, the crop height might be estimated by adding the crop height change to the crop height estimated at the previous time.

6.3.2 Crop classification using polarimetric SAR data and optical remotely sensed data based on deep learning method

Deep learning (DL) methods have become a hotspot in the machine learning area in recent years. By simulating human neural networks organized in a deep architecture, DL algorithms have excellent learning ability (Zhang, Zhang, & Du, 2016). Algorithms such as deep belief networks (DBNs) (Hinton, Osindero, & Teh, 2006), restricted Boltzmann machines (RBMs) (Freund & Haussler, 1994), convolutional neural networks (CNNs)

(LeCun, Bottou, Bengio, & Haffner, 1998) have been applied to hyperspectral and polarimetric SAR remote sensing image classification (Chen et al., 2014; Chen, Zhao, Member, Jia, & Member, 2015; Geng et al., 2015; Hou, Luo, Wang, & Jiao, 2015; Z. Lin, Chen, Zhao, & Wang, 2013; Lv et al., 2015; Lv, Dou, Niu, Xu, & Li, 2014; Yue, Zhao, Mao, & Liu, 2015). By combining multi-temporal SAR and optical data, spatial, temporal, spectral and polarimetric features can be generated. Therefore, future work can investigate the potential of deep learning approaches.

6.3.3 Crop yield forecasting using Unmanned Aerial Vehicle (UAV)-based remotely sensed data

The SAFY model is used for crop biomass or yield estimation, and it needs temporal LAI as inputs parameters. Chapter 5 improved a crop phenology model based on the daily fAPAR obtained from the fusion of three Landsat-8 and seven MODIS data and the CSDM, and proposed a framework to implement the SAFY model by forcing the phenological information and calibrating using the original and synthetic remotely sensed GAI. However, if the number of cloud-free Landsat images or MODIS images during the growing season is less than three, the SAFY model cannot be implemented. The Radarsat-2 polarimetric SAR data can provide alternative information at field-scale, but it is not suitable for sub-field scale analysis due to the speckle noise.

In recent years, unmanned aerial vehicle (UAV)-based images have become popular in precision agriculture applications, and they have a great potential in sub-field-level measurement of LAI due to their flexibility, low cost and high spatial resolution. Generally, a crop surface model (Bendig et al., 2015) was used for crop biomass estimation using the UAV data. In the crop surface model, crop height needs to be retrieved from the point cloud generated from the UAV images, and a regression model is built between the crop height and biomass. The limitation of this model is that it is still unclear which combination of satellite data and crop modelling is most effective and whether the models can be applied successfully at different spatial scales.

Future work may focus on assimilating real-time UAV remotely sensed crop biophysical variables to the SAFY-WB model, which coupled with a water balance model, to predict crop yield.

References

- Bendig, J., Yu, K., Aasen, H., Bolten, A., Bennertz, S., Broscheit, J., Bareth, G. (2015). Combining UAV-based plant height from crop surface models, visible, and near infrared vegetation indices for biomass monitoring in barley. *International Journal of Applied Earth Observation and Geoinformation*, 39, 79–87.
<http://doi.org/10.1016/j.jag.2015.02.012>
- Chen, Y., Lin, Z., Zhao, X., Member, S., Wang, G., & Gu, Y. (2014). Deep learning-based classification of hyperspectral data. *IEEE Journal of Selected Topics in Applied Earth Observations and Remote Sensing*, 7(6), 2094–2107.
<http://doi.org/10.1109/JSTARS.2014.2329330>
- Chen, Y., Zhao, X., Member, S., Jia, X., & Member, S. (2015). Spectral – spatial classification of hyperspectral data based on deep belief network, 8(6), 2381–2392.
- Freund, Y., & Haussler, D. (1994). *Unsupervised learning of distributions on binary vectors using two layer networks*. Santa Cruz.
- Geng, J., Fan, J., Wang, H., Ma, X., Li, B., & Chen, F. (2015). High-resolution SAR image classification via deep convolutional autoencoders. *IEEE Geoscience and Remote Sensing Letters*, 12(11), 2351–2355.
<http://doi.org/10.1109/LGRS.2015.2478256>
- Hinton, G. E., Osindero, S., & Teh, Y. W. (2006). A fast learning algorithm for deep belief nets. *Neural Computation*, 18(7), 1527–1554.
<http://doi.org/10.1162/neco.2006.18.7.1527>
- Hou, B., Luo, X., Wang, S., & Jiao, L. (2015). *Polarimetric SAR images classification using deep belief networks with learning feature*. *IEEE International Geoscience and Remote Sensing Symposium July 2015*, (pp. 2366–2369).
<http://doi.org/10.1109/IGARSS.2015.7326284>
- Hutt, C., Tilly, N., Schiedung, H., & Bareth, G. (2016). Potential of multitemporal tandem-x derived crop surface models for maize growth monitoring. *International Archives of the Photogrammetry, Remote Sensing and Spatial Information Sciences - ISPRS Archives*, 41(July), 803–808.
<http://doi.org/10.5194/isprsarchives-XLI-B7-803-2016>

- Kumar, S., & Khati, U. G. (2010). Polarimetric SAR interferometry (PolInSAR) and inversion modelling.
- LeCun, Y., Bottou, L., Bengio, Y., & Haffner, P. (1998). Gradient-based learning applied to document recognition. *Proceedings of the IEEE*, 86(11), 2278–2324.
<http://doi.org/10.1109/5.726791>
- Li, Y., Liu, T., Lampropoulos, G., McNairn, H., Shang, J., & Touzi, R. (2014). Radarsat-2 POLInSAR coherence optimization for agriculture crop change detection. *International Geoscience and Remote Sensing Symposium (IGARSS)*, 4588–4591.
<http://doi.org/10.1109/IGARSS.2014.6947514>
- Lin, Z., Chen, Y., Zhao, X., & Wang, G. (2013). Spectral-spatial classification of hyperspectral image using autoencoders. *2013 9th International Conference on Information, Communications & Signal Processing*, (61301206), 1–5.
<http://doi.org/10.1109/ICICS.2013.6782778>
- Lv, Q., Dou, Y., Niu, X., Xu, J., & Li, B. (2014). Classification of land cover based on deep belief networks using polarimetric radarsat-2 data. *IEEE Geoscience and Remote Sensing Symposium*, 4679–4682.
<http://doi.org/10.1109/IGARSS.2014.6947537>
- Lv, Q., Dou, Y., Niu, X., Xu, J., Xu, J., & Xia, F. (2015). Urban land use and land cover classification using remotely sensed SAR data through Deep Belief Networks, *2015*.
- McNairn, H., & Brisco, B. (2004). The application of C-band polarimetric SAR for agriculture: A review. *Canadian Journal of Remote Sensing*.
<http://doi.org/10.5589/m03-069>
- Srivastava, H. S., Patel, P., & Navalgund, R. R. (2006). Application potentials of synthetic aperture radar interferometry for land-cover mapping and crop-height estimation. *Current Science*, 91(6), 783–788.
- Xie, Q., Zhu, J., Wang, C., Fu, H., Lopez-Sanchez, J. M., & Ballester-Berman, J. D. (2017). A modified dual-baseline PolInSAR method for forest height estimation. *Remote Sensing*, 9(8), 1–17. <http://doi.org/10.3390/rs9080819>

- Yue, J., Zhao, W., Mao, S., & Liu, H. (2015). Spectral-spatial classification of hyperspectral images using deep convolutional neural networks. *Remote Sensing Letters*, 6(6), 468–477. <http://doi.org/10.1080/2150704X.2015.1047045>
- Zhang, L., Zhang, L., & Du, B. (2016). Deep learning for remote sensing data: A technical tutorial on the state of the art. *IEEE Geoscience and Remote Sensing Magazine*, 4(2), 22–40. <http://doi.org/10.1155/2016/7954154>

Appendices

Appendix A: Polarimetric SAR basics

A Synthetic Aperture Radar is an imaging radar that sequentially transmits microwave pulses and receives the backscatters by the radar antenna. Due to the platform movement, the consecutive time of transmission/reception translates into different positions. A virtual aperture that is much longer than the physical antenna length can be constructed using an appropriate coherent combination of the received signals (Moreira et al., 2013).

Polarizations

The polarization of the radiation is an important property of microwave energy propagation and scattering. For a plane electromagnetic (EM) wave (Figure A-1), polarization refers to the electric vector in the plane perpendicular to the direction of propagation, and the orientation and shape of the pattern traced by the tip of the vector (Natural Resources Canada, 2015).

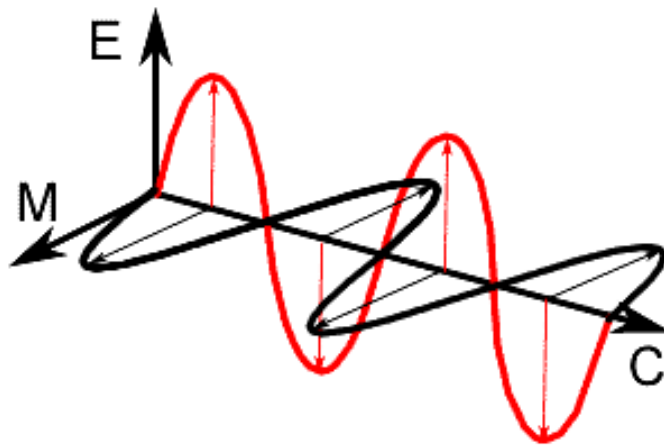


Figure A-1: Example of EM wave. E: Electric vector, M: Magnetic vector, C: Propagation direction (<https://earth.esa.int/handbooks/asar/CNTR5-5.html>)

A radar system can have one, two or all four of the following transmit/receive polarization combinations:

- (1) HH - for horizontal transmit and horizontal receive
- (2) VV - for vertical transmit and vertical receive

- (3) HV - for horizontal transmit and vertical receive, and
- (4) VH - for vertical transmit and horizontal receive.

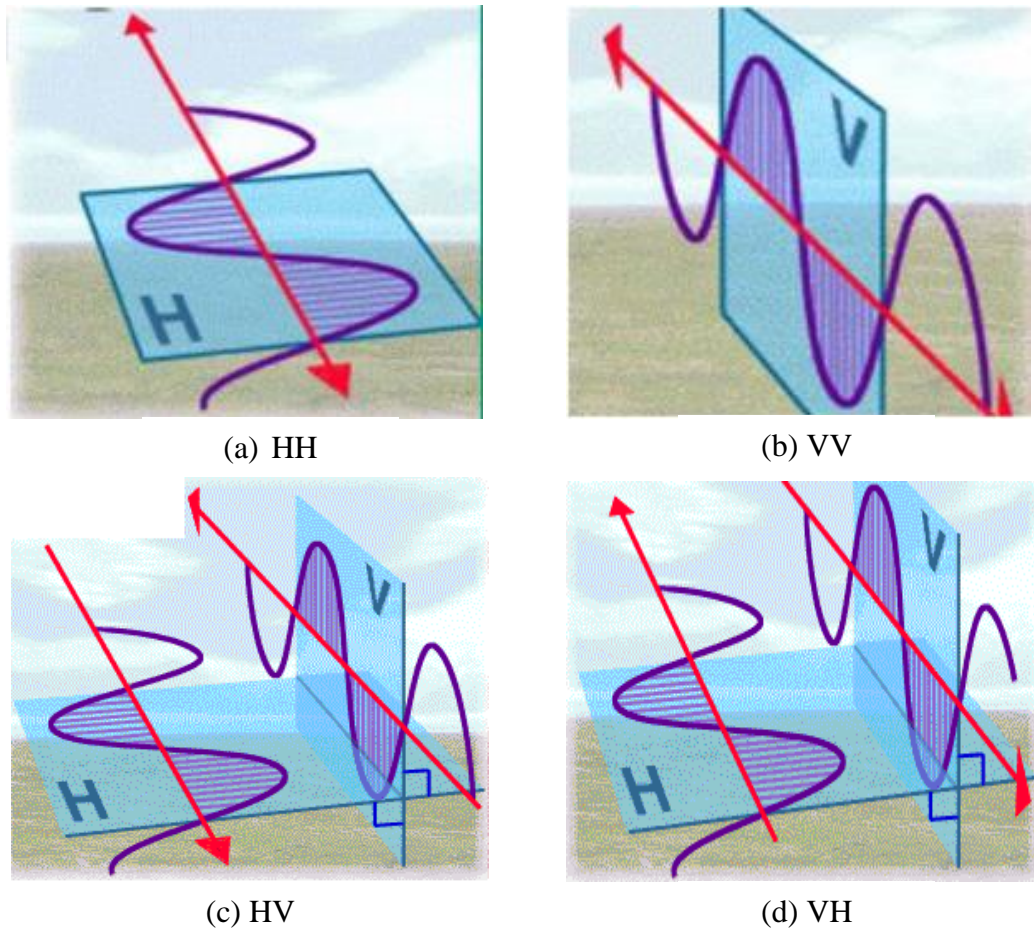


Figure A-2: Examples of the four polarizations: (a) HH, (b) VV, (c) HV, (d) VH (Retalis, 2010)

Incidence angle

Unlike the optical satellite data such as Landsat, MODIS and most airborne images, radar data are collected looking off to the side of the spacecraft. Because radar measures the time that it takes for the microwave signal to go from the spacecraft to the ground and back, the side looking is necessary to avoid the confusion of signals coming back at the same time from the two opposite sides of the spacecraft ground track.

Figure A-3 illustrates some of the common terms used to describe the geometry of a radar image, including the incidence angle, which is the angle at which the radar beam hits the surface.

The wavelength, polarization and incidence angle affect how a radar system observes the elements on the earth surface. Therefore, radar data collected at different incidence angle, polarization and wavelength combinations may provide different and complementary information. The primary description of how a radar target or surface feature scatter's EM energy is given by the scattering matrix. And other forms of polarimetric information such as the polarimetric decompositions can be derived from the scattering matrix, (Natural Resources Canada, 2015).

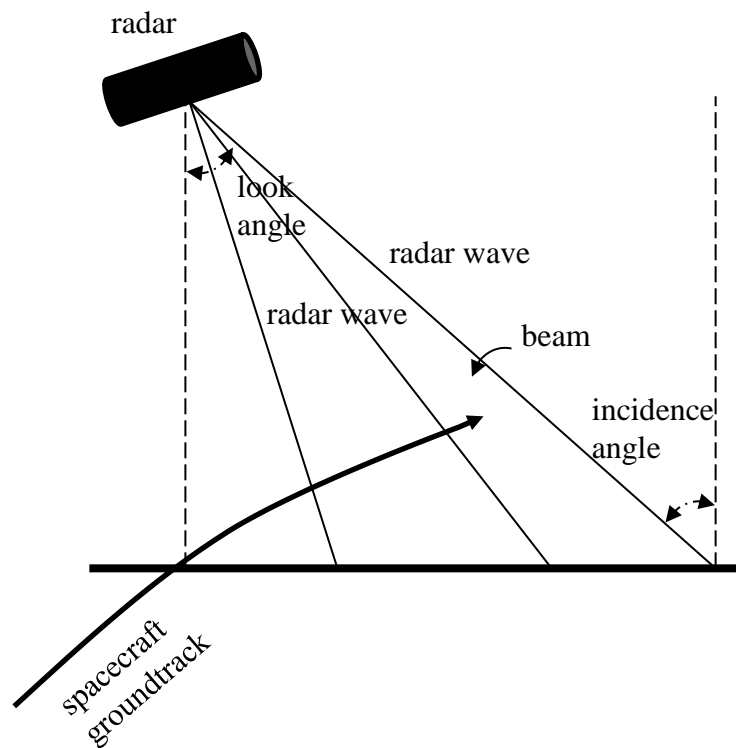


Figure A-3 Illustration of radar geometry

Radarsat-2 polarimetric SAR

Radarsat-2 is a C-band (5.3 GHz) polarimetric SAR satellite which was launched in 2007. It has the spatial resolutions varying from 3 to 100 meters, and four polarizations.

Imaging can be carried out in one of several different beam modes, each of which offers a unique set of imaging characteristics. The Radarsat-2 beam modes are shown in Figure A-4.

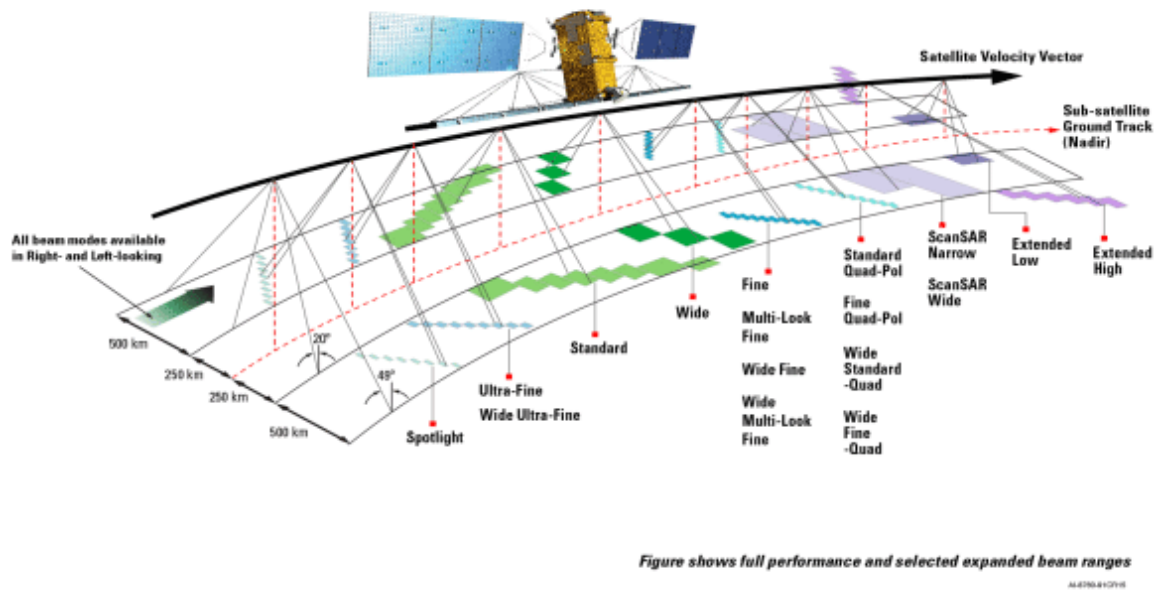


Figure A-4: Radarsat-2 SAR beam modes (MacDonald, Dettwiler and Associates Ltd, 2016)

During imaging, the SAR instrument may be operated in one of three fundamental imaging sensor modes: Single Beam, ScanSAR, and Spotlight. In this thesis, the Wide Fine Quad Polarization mode is used, so I mainly introduce the single beam mode (Figure A-5).

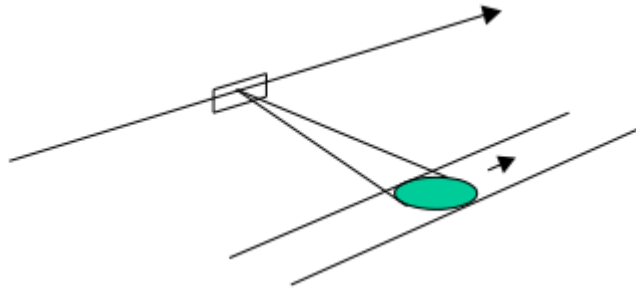


Figure A-5: Single beam mode (MacDonald, Dettwiler and Associates Ltd, 2016)

In Single Beam imaging, the following beam modes are available:

- (a) Standard. Standard Beam Mode allows imaging over a wide range of incidence angles with a set of image quality characteristics which provides a balance between fine resolution and wide coverage, and between spatial and radiometric resolutions.
- (b) Wide. The Wide Swath Beam Mode allows imaging of wider swaths than Standard Beam Mode, but at the expense of slightly coarser spatial resolution in some cases.
- (c) Fine. The Fine Resolution Beam Mode is intended for applications which require finer spatial resolution than Standard Beam Mode.
- (d) Wide Fine. The Wide Fine Resolution Beam Mode is intended for applications which require both a finer spatial resolution and a wide swath.
- (e) Multi-Look Fine. The Multi-Look Fine Resolution Beam Mode covers the same swaths as the Fine Resolution Beam Mode.
- (f) Wide Multi-Look Fine. The Wide Multi-Look Fine Resolution Beam Mode offers a wider coverage alternative to the regular Multi-Look Fine Beam Mode, while preserving the same spatial and radiometric resolution, but at the expense of higher data compression ratios (which leads to higher signal-dependent noise levels).
- (g) Extra-Fine. The Extra-Fine Resolution Beam Mode nominally provides similar swath width and incidence angle coverage as the Wide Fine Beam Mode, at even finer resolutions, but with higher data compression ratios and noise levels.

- (h) Ultra-Fine. The Ultra-Fine Resolution Beam Mode is intended for applications which require very high spatial resolution.
- (i) Wide Ultra-Fine. The Wide Ultra-Fine Resolution Beam Mode provides the same spatial resolution as the Ultra-Fine mode as well as wider coverage, but at the expense of higher data compression ratios (which leads to higher signal-dependent noise levels).
- (j) Extended High (High Incidence). In the Extended High Incidence Beam Mode, six Extended High Incidence Beams, EH1 to EH6, are available for imaging in the 49 to 60 degree incidence angle range.
- (k) Extended Low (Low Incidence). In the Extended Low Incidence Beam Mode, a single Extended Low Incidence Beam, EL1, is provided for imaging in the incidence angle range from 10 to 23 degrees with nominal ground swath coverage of 170 km.
- (l) Standard Quad Polarization. In the Quad Polarization Beam Mode, the radar transmits pulses alternately in horizontal (H) and vertical (V) polarizations, and receives the return signals from each pulse in both H and V polarizations separately but simultaneously.
- (m) Wide Standard Quad Polarization. The Wide Standard Quad Polarization Beam Mode operates the same way as the Standard Quad Polarization Beam Mode but with higher data acquisition rates, and offers wider swaths of approximately 50 km at equivalent spatial resolution.
- (n) Fine Quad Polarization. The Fine Quad Polarization Beam Mode provides full polarimetric imaging with the same spatial resolution as the Fine Resolution Beam Mode.
- (o) **Wide Fine Quad Polarization.** The Wide Fine Quad Polarization Beam Mode operates the same way as the Fine Quad Polarization Beam Mode but with higher data acquisition rates, and offers a wider swath of approximately 50 km at equivalent spatial resolution.

Appendix B: Principal component analysis (PCA)

Principal component analysis (PCA) is a mathematical technique that transforms an original set of image bands into a new set of components that are uncorrelated and are ordered in terms of the amount of the original variance that is explained (Jensen, 2016).

Original multispectral or hyperspectral image channels may be correlated. That is, images from different bands often appear similar and convey the same information. PCA has been used to reduce the redundancy in multispectral or hyperspectral data and by reducing a larger data dimension into a smaller set of 'representative' dimension, called 'principal components', which account for most of the variance in the original variables (Zeng, 2014).

As in the example provided in Figure A-1, two image bands can be represented by a coordinate system PC_1 and PC_2 , where the majority of information can be described merely by the first component PC_1 .

To compute each component specifically for remote sensing bands, the covariance matrix for all the bands is computed firstly. Then the eigenvalues $E = [\lambda_{11}, \lambda_{22}, \lambda_{33}, \dots, \lambda_{nn}]$ and eigenvectors $EV = [a_{kp} \dots \text{for } k=1 \text{ to } n \text{ bands, } p=1 \text{ to } n \text{ components}]$ of the covariance matrix are computed. Finally, the eigenvalues are sorted in descending order. With the eigenvector, each principle component can be calculated by summarized each old band with given weight:

$$DN'_i = \sum_{k=1}^n (a_{ki} \times DN_k), \quad k = 1, \dots, n \quad (\text{B-1})$$

Where DN is the original bands, DN' is the new principle components.

Principal Components Analysis

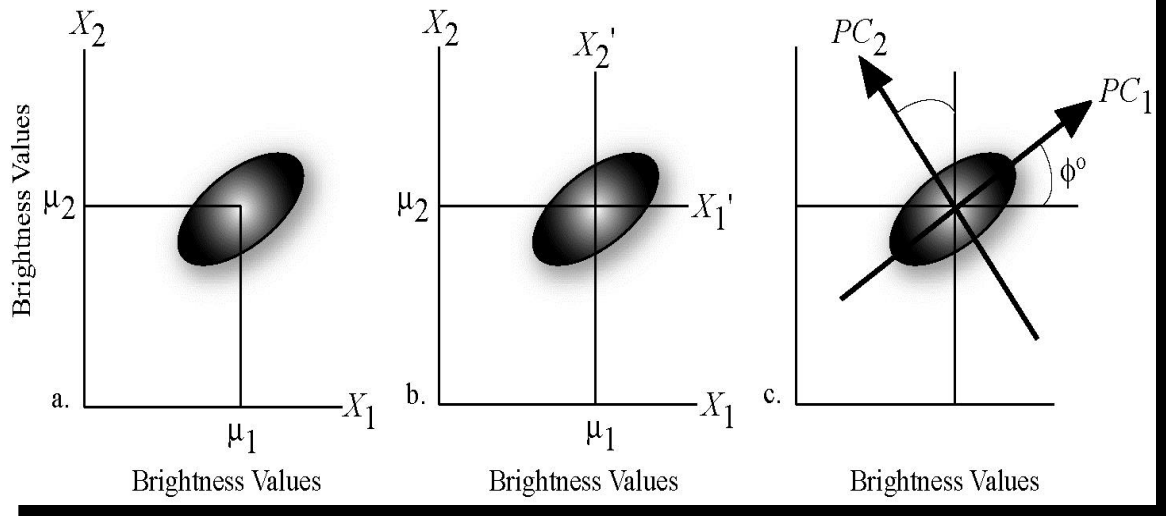


Figure B-1: The spatial relationship between the first two principal components: (a) Scatter-plot of data points collected from two remotely bands labeled X_1 and X_2 with the means of the distribution labeled μ_1 and μ_2 . (b) A new coordinate system is created by shifting the axes to an X' system. (c) The X' axis system is then rotated about its origin (μ_1, μ_2) so that PC_1 is projected through the semi-major axis of the distribution of points and the variance of PC_1 (Component 1) is a maximum. PC_2 (Component 2) must be perpendicular to PC_1 (Jensen, 2016).

Appendix C: Minimum/Maximum Autocorrelation Factors (MAF)

Minimum/Maximum Autocorrelation Factors (MAF) (Switzer & Green, 1984) is a noise separation procedure to avoid the signal blurring introduced through smoothing or spatial averaging procedure.

Let the spatial covariance function of a multivariate stochastic variable, Z_k , where k denotes spatial position and Δ a spatial shift, be $\Gamma(\Delta) = Cov\{Z_k, Z_{k+\Delta}\}$. Evidently, $\Gamma^T(\Delta) = \Gamma(-\Delta)$. Then by letting the variance-covariance matrix of Z_k be Σ and defining the variance-covariance matrix $\Sigma_\Delta = D\{Z_k - Z_{k+\Delta}\}$, $D\{\cdot\}$ is the variance-covariance matrix of its argument, then

$$\Sigma_\Delta = 2\Sigma - \Gamma(\Delta) - \Gamma(-\Delta) \quad (C-1)$$

The covariance between a linear combination of the original variables and the shifted variables can be computed

$$Cov\{\omega_i^T Z_k, \omega_i^T Z_{k+\Delta}\} = \omega_i^T \Gamma(\Delta) \omega_i = \omega_i^T \Gamma^T(\Delta) \omega_i = \frac{1}{2} \omega_i^T (\Gamma(\Delta) + \Gamma(-\Delta)) \omega_i = \omega_i^T (\Sigma - \frac{1}{2} \Sigma_\Delta) \omega_i \quad (C-2)$$

Thus the autocorrelation in shift Δ of a linear combination of the mean-centered original variables, Z_k , is

$$Corr\{\omega_i^T Z_k, \omega_i^T Z_{k+\Delta}\} = 1 - \frac{\frac{1}{2} \omega_i^T \Sigma_\Delta \omega_i}{\omega_i^T \Sigma \omega_i} \quad (C-3)$$

In order to minimize that correlation, the Rayleigh coefficient must be maximized

$$R(\omega) = \frac{\omega_i^T \Sigma_\Delta \omega_i}{\omega_i^T \Sigma \omega_i} \quad (C-4)$$

The MAF transform is given by the set of conjugate eigenvector of Σ_Δ with respect to Σ , $W=[\omega_1, \dots, \omega_m]$, corresponding to the eigenvalues $k_1 \leq \dots \leq k_m$. The resulting new

variables are ordered so that the first MAF is the linear combination that exhibits maximum autocorrelation. The autocorrelation of the i th component is $1 - \frac{1}{2}k_i$ (Larsen, 2002).

Appendix D: Field data collection forms and photos

Table D-1: Biomass Field Datasheet (Corn/Soybean)

Recorded by:		Assisted by:				Date:	Weather:	Camera name:		
Site Name	Point ID	Photo #	Phenology	Width (cm)	Length (m)	# of plants	Total # of cobs/pods	# of cobs/pods of a plant		
								1		
								2		
								3		
									1	
									2	
									3	
Notes										
								1		
								2		
								3		
									1	
									2	
									3	
Notes										

Table D-2: Biomass Lab Datasheet (Corn)

Recorded by:				Date:			
Site name	Point ID	Total fresh weight of stalks and cobs without bags(g)	Fresh weight of stalks without bag (g)		Fresh weight of cobs without bag (g)	Fresh weight of seeds	
		Total dry weight of stalks and cobs without bags(g)	Dry weight of stalks without bag (g)		Dry weight of cobs without bag (g)	Dry weight of seeds	
		Total fresh weight of stalks and cobs without bags(g)	Fresh weight of stalks without bag (g)		Fresh weight of cobs without bag (g)	Fresh weight of seeds	
		Total dry weight of stalks and cobs without bags(g)	Dry weight of stalks without bag (g)		Dry weight of cobs without bag (g)	Dry weight of seeds	
		Cob ID	# of rows per cob	# of kernels per row	# of seeds a cob	Fresh weight of seeds of a cob	Dry weight of seeds of a cob
		1					
		2					
		3					
		4					
	5						
	6						
Notes							

Table D-3: Biomass Lab Datasheet (Soybean)

Recorded by:			Date:			
Site name	Point ID	Fresh weight of stalks and pods without bag (g):	Fresh weight of stalks without bag (g)	Fresh weight of pods without bag (g)	Fresh weight of seeds	
		Dry weight of paper bag for stalks (g)	Dry weight of stalks without bag (g)	Dry weight of pods without bag (g)	Dry weight of seeds	
		Fresh weight of paper bag for stalks(g):	Fresh weight of stalks without bag (g)	Fresh weight of pods without bag (g)	Fresh weight of seeds	
		Dry weight of paper bag for stalks (g)	Dry weight of stalks without bag (g)	Dry weight of pods without bag (g)	Dry weight of seeds	
			Pod ID	# of seeds of per pod	Average # of seeds of a pod	
			1			
			2			
			3			
4						
5						
		6				
		7				
		8				
		9				
	10					
Notes						



Figure D-1: Work photos

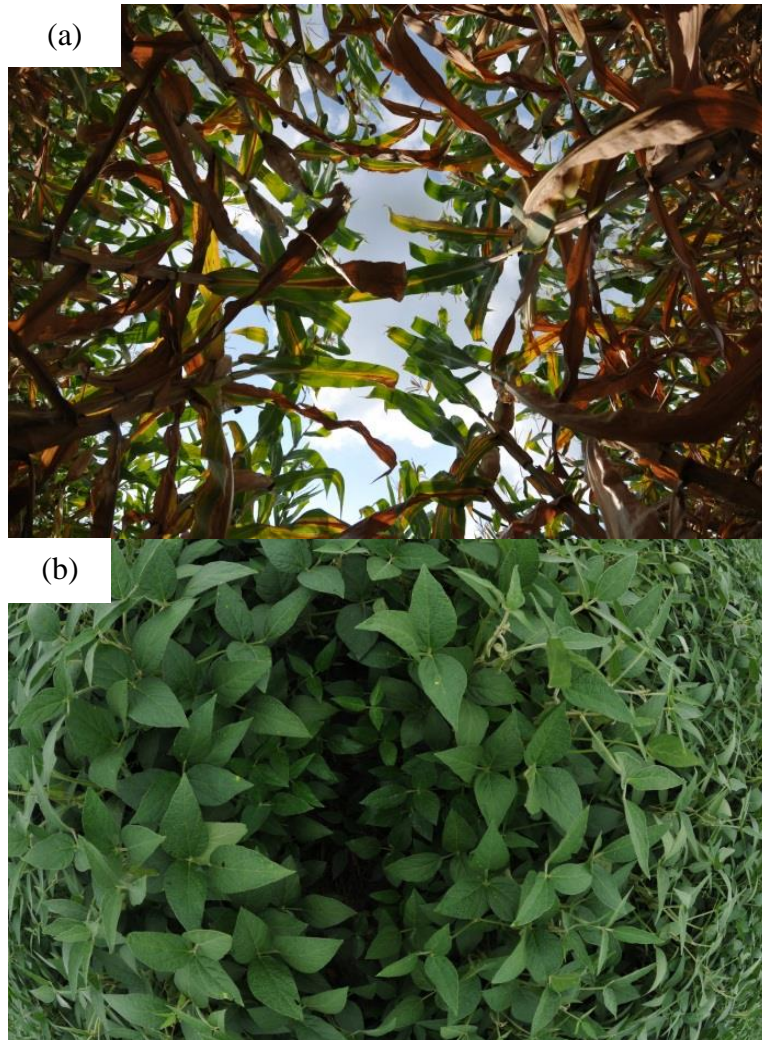


Figure D-2: Examples of hemispherical photos (a) corn, (b) soybean

Digital Hemispherical Photography Field Datasheet

DHP Field Datasheet		DHP Camera #: 558266	
Recorded by: SY		Assisted by: HXD	
Site Name (sample ID)		S20-02	
Date	July 9. 15	Time	4:55
Crop	Soybean.		
Description			
DHP photo# range (starting & ending photo #)	9601 --- 9607, 9608 --- 9614		
DHP data sheet#			
Regular camera name	0		
Landscape photo #	949		
Nadir photo #	950		
Along the row photo #	951		
Against the row photo #	952		
Close-up photo # (take multiples when needed)	953	954	955
Crop heights of 3 plants (cm)	25	22	24
Crop phenology of majority of plants near sample site	S1		
Notes	Up or Down\		
	Down		

Figure D-3: Example of hemispherical photos recoding sheets

Biomass Field Datasheet (Soybean)

Recorded by:		Study Area:		Date:	Weather:			
BGM		Kandua		15-10-02	Cloud			
Site name/ Point ID	BUCH	Plant density			Biomass			
		# of plants /row	Row spacing (cm)	# of plants	Width (m)	Length (m)	# of rows	
S129-001	98 99	1	17	75	10+8	0.5	0.5	1
		2	16	80				
		3	16	75				
		4	17	75				
		Avg						
S129-002	96 97	1	20	76	11+12	0.5	0.5	1
		2	15	80				
		3	17	80				
		4	17	80				
		Avg						
S129-003	99	1	20	80	12+11	0.5	0.5	1
		2	21	80				
		3	12	80				
		4	18	50				
		Avg						
		1				0.5	0.5	
		2						
		3						
		4						
		Avg						
Notes								

Page 2

Figure D-4: Example of biomass recoding sheets

Study area: _____ Field Log Sheet Date: 27/07/2015

FIELD NO.	Time	UTM Easting	UTM Northing	GPS ID	PHOTO NO.		Land cover crop type	BBCH	Crop Height (cm)		COMMENTS
028	12:20				Landscape	0403	corn	65	1	276	2 cobs/plant
					Along the row	0404			2	282	
					Against the row	0405			3	275	
					Close up	0406, 0407					
					Nadir	0408			ave		
035	12:23				Landscape	0409	corn	65	1	242	
					Along the row	0410			2	255	
					Against the row	0411			3	252	
					Close up	0412, 0413					
					Nadir	0414			ave		
S14	12:35				Landscape	0416	soybean	67-69	1	66	flower decolor pods visible
					Along the row	0417			2	73	
					Against the row	0418			3	72	
					Close up	0420, 0419					
					Nadir	0421			ave		
S13	12:40				Landscape	0422	soybean	65-67	1	41	
					Along the row	0423			2	45	
					Against the row	0424			3	37	
					Close up	0425, 0426					
					Nadir	0427			ave		

Recorded by: chh Page: 3

Figure D-5: Example of general survey recoding sheets

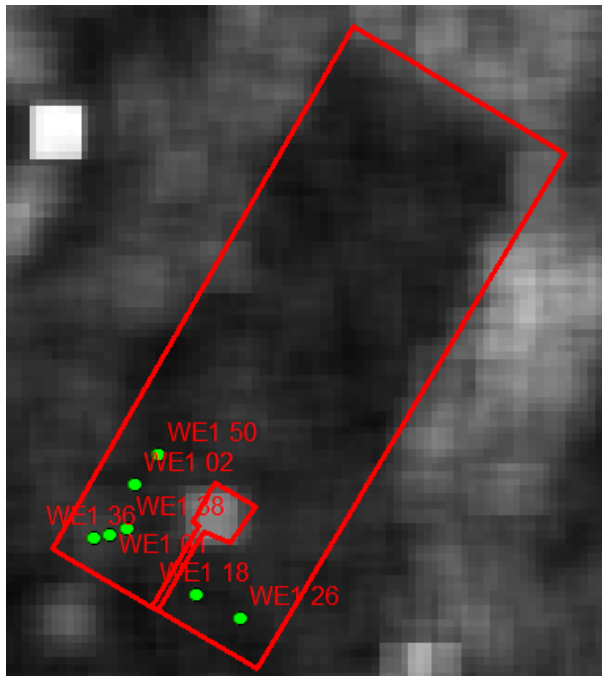


Figure D-6 (a)

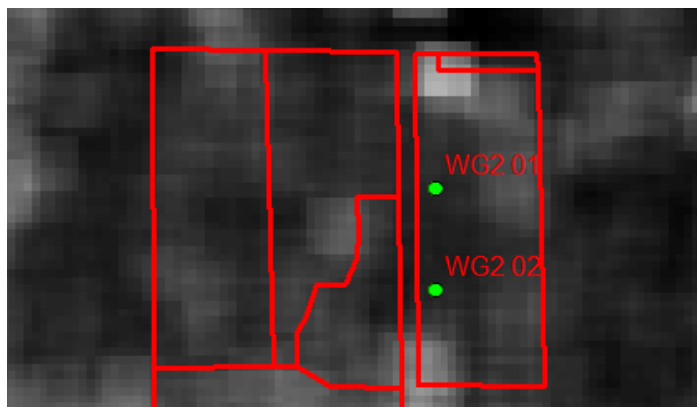


Figure D-6 (b)

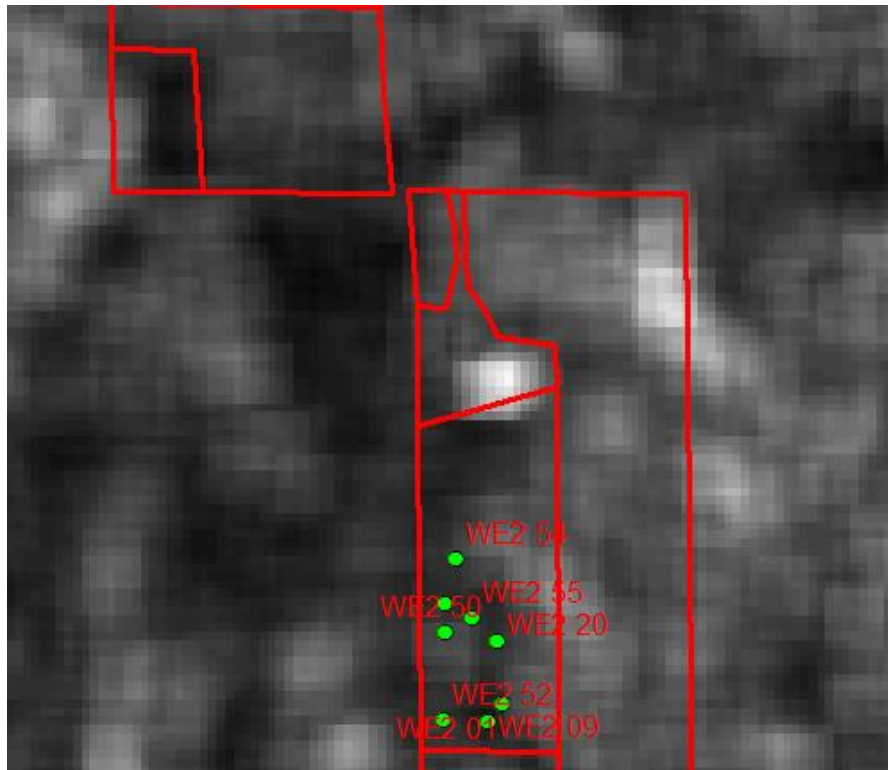


Figure D-6 (c)

Figure D-6: Detailed locations of the winter wheat sample points and Radarsat-2 image for Stratford study site

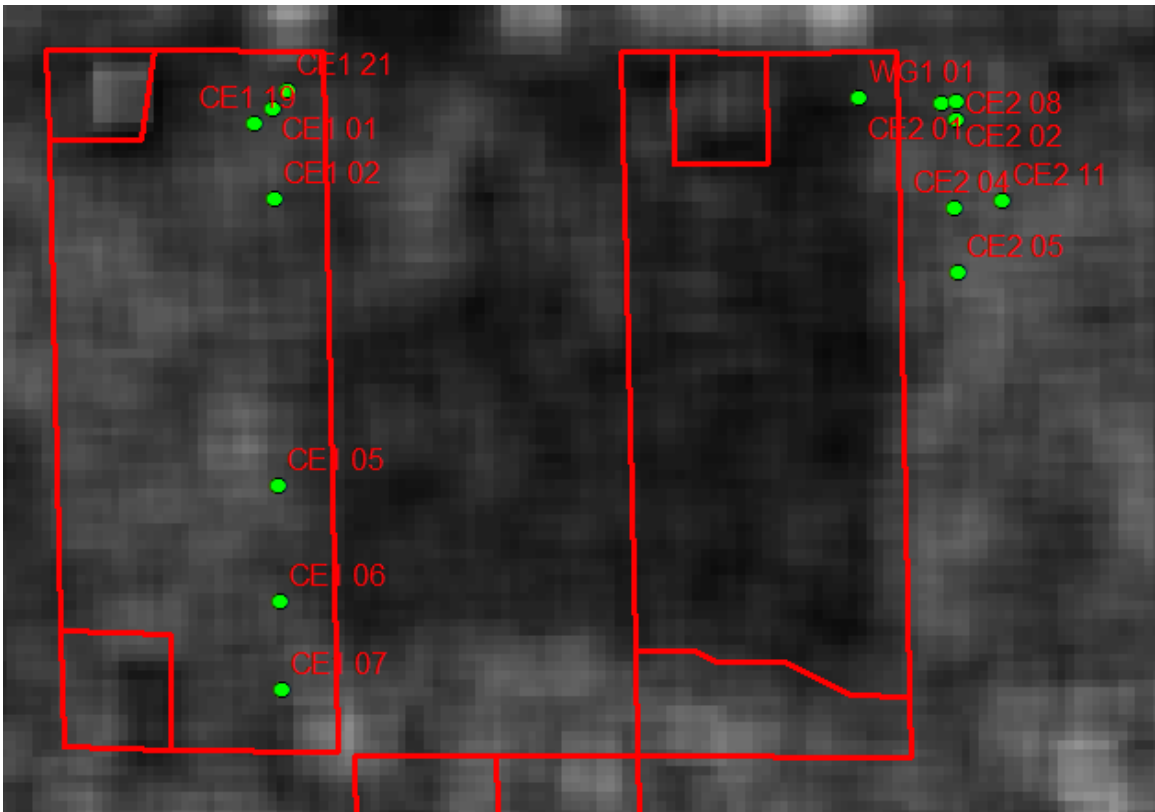


Figure D-7 (a)

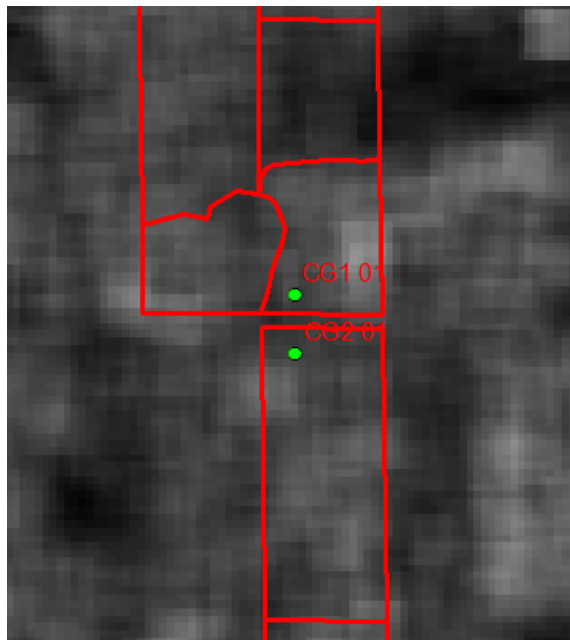


Figure D-7 (b)

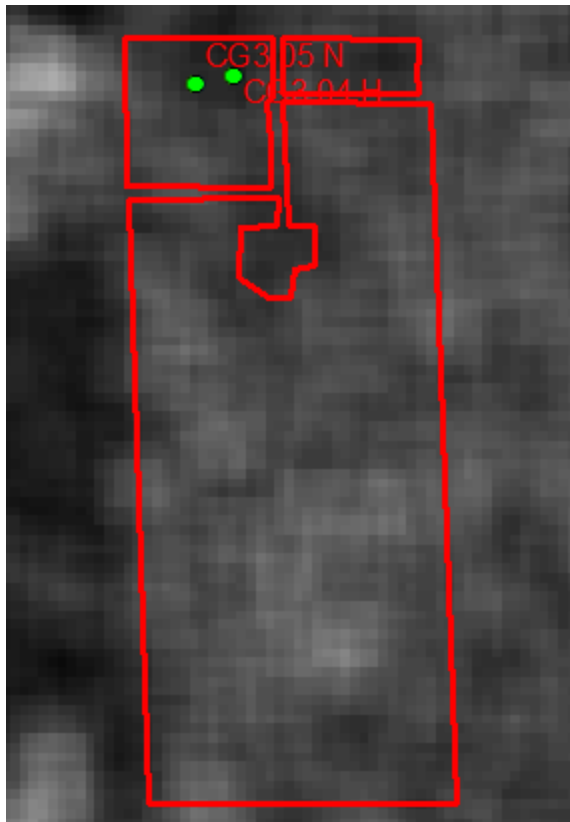


Figure D-7 (c)

Figure D-7: Detailed locations of the corn sample points and Radarsat-2 image for Stratford study site

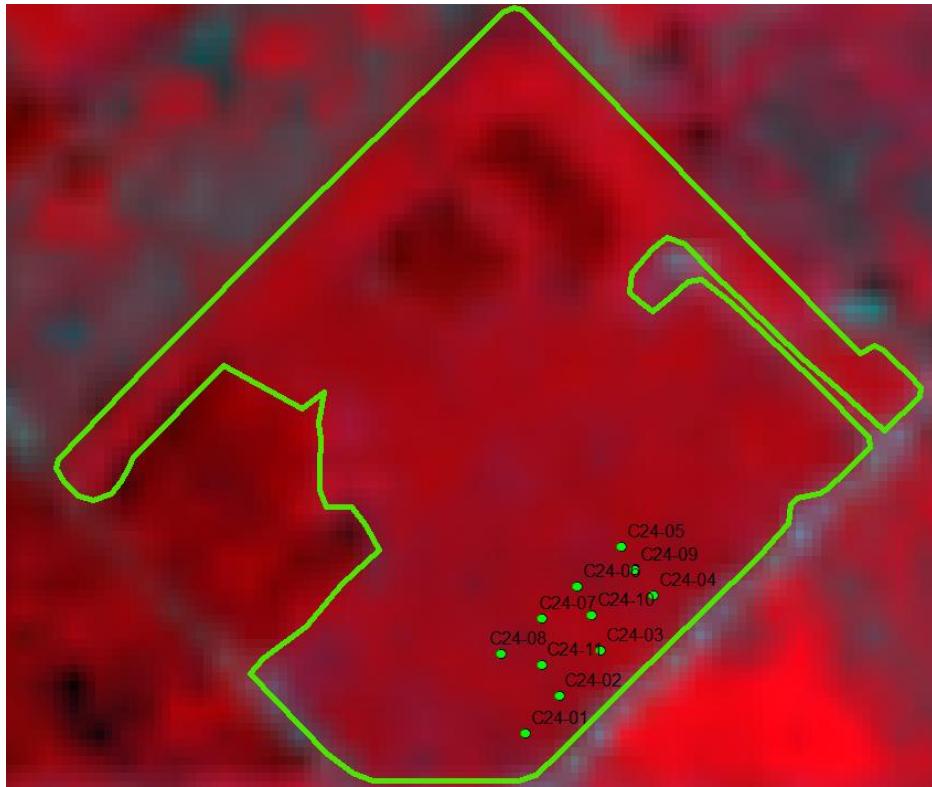


Figure D-8 (a)

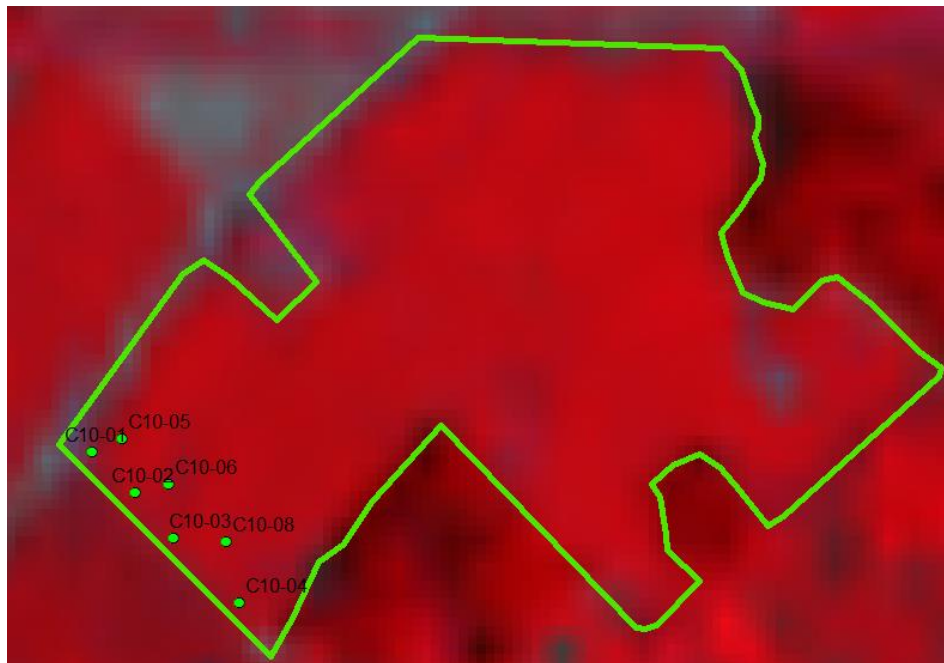


Figure D-8 (b)

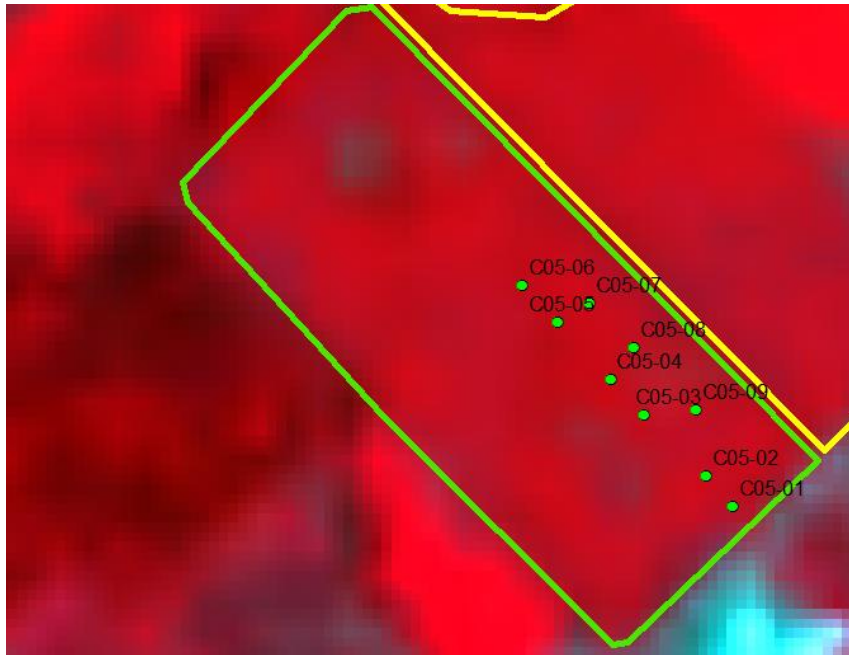


Figure D-8 (c)

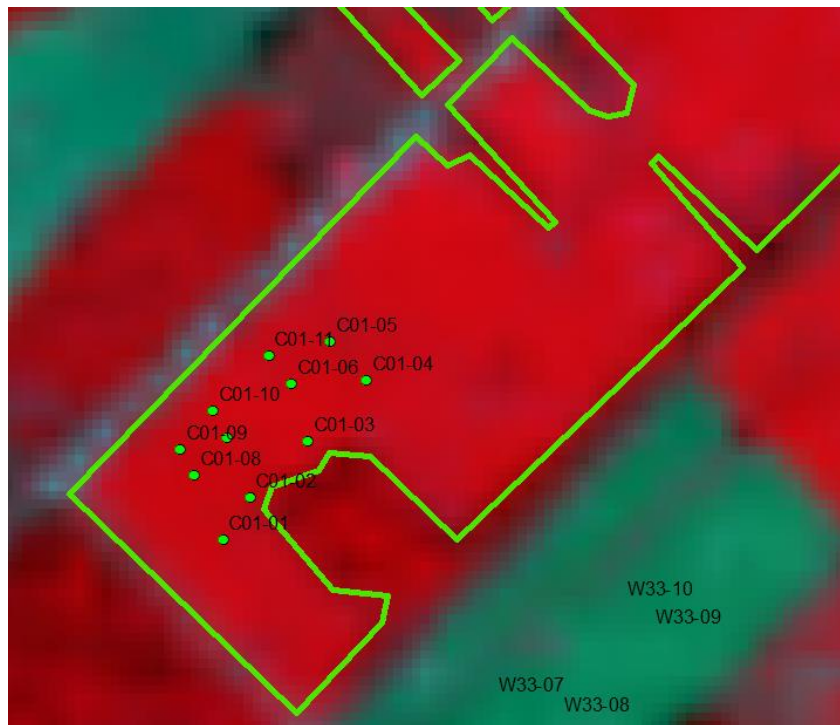


Figure D-8 (d)

Figure D-8: Detailed locations of the corn sample points and Landsat-8 image for Komoka study site

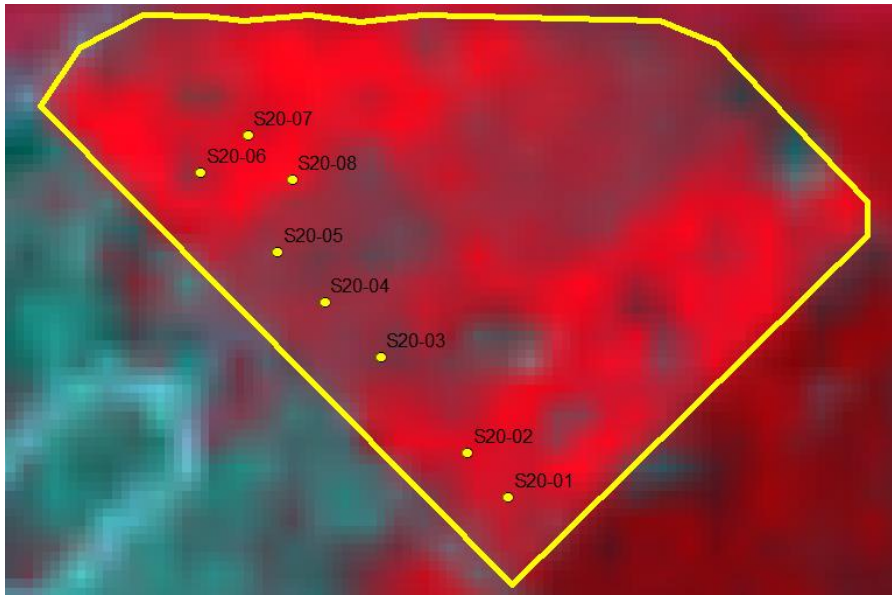


Figure D-9 (a)

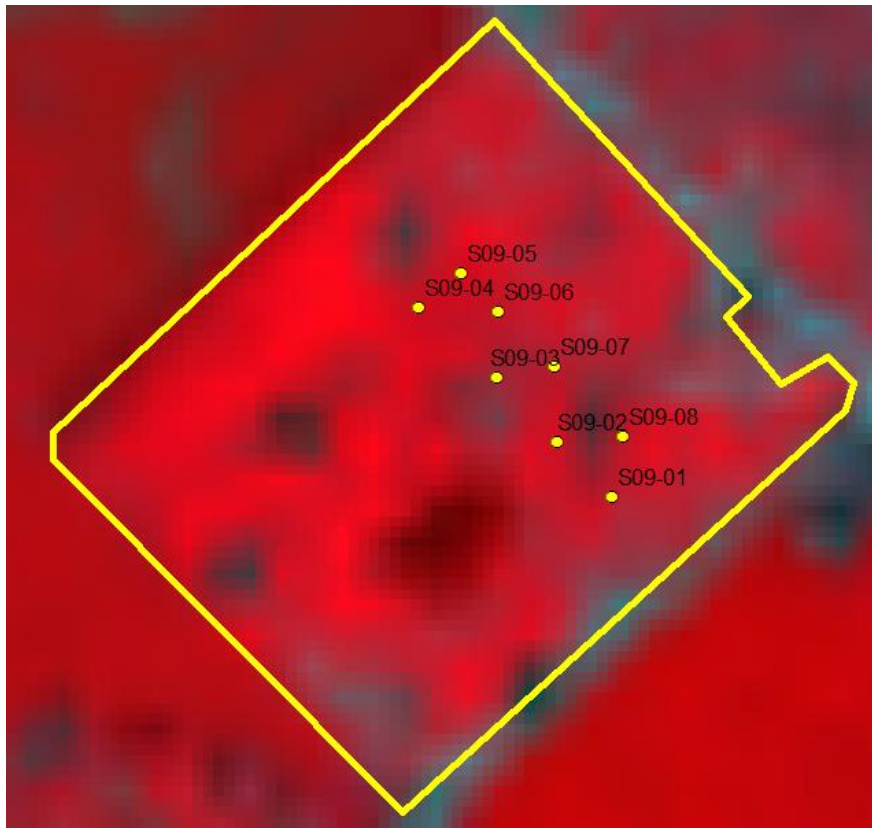


Figure D-9 (b)

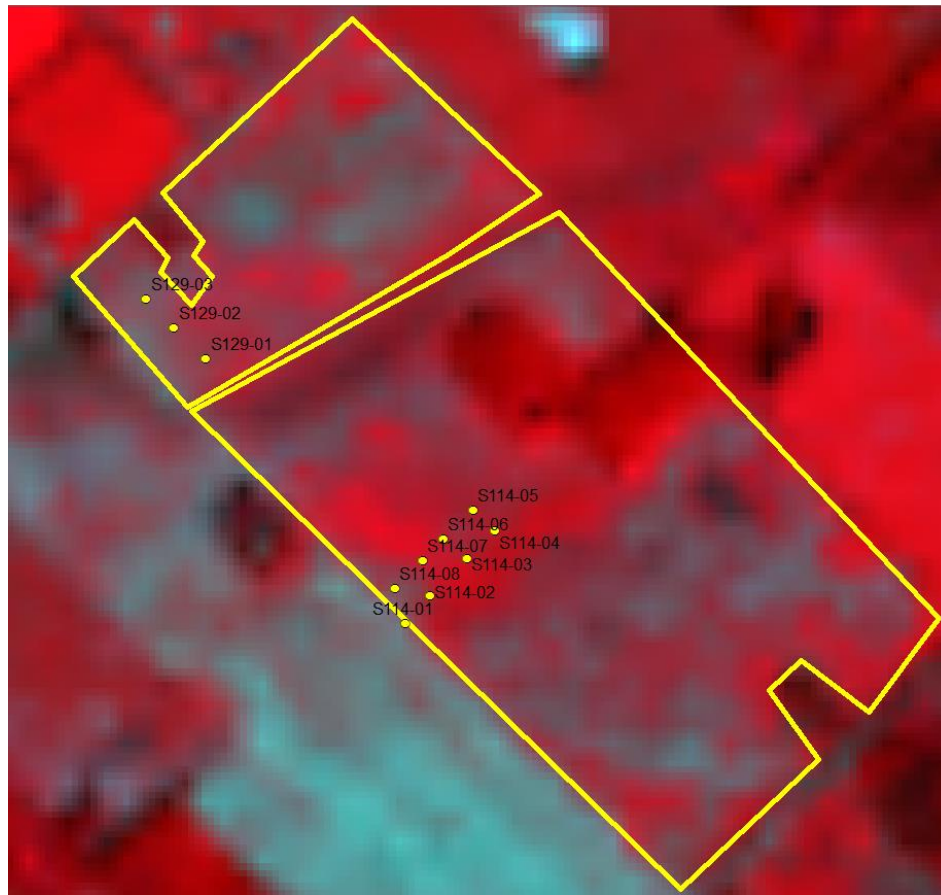


Figure D-9 (c)

Figure D-9: Detailed locations of the soybean sample points and Landsat-8 image for Komoka study site

Appendix E: Copyright Releases from Publications

Chapter 2:

The rights retained by the authors was specified in the Assignment of Copyright: terms & Conditions by Taylor& Francis Group:

RIGHTS RETAINED BY YOU AS AUTHOR

4. These right are personal to you, and your co-authors, and cannot be transferred by you to anyone else. Without prejudice to your rights as author set out below, you undertake that the fully reference-lined Version of Record (VoR) will not be published elsewhere without out prior written consent. You assert and retain the following rights as author(s):

viii. The right to include the article in a thesis or dissertation that is not to be published commercially, provided that acknowledgement to prior publication in the Journal is given.

Acknowledgement: This chapter is derived from an article published in International Journal of Remote Sensing (Published online: 29 Nov 2017) (copyright Taylor & Francis), available online: <https://www.tandfonline.com/doi/full/10.1080/01431161.2017.1407046>

Chapter 3:

This chapter is published by MDPI, which is Open Access. The published material can be re-used without obtaining permission as long as a correct citation to the original publication is given.

Acknowledgement: This chapter is derived from an article published in Remote Sensing (Published online: 4 Nov 2017), available online: <http://www.mdpi.com/2072-4292/9/11/1125/htm>

Chapter 4:

Canadian Journal of Remote Sensing - Decision on Manuscript ID CJRS-17-0076.R2

CJRS-JCT Editor-Rédactrice

22 May 2018 at 22:30

To: Chunhua Liao

Bonjour Chunhua Liao,

Yes, please go ahead and include the CJRS paper in your thesis. You can use the final Word version that was accepted for publication on March 31, 2018 and reformatted it in your thesis as suited by your university. You can write that your paper is part of the EO Summit 2017 Special Issue that will normally be published in CJRS-JCT vol. 44 issue 4 (August 2018). However, your paper could be on line before.

Best regards,

Monique

Monique Bernier

Editor in Chief – Rédactrice

Canadian Journal of Remote Sensing (CJRS)

Journal Canadien de télédétection (JCT)

Acknowledgement: This chapter is derived from an article accepted by EO Summit 2017 Special Issue of Canadian Journal of Remote Sensing (Will be published in CJRS-JCT vol. 44 issue 4).

References for Appendices

- Jensen, J. R. (2016). *Introductory digital image processing: a remote sensing perspective* (4th edition). Glenview, IL: Pearson Education, Inc.
- Larsen, R. (2002). Decomposition using maximum autocorrelation factors. *Journal of Chemometrics*, 16(8–10), 427–435. doi.org/10.1002/cem.743
- MacDonald, Dettwiler and Associates Ltd (MDA). (2016). *Radarsat-2 product description*. Retrieved from https://mdacorporation.com/docs/default-source/technical-documents/geospatial-services/52-1238_rs2_product_description.pdf?sfvrsn=10
- Moreira, A., Prats-Iraola, P., Younis, M., Krieger, G., Hajnsek, I., & Papathanassiou, K. P. (2013). A tutorial on synthetic aperture radar. *IEEE Geoscience and Remote Sensing Magazine*, 1(1), 6-43. doi:10.1109/MGRS.2013.2248301
- Natural Resources Canada. (2015 May 20). *Radar Polarimetry*. Retrieved from <http://www.nrcan.gc.ca/earth-sciences/geomatics/satellite-imagery-air-photos/satellite-imagery-products/educational-resources/9275>
- Retalis, A. (2010). *Fundamentals of satellite remote sensing*. Oxford, UK: Blackwell Publishing Ltd. doi:10.1111/j.1477-9730.2010.00613.x
- Switzer, P., & Green, A. A. (1984). *Min/max autocorrelation factors for multivariate spatial imagery*.
- Zeng, C. (2014). *Automated building information extraction and evaluation from high-resolution remotely sensed data*. University of Western Ontario. Retrieved from <https://ir.lib.uwo.ca/etd/2076>

Curriculum Vitae

Name: Chunhua Liao

Post-secondary Education and Degrees: Southwest Jiaotong University
Chengdu, Sichuan, China
2006-2010 B.E.

Peking University
Beijing, China
2010-2013 M.E.

The University of Western Ontario
London, Ontario, Canada
2014-2018 Ph.D.

Honours and Awards: Ontario Trillium Scholarship
2014-2018

IGARSS Travel Grant
2016

Related Work Experience Teaching Assistant
The University of Western Ontario
Sept. 2014- April.2018

Research Assistant
The University of Western Ontario
Sept. 2014- April.2018

Lecturer
The University of Western Ontario
Sept. 2017-Dec. 2017

Publications:

Peer-reviewed articles:

Chunhua Liao, Jinfei Wang, Xiaodong Huang, & Jiali Shang. (2018). Contribution of minimum noise fraction transformation of multi-temporal RADARSAT-2 polarimetric SAR data to cropland classification. *Canadian Journal of Remote Sensing*. 44(4). (*In press*).

Chunhua Liao, Jinfei Wang, Jiali Shang, Xiaodong Huang, Jianguai Liu, & Ted Huffman. (2018). Sensitivity study of RADARSAT-2 polarimetric SAR parameters to crop height

and fractional vegetation cover of corn and winter wheat in Southwest Ontario, Canada. *International Journal of Remote Sensing*, 39(5): 1475-1490.

Chunhua Liao, Jinfei Wang, Ian Pritchard, Jianguai Liu, & Jiali Shang. (2017). A spatio-temporal vegetation index image fusion model for generating high spatial and temporal resolution NDVI images in cropland areas. *Remote Sensing*, 9(11):1125.

Xiaodong Huang, Jinfei Wang, Jiali Shang, **Chunhua Liao**, & Jianguai Liu. (2017) Application of polarization signature to land cover scattering mechanism analysis and classification using multi-temporal C-band polarimetric RADARSAT-2 imagery. *Remote Sensing of Environment*, 193:11-28.

Chunhua Liao, Xianfeng Zhang, Quan Sun, Jiepeng Zhao, Xuyang Wang, & Huiyi Bao. (2011). Fractional vegetation cover estimation using HJ-1 spaceborne hyperspectral data. *Remote Sensing Information*, 65-70 (in Chinese).

Chunhua Liao, Xianfeng Zhang, & Yu Liu. (2012). Remote sensing inversion of fractional vegetation cover in arid areas using a multiple endmember spectral unmixing strategy. *Chinese Journal of Applied Ecology*, 3(12):3243-3249 (in Chinese).

Xianfeng Zhang, **Chunhua Liao**, Jonathan Li, & Quan Sun. (2013). Fractional vegetation cover estimation in arid and semi-arid environments using HJ-1 satellite hyperspectral data. *International Journal of Applied Earth Observation and Geoinformation*, 21: 506-512.

Xianfeng Zhang, **Chunhua Liao**, Yu Liu, & Jonathan Li. (2013). An Iconmap-based exploratory analytical approach for multivariate geospatial data. *Science China*. (1): 194-203.

Huiyi Bao, Xianfeng Zhang, **Chunhua Liao**, & Changxiong Wang. (2013). Co-inversion of snow parameters in Xinjiang based on MODIS and AMSR-E data. *Journal of Natural Disasters*, 4 (in Chinese).

Jiepeng Zhao, Xianfeng Zhang, **Chunhua Liao**, & Huiyi Bao. (2011). TVDI based soil moisture retrieval from remotely sensed data over large areas. *Remote Sensing Technology and Application*, 26(6):742-750 (in Chinese).

Conference Proceedings:

Chunhua Liao, Jinfei Wang. (2016). Evaluation of spatio-temporal data fusion methods for generating NDVI time series in cropland areas. *2016 IEEE International Geoscience and Remote Sensing Symposium (IGARSS)*, 2570 – 2573.

Chunhua Liao, Yang Lv, Xianfeng Zhang. (2013). Locust plague risk assessment in Xinjiang/China integrating quantitative remote sensing and GIS technologies. *The 5th International Conference on Geoinformation Technologies for Natural Disaster Management (GiT4NDM 2013)*. 137-142.

Chunhua Liao, Xianfeng Zhang, Huiyi Bao. (2012). Estimation of fractional vegetation cover by unmixing HJ-1 hyperspectral data. *The Second International Workshop on Earth Observation and Remote Sensing Applications (EORSA)*, 278 - 281.

Co-authored books and book Chapters:

Xianfeng Zhang, **Chunhua Liao**. (2014). *Ecological and environment variables co-inversion based on remote sensing technology*. Science Press. (in Chinese)

Xianfeng Zhang, **Chunhua Liao**. (2012). *Fractional vegetation cover mapping from the HJ-1 small satellite hyperspectral data. Advances in Mapping from Aerospace Imagery (Chapter 9)*. CRC Press. 204-220.

Patent:

Xianfeng Zhang, **Chunhua Liao**, Shuling Pan. (2014). A Remote Sensing-Based Progressive approach for risk prediction of rangeland locust hazard. CN 201410165284.